Effets d'optique non-linéaire d'ordre trois dans les cavités à cristaux photoniques en silicium : auto-oscillations GHz dues aux porteurs libres et diffusion Raman stimulée

Nicolas Cazier

UNIVERSITÉ PARIS SUD

Comprendre le monde, construire l'avenir®

STITS ECOLE DOCTORALE

UNIVERSITE PARIS-SUD

ÉCOLE DOCTORALE : STITS

Laboratory : *Institut d'Electronique Fondamentale*

***DISCIPLINE** PHYSICS*

PHD THESIS

presented the 13/12/2013

by

Nicolas CAZIER

Nonlinear optical effects of the third order in silicon photonic crystal cavities : High frequency self-induced oscillations and stimulated Raman scattering.

Thesis Advisor	Xavier Checoury	(Institut d'Electronique Fondamentale)
Composition of the jury :		
Referees :	Isabelle ROBERT-PHILIP	(CNRS - LPN)
	Yannick DUMEIGE	(Université de Rennes 1)
Examinators :	Nicolas DUBREUIL	(Institut d"Optique)
	Didier ERASME	(Telecom Paris-Tech)
	Philippe BOUCAUD	(Institut d'Electronique Fondamentale)

Abstract

In this thesis, we studied third order nonlinear optical effects in photonic crystal cavities. The first of those effects is is the phenomenon of high frequency (GHz) self-pulsing in these cavities, which originates from a modulation of the transmission of the cavity due to the interaction between the free-carrier dispersion and the two-photon absorption. We have observed these self-induced oscillations for the first time in silicon photonic crystal nanocavities, with a frequency of about 3 GHz and a high spectral purity. We have developed a model to analyze the mechanisms that govern the onset of these oscillations, as well as the amplitudes of the fundamental and harmonic frequencies of these oscillations. This self-pulsing phenomenon would allow us to realize realize ultra-compact microwave sources made of silicon. The second phenomenon studied is that of Raman scattering, which is the only way to obtain lasers fully in silicon demonstrated so far. The Raman scattering was measured first in narrow photonic crystals waveguides (W0.63) of length 100 microns, where we could obtain a number of Stokes photons up to 9, showing that the stimulated Raman scattering predominated in these waveguides, although we have not been able to obtain a true Raman laser effect in them. We then measured the Raman scattering in doubly resonant nanocavities specifically designed from these waveguides to optimize the Raman effect, with quality factors up to 235000 for the Stokes resonance. Although we could only measure spontaneous Raman scattering in these cavities, with a Purcell factor of 2.9, the theoretical study that we conducted on the Raman lasers, which agrees perfectly with the experimental results, shows that it would be possible to obtain a Raman laser in these cavities with a threshold below the milliwatt, provided we reduce the losses due to the free-carrier absorption. This could be accomplished by decreasing the free-carrier lifetime, for example by removing the free carriers from the silicon using a MSM junction.

Keywords : photonic crystals, silicon, non-linear optics, nanocavities, self-pulsing, microwaves, Raman scattering, lasers.

This document is an english translation I did of my PhD thesis, “Effets d’optique non-linéaire d’ordre trois dans les cavités à cristaux photoniques en silicium : Auto-oscillations GHz dues aux porteurs libres et diffusion Raman stimulée”, which was written originally in french. As english is not my native language, there may still be a few grammatical or spelling mistakes in it this thesis. I apologize in advance for those mistakes, and hope that this will not be a problem for the reader.

Nicolas Cazier

Acknowledgements

I would also like to thank the following members of the CTU (Centrale Technologique Universitaire) for helping me during the fabrication of the photonic crystals in the clean room of the Institut d'Electronique Fondamentale : Abdel Aassime, Fabien Bayle, Benoît Bélier, David Bouville, Jean-René Coudevylle, Sylvain David, François Maillard, Delphine Neel and Cédric Villebasse.

I also want to thank all my colleagues of the Photonics department of the IEF with whom I worked during the three years of my PhD thesis : Sébastien Sauvage, Moustapha El Kurdi, Guy Fishman, Paul Crozat, Iännis Roland, Dac Trung Nguyen, Malo de Kersauzon, Abdelhamid Ghrib, Mathias Prost and Candice Blin.

I also thank my family for supporting and encouraging me throughout this thesis.

This thesis was supported by the Agence Nationale de la Recherche (ANR) through the project PHLORA (ANR 2010 JCJC 0304 01).

Contents

1 Photonic Crystal nanocavities. 7

1.1 Introduction. . . . 7

1.2 Silicon Photonic Crystals 8

1.2.1 Definition and examples of photonic crystals 8

1.2.2 2D photonic crystals in a silicon membrane. . . . 9

1.2.3 Photonic crystals waveguides and nanocavities. . . . 10

1.2.4 Simulation of photonic crystal structures. . . . 13

1.2.4.1 Plane-wave method. . . . 13

1.2.4.2 FDTD method. . . . 15

1.3 Fabrication of the photonic crystals. . . . 16

1.3.1 Electron-beam lithography. . . . 16

1.3.1.1 GDS mask. . . . 16

1.3.1.2 Spin-coating of the sample. . . . 18

1.3.1.3 Raith 150 versus Nanobeam 4. . . . 18

1.3.2 Inductively Coupled Plasma Reactive Ion Etching of silicon. . . . 22

1.3.3 Cutting the substrate the diamond blade saw. . . . 25

1.3.4 Wet etching with hydrofluoric acid. . . . 27

1.3.5 Measurement of the sample's transmission. . . . 28

1.4 Modeling of nonlinear optical effects in nanocavities. . . . 28

1.4.1 Cavity in the linear regime. . . . 29

1.4.2 Nonlinear optics. . . . 32

1.4.2.1 Nonlinear polarization and susceptibility of silicon. . . . 32

1.4.2.2 Two-photon absorption and Kerr effect. . . . 33

1.4.2.3 Free-carrier absorption and dispersion. 36
1.4.2.4 Thermal dispersion. 39
1.4.2.5 Full equations system and modal volume of the cavity. . 40
1.4.3 Raman scattering. 41
1.4.3.1 What is Raman scattering ? 41
1.4.3.2 Stimulated Raman scattering in silicon. 43
1.4.3.3 Raman scattering in a doubly resonant cavity. 45
1.5 Conclusion. 49

2 High-frequency self-induced oscillations in a nanocavity. 51
2.1 Introduction. 51
2.2 Experimental setup used for the measurements. 53
2.3 The equations of the nanocavity. 55
2.4 Linearization around the steady-state solutions. 60
2.4.1 Linearized equation in matrix form. 60
2.4.1.1 Steady-state solutions. 61
2.4.1.2 Small variations around an equilibrium point. 62
2.4.2 Simplified expression of the frequency at high power. 63
2.5 Amplitude of the oscillations and spectral purity. 66
2.5.1 Numerical simulation of the equations with MATLAB. 66
2.5.2 Solving the equations by an harmonic analysis. 68
2.5.2.1 Solving the equations when neglecting the nonlinear absorptions. 69
2.5.2.2 Solving the equations in the general case. 72
2.5.3 Comparison with the case of a microring resonator. 75
2.6 Detailled analysis of the experimental results. 78
2.6.1 Summary of experimental results. 78
2.6.2 Determining the effective volume and free-carrier lifetime. 79
2.6.3 Comparison with the numerical simulations. 81
2.6.4 Self-pulsing due to the thermal effects. 83
2.6.5 Performances of the microwave source and how to improve them. 84
2.7 Conclusion. 88

3 Raman scattering in a nanocavity. 89

3.1 Introduction. . . . 89

3.2 Raman laser - Theoretical approach. . . . 90

3.2.1 The equations of a Raman laser. . . . 91

3.2.2 Steady-state solutions. . . . 92

3.2.2.1 Case where we neglect the other nonlinear effects. . . . 92

3.2.2.2 General case. . . . 94

3.2.3 Frequency response for a small modulation of the Raman laser. . 96

3.2.4 Relative Intensity Noise of the Raman laser. . . . 99

3.2.4.1 Definition of the RIN. . . . 100

3.2.4.2 Langevin noise sources. . . . 101

3.2.4.3 Noise spectral densities of the photons. . . . 102

3.2.4.4 Partition noise and RIN. . . . 103

3.2.4.5 Factor of Henry and frequency noise. . . . 105

3.3 Raman scattering in a doubly resonant cavity. . . . 108

3.3.1 Stimulated Raman scattering in W0.63 waveguides of length of 100 microns. . . . 108

3.3.2 Raman scattering in a doubly resonant cavity of length 12 periods. 125

3.3.3 Comparison with the Raman laser of Takahashi. . . . 138

3.4 Conclusion. . . . 142

CONTENTS

General introduction.

The field of non-linear optics in silicon has strongly expanded in recent times because of its numerous potential applications in integrated optics, photonics and opto-electronics. Silicon is not only silicon the semiconductor the most used in the microelectronics industry and has the property of guiding light to the wavelengths most used in telecommunication, but it has the advantage of presenting plenty of strong non-linear effects which could be used to design components for integrated optics and opto-electronics : two-photon absorption, optical Kerr effect, free carriers absorption and dispersion, thermal dispersion and stimulated Raman scattering.

The strength of those non-linear optical effects being usually quite weak, especially for nanometric-sized components, the only way to observe and exploit them without resorting to very high optical powers is to use optical resonators such as micro-disks or photonic crystal nanocavities to reinforce those non-linear phenomena. The importance of non-linear effects in this kind of resonators typically increases with the ratio between the quality factor of the resonator and its modal volume. Photonic crystals nanocavities are particularly interesting in that case, owing to their very high quality factors, which can reach several millions, and their very small modal volumes.

We have studied in particular two non-linear phenomena in silicon photonic crystals nanocavities during this thesis. The first of them is a self-pulsing phenomenon at high frequency (GHz) in those nanocavities, which has for origin the interaction between two separate non-linear effects, and is therefore particularly complicated. These effects are the free-carrier dispersion and the two-photon absorption which will create those free carriers. We were the first to observe this kind of non-attenuated oscillations, with a frequency of 3 GHz and a high spectral purity, in silicon photonic crystal nanocavities [1]. We were interested in studying this phenomenon for two reasons : first because of its potential applications to microwave photonics, particularly to the realization of ultra-compact microwave sources in silicon, and second because it allowed us to measure the free-carrier lifetime in our cavity and to evaluate the strength of the free-carrier absorption. This absorption is the main hindrance to the other non-linear phenomenon which we have studied, which is stimulated Raman scattering.

Another very interesting application of photonic crystal nanocavities is indeed the real-

ization of active components in silicon, and in particular the realization of lasers. Indeed, silicon having an indirect band gap, it is very inefficient for emitting light, which hinders the realization of classical semiconductor lasers using this material. Only the use of stimulated Raman scattering, a non-linear optical effect, has made possible the realization of silicon lasers up to now. But most Raman lasers in silicon obtained to date had the inconvenient of requiring very long cavities (more than 1 cm) or ring cavities with a high surface area (about 1 cm²) to obtain the necessary gain to the laser effect, which made them useless for integrated optics. Photonic crystals would allow us to increase the strength of Raman scattering without having to increase the size of the component and thus obtain Raman nanolasers in silicon. The only example of silicon Raman laser of nanometric size has thus been demonstrated in a silicon photonic crystal cavity by Takahashi [2], but this result is quite recent and has been published only a few months ago.

This thesis is divided in three chapters. The first chapter is used for a general presentation of photonic crystal nanocavities. It begins by defining what is a photonic crystal, and presents several examples of photonic crystals waveguides and cavities used during this thesis, as well as the numerical methods used to simulate those crystals, before detailing the different steps of the fabrication of those crystals, fabrication which was done in the clean room of the IEF. We ended this chapter with a modeling of the different non-linear optical effects existing in those nanocavities and a presentation of the equations used to model those nanocavities. The second chapter describes the phenomenon of high-frequency self-induced oscillations in those cavities, which is created by the interaction between two-photon absorption and free-carrier dispersion, and its application to the field of microwave photonics. The third chapter describes the Raman scattering in photonic crystal nanocavities in silicon with two resonances, and examines the possibility of realizing a silicon Raman nanolaser using those cavities.

Chapter 1

Photonic Crystal nanocavities.

1.1 Introduction.

In recent years, there has been an increasing interest for photonic crystals nanocavities, which are structures able to strongly confine light and thus obtain very high quality factors. These cavities have indeed numerous applications, such as the realization of very small filters [3, 4] or of nanolasers with very low thresholds [5, 6, 7, 8]. In particular, photonic crystals nanocavities are characterised by their very small modal volumes, of the order of $(\lambda/n)^3$, where λ is the wavelength in vacuum of the resonance mode of the cavity and n is the optical index of the material constituting the cavity [9, 10, 11]. Since the strength of light-matter interactions in the cavity depends on the ratio between the quality factor of the cavity and its modal volume, the non-linear optical effects are particularly important in photonic crystal cavities. For this reason, the field of non-linear optics in photonic crystals presents a strong interest for photonic applications and all-optical signal processing [12]. The existence of numerous non-linear phenomena such as two-photon absorption (TPA), third-harmonic generation, four-wave mixing, optical bistability, stimulated Raman scattering has been demonstrated in photonic crystals by different groups [13, 14, 15, 16]. During this thesis, two non-linear effects in silicon photonic crystal nanocavities have been particularly studied : the high frequency self-induced oscillations induced by free-carrier absorption, and the stimulated Raman scattering, which is the only phenomenon allowing the realization of lasers fully in silicon.

The first chapter presents a general description of these silicon photonic crystal nanocavities. It is divided in three parts. The first part is dedicated to the photonic crystals themselves. It begins by defining what a photonic crystal is and giving several examples of these photnic crystals, before describing in particular two-dimensional photonic crystals etched in a silicon membrane, which we studied during this thesis. It then describes rapidly the methods used to create waveguides and cavities inside those photonic crystals,

as well as the softwares used to simulate these crystals, waveguides, and cavities. The second part is dedicated to the fabrication of these silicon photonic crystal nanocavities, which was done in the clean room of the IEF, and to the description of the different steps of this fabrication : e-beam lithography, inductively coupled plasma reactive ion etching, substrate cutting with a diamond blade saw, wet etching to create the silicon membrane, and finally measurements of the transmission of the fabricated photonic crystals. The third part describes the mathematical model used for non-linear optical effects in those nanocavities. It begins by describing the equations of the cavity in linear regime obtained using temporal coupled-mode theory, then the non-linear electrical polarization which created those non-linear optical phenomena, before using this non-linear polarization to modify the cavity equations to take into account the different non-linear optical effects having an influence on our experimental measures : the two-photon absorption, the free-carrier absorption and dispersion, the thermal dispersion, and finally the stimulated and spontaneous Raman scattering which are behind the Raman lasers.

1.2 Silicon Photonic Crystals

1.2.1 Definition and examples of photonic crystals

Photonic crystals are structures whose dielectric constant varies periodically in one or more directions of space, so called by analogy with real crystals, which are periodic arrangements of atoms or molecules. In a real crystal, the periodic variation of the electric potential causes the appearance of forbidden energy bandgaps where the electrons can not travel. A similar phenomenon occurs in photonic crystals, due to interference of light at the interfaces between different dielectric materials of the photonic crystal : when the difference between the dielectric constants of these materials is large enough, forbidden energy bandgaps where photons can not travel may appear, similar to those of electrons in atomic crystals. Concretely, this means that the light can not propagate for some bands of wavelengths in certain directions of the photonic crystal [17]. This feature allows us to use photonic crystals to control the propagation of light and thus design waveguides and nanocavities using these photonic crystals.

The simplest photonic crystals are those in one dimension. They consist of a stack of several layers of different refractive index materials (see Fig. 1.1a), known as a Bragg mirror because it will reflect almost all light at normal incidence for the frequencies inside its bandgap. But this type of relatively simple structure has been known for over a century [17], and is of a limited interest regarding the manipulation of light, since it can only confine photons in a single dimension of space. For this reason, research on photonic crystals tend to focus on structures in two or three dimensions (see Fig. 1.1b and c), since

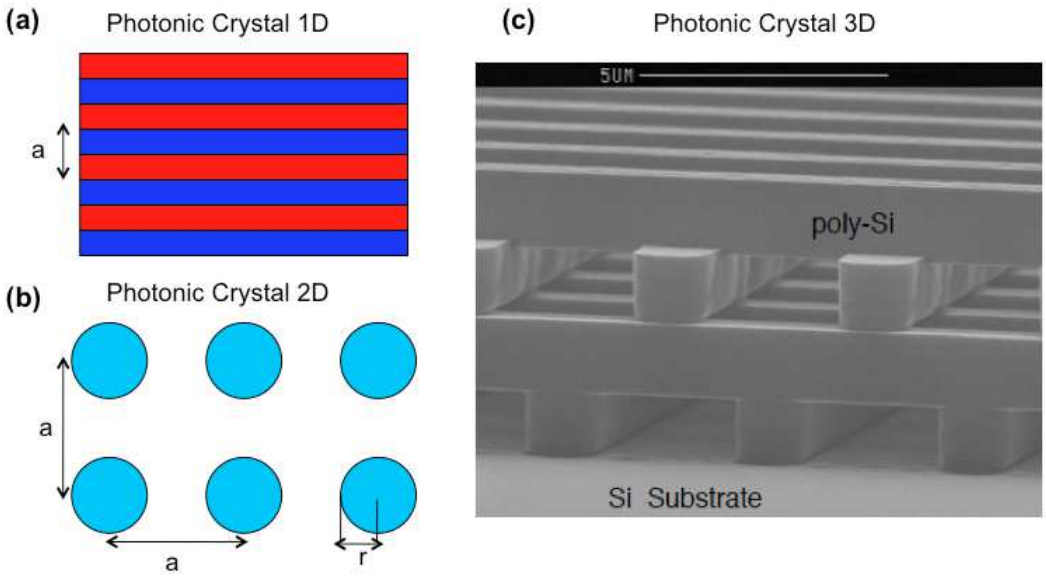

Figure 1.1: Some classic examples of photonic crystals. (a) 1D photonic crystal (Bragg mirror) made of alternating layers of materials with different electrical constants, with a thickness of $a/2$ (where a is the period of the photonic crystal) (b) 2D photonic crystal composed of columns of dielectric material with a radius r, distributed over a square mesh with a period a. (c) SEM image of a 3D photonic crystal silicon, of woodpile type (figure reprinted with permission from Macmillan Publisher Ltd : Nature, Ref. [20], copyright 1998).

the works of E. Yablonovitch and S. John in 1987 [18, 19].

1.2.2 2D photonic crystals in a silicon membrane.

At first glance, 3D photonic crystals seem to be more useful than 2D photonic crystals for designing waveguides and cavities because they are the only ones with a complete bandgap confining light in all dimensions of space. Unfortunately, these 3D photonic crystals are much more difficult to make than 2D photonic crystals, which limit their applications at the moment. Since 2D photonic crystals are easier to make and more compatible with integrated optics, we decided to work with them. The material used to fabricate these photonic crystals is silicon, since it is the least expensive semiconductor and therefore the most widely used in microelectronics. It is therefore the ideal material for integrated optics.

The basic structure that we studied is composed of a triangular lattice of air holes in a silicon matrix. This type of photonic crystal has a forbidden bandgap for transverse electric modes (TE), i.e. modes whose electric field is orthogonal to the axis of the holes (see Fig. 1.2a). This triangular array serves to confine the light horizontally in the photonic crystal, but not vertically. In order to confine the photons in all three dimensions of space, we used photonic crystals consisting of a thin membrane of silicon in which the triangular lattice

of air holes was etched. This type of structure will confine light horizontally through the network of air holes, and vertically through the air/silicon interface and the total internal reflection (see Fig. 1.2b).

Indeed, far from the silicon membrane, the modes unconfined in the silicon behave like plane waves, and therefore have as dispersion relation $\omega = c|\overrightarrow{k}| = c\sqrt{k_x^2 + k_y^2 + k_z^2}$. For a given value of $\overrightarrow{k_{||}} = \overrightarrow{k_x} + \overrightarrow{k_y}$, the vector $\overrightarrow{k_z}$ can take any value. For an unconfined mode, we need to have the relation $\omega \geqslant c|\overrightarrow{k_{||}}|$. Therefore, any mode whose frequency is below this value, i.e. any mode for which we have $\omega < c|\overrightarrow{k_{||}}|$, will have to remain confined in the silicon membrane and thus in the photonic crystal. The curve $\omega = c|\overrightarrow{k_{||}}|$ is therefore called the light line and the region of band diagram located above this line is therefore called the light cone [17].

Of course, the presence of the light cone is not the only difference between the band diagram of the 2D photonic crystal in a block of silicon of infinite size and its equivalent in the form of silicon membrane. The forbidden bandgap for the silicon membrane is indeed higher in frequency than for the 2D photonic crystal, due to the lower dielectric constant of the air surrounding the silicon membrane. Since the normalized central frequency of the bandgap is 0.28, if we want this bandgap to be centered around $\lambda_0 = 1500$ nm, i.e. around the band of wavelengths most commonly used in telecommunications, the period of the photonic crystal must be equal to $a = 0.28 \times \lambda_0 = 420$ nm. Typically, a photonic crystal with a length of 20 periods will then have a size of less than 10 microns. An optical system based on the use of photonic crystals will thus be of a very small size, ideal for applications to the fields of integrated optics and opto-electronics.

1.2.3 Photonic crystals waveguides and nanocavities.

To obtain a waveguide from the photonic crystal described above is relatively simple : it suffices to remove a row of holes in the direction ΓK of the triangular lattice of air holes, thereby introducing a linear defect in the structure (see Fig. 1.3a). This defect will then become a waveguide, called waveguide W1, for some of the frequencies in the forbidden bandgap of the photonic crystal. Concretely, this means that a new mode (actually several modes, even and odd along the y direction, but we are concerned only with the odd mode, which is the one we used for our cavities) will appear within the forbidden bandgap inside the band diagram of the photonic crystal band (see Fig. 1.3c). This new mode corresponds to the mode of the waveguide W1 (see Fig. 1.3b).

One of the advantages of the photonic crystals waveguides is the effect of slow light which enhances nonlinear effects in these crystals [22, 12, 14]. This is due to the very low values of the group velocity $v_g = d\omega/dk$ for the guided mode in these crystals, which will slow down the passage of light in the material forming the photonic crystal and will

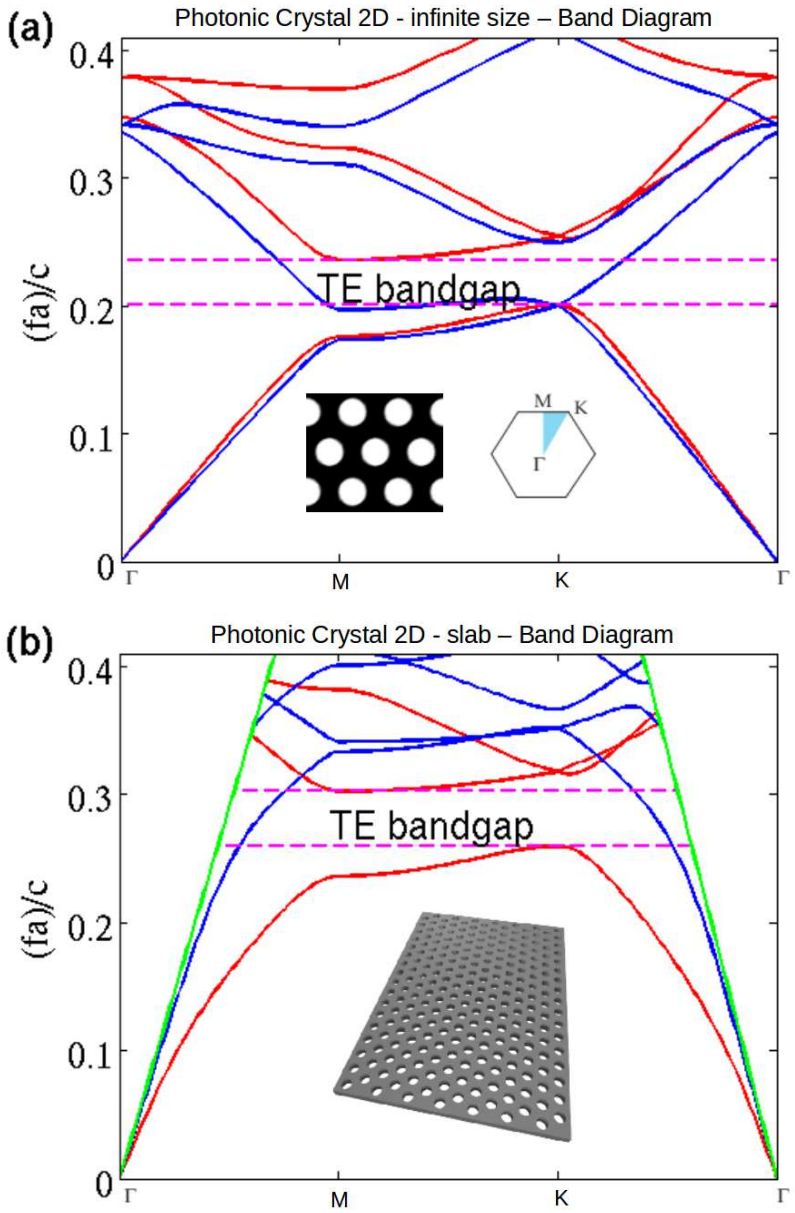

Figure 1.2: (a) The band diagram of a photonic crystal composed of a triangular lattice of air holes in a block of silicon of infinite size (calculated using the software MPB), describing the dispersion relation of the structure between the normalized frequency $(f \times a)/c$ (where c is the speed of light in vacuum and a the period of the photonic crystal) and the wave vector $\overrightarrow{k}$. The diameter of the holes is $r = 0.25 \times a$. The transverse electric modes (TE) are in red, and the transverse magnetic modes (TM) in blue. This type of photonic crystal has a forbidden bandgap for TE modes (pink dotted lines). The modeled structure and the first Brillouin zone are also shown in the diagram. (b) The band diagram for the same photonic crystal, but this time consisting of a silicon membrane of thickness $a/2$ in which the network of air holes was etched. The photonic crystal in question is shown in the diagram (image from [21]). The light cone, below which the modes stay confined within the silicon membrane, is shown in green.

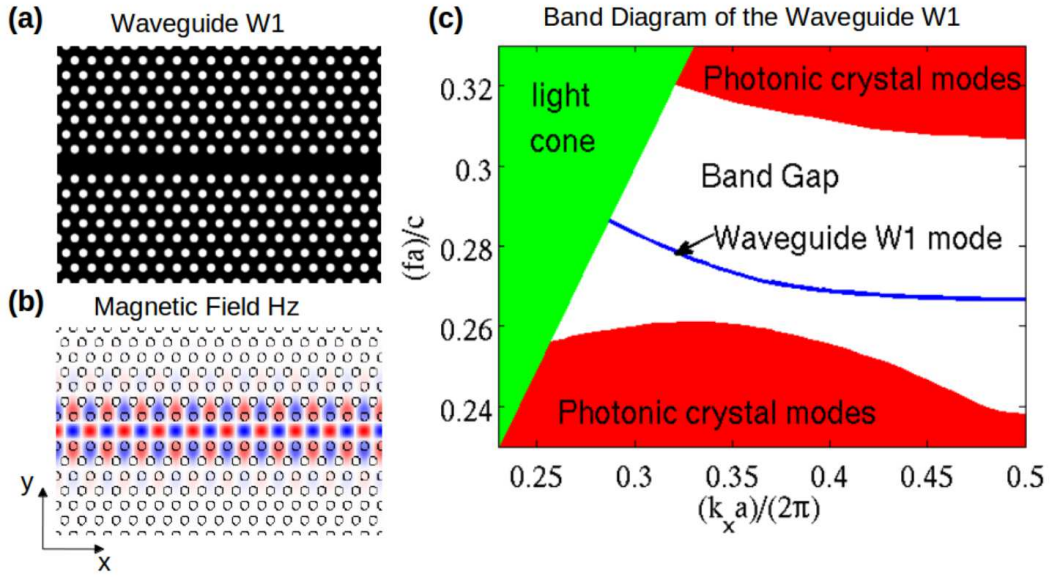

Figure 1.3: (a) Schematic of a waveguide W1 in the direction ΓK for a photonic crystal period with radius $r = 0.25 \times a$, in a silicon slab of thickness $h = 0.48 \times a$. Its width is equal to $\sqrt{3}a$. (b) The component H_z of the magnetic field of the guided mode for $k_x = \pi/a$ (i.e. for the point K of the Brillouin zone), simulated using software MPB. This mode is odd in y there, but seems even because $\overrightarrow{H}$ is a pseudo-vector. (c) The band diagram of the waveguide W1 (for TE modes). Only the bands for the odd modes are shown. The modes of the photonic crystal are in red, the odd guided mode is in blue, and the light cone is in green. Around the point $k_x = \pi/a$ (point K), the light group velocity $v_g = d\omega/dk$ for the guided mode is almost equal to zero.

therefore amplify the light/matter interactions and the nonlinear effects. This results in a dispersion curve flat or nearly flat at the edge of the Brillouin zone in the band diagram of the photonic crystal, for example near the point K in the case of W1 guide (see Fig. 1.3c).

There are many ways to design a photonic crystal cavity. The simplest is to just remove a few holes of the photonic crystal, creating a point defect inside the crystal [23, 9], along the same principle as for the design of the waveguides W1 (where the defect is linear). Nanocavities with quality factors up to 3.2×10^5 have been obtained with this method [24]. Another method is to take a classical waveguide W1, but to vary the period of the photonic crystal around the waveguide, creating what is called a double-heterostructure cavity [10, 25], where the period is larger in the middle of the waveguide W1 guide than on its ends, creating a nanocavity within the waveguide W1. Quality factors up to 3.9×10^6 could be measured in these cavities [25].

A third kind of cavity, which is the one we studied, are those designed by local modulation of the width of the waveguide, i.e. by shifting some of the holes surrounding the waveguide of a specific distance. These were originally presented in 2006 by Kuramochi [26]. An example of this kind of cavity is shown in figure 1.4. Quality factors of up to 2×10^6 were measured for this kind of cavity in silicon by our team [27]. The experimental measurements presented in Chapter 2 of this thesis were performed on a cavity of this kind.

1.2.4 Simulation of photonic crystal structures.

To predict the behavior of the photonic crystal structures that we made, I used during my thesis two different numerical simulation techniques. The first is the plane-wave method [28], which allowed us to calculate the band diagrams of these structures, and the second is the FDTD (Finite Difference Time Domain) method [29], which allowed us to calculate their transmission spectra and their resonance frequencies.

1.2.4.1 Plane-wave method.

The plane-wave method is used to simulate periodic structures of infinite size and allow us to calculate the band diagram of a photonic crystal. Due to the periodicity of the photonic crystal, we can apply the Bloch theorem and express the magnetic field for each wave vector $\vec{k}$ of the Brillouin zone in the following form :

$$\vec{H}_{\vec{k}}(\vec{r}) = e^{i\vec{k}.\vec{r}}\,\vec{u}_{\vec{k}}(\vec{r}) \tag{1.1}$$

where $\vec{u}_{\vec{k}}$ is a periodic function with the same period as the photonic crystal ($\vec{r}$ being the position vector). We then just have to insert this expression in the classical equation of

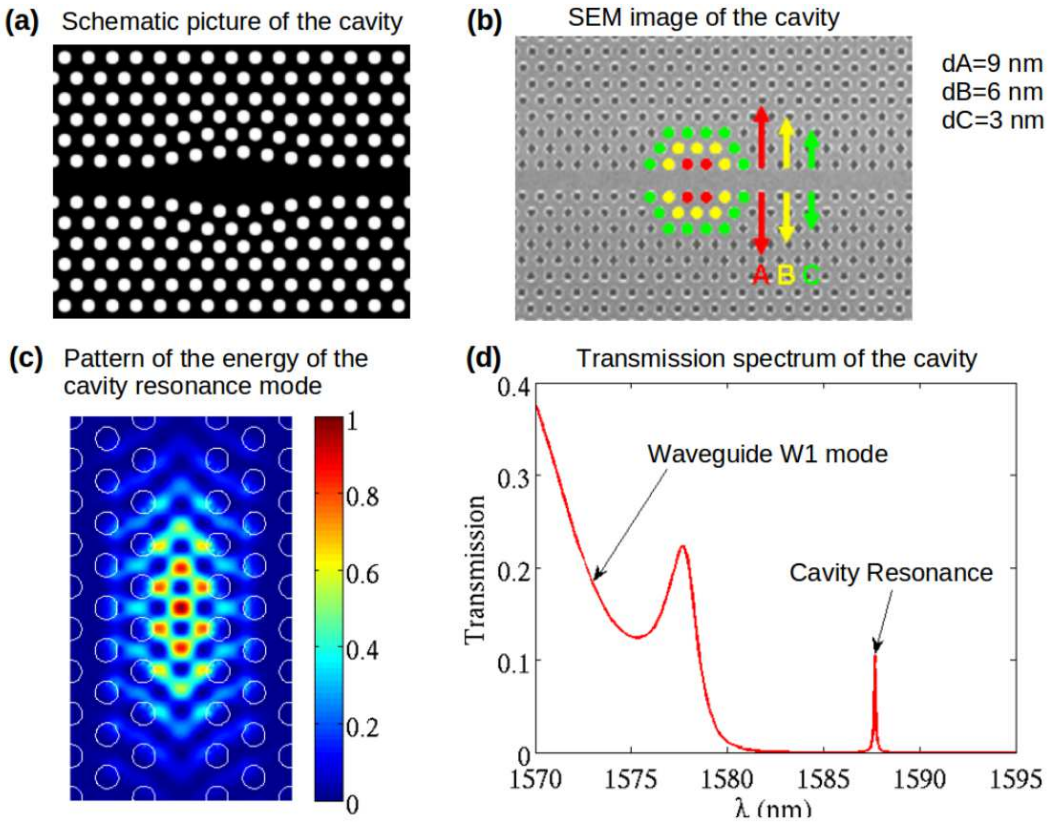

Figure 1.4: An example of a cavity of the kind created by Kuramochi, created by local width modulation of a waveguide W1 [26]. (a) Schematic of the cavity in question. Its period is $a = 420$ nm, the radius of the holes is $r = 105$ nm and the thickness of the silicon plate is $h = 200$ nm. The holes shifts were greatly exaggerated for the sake of clarity: it is in fact only of a few nanometers for the actual cavity and thus almost invisible. (b) SEM (scanning electron microscope) image of the cavity [27]. The holes colored in red, yellow and green have been moved to 9, 6 and 3 nm respectively in the transverse directions to create the cavity. (c) The pattern of the energy of the resonance mode of the cavity, simulated by FDTD (Finite Difference Time Domain) with the MEEP software. (d) The transmission of the cavity calculated by FDTD. For this cavity, the wavelength of the resonance is $\lambda_0 = 1587.7$ nm and the quality factor is $Q = 1.3 \times 10^4$.

propagation of the electromagnetic waves:

$$\nabla \times \left(\frac{1}{\varepsilon_r(\vec{r})} \nabla \times \vec{H}(\vec{r}) \right) = \left(\frac{\omega}{c} \right)^2 \vec{H}(\vec{r}) \tag{1.2}$$

to obtain the following equation concerning $\vec{u}_{\vec{k}}$ [17]:

$$\left(i\vec{k} + \nabla \right) \times \left(\frac{1}{\varepsilon_r(\vec{r})} \left(i\vec{k} + \nabla \right) \times \vec{u}_{\vec{k}}(\vec{r}) \right) = \left(\frac{\omega(\vec{k})}{c} \right)^2 \vec{u}_{\vec{k}}(\vec{r}) \tag{1.3}$$

We can then calculate for each wave vector $\vec{k}$ of the first Brillouin zone the eigenvalues $\omega_n(\vec{k})$ of equation 1.3 to obtain the dispersion curves of the photonic crystal and thus its band diagram (n is used to number the eigenvalues and therefore also represents the number of the band). All band diagrams shown in this thesis were calculated using the plane-wave method by FFT (Fast Fourier Transform) using the MPB software (MIT Photonic-Bands). MPB is a free software developed specifically by Joannopoulos of the Massachusetts Institute of Technology team [17] to calculate the band diagrams of a photonic crystal. To use this software, we just have to define a cell that will represent a period of the photonic crystal we want to simulate and a periodic array along which this cell will be replicated to create a photonic crystal of infinite size. For a waveguide we need to define a cell that will represent a period of the waveguide, along with the surrounding photonic crystal, in order to simulate it correctly.

1.2.4.2 FDTD method.

The FDTD method is probably the most commonly used method in our field to perform electromagnetic waves simulations. Unlike the plane-wave method, it is not limited to periodic structures. This makes it very useful for simulating photonic crystals of finite dimensions, and specifically to calculate the transmission spectra of photonic crystals waveguides [30] or the resonant frequencies and the pattern of the electric field of the photonic crystal nanocavities [26]. The edges of the cell containing the structure we want to simulate are then covered by PML (Perfectly Matched Layer), layers of artificial absorbing material that will eliminate any reflection on the edges of the cell which could disrupt the simulation [31]. The FDTD method has nevertheless the disadvantage of having computation times far higher than the plane-wave method. The FDTD simulations we have performed in this thesis were all made using the free software MEEP (MIT Electromagnetic Equation Propagation), which was developed by Joannopoulos at MIT, like the MPB software we used for the plane-wave method [17]. The modal volume of the cavities that we studied in this thesis were all calculated from the electric field patterns obtained using the FDTD simulation of these cavities. The resonance frequencies and quality fac-

tors of these cavities were then determined using either the Prony method or the Padé approximant method, which have been implemented for MATLAB by X. Checoury.

1.3 Fabrication of the photonic crystals.

After finishing the modeling of our photonic crystal structures using the software described above, and determining what should be the parameters of the structure that we want to study, we need to fabricate this structure. This fabrication is done in four steps. In the first step, electron beam lithography is used to expose the resist which will be used as a mask during the etching step. Then, in the second step, plasma ion etching is used to etch the holes of the photonic crystal in the silicon layer. Thereafter, the sample is cut with a diamond blade saw in order to free the access waveguides to the photonic crystal. And finally, a wet etching is used to remove the silica below the photonic crystal and create the silicon membrane. After the fabrication, we need to measure the transmission of the sample to ensure that all the steps of the fabrication went well and that the structure produced corresponds to the simulated structure.

1.3.1 Electron-beam lithography.

It goes without saying that the fabrication of photonic crystals must be as accurate as possible if we want the structures to behave in the way predicted by our simulations. For example, for a waveguide W1, an error of a few nanometers on the position of some of the holes in the first row of the photonic crystal during the lithography can unwittingly create a nanocavity inside the waveguide, and thus greatly modify its behavior. A slightly larger or smaller hole in the photonic crystal can create in the same way a nanocavity. The very small size of the holes of the photonic crystal, with radius of the order of 100 nm, will amplify the importance of these defects and make the photonic crystals more difficult to fabricate. For these reasons, electron-beam lithography is the method of choice for the fabrication of photonic crystals, due to its high accuracy. It is therefore this method that I used during my thesis.

1.3.1.1 GDS mask.

The first step of the electron beam lithography is to create a mask of the structure in GDS format. These masks were created using the L-Edit software, a software used for the design of integrated circuits which can generate masks in GDS format. This software is very useful because it has a C++ compiler that allows the user to create sub-programs

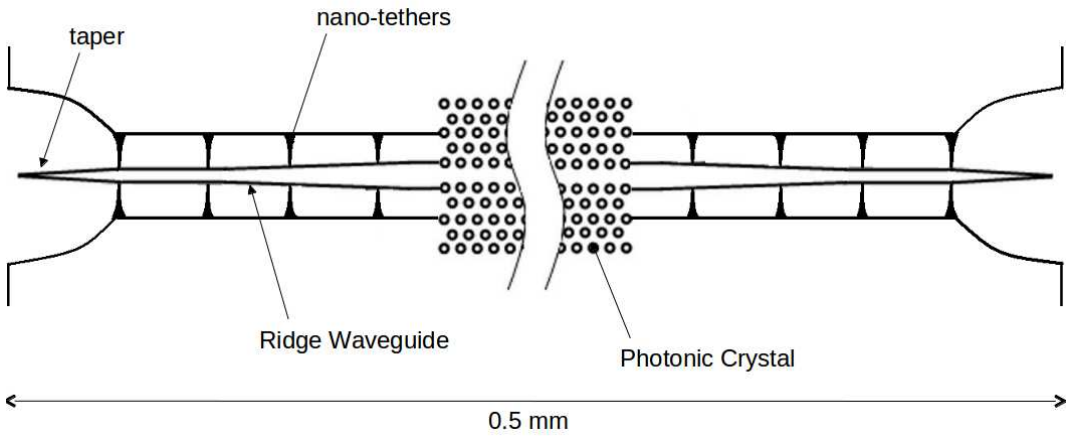

Figure 1.5: Schematic structure of the GDS mask, with the photonic crystal, the access waveguides and their tapers [21].

within the mask, allowing us to automatically generate the masks of the photonic crystals and their access waveguides, greatly simplifying the creation of the GDS mask.

Each structure to be exposed is divided into three parts (see Fig. 1.5). In the center is a membrane photonic crystal, usually crossed by a waveguide created by removing a row of holes, possibly with a nanocavity in the middle of the photonic crystal. We decided to use membrane photonic crystals rather than photonic crystals etched into a silicon layer based on silica, because the electric fields will be better confined in these crystals, allowing us to obtain much better quality factors. In addition, these crystals will be symmetrical with respect to the plane z = 0, because we have air on both sides of the silicon slab forming the crystals, which facilitates the simulations and the design of these photonic crystals with MEEP and MPB. On each side is a ridge type waveguide, held suspended by nano-tethers. These waveguides should be suspended if we want to obtain membrane photonic crystals. The width of the waveguide is typically 500 nanometers, but expands (or shrinks) progressively as it approaches the photonic crystal to have the same width as the waveguide of the photonic crystal, to facilitate the coupling between the two waveguides. These waveguides are used to inject light into the photonic crystal and to collect it. At the ends of these waveguides are tapers, through which light is injected or collected using a focusing optical fiber. The total losses we measured in a ridge waveguide without a photonic crystal in the middle are of 16 dB, from which we can infer that the total losses between the optical fiber and the entrance (or exit) of the photonic crystal are 8 dB. The total width of the structure is 500 microns, but there are usually several hundred structures on each fabricated sample, so the total length of the completed sample is of a few centimeters (its width will still be of 500 microns).

1.3.1.2 Spin-coating of the sample.

The substrate on which we made photonic crystals is a SOI (Silicon on Insulator) kind of substrate, oriented along the crystallographic direction [100] of silicon. It consists of three layers : a thin layer of intrinsic silicon, of thickness 200 nm, in which we will etch the photonic crystals, an intermediate silica layer, of thickness 2 microns, which will then be partially removed during the wet etching to create a membrane photonic crystal, and a silicon layer, of thickness 750 microns, used to support the other two. The SOI wafer, originally provided by the company SOITEC of Grenoble, has a diameter of 8 inches (or 20 cm), but was cut into small squares of 1 or 2 centimeter with a diamond blade saw for the e-beam lithography.

Before spin-coating the sample, the substrate is cleaned with acetone and isopropanol in order to remove any particles that may prevent the resin from spreading properly. Ultrasonic treatment is performed if necessary to remove particularly tough particles. The resist we have chosen for the e-beam lithography is the ZEP 520A electronic resist provided by the Japanese company Zeon Corporation, as it is the one that allows us to obtain the best resolution in electron beam lithography whilst having good resistance to plasma etching. To obtain a good resolution during the lithography, we must obtain a layer of resist that is very thin while still thick enough to withstand the plasma etching that will follow the e-beam lithography. For this, the resist must first be diluted in proportion 1:1 with anisole. We must then wait 15 minutes for the diluted resist to homogenize.

This diluted resist is then deposited on the substrate by spin-coating. The program used is relatively simple : the spin coater speeds for three seconds until it reaches a speed of 4000 revolutions per minute, which is then maintained for 1 minute. This allows us to obtain a final resist layer thickness of 150 nm. The resist must then be prebaked on a hot plate at 180 ° C for 150 seconds.

1.3.1.3 Raith 150 versus Nanobeam 4.

The principle of electron beam lithography is relatively simple. An electron beam is emitted by an electron source and then accelerated with a voltage source. A series of magnetic coils allows us to deflect and focus the electron beam onto the spot of the substrate that we want to expose. An example of electron beam lithography apparatus (originally described in Ref. [32]) is shown in figure 1.6. Other important elements of the electronic lithography apparatus figuring on this diagram are the aperture placed just before the substrate to allow us to control the convergence angle of the beam, and the electrodes used to cut the beam by deflecting it so that it no longer passes through the aperture. The electron beam will thus reproduce the entire GDS mask, spot by spot, in order to expose the entire

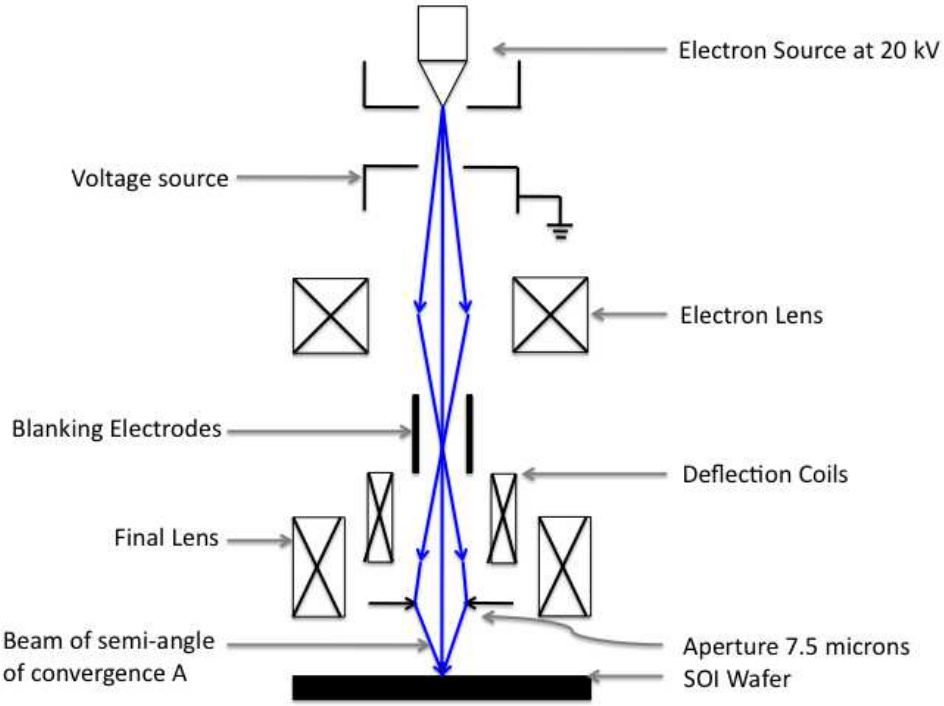

Figure 1.6: Diagram of an electron beam lithography apparatus, with the electron source and the voltage source used to accelerate it, the magnetic coils used for focusing (electron lens) or deflect the beam (deflection coils), the aperture used for controlling the half-angle of convergence α of the beam and the electrodes used to cut the beam by deflecting it so it will no longer pass through the aperture (blanking electrodes).

structure. Electron beam lithography is thus extremely long when compared with photolithography, where the entire structure is exposed in a few seconds, while electron beam lithography typically lasts several hours.

We have in the clean room of the IEF two different e-beam lithography apparatus : the Raith 150 [33] and Nanobeam 4. The Raith 150 is the older machine, and has a theoretical resolution of 2 nm for an acceleration voltage of 20 kV and an aperture size of 7.5 microns [21]. The Nanobeam 4 is a new machine installed during the first year of my PhD, and has a theoretical resolution of 1 nm. But as this machine is new, we had to make a lot of tests in order to make it work and fix any bugs which appeared. Most of the samples at the beginning of my thesis have been done using the Raith 150, and those done towards the end of my thesis were made using the Nanobeam 4. Another important difference is that the Raith 150 needs to be used in line mode to achieve sufficient accuracy for photonic crystals, while the Nanobeam 4 is used in surface mode. Finally, the Nanobeam 4 is inherently faster than the Raith 150 by a factor close to 10. Therefore, we had to use different GDS masks for each machine (see Fig. 1.7).

The nano-tethers profile for each mask follows the square root function $x \rightarrow \sqrt{x}$, and these

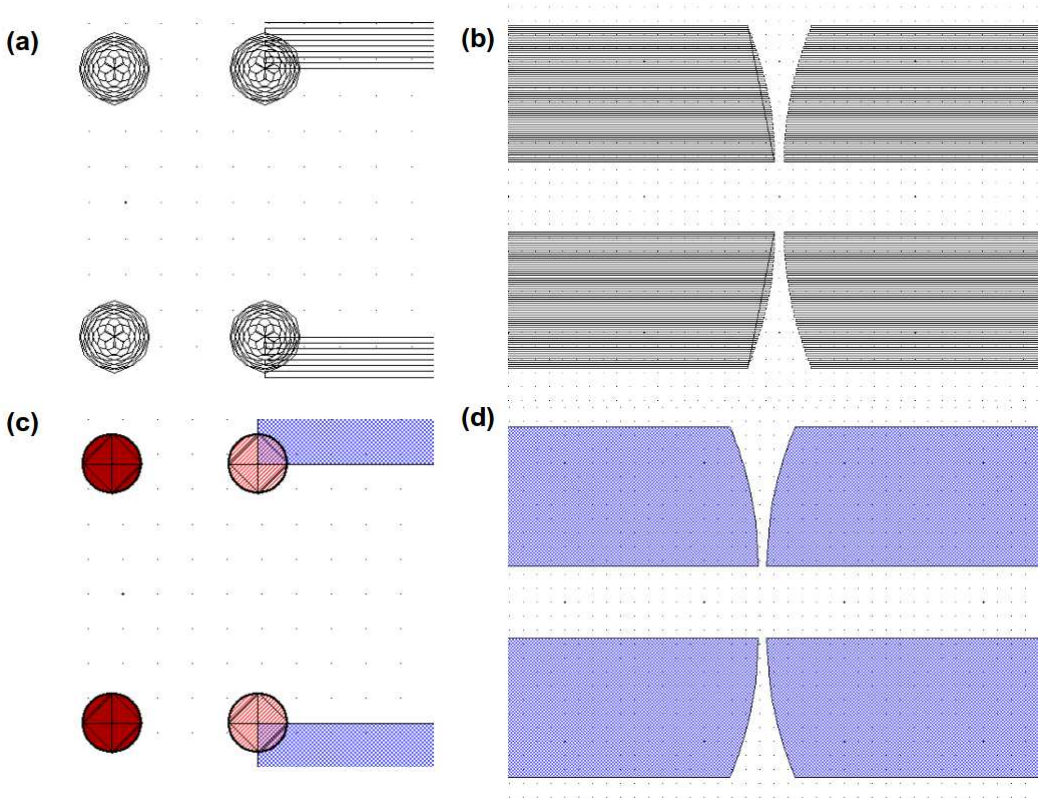

Figure 1.7: (a) The entrance of the photonic crystal and (b) nano-tethers of the GDS mask in line mode for the Raith 150. (c) The entrance of the photonic crystal and (d) nano-tethers of the GDS mask in the surface mode for the Nanobeam 4. The spiral pattern of the holes for the line mode of the Raith can be seen. The lighter color of the first holes of the photonic crystal for the surface mode of the Nanobeam indicates a dose slightly less important than the dose used for the holes of the photonic crystal.

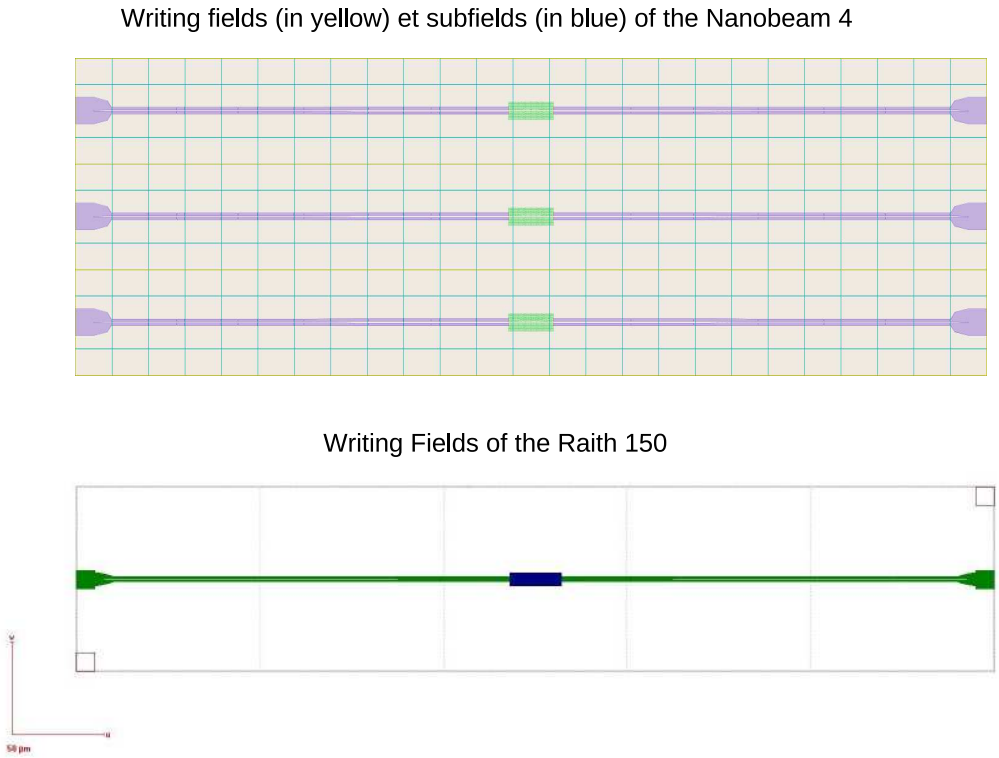

Figure 1.8: The writing fields of the electron beam lithography apparatus for the Nanobeam 4 (above) and the Raith 150 (below).

tethers are wider outside ($W_{ext} = 470$ nm) than inside ($W_{in} = 60$ 60 nm) to prevent light from escaping through the tethers and thus to limit losses in the access waveguides while respecting the constraints of mechanical stability. The first tether of the waveguide, which has to support the taper, must have a slightly larger width ($W_{in}^{1er} = 80$ nm). The pattern of the holes in the line mode consists of a spiral, optimized to obtain well-circular holes [27, 21]. A defect of this kind of design is that the dose of exposure depends on the hole size, the larger holes requiring a higher dose to compensate for the greater distance between the lines of the spiral. The encoded size of the holes must also be smaller than the size we want to get (92% of the radius required for the holes in the line mode of the Raith and 85% of the radius required for the holes of the surface mode of the Nanobeam). One notices that there is an overlap between the pattern of the waveguide and the holes of the first column of the photonic crystal. This poses no problem for the Raith, but this requires putting a slightly lower dose (90% of the normal dose of a hole) for the holes in the Nanobeam lithography, so that they won't have a size greater than the others.

Another important difference between the Raith 150 and the Nanobeam 4 concerns the writing fields. Indeed, the electron beam can not go through the entire sample while maintaining sufficient accuracy during the electron beam lithography. The mask structure

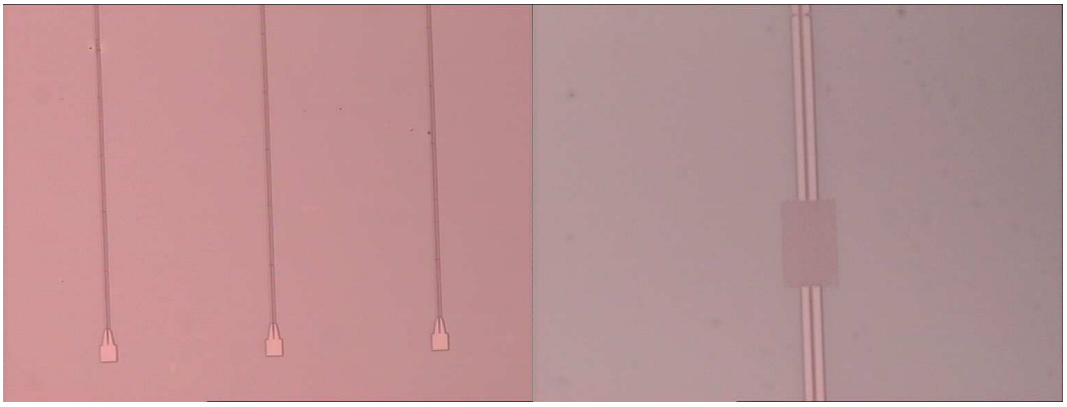

Figure 1.9: Images taken with an optical microscope of the access waveguides (left) and of a photonic crystal (right) made with the Raith 150 after development of the ZEP 520 A resist using ZED-N50.

is thus divided into a series of writing fields. The electron beam will then expose the writing field just below him, then the stage on which the substrate is placed will move so that the next writing field is put below the beam and can be exposed, and so on. This can cause errors when fitting the fields if these writing fields are not perfectly aligned. In the case of the Raith in particular, we must use writing fields of 100 microns by 100 microns, which divides the figure into five parts (see Fig. 1.8-below). So we need to be very careful when using the fitting fields procedure to obtain waveguides that are intact. We do not have the same problem with the Nanobeam, where writing fields may be 500 microns long without problem. But each main writing field of the Nanobeam is divided into writing subfields of length 20 microns, for which there can also be fitting fields problems (see Fig. 1.8-above).

When the electron beam lithography is complete, the ZEP 520 A resist is developed by soaking it for 90 seconds in ZED-N50, which is a specialized developer for this resist, and will remove only the resist exposed by the electrons (positive resist). The sample is then rinsed with isopropanol, a solvent of ZED-N50, then dried with nitrogen. Images of the sample after exposure can be seen in figure 1.9. We can then proceed to the next step, i.e. the plasma etching of silicon.

1.3.2 Inductively Coupled Plasma Reactive Ion Etching of silicon.

To obtain a photonic crystal of good quality, it is necessary for the sides of the air holes etched into the silicon wafer to be as vertical as possible, so that the radius of the holes remains constant regardless of depth. The silicon etching therefore requires a high anisotropy, since we want the bottom of the holes to be etched much faster than the walls. For this, we use the ICP-RIE etching (Inductively Coupled Plasma - Reactive Ion Etching), shown schematically in figure 1.10) [34]. The main advantage of ICP-RIE is

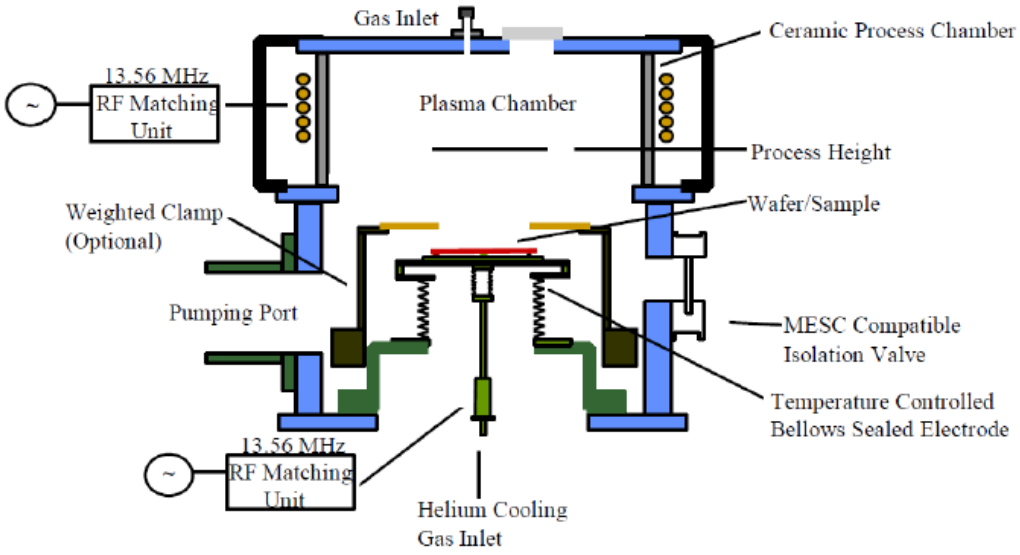

Figure 1.10: Diagram of an ICP-STS etching system of the kind used during my thesis (figure reprinted from Sensors and Actuators A-physical, vol. 74, A. M. Hynes, H. Ashraf, J. K. Bhardwaj, J. Hopkins, I. Johnston, and J. N. Shepherd, "Recent advances in silicon etching for mems using the ase (tm) process," pp. 13–17, Copyright 1999 [34], with permission from Elsevier).

the use of coils powered by a 13.56 MHz radio-frequency generator, which creates a magnetic field whose energy will allow us to ionize the gases present regardless of the rate of acceleration of ions as in a RIE system (Reactive Ion Etching) [21]. For this, a second generator is connected to the plate in order to independently control the potential of the sample to be etched relative to the magnetic coils generating the plasma.

We used a mixture of gases SF_6 and C_4F_8 to maximize the etching anisotropy . Among these gases, the SF_6 will be used for etching of the silicon by creating fluorine radicals F^* by the following chemical reaction [21, 34] :

$$SF_6 + e^- \rightarrow S_xF_y^+ + S_xF_y^* + F^* + e^- \tag{1.4}$$

$$Si + F^* \rightarrow Si - nF \tag{1.5}$$

$$Si - nF \rightarrow Si - F_{x(ads)} \tag{1.6}$$

$$Si - F_{x(ads)} \rightarrow Si - F_{x(gaz)} \tag{1.7}$$

while the gas C_4F_8 will serve to passivate the sides of the holes and thus prevent their

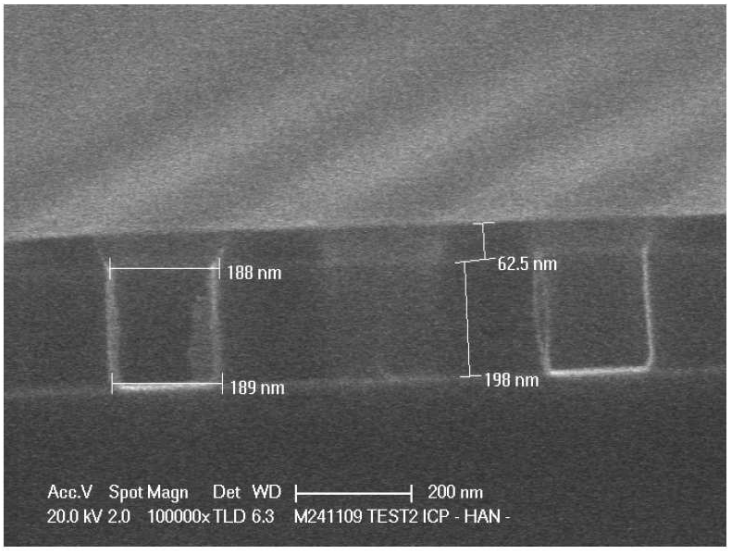

Figure 1.11: SEM sectional view of the holes made through the etching process of Zheng Han (image from [21]). The profile of the holes is an almost perfect cylinder.

etching by the SF_6 by depositing a polymer layer $(C_xF_y)_n$, by the following chemical reaction [21, 35] :

$$C_4F_8 + e^- \rightarrow C_xF_y^+ + C_xF_y^* + F^* + e^- \tag{1.8}$$

Of course, it goes without saying that the polymers $(C_xF_y)_n$ will also passivate the bottom of the holes, not only the sides. To remove the polymer layer at the bottom of the holes, but not on the sides and thus allow the anisotropic etching, we must give the plasma ions created a very strong directional energy using the coils coupled to the 13.56 MHz radio-frequency generators [34].

In our case, we used the etching process optimized by Zheng Han for etching silicon on SOI [21] to obtain holes that are very vertical (see Fig. 1.11). The parameters of this process are given by the following table:

Parameters	Values
Temperature :	10°C
Base pressure :	5 mTorr
Gas SF_6 flow :	200 sccm*
Gas C_4F_8 flow :	200 sccm*
Power of the 1^{er} generator (connected to the coils) :	2200 W
Power of the 2^e generator (connected to the plate) :	40 W
Duration of the etching process :	18 s

*sccm = standard cubic centimeter per minute

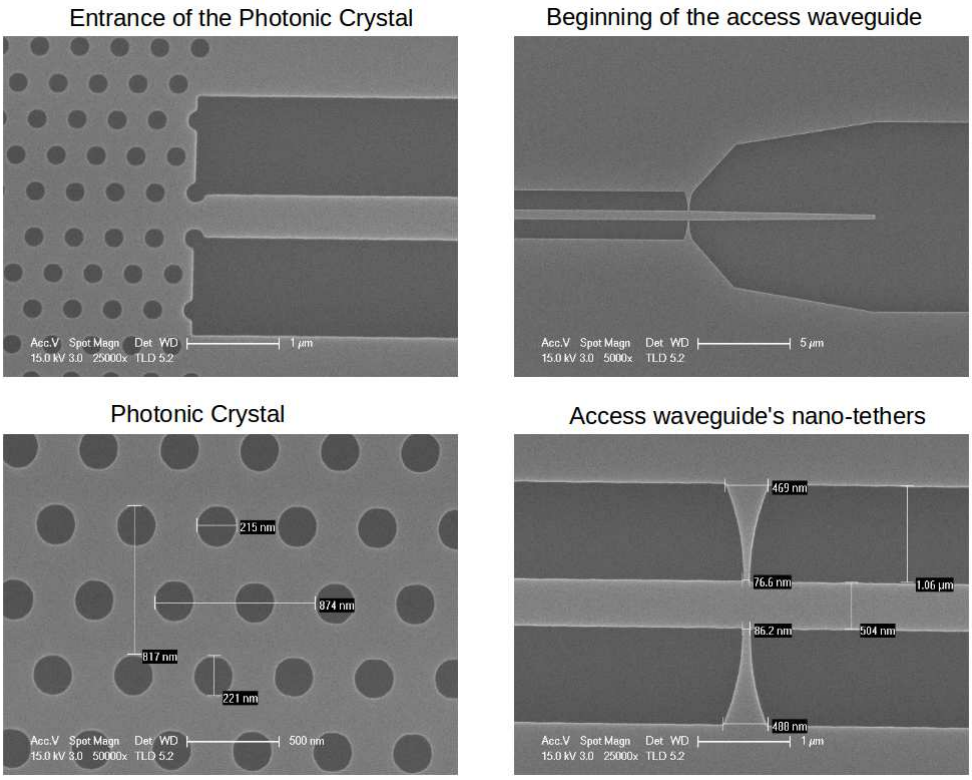

Figure 1.12: SEM images taken after the ICP etching of a structure I made using the Nanobeam 4.

After verifying that the ICP etching process is successful, we can remove the resist ZEP 520 A using the remover ZD MAC adapted to this resist. The sample is soaked in ZD MAC for about 2 minutes before being rinsed with isopropanol and dried with nitrogen. It is possible that traces of resist remain on the sample after treatment. To remove them, we usually put the sample through a oxygen plasma cleaning process for a short period. This oxygen plasma cleaning process was performed using the PICO plasma etching machine, manufactured by Plasma Surface Technology, which is much easier to use than the ICP. The oxygen plasma was used with an oxygen pressure between 0.6 and 0.8 mbar and an excitation power of 160 W. The duration of the process is usually a minute (the speed of the resist removal by the oxygen plasma is 1 nm/s, which is more than enough to remove all traces of resist). Once the resist is removed, we can observe the sample with the SEM to ensure that the entire process - electron beam lithography + ICP etching - was successful (see 1.12 for an example).

1.3.3 Cutting the substrate the diamond blade saw.

The next step consists in cutting the silicon substrate using a diamond blade saw to free the access to the tapers on which we will focus the lensed fibers. For this, we have etched a square of 10 microns just before the taper, in the middle of which we will cut the substrate.

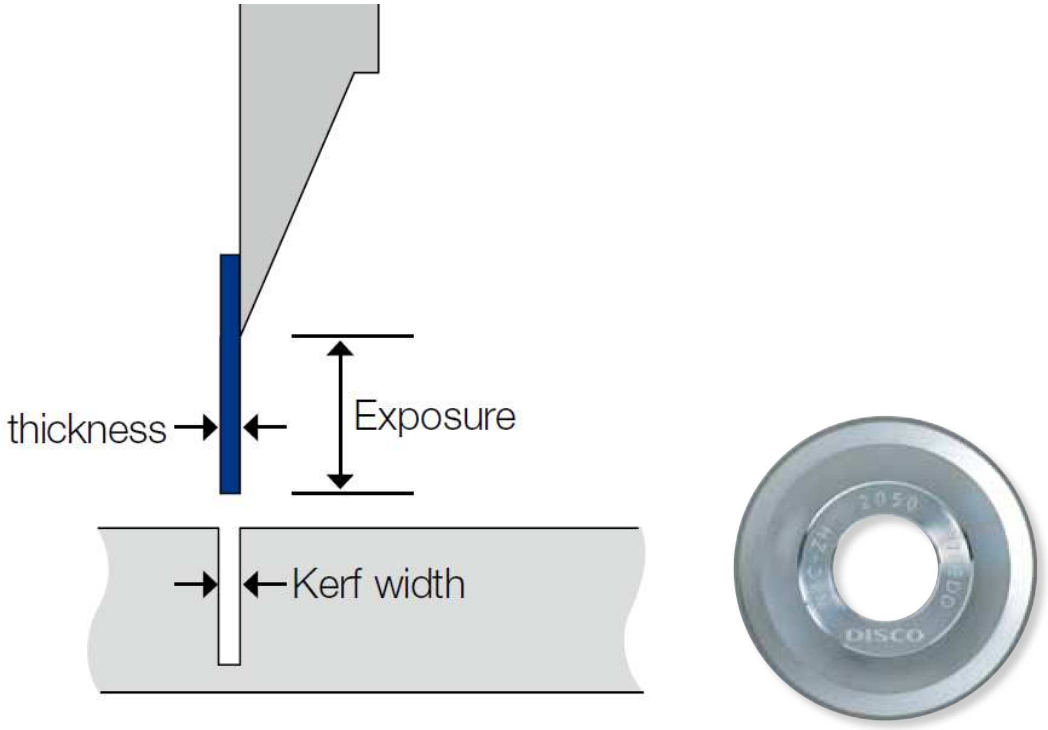

Figure 1.13: Schematic (left) of a blade of NBC-ZH series. The aluminum hub is gray and the blade recovered with diamond is shown in blue. On the right, a photo of the blade (Images from the manufacturer's brochure of the diamond blade saw DISCO).

We used for that the diamond blade saw DISCO DAD 641 owned by the IEF. For cutting the substrate, we must choose a blade with a cutting depth of at least 750 microns (the thickness of the silicon substrate) and whose grain size is less than 5 microns (to avoid creating too big fragments of the substrate that could accidentally destroy the taper when cutting).

For this, we chose the blades of the NBC-ZH series, consisting of an aluminum hub on which was glued an ultra-fine diamond blade (see Fig. 1.13). These blades are specially adapted for cutting wafers of silicon or other semiconductors. I used during my thesis the blades NBC-ZH202O-SE, which have a maximal cutting depth of 790 microns, a cut width of 33 microns and a grain size of 2.75 microns. Cutting depth has been chosen so as to leave 20 micron of silicon uncut, to easily cleave the sample after cutting. The parameters used for cutting are shown in the following table:

Parameters	Values
Rotational speed of the blade :	24000 revolutions per minute
Cutting speed	1.4 mm/s
Cutting depth	730 microns (20 microns left)

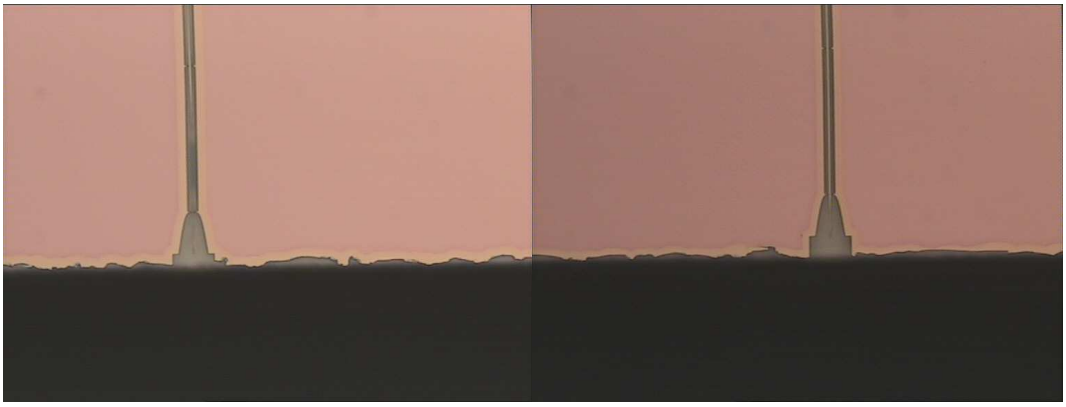

Figure 1.14: Images of the entrance of the access waveguides after the diamond blade saw cutting and the etching with hydrofluoric acid. Left: A waveguide fallen at the level of the first tethers. Right: An intact waveguide. We can see the fragments of size less than 3 microns which appeared during the cutting of the sample by the diamond blade saw. You can also see through the places where the silica was removed below the silicon layer (lighter areas around the waveguides).

1.3.4 Wet etching with hydrofluoric acid.

There remains now only one step in the fabrication of the photonic crystal. This step consists in removing the silica below the photonic crystal in order to obtain a membrane photonic crystal and suspended access waveguides. For this, we used wet etching with hydrofluoric acid (HF), an acid that will attack the silica but not (or almost not) the silicon. This acid will then go through the holes of the silicon photonic crystal and etch the silica just below.

Actually, we used a mixture of acids : HF (diluted to 50%) and $NH_4 - HF$ (7:1), also known as BHF (Buffered Hydrofluoric Acid), in 1:1 volume ratio in order to stabilize the etching rate of the silica. The equations of the etching reaction are [21] :

$$NH_4F \rightarrow NH_3 + HF \tag{1.9}$$

$$SiO_2 + 4HF \rightarrow SiF_4 + 2H_2O \tag{1.10}$$

At 20 °C, the etching rate is of 1 micron per minute for this mixed solution. We need to keep the sample immersed in this solution for at least 2 minutes, since the thickness of the silica layer is 2 microns. To make sure that we removed all the silica, we kept the sample in this solution for 2 min 30 s. Indeed, silica being hydrophilic, there is a risk that the taper will get stuck by a drop of water against the silica by capillary even if the silica remaining is very small. The silicon substrate below the silica is hydrophobic, therefore this problem does not occur once all the silica is removed. The suspended access waveguides are very

fragile once the silica is removed due to the thinness of the tethers. So we need to be very careful when handling the samples in order not to break them (see Fig 1.14).

1.3.5 Measurement of the sample's transmission.

The last step consists in measuring the transmission spectrum of the waveguides and photonic crystal nanocavities to verify that the resonant frequencies are where our simulations predicted. For this, we used the following measurement apparatus (see Fig. 1.15), formed by a tunable laser source (Santec TSL 510), which can be used to do a wavelength sweep, whose beam is then sent to the sample by means of a polarization-maintaining optical fiber to ensure that we will truly send a TE mode inside the photonic crystal, and which is then collected by an ordinary output optical fiber. The output signal is then detected by a photodiode connected to an oscilloscope which will record the transmission spectrum. Knowing the sweep speed of the laser source, we can make the connection between the oscilloscope signal and wavelength. We can then deduce from this transmission spectrum the resonance frequency and the quality factor of the cavity and compare them with the simulation. Part of the signal is redirected by a coupler inserted into the output optical fiber to a powermeter, which can be used to measure the transmission coefficient of the resonance, or to ensure that the optical fibers are really focussed on the tapers of the sample. An infrared camera is used to observe the sample from above and check that the access waveguides are transmitting light properly and that the nanocavity "lights up" when we are at its resonance frequency.

1.4 Modeling of nonlinear optical effects in nanocavities.

The very high quality factors and the great compactness of photonic crystal nanocavities allows us to obtain very intense electric fields within these cavities, which results in a reinforcement of the non-linear optical phenomena. These cavities are therefore ideal for studying these phenomena. However, we need for that a model describing these nonlinear effects which is adapted to these cavities. To develop this model, we have first modeled the behavior of these cavities in the linear regime with the temporal coupled-mode theory. We then added to this model the different terms corresponding to existing non-linear optical phenomena in silicon, which we calculated from the expression of the non-linear dielectric polarization of silicon. We first added the phenomena corresponding to the influence of bound electrons on the polarization, i.e. the two-photon absorption and the Kerr effect. This two-photon absorption will create many free carriers in the cavity (electrons and holes), which will also have an influence on the polarization, creating two new phenomena, called the free-carrier dispersion and absorption. Another consequence of

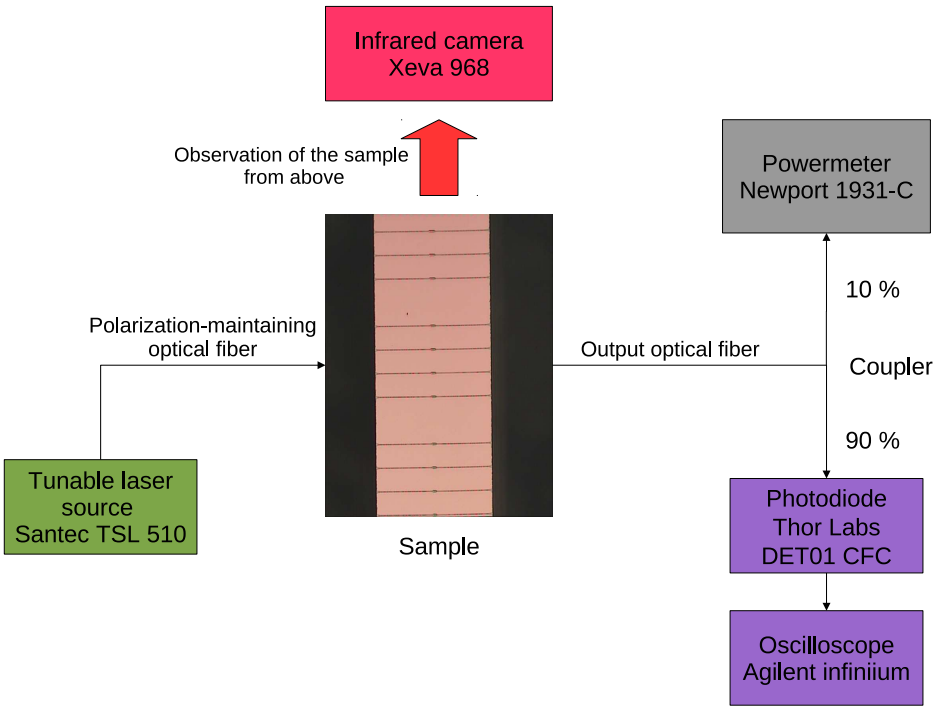

Figure 1.15: Measurement apparatus used to measure the transmission spectrum of the photonic crystal.

these absorption effects is that they will increase the temperature of the cavity, which will create a phenomenon of thermal dispersion, which we also added to our equations. The last phenomenon that we added to our model is more complex: it is the Raman scattering, which originates from the interaction between photons and optical phonons within the cavity, and on which are based the lasers of the Raman kind.

1.4.1 Cavity in the linear regime.

Before considering the influence of nonlinear effects on our photonic crystal nanocavities, we must first model the behavior of our nanocavity at low power, where the nonlinear effects are negligible and its behavior is linear, using the temporal coupled-mode theory [17, 36, 37]. For this, we assume that the spatial pattern of the electric field of the resonant mode of the cavity remains the same and that only its amplitude over time will change. Then we can decompose the expression of the electric field in the cavity in this way :

$$\overrightarrow{E}(\overrightarrow{r},t) = A(t) \times \overrightarrow{E}_0(\overrightarrow{r}) \times e^{-i\omega t} \tag{1.11}$$

where ω is the angular frequency of the excitation and $A(t)$ is the complex amplitude of an envelope function varying much more slowly than the termexp$(-i\omega t)$. The amplitude

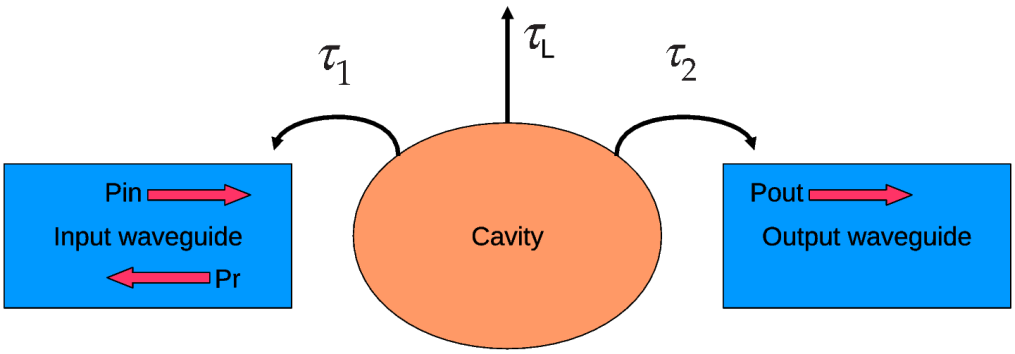

Figure 1.16: Abstract diagram showing the cavity and its coupling to the input and output waveguides.

$A(t)$ and the electric field $\vec{E_0}(\vec{r})$ are normalized so that $|A|^2$ corresponds to the energy stored in the cavity for the resonance mode :

$$\iiint_V \frac{1}{2}\varepsilon(\vec{r}) \left\| \vec{E}_0(\vec{r}) \right\|^2 d\vec{r}^3 = 1 \tag{1.12}$$

and

$$|A(t)|^2 = \iiint_V \frac{1}{2}\varepsilon(\vec{r}) \left\| \vec{E}(\vec{r},t) \right\|^2 d\vec{r}^3 \tag{1.13}$$

where V represents the volume of all space.

We will now apply the temporal coupled-mode theory to determine the equation governing the variations of $A(t)$. In the case of a cavity with a resonance frequency $\omega_0/(2\pi)$ and a quality factor Q coupled directly with an input waveguide and output waveguide (see Fig. 1.16), if we designate by τ_1 the characteristic time associated for the amplitude with the coupling in the input guide, by τ_2 the one associated with the exit guide and by τ_L the one associated with the off-plane radiation of the cavity and with possible sources of linear absorption, then we obtain the following equations on the amplitude [17, 36] :

$$\frac{dA}{dt} = i(\omega - \omega_0)A - (\frac{1}{\tau_1} + \frac{1}{\tau_2} + \frac{1}{\tau_L})A + \sqrt{\frac{2P_{in}}{\tau_1}} \tag{1.14}$$

$$P_{out} = \frac{2|A|^2}{\tau_2} \tag{1.15}$$

This equation can be simplified if we take into account the fact that our structure is symmetric, as is usually the case for photonic crystal cavities : we have then $\tau_1 = \tau_2 = \tau_C$. In addition, thanks to the definition of the quality factor Q of the cavity, we know that

the overall characteristic time associated with the decrease in amplitude of the cavity is equal to $\tau = 2Q/\omega_0$ [38], so we have $1/\tau_1 + 1/\tau_2 + 1/\tau_L = 1/\tau = \omega_0/(2Q)$. The above equations then become :

$$\frac{dA}{dt} = i(\omega - \omega_0)A - \frac{\omega_0}{2Q}A + \sqrt{\frac{2P_{in}}{\tau_C}} \tag{1.16}$$

$$P_{out} = \frac{2|A|^2}{\tau_C} \tag{1.17}$$

If we solve these equations for the steady state regime (A constant, $dA/dt = 0$), then equation 1.16 gives us the following expression for the amplitude A :

$$A = \frac{1}{\frac{\omega_0}{2Q} - i(\omega - \omega_0)} \times \sqrt{\frac{2P_{in}}{\tau_C}} \tag{1.18}$$

By injecting this expression of A in equation 1.17, we can calculate the transmission of the cavity:

$$T(\omega) = \frac{P_{out}}{P_{in}} = \frac{4}{\tau_C^2} \times \frac{\left(\frac{2Q}{\omega_0}\right)^2}{1 + 4Q^2\left(\frac{\omega - \omega_0}{\omega_0}\right)^2} \tag{1.19}$$

This expression of the transmission is actually a Lorentzian peak [39]. At resonance, the transmission is maximal, so we have $T(\omega_0) = T_{max} = \frac{4}{\tau_C^2} \times \left(\frac{2Q}{\omega_0}\right)^2$, from which we can deduce the value of the characteristic time related to the coupling $\tau_C = \frac{4Q}{\omega_0} \times \frac{1}{\sqrt{T_{max}}}$. The equations of our nanocavity in the linear regime then become :

$$\frac{dA}{dt} = i(\omega - \omega_0)A - \frac{\omega_0}{2Q}A + \sqrt{\frac{\omega_0\sqrt{T_{max}}P_{in}}{2Q}} \tag{1.20}$$

$$P_{out} = \frac{\omega_0\sqrt{T_{max}}|A|^2}{2Q} \tag{1.21}$$

The parameters ω_0 and T_{max} are easily determined by measuring the transmission spectrum of the cavity at low power. The quality factor is then easily calculated from this transmission spectrum using the formula (derived from equation 1.19) $Q = \omega_0/\triangle\omega_{1/2}$, where $\triangle\omega_{1/2}$ is the full width at half maximum of the resonance peak [39]. These equations allow us to determine the evolution of the energy in the cavity in the linear regime. We will now be adding the terms describing the nonlinear effects.

1.4.2 Nonlinear optics.

1.4.2.1 Nonlinear polarization and susceptibility of silicon.

One of the advantages of photonic crystal nanocavities is the importance of nonlinear optical effects in these cavities, which makes them very useful for studying these effects. To model these cavities properly, we will have to modify the equation 1.20 to take into account these nonlinear effects. To understand where these nonlinear effects come from and model them, we will have to start from the basic equations of electromagnetic waves, i.e. the Maxwell's equations [17], which are :

$$\nabla.\overrightarrow{H} = 0 \tag{1.22}$$

$$\nabla.\overrightarrow{D} = \rho \tag{1.23}$$

$$\nabla \times \overrightarrow{E} + \mu_0 \frac{\partial \overrightarrow{H}}{\partial t} = \overrightarrow{0} \tag{1.24}$$

$$\nabla \times \overrightarrow{H} - \frac{\partial \overrightarrow{D}}{\partial t} = \overrightarrow{J} \tag{1.25}$$

The nonlinearity of the material (in this case silicon) is then expressed through the relation [40] :

$$\overrightarrow{D} = \varepsilon \overrightarrow{E} + \overrightarrow{P}^{NL} \tag{1.26}$$

where $\overrightarrow{P}^{NL}$ is the nonlinear polarization vector of the material (the contribution of the linear polarization $\overrightarrow{P}^{L} = \chi^{L}\overrightarrow{E}$ is included in the expression of the dielectric permitivity of silicon : $\varepsilon = \varepsilon_0 \varepsilon_{Si} = \varepsilon_0 \left(1 + \chi^{L}\right)$, where χ^{L} is the linear susceptibility of silicon). By injecting this term in Maxwell's equations and assuming that the medium has neither charges nor current, we then obtain the equation of propagation of electromagnetic waves in a nonlinear medium :

$$\nabla \times \nabla \times \overrightarrow{E} + \frac{\varepsilon}{\varepsilon_0 c^2}\frac{\partial^2 \overrightarrow{E}}{\partial t^2} = -\frac{1}{\varepsilon_0 c^2}\frac{\partial^2 \overrightarrow{P}^{NL}}{\partial t^2} \tag{1.27}$$

The nonlinear polarization $\overrightarrow{P}^{NL}(\omega)$ is usually expressed as a Taylor series, but it is usually limited to the terms of second and third order of this series. In addition, due to the central symmetry of the lattice of silicon, the even terms of the Taylor series of $\overrightarrow{P}^{NL}(\omega)$ are null in the silicon. We can then approximate the general expression of $\overrightarrow{P}^{NL}(\omega)$ in silicon by the third term of the Taylor series. The nonlinear polarization can then be written as [40, 41] :

$$P_i^{NL}(\omega_o+\omega_n+\omega_m)=\varepsilon_0\sum_{jkl}\sum_{(mno)}\chi^{(3)}_{ijkl}(\omega_o+\omega_n+\omega_m,\omega_o,\omega_n,\omega_m)\times E_j(\omega_o)E_k^*(\omega_n)E_l(\omega_m) \tag{1.28}$$

where $\chi^{(3)}_{ijkl}$ is the term of third order of the nonlinear susceptibility of silicon. It is usually expanded as $\chi^{(3)}_{ijkl}=\chi^e_{ijkl}+\chi^R_{ijkl}$, where χ^e_{ijkl} represents the contribution to the nonlinear susceptibility of the bound electrons and χ^R_{ijkl} represents the contribution of optical phonons. The nonlinear optical phenomenon associated with the susceptibility of phononic origin is called Raman scattering. The nonlinear optical phenomena associated by the susceptibility of electronic origin are the two-photon absorption and the Kerr effect.

1.4.2.2 Two-photon absorption and Kerr effect.

We will first calculate the terms due to the two-photon absorption and the Kerr effect, which both originate from the nonlinear susceptibility of electronic origin. For this, we will first calculate the expression of the nonlinear polarization of electronic origin in silicon. The crystal lattice of silicon being from the m3m symmetry class, the third order susceptibility of electronic origin has only four independent components [41, 40] :

$$\chi^e_{ijkl}=\chi^e_{1122}\delta_{ij}\delta_{kl}+\chi^e_{1212}\delta_{ik}\delta_{jl}+\chi^e_{1221}\delta_{il}\delta_{jk}+(\chi^e_{1111}-\chi^e_{1122}-\chi^e_{1212}-\chi^e_{1221})\delta_{ijkl} \tag{1.29}$$

where δ_{ij} is equal to 1 if $i=j$ and to 0 if $i\neq j$, and δ_{ijkl} is equal to 1 if $i=j=k=l$ and to 0 if otherwise.

In the case where the electromagnetic wave propagating in the medium has a single frequency ω, we are only interested by the value of $\chi^e_{ijkl}(-\omega,\omega,-\omega,\omega)$, and the equation 1.29 is then simplified considerably due to the intrinsic permutation symmetry of the susceptibility : $\chi^e_{1122}(-\omega,\omega,-\omega,\omega)=\chi^e_{1221}(-\omega,\omega,-\omega,\omega)$. In addition, when the photon energy $\hbar\omega$ is less than the energy bandgap of silicon $E_G=1.1$ eV, which is the case for the wavelengths where we make our measurements ($\hbar\omega=0.8$ eV for $\lambda=1550$ nm), we also have the approximation $\chi^e_{1212}(-\omega,\omega,-\omega,\omega)=\chi^e_{1122}(-\omega,\omega,-\omega,\omega)$ [41]. We then obtain for $\chi^e_{ijkl}(-\omega,\omega,-\omega,\omega)$:

$$\chi^e_{ijkl}=\chi^e_{1122}(\delta_{ij}\delta_{kl}+\delta_{ik}\delta_{jl}+\delta_{il}\delta_{jk})+(\chi^e_{1111}-3\chi^e_{1122})\delta_{ijkl} \tag{1.30}$$

We can still simplify the problem by choosing to ignore the anisotropy of silicon : $\chi^e_{1111}-3\chi^e_{1122}=0$. The susceptibility of electronic origin then becomes $\chi^e_{ijkl}=\frac{1}{3}\chi^e_{1111}(\delta_{ij}\delta_{kl}+\delta_{ik}\delta_{jl}+\delta_{il}\delta_{jk})$ and the equation 1.28 then becomes :

$$P_i^{NL}(\omega) = \varepsilon_0 \sum_{\substack{\omega_{j,k,l}\in\{-\omega,\omega\},\\ \omega_j+\omega_k+\omega_l=\omega}} \chi^e_{ijkl}(-\omega,\omega_j,\omega_k,\omega_l)E_j(\omega_j)E_k^*(\omega_k)E_l(\omega_l) = \frac{3}{4}\chi^e_{1111}\left\|\overrightarrow{E}(\omega)\right\|^2 E_i(\omega) \tag{1.31}$$

The nonlinear susceptibility can then be decomposed into real and complex parts as $\chi^e_{1111} = \chi^e_r + i\chi^e_i$, which will respectively correspond to a dispersion and a nonlinear absorption. However, these two phenomena are usually rather described using the parameters $n_2 = 3\chi^e_r/(4\varepsilon_0 c n_0^2)$, called the Kerr effect coefficient, and $\beta^{TPA} = 3\omega\chi^e_i/(2\varepsilon_0 c^2 n_0^2)$, called the two-photon absorption (or TPA) coefficient [41], where $n_0 = \sqrt{\varepsilon/\varepsilon_0} = 3.48$ is the refractive index of silicon [42]. If we designate by $I = \frac{1}{2}n_0\varepsilon_0 c\left\|\overrightarrow{E}(\overrightarrow{r},t)\right\|^2 = \frac{1}{2}n_0\varepsilon_0 c\left\|\overrightarrow{E_0}(\overrightarrow{r})\right\|^2|A(t)|^2$ the optical intensity, or irradiance, then we can express the nonlinear polarization as:

$$\overrightarrow{P}^{NL} = 2n_0\varepsilon_0(n_2 I + i\frac{c}{2\omega}\beta^{TPA}I)\overrightarrow{E} \tag{1.32}$$

By reinjecting the expression of the nonlinear polarization in equation 1.27, and by taking into account the fact that the optical intensity varies much more slowly with time than the electric field $\overrightarrow{E}(\overrightarrow{r},t) = A(t)\overrightarrow{E}_0(\overrightarrow{r})e^{-i\omega t}$, we then get the following equation :

$$\nabla\times\nabla\times\overrightarrow{E} - \frac{\omega^2 n_0^2}{c^2}\overrightarrow{E} = \frac{\omega^2 n_0^2}{c^2}\left(\frac{2n_2 I}{n_0} + \frac{ic\beta^{TPA}I}{n_0\omega}\right)\overrightarrow{E} \tag{1.33}$$

which we can also write as :

$$\nabla\times\nabla\times\overrightarrow{E} + \frac{\omega^2 n_0'^2}{c^2}\overrightarrow{E} = 0 \tag{1.34}$$

which is in fact the equation of propagation of electromagnetic waves in a medium whose refractive index is :

$$n_0' \sim n_0 + n_2 I + i\frac{c}{2\omega}\beta^{TPA}I \tag{1.35}$$

This result is relatively easy to interpret because it amounts to considering that the refractive index of silicon varies with the optical intensity I. The variation of the real part of the optical index $n_2 I$ truly corresponds to a dispersion phenomenon, as mentioned earlier, called the optical Kerr effect. The Kerr coefficient n_2 is equal to 4.4×10^{-18} m^2/W in silicon at 1550 nm [43]. The variation of the imaginary part of the index $\frac{i}{2}\frac{c}{\omega}\beta^{TPA}I$ is a nonlinear absorption phenomenon, whose optical absorption coefficient is equal to $\alpha^{TPA} = \beta^{TPA}I$ [44]. This phenomenon is called the two-photon absorption because it is in fact a quantum phenomenon in which the semiconductor absorbs the energy of two photons $2\times\hbar\omega$ and thus makes an electron move from the valence band of the semi-

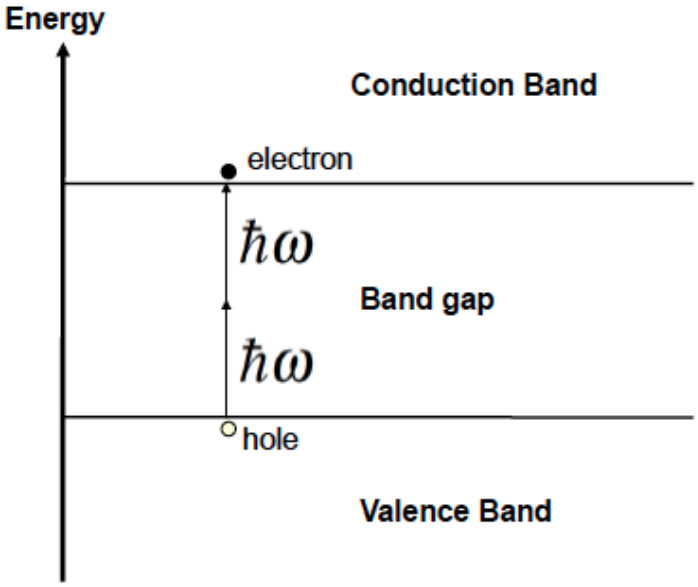

Figure 1.17: Diagram of the two-photon absorption process in a semiconductor. The material absorbs two photons of energy $\hbar\omega$, creating thereby a electron-hole pair of free carriers.

conductor to the conduction band, creating an electron-hole pair of free carriers (see Fig. 1.17). Therefore, it can only take place when we have $2\hbar\omega \geqslant E_G$, where $E_G = 1.1$ eV is the energy of the forbidden bandgap of silicon. This is the case for the wavelengths we use : for $\lambda = 1550$ nm, we have $2\hbar\omega = 1.6$ eV, and the two-photon absorption coefficient of silicon is then equal to$\beta^{TPA} = 8.4 \times 10^{-12}$ m/W [43].

We must now make the connection between the previously calculated two-photon absorption coefficient and the energy losses due to this absorption in our cavity. If we designate by τ_{TPA} the characteristic time associated with the local energy losses due to the two-photon absorption in the cavity then, according to the definition of the absorption coefficient, we have $1/\tau_{TPA} = (c/n_0)\alpha^{TPA} = (c/n_0)\beta^{TPA} I$ [44]. If we designate by $u_E = \frac{1}{2} n_0^2 \varepsilon_0 \left\| \overrightarrow{E} \right\|^2$ the local energy density associated with the electromagnetic field $\overrightarrow{E}$, then the power density lost locally by two-photon absorption is :

$$P_{local}^{TPA} = \frac{u_E}{\tau_{TPA}} = \frac{c}{n_0}\beta^{TPA} I \times \left(\frac{1}{2} n_0^2 \varepsilon_0 \left\| \overrightarrow{E} \right\|^2 \right) = \frac{1}{4}\beta^{TPA} n_0^2 \varepsilon_0^2 c^2 \left| A(t) \right|^4 \left\| \overrightarrow{E_0}(\overrightarrow{r}) \right\|^4 \quad (1.36)$$

To obtain the total power lost by two-photon absorption in the entire photonic crystal, we only need to integrate this expression throughout the silicon part of the cavity :

$$P_{total}^{TPA} = \frac{1}{4}\beta^{TPA} n_0^2 \varepsilon_0^2 c^2 \left| A(t) \right|^4 \iiint_{Si} \left\| \overrightarrow{E_0}(\overrightarrow{r}) \right\|^4 dr^3 \quad (1.37)$$

By definition of $\overrightarrow{E_0}$, we know that $\left\|\overrightarrow{E_0}(\overrightarrow{r})\right\| = \left\|\overrightarrow{E}(\overrightarrow{r},t)\right\| / |A(t)|$, which gives us:

$$P_{total}^{TPA} = \frac{1}{4}\beta^{TPA} n_0^2 \varepsilon_0^2 c^2 |A(t)|^4 \frac{\iiint_{Si} \left\|\overrightarrow{E}(\overrightarrow{r},t)\right\|^4 dr^3}{\left(\iiint_V \frac{1}{2}\varepsilon_0 n(\overrightarrow{r})^2 \left\|\overrightarrow{E}(\overrightarrow{r},t)\right\|^2 dr^3\right)^2} = \beta^{TPA}\frac{c^2}{n_0^2}\frac{|A(t)|^4}{V_{TPA}} \tag{1.38}$$

where V_{TPA} is the characteristic volume of the two-photon absorption, which is defined as [13, 44] :

$$V_{TPA} = \frac{\left(\iiint_V n(\overrightarrow{r})^2 \left\|\overrightarrow{E}(\overrightarrow{r},t)\right\|^2 dr^3\right)^2}{\iiint_{Si} n_0^4 \left\|\overrightarrow{E}(\overrightarrow{r},t)\right\|^4 dr^3} \tag{1.39}$$

It may be noted that this volume V_{TPA} is independent of time, although it is expressed as a function to $\overrightarrow{E}(\overrightarrow{r},t)$. It can be calculated using this formula from the FDTD simulation done with MEEP of the cavity. For example, in the case of the cavity Kuramochi kind depicted in figure 1.4, this volume is equal to $V_{TPA} = 4.8341 \times 10^{-19}\ m^3$. The smaller this volume, the more important the two-photon absorption in the cavity will be.

Using the relation $P_{total}^{TPA} = -\left(\frac{d|A|^2}{dt}\right)_{TPA} = -2|A|\left(\frac{d|A|}{dt}\right)_{TPA}$, we can deduce that $\left(\frac{d|A|}{dt}\right)_{TPA} = -\frac{c^2}{n_0^2}\frac{\beta^{TPA}|A|^3}{2V_{TPA}}$ and thus change the equation 2.20 to include the term corresponding to the two-photon absorption :

$$\frac{dA}{dt} = i(\omega-\omega_0)A - \frac{\omega_0}{2Q}A - \frac{c^2}{n_0^2}\frac{\beta^{TPA}|A|^2}{2V_{TPA}}A + \sqrt{\frac{\omega_0\sqrt{T_{max}}P_{in}}{2Q}} \tag{1.40}$$

The Kerr effect having the same dependence on the electric field in the cavity than the two-photon absorption, the average index variation of the whole cavity is equal to $\delta n_0^{Kerr} = \frac{c}{n_0}\frac{n_2|A|^2}{V_{Kerr}}$, with $V_{Kerr} = V_{TPA}$ [13]. This results in a change of the resonant frequency of the cavity $\frac{\delta\omega_0^{Kerr}}{\omega_0} = -\frac{\delta n_0^{Kerr}}{n_0}$, which gives us for the equation 1.40 the following expression :

$$\frac{dA}{dt} = i(\omega-\omega_0)A - \frac{\omega_0}{2Q}A - \frac{c^2}{n_0^2}\frac{\beta^{TPA}|A|^2}{2V_{TPA}}A + i\frac{\omega_0 c}{n_0^2}\frac{n_2|A|^2}{V_{TPA}}A + \sqrt{\frac{\omega_0\sqrt{T_{max}}P_{in}}{2Q}} \tag{1.41}$$

1.4.2.3 Free-carrier absorption and dispersion.

The silicon used for fabricating the photonic crystal cavities is usually intrinsic. Therefore, the free carriers' density, and their influence on the cavity behavior, is normally very

low. However, the strong two-photon absorption existing in photonic crystal cavities, which is a consequence of their very small size and their high quality factor, will create a very large amount of free carriers in these cavities, which will change the polarization of the material and create absorption and dispersion within the cavity. So we will need to add the terms describing the effects of free carriers to our model.

The calculations are actually quite similar to those performed for the two-photon absorption. The vector of nonlinear polarization created by the free carriers can be estimated from the Drude model and is [41] :

$$\overrightarrow{P}^{fc} = 2n_0\varepsilon_0(n_{fc} + i\frac{c}{2\omega}\alpha_{fc})\overrightarrow{E} \tag{1.42}$$

with $n_{fc} = \frac{-q^2}{2\varepsilon_0 n_0 \omega^2}\left(\frac{N_e^d}{m_e^*} + \frac{N_h^d}{m_h^*}\right)$ the free-carrier dispersion and $\alpha_{fc} = \frac{-q^2}{\varepsilon_0 n_0 \omega^2}\left(\frac{N_e^d}{\mu_e m_e^{*2}} + \frac{N_h^d}{\mu_h m_h^{*2}}\right)$ the free-carrier absorption, where N_e^d and N_h^d are the densities of the free electrons and holes, m_e^* and m_h^* are their effective masses, μ_e and μ_h their mobility and q is the electron charge. The free electrons and holes being created in equal quantity by the two-photon absorption, we have $N_e^d = N_h^d$, and we can then write that $n_{fc} = \sigma_i N_e^d$ and $\alpha_{fc} = \sigma_r N_e^d$. In silicon, for the wavelengths and densities of free carriers we use, the values of σ_r and σ_i measured are slightly higher than those given above by the Drude model and are equal to $\sigma_r = 1.45\times10^{-21}\times\left(\frac{\omega_r}{\omega}\right)^2 m^2$ and $\sigma_i = -5.3\times10^{-27}\times\left(\frac{\omega_r}{\omega}\right)^2 m^3$, where $\lambda_r = 2\pi c/\omega_r =$ 1550 nm [41].

If we now designate by τ_{FCA} the characteristic time associated with the local energy losses due to free-carrier absorption in the cavity, then we have $1/\tau_{FCA} = (c/n_0)\alpha_{fc}$, which gives us for the power density absorbed locally by the free carriers :

$$P_{local}^{FCA} = \frac{u_E}{\tau_{FCA}} = \frac{c}{n_0}\alpha_{fc}\times\left(\frac{1}{2}n_0^2\varepsilon_0\left\|\overrightarrow{E}\right\|^2\right) = \frac{1}{2}\sigma_r N_e^d(\overrightarrow{r})n_0\varepsilon_0 c\,|A(t)|^2\left\|\overrightarrow{E_0}(\overrightarrow{r})\right\|^2 \tag{1.43}$$

By integrating this expression over the whole cavity, we obtain :

$$P_{total}^{FCA} = \frac{c}{n_0}\sigma_r|A(t)|^2\frac{\iiint_{Si} N_e^d(\overrightarrow{r})n_0^2\left\|\overrightarrow{E}(\overrightarrow{r},t)\right\|^2 dr^3}{\iiint_V n(\overrightarrow{r})^2\left\|\overrightarrow{E}(\overrightarrow{r},t)\right\|^2 dr^3} = \sigma_r\frac{c}{n_0}\frac{|A(t)|^2 N_e}{V_{FCA}} \tag{1.44}$$

where $N_e = \iiint_{Si} N_e^d(\overrightarrow{r})dr^3$ is the total number of free electrons (or electron/hole pairs) in the cavity and where V_{FCA} is the characteristic volume of free-carrier absorption, which

is defined as :

$$V_{FCA} = \frac{\left(\iiint_V n(\overrightarrow{r})^2 \left\|\overrightarrow{E}(\overrightarrow{r},t)\right\|^2 dr^3\right)\left(\iiint_{Si} N_e^d(\overrightarrow{r})dr^3\right)}{\iiint_{Si} N_e^d(\overrightarrow{r})n_0^2 \left\|\overrightarrow{E}(\overrightarrow{r},t)\right\|^2 dr^3} \tag{1.45}$$

Free-carrier dispersion having the same dependency on the electric field and on the free carriers' density in the cavity than the free-carrier absorption, the average index variation of the cavity is equal to $\delta n_0^{fc} = \frac{\sigma_i N_e}{V_{FCA}}$, which results in a change in the resonant frequency of the cavity $\frac{\delta\omega_0^{fc}}{\omega_0} = -\frac{\delta n_0^{fc}}{n_0}$, which allows us to modify the equation 1.41 to take into account the influence of free carriers :

$$\frac{dA}{dt} = i\triangle\omega A - \frac{\omega_0}{2Q}A - \frac{c^2}{n_0^2}\frac{\beta^{TPA}|A|^2}{2V_{TPA}}A - \frac{c}{n_0}\frac{\sigma_r N_e}{2V_{FCA}}A + \sqrt{\frac{\omega_0\sqrt{T_{max}}P_{in}}{2Q}} \tag{1.46}$$

where $\triangle\omega$ represents the detuning between the input laser frequency $\omega/(2\pi)$ and the frequency of the cavity resonance, taking into account all of the dispersion effects :

$$\triangle\omega = \omega - \omega_0 + \frac{\omega_0 c}{n_0^2}\frac{n_2|A|^2}{V_{TPA}} + \frac{\omega_0}{n_0}\frac{\sigma_i N_e}{V_{FCA}} \tag{1.47}$$

For our model to be complete, we must now add a second equation describing the evolution of the number of electron/hole pairs N_e created by two-photon absorption in the cavity. We know that the rate of photons destroyed by two-photon absorption in the cavity is equal to $P_{globale}^{TPA}/(\hbar\omega)$ and that for each pair of photons destroyed, an electron/hole pair is created. We also know that the free-carrier absorption does not generate new free carriers. If we designate by τ_{fc} the free-carrier lifetime in the cavity, then we obtain the following equation for N_e :

$$\frac{dN_e}{dt} = -\frac{N_e}{\tau_{fc}} + \frac{1}{2}\frac{c^2}{n_0^2}\frac{\beta^{TPA}|A|^4}{\hbar\omega V_{TPA}} \tag{1.48}$$

Theoretically, there is no linear absorption in silicon for the wavelengths we used, since we are in the silicon bandgap. However, this is not quite the case, since a very small residual linear absorption equal to $\alpha_{lin} = 16$ dB/m $= 3.68\ m^{-1}$ was measured in silicon photonic crystal cavities by my colleague Laurent Haret [45, 36]. This residual linear absorption was also detected by Notomi in Japan [46] and is probably either caused by the presence of small impurities in the silicon used to make our cavities, or linked to the fabrication process. If we take this linear absorption into account, then the total power

lost in the cavity due to linear absorption is equal to:

$$P_{total}^{lin} = \frac{c}{n_0}\alpha_{lin}|A(t)|^2 \frac{\iiint_{Si} n_0^2 \left\|\overrightarrow{E}(\overrightarrow{r})\right\|^2 dr^3}{\iiint_{V} n(\overrightarrow{r})^2 \left\|\overrightarrow{E}(\overrightarrow{r})\right\|^2 dr^3} = \alpha_{lin}\frac{c}{n_0}\frac{|A|^2}{R_{eff}} \tag{1.49}$$

where $1/R_{eff}$ represents the fraction of the optical mode inside the silicon, which is defined as :

$$R_{eff} = \frac{\iiint_{V} n(\overrightarrow{r})^2 \left\|\overrightarrow{E}(\overrightarrow{r})\right\|^2 dr^3}{\iiint_{Si} n_0^2 \left\|\overrightarrow{E}(\overrightarrow{r})\right\|^2 dr^3} \tag{1.50}$$

Each photon absorbed in this way creates an electron-hole pair, which modifies the equation 3.3 as follow :

$$\frac{dN_e}{dt} = -\frac{N_e}{\tau_{fc}} + \frac{1}{2}\frac{c^2}{n_0^2}\frac{\beta^{TPA}|A|^4}{\hbar\omega V_{TPA}} + \frac{c}{n_0}\frac{\alpha_{lin}|A|^2}{\hbar\omega R_{eff}} \tag{1.51}$$

Linear absorption losses have already been taken into account in the equation 1.20 by the definition we gave of the quality factor Q, so we do not need to modify this equation.

1.4.2.4 Thermal dispersion.

Most of the power absorbed optically by the two-photon, free-carrier and linear absorptions will be returned to the silicon as heat by different mechanisms : first, the free carriers created by two-photon absorption will restore the energy provided by the two-photon absorption in excess to the gap $2\hbar\omega - E_G$ to the crystal lattice in the form of phonons. Similarly, the free carriers excited toward higher energy levels by the free-carrier absorption will restore the absorbed energy in the form of phonons when going down towards the bottom of the conduction band. Once at the bottom of the conduction band, the free carriers will recombine, emitting again phonons. All this will increase the average temperature of the cavity, which will change its behavior by introducing a factor of thermal dispersion in our equations [47]. The free-carrier lifetime being very short (below the nanosecond) compared to the cooling time of the cavity (which is in tens of nanoseconds - see Chapter 2), we can consider that the restoration of the optically absorbed energy to the silicon will be instantaneous. If we designate by $\triangle T$ the average difference in temperature in the cavity caused by the absorption effects, by V_{eff}^T the effective thermal volume of the cavity and by R_T the thermal resistance of the cavity, then the equation describing

the evolution of the temperature of the cavity is [48] :

$$(\rho_{Si} C_p^{Si} V_{eff}^T) \frac{d\triangle T}{dt} = -\frac{\triangle T}{R_T} + P_{total}^{TPA} + P_{total}^{FCA} + P_{total}^{lin} \tag{1.52}$$

where $\rho_{Si} = 2.33$ g/cm³ is the density of silicon and $C_p^{Si} = 0.7$ J/(g×K) is its thermal capacity. Replacing the total absorption powers by the previously calculated expressions, this equation becomes :

$$\rho_{Si} C_p^{Si} V_{eff}^T \frac{d\triangle T}{dt} = -\frac{\triangle T}{R_T} + \frac{c^2}{n_0^2} \frac{\beta^{TPA} |A|^4}{V_{TPA}} + \frac{c}{n_0} \frac{\sigma_r |A|^2 N_e}{V_{FCA}} + \frac{c}{n_0} \frac{\alpha_{lin} |A|^2}{R_{eff}} \tag{1.53}$$

At room temperature, the index variation caused by the temperature is $n_T = \frac{dn}{dT} = 1.86 \times 10^{-4}\, K^{-1}$, which corresponds to a variation of the resonant frequency of the cavity $\delta\omega_0^T = -\frac{\omega_0}{n_0}\delta n_0^T = -\frac{\omega_0}{n_0} \times (n_T \triangle T)$ [47]. The equation 1.47 on the detuning $\triangle\omega$ is then modified as follows to account for the thermal dispersion.

$$\triangle\omega = \omega - \omega_0 + \frac{\omega c}{n_0^2} \frac{n_2 |A|^2}{V_{TPA}} + \frac{\omega_0}{n_0} \frac{\sigma_i N_e}{V_{FCA}} + \frac{\omega_0}{n_0} n_T \triangle T \tag{1.54}$$

1.4.2.5 Full equations system and modal volume of the cavity.

In the end, we obtain a system of four equations describing the nonlinear behavior of a silicon nanocavity with a single resonance : one on the amplitude of the electric field in the cavity, one on the detuning between the frequencies of the laser and of the resonance of the cavity, one on the number of free carriers, and the last one on the temperature of the cavity:

$$\frac{dA}{dt} = i\triangle\omega A - \frac{\omega_0}{2Q} A - \frac{c^2}{n_0^2} \frac{\beta^{TPA} |A|^2}{2V_{TPA}} A - \frac{c}{n_0} \frac{\sigma_r N_e}{2V_{FCA}} A + \sqrt{\frac{\omega_0 \sqrt{T_{max}} P_{in}}{2Q}} \tag{1.55}$$

$$\triangle\omega = \omega - \omega_0 + \frac{\omega c}{n_0^2} \frac{n_2 |A|^2}{V_{TPA}} + \frac{\omega_0}{n_0} \frac{\sigma_i N_e}{V_{FCA}} + \frac{\omega_0}{n_0} n_T \triangle T \tag{1.56}$$

$$\frac{dN_e}{dt} = -\frac{N_e}{\tau_{fc}} + \frac{1}{2} \frac{c^2}{n_0^2} \frac{\beta^{TPA} |A|^4}{\hbar\omega V_{TPA}} + \frac{c}{n_0} \frac{\alpha_{lin} |A|^2}{\hbar\omega R_{eff}} \tag{1.57}$$

$$\rho_{Si} C_p^{Si} V_{eff}^T \frac{d\triangle T}{dt} = -\frac{\triangle T}{R_T} + \frac{c^2}{n_0^2} \frac{\beta^{TPA} |A|^4}{V_{TPA}} + \frac{c}{n_0} \frac{\sigma_r |A|^2 N_e}{V_{FCA}} + \frac{c}{n_0} \frac{\alpha_{lin} |A|^2}{R_{eff}} \tag{1.58}$$

It is this system of equations that will be used in Chapter 2 to describe the phenomenon of high-frequency self-induced oscillations in a nanocavity. Note that we can also express

this system as a system of three independent differential equations, by re-injecting the expression of $\triangle\omega$ given by the equation 1.56, the only one which is not a differential equation, inside in equation 1.55 on the evolution of the amplitude. It is evident from these equations that the non-linear effects will be greater when the characteristic volumes V_{TPA}, V_{FCA} are smaller. The importance of these non-linear effects is usually estimated instead by using the modal volume, i.e. the characteristic volume occupied by the resonant mode of the cavity, which is used to estimate the confinement of this mode electromagnetic field in the cavity, and which is defined as :

$$V_m = \frac{\iiint_V n(\overrightarrow{r})^2 \left\| \overrightarrow{E}(\overrightarrow{r},t) \right\|^2 dr^3}{max\left(n(\overrightarrow{r})^2 \left\| \overrightarrow{E}(\overrightarrow{r},t) \right\|^2 \right)} \tag{1.59}$$

The different characteristics volumes defined above for the nonlinear effects are of the same order of magnitude as the modal volume, and it is therefore considered that the non-linear optical effects in the cavity are proportional to $1/V_m$. Similarly, we can consider that the linear optical effects in the cavity are proportional to $1/Q$. We can therefore consider that the importance of nonlinear effects compared to linear effects in the cavity will be proportional to the ratio Q/V_m. In other words, the smaller the size of the cavity and the larger its quality factor, the more important nonlinear phenomena in the cavity will be. The photonic crystal nanocavities have the advantage of having both high quality factors and extremely small modal volumes : in the case of a Kuramochi type nanocavity such as the one described in figure 1.4, the modal volume of the mode resonance calculated from the FDTD simulation is equal to $V_m = 0.124\ \mu m^3$, with quality factors that can go up to several millions. These nanocavities are therefore particularly interesting to study nonlinear optical phenomena.

There remains an important nonlinear phenomenon that can not be described by this system of equations, because it involves photons of different frequencies, which complicates our equations : that phenomenon is the Raman scattering, which has for origin the interaction of the photons with the optical phonons in the cavity. This phenomenon will be discussed in more detail in Chapter 3 of this thesis, which concerns the Raman lasers, but we are already going to modify our system of equations to include it.

1.4.3 Raman scattering.

1.4.3.1 What is Raman scattering ?

Raman scattering is a phenomenon both acoustic and optical wherein a portion of the light traveling through a material will interact with phonons, i.e. with the vibrations of

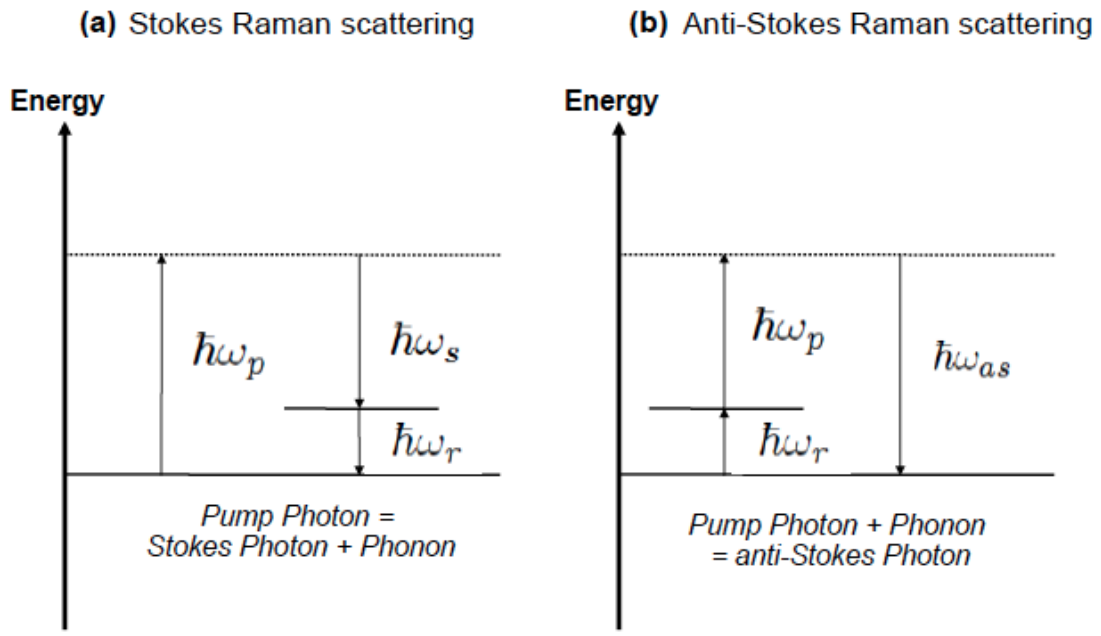

Figure 1.18: (a) Diagram of the Stokes Raman scattering process : The material absorbs a photon of frequency ω_p and emits a new phonon of frequency ω_r and a new photon of frequency $\omega_s = \omega_p - \omega_r$. (b) Diagram of the anti-Stokes Raman scattering process : The material absorbs a photon of frequency ω_p and a phonon of frequency ω_r and emits a new photon of frequency $\omega_{as} = \omega_p + \omega_r$.

the material and will be shifted in frequency by the absorption or emission of a phonon. This phenomenon was discovered by C. V. Raman in 1928 [40, 49]. There are two types of Raman scattering: the Stokes Raman scattering in which the photon is shifted toward a smaller frequency by the emission of a phonon, and the anti-Stokes Raman scattering in which the photon is shifted toward a greater frequency by the absorption of a phonon (see Fig. 1.18). The Stokes Raman scattering is usually much stronger than the anti-Stokes Raman scattering (typically of at least an order of magnitude) [40]. We will therefore neglect the anti-Stokes scattering afterwards.

The process described above is called the spontaneous Raman diffusion, and is usually extremely weak. However, when the material is excited by a high intensity laser, a much more efficient version of Raman scattering, which is known as the stimulated Raman scattering, is possible. This is a nonlinear phenomenon wherein the presence in the material of both the photons at the pump laser frequency f_p and at the frequency of the Stokes Raman scattering f_s will cause a modulation of the electric field intensity at the frequency $f_p - f_s = f_r$, i.e. at the Raman phonon frequency. This modulation will in turn increase the amplitude of the crystalline vibrations of the material, thereby increasing the efficiency of Raman scattering, which will create more photons at the Stokes frequency, and so on. 10% or more of the energy of the pump laser can thus be converted to the Stokes frequency [40].

While the spontaneous Raman scattering will be proportional to the number of photons at the frequency of the pump laser in the cavity, the stimulated Raman scattering will be proportional to both the number of photons at the pump laser frequency and number of photons at the Stokes frequency, and will therefore be nonlinear. The probability per unit time that a photon is emitted by Raman scattering in the Stokes mode has therefore the following form [21, 40, 50] :

$$\phi_s = G_r N_p (N_s + 1) \tag{1.60}$$

where N_p is the number of photons at the pump frequency, N_s is the number of photons at the frequency Stokes and G_r is a constant depending on the material, known as the Raman gain. The $G_r N_p$ factor then represents the contribution of the spontaneous Raman scattering and the $G_r N_p N_s$ factor that of the stimulated Raman scattering.

1.4.3.2 Stimulated Raman scattering in silicon.

In silicon, Raman scattering takes the form of a very narrow Lorentzian peak, centered around the frequency $f_s = f_p - f_R$, with $f_R = \omega_R/(2\pi) = 15.6$ THz the frequency of the Raman shift in silicon, and whose full width at half maximum is $\triangle f_R = \triangle\omega_R/(2\pi) = 105$ GHz [51], which corresponds to about 1 nm for a Stokes wavelength around 1670 nm. If we designate by $\overrightarrow{E_p}(\overrightarrow{r},t) = A_p(t) \times \overrightarrow{E}_{p_0}(\overrightarrow{r}) \times e^{-i\omega_p t}$ the electric field of the mode corresponding to the photons at the pump frequency and $\overrightarrow{E_s}(\overrightarrow{r},t) = A_s(t) \times \overrightarrow{E}_{s_0}(\overrightarrow{r}) \times e^{-i\omega_s t}$ the mode corresponding to the photons at the Stokes frequency, then the nonlinear polarization created by stimulated Raman scattering in silicon is equal to [21, 41, 49] :

$$P_i^{NL}(\omega) = \frac{-\varepsilon_0 \omega_R g_{ijkl}^R \triangle\omega_R}{\omega_R^2 - (\omega-\omega_p)^2 + i(\omega-\omega_p)(\triangle\omega_R)} \times E_j(\omega_p) E_k^*(\omega_p) E_l(\omega) \tag{1.61}$$

where g_{ijkl}^R is a constant independent of the frequency which represents the gain of stimulated Raman scattering in silicon. For frequencies ω near the Stokes frequency $\omega_s = \omega_p - \omega_R$, we have $\omega - \omega_p \approx -\omega_R$ and $\omega_R^2 - (\omega-\omega_p)^2 = (\omega_R + \omega - \omega_p)(\omega_R - \omega + \omega_p) \approx 2\omega_R(\omega - \omega_s)$, and the equation 1.61 then becomes :

$$P_i^{NL}(\omega) = \frac{-i\varepsilon_0 g_{ijkl}^R}{1 + 2i\left(\frac{\omega-\omega_s}{\triangle\omega_R}\right)} \times E_j(\omega_p) E_k^*(\omega_p) E_l(\omega) \tag{1.62}$$

Assuming initially that the gain g_{ijkl}^R is scalar and real, then the equation 1.62 becomes :

$$\overrightarrow{P}_s^{NL}(\omega) = \frac{-i\varepsilon_0 g_R \left\|\overrightarrow{E_p}\right\|^2}{1 + 2i\left(\frac{\omega-\omega_s}{\triangle\omega_R}\right)} \times \overrightarrow{E_s}(\omega) \tag{1.63}$$

with $g_R > 0$. By injecting this expression in equation 1.27, and using the fact that $\left\|\overrightarrow{E_p}(\overrightarrow{r},t)\right\|^2 = |A_p(t)|^2 \left\|\overrightarrow{E}_{p_0}(\overrightarrow{r})\right\|^2$ varies much more slowly with time than the electric fields $\overrightarrow{E_p}(\overrightarrow{r},t) = A_p(t)\overrightarrow{E}_{p_0}(\overrightarrow{r})e^{-i\omega_p t}$ and $\overrightarrow{E_s}(\overrightarrow{r},t) = A_s(t)\overrightarrow{E}_{s_0}(\overrightarrow{r})e^{-i\omega t}$, we obtain :

$$\nabla \times \nabla \times \overrightarrow{E_s} - \frac{\omega^2 n_0^2}{c^2}\overrightarrow{E_s} = \frac{\omega^2 n_0^2}{c^2}\left(\frac{-ic}{\omega n_0}\frac{g_R^B I_p}{1+2i\left(\frac{\omega-\omega_s}{\triangle\omega_R}\right)}\right)\overrightarrow{E_s} \tag{1.64}$$

where $g_R^B = 2\omega\chi_R/(\varepsilon_0 c^2 n_0^2)$ is the Raman gain in bulk silicon [37] and $I_p = \frac{1}{2}n_0\varepsilon_0 c\left\|\overrightarrow{E_p}\right\|^2$ is the optical intensity of the pump mode. If we choose to ignore the very low dispersion due to stimulated Raman scattering to keep only the gain factor, then this equation is equivalent to a modification of the complex refractive index of the material equal to :

$$n_0^{|} \sim n_0 - i\frac{c}{2\omega}\frac{g_R^B I_p}{1+4\left(\frac{\omega-\omega_s}{\triangle\omega_R}\right)^2} \tag{1.65}$$

We can note that, unlike the equation 1.35 on the two-photon absorption, the imaginary part of the variation of the refractive index is negative. This corresponds therefore a gain, not to an absorption. The value of the Raman gain in the bulk silicon g_R^B is badly known and varies according to the measurements between 8.9 cm / GW [52] and 76.5 cm / GW [53].

The Stokes power generated locally by stimulated Raman scattering is then equal to :

$$P_{local}^R(\omega) = \frac{\frac{c}{n_0}g_R^B I_p}{1+4\left(\frac{\omega-\omega_s}{\triangle\omega_R}\right)^2} \times \left(\frac{1}{2}n_0^2\varepsilon_0\left\|\overrightarrow{E_s}\right\|^2\right) = \frac{\frac{1}{4}n_0^2\varepsilon_0^2 c^2 g_R^B |A_p|^2 |A_s|^2}{1+4\left(\frac{\omega-\omega_s}{\triangle\omega_R}\right)^2}\left\|\overrightarrow{E}_{p_0}\right\|^2\left\|\overrightarrow{E}_{s_0}\right\|^2 \tag{1.66}$$

By integrating this expression on the silicon part of the cavity, we obtain the overall power generated by the Stokes stimulated Raman scattering in the cavity :

$$P_{total}^R(\omega) = \frac{c^2}{n_0^2}\frac{g_R^B |A_p|^2 |A_s|^2}{\left(1+4\left(\frac{\omega-\omega_s}{\triangle\omega_R}\right)^2\right)V_R} \tag{1.67}$$

where V_R is the characteristic volume of Raman scattering, which is defined as :

$$V_R = \frac{\left(\iiint_V n(\overrightarrow{r})^2\left\|\overrightarrow{E}_p(\overrightarrow{r})\right\|^2 dr^3\right)\left(\iiint_V n(\overrightarrow{r})^2\left\|\overrightarrow{E}_s(\overrightarrow{r})\right\|^2 dr^3\right)}{\iiint_{Si} n_0^4\left\|\overrightarrow{E}_p(\overrightarrow{r})\right\|^2\left\|\overrightarrow{E}_s(\overrightarrow{r})\right\|^2 dr^3} \tag{1.68}$$

We can now modify the result to take into account the fact that the gain of the Raman

scattering is not scalar, and has in fact the form $g^R_{ijkl} = -ig^R(\sum_{n=x,y,z} R^n_{ij}R^n_{kl})$, with R^n the components of the Raman tensor in silicon. Assuming that the axes of the coordinate system (x, y, z) are oriented along the crystallographic axes of silicon [100], [010], [001] (the axes directions are indicated by the Miller indices), then these tensors will have the expressions: $R^x_{ij} = \delta_{iy}\delta_{jz} + \delta_{iz}\delta_{jy}$, $R^y_{ij} = \delta_{ix}\delta_{jz} + \delta_{iz}\delta_{jx}$ and $R^z_{ij} = \delta_{ix}\delta_{jz} + \delta_{iy}\delta_{jx}$. If we designate by $\xi^{(3)}_{ijkl} = \sum_{n=x,y,z} R^n_{ij}R^n_{kl}$ the tensor whose components are equal to 0 if the corresponding components of g^R_{ijkl} are null and equal to 1 if this is not the case, then the expression of the Raman volume becomes :

$$V_R = \frac{\left(\iiint_V n(\overrightarrow{r})^2 \left\|\overrightarrow{E}_p(\overrightarrow{r})\right\|^2 dr^3\right)\left(\iiint_V n(\overrightarrow{r})^2 \left\|\overrightarrow{E}_s(\overrightarrow{r})\right\|^2 dr^3\right)}{\iiint_{Si} n_0^4 \overrightarrow{E}^*_s(\overrightarrow{r})\xi^{(3)}_{ijkl}\overrightarrow{E}_p(\overrightarrow{r})\overrightarrow{E}^*_p(\overrightarrow{r})\overrightarrow{E}_s(\overrightarrow{r})dr^3} \tag{1.69}$$

It is this expression that will be used later to calculate the Raman volume of our cavity. This Raman volume, and thus the Raman gain, can vary greatly depending on the direction of propagation of the pump and Stokes waves relative to the crystallographic axes of silicon, and it is therefore necessary to choose the right direction for our cavities in order to maximize the gain .

We can see that the equation 1.67 on the Stokes power generated in the cavity truly corresponds to the expression of a Lorentzian peak with a full width at half maximum $\triangle\omega_R$ and centered on the Stokes frequency $\omega_s = \omega_p - \omega_R$. However, this expression of the Stokes power is correct only if we are in a waveguide with no resonances. Typically, a nanocavity adapted to Raman scattering will have a resonance at a frequency close to the Stokes frequency, used for increasing the number of Stokes photons in the cavity and amplifying the stimulated Raman scattering. This resonance will usually be narrower than the Lorentzian peak of the Raman gain, truncating part of this peak. We must take this into account when writing the equations describing the Raman scattering in our cavities.

1.4.3.3 Raman scattering in a doubly resonant cavity.

Specifically, in order to write the equations describing the Raman scattering in our cavities, we will assume that the Raman scattering takes place in a cavity with two resonance frequencies ω_{p_0} and ω_{s_0} such as the frequency difference $\omega_{p_0} - \omega_{s_0}$ will be very close to the Raman shift frequency ω_R. If we designate by ω_p the pump laser frequency and by $\omega_s = \omega_p - \omega_R$ the Stokes frequency, then the power generated by the stimulated Raman

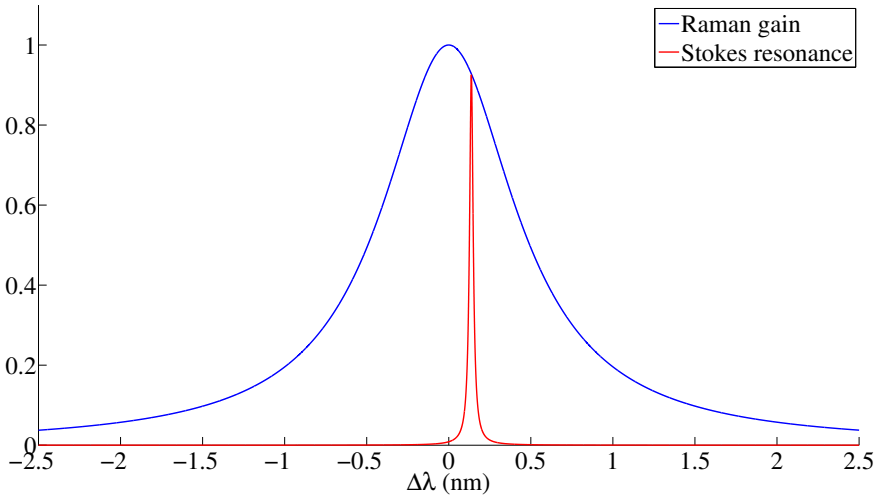

Figure 1.19: Comparison of the Lorentzian peak of the Raman gain (in blue) and the Lorentzian peak of the resonance ω_{s_0} used for the Stokes, with $Q_s = 10000$ (in red). It is obvious that only the Stokes photons of frequency $\omega \approx \omega_{s_0}$ will stay in the cavity, the other disappearing quickly after being created, and that only the Raman power generated at the frequency ω_{s_0} will be significant.

scattering in the cavity is given by :

$$P^R_{total}(\omega) = \frac{c^2}{n_0^2} \frac{g_R^B \left|A_p\right|^2 H_{s_0}(\omega) \hbar \omega_{s_0} N_s}{\left(1 + 4\left(\frac{\omega - \omega_s}{\triangle \omega_R}\right)^2\right) V_R} \tag{1.70}$$

with $\left|A_p\right|^2$ the energie of the mode corresponding to the resonance frequency ω_{p_0}, $N_s = \left|A_s\right|^2 / (\hbar \omega_{s_0})$ the number of photons in the cavity at the frequency ω_{s_0} of the resonance used for the Stokes, and $H_{s_0}(\omega)$ the normalized frequency response of the cavity for this Stokes resonance. Typically, the Stokes resonance peak will be much narrower than the Lorentzian peak of the Raman gain by a factor of about 10 to 100 (see Fig. 1.19). This means that only the Stokes photons created whose frequency ω is very close to the Stokes resonance frequency ω_{s_0} will have an important lifetime, the other disappearing quickly after they are created. We will therefore neglect the Stokes photons with a frequency $\omega \neq \omega_{s_0}$, which allows us to approximate the total Stokes power generated by the stimulated Raman scattering by :

$$P^R_{total} = \frac{c^2}{n_0^2} \frac{g_R^B \left|A_p\right|^2 \hbar \omega_{s_0} N_s}{\left(1 + 4\left(\frac{\omega_{s_0} - \omega_s}{\triangle \omega_R}\right)^2\right) V_R} \tag{1.71}$$

If we neglect the other nonlinear effects, then the equation on the number of Stokes pho-

tons in the cavity has the following form :

$$\frac{dN_s}{dt} = -\frac{N_s}{\tau_s} + \frac{P_{total}^R}{\hbar\omega_{s_0}} = -\frac{N_s}{\tau_s} + \frac{c^2}{n_0^2}\frac{g_R^B \left|A_p\right|^2 N_s}{\left(1+4\left(\frac{\omega_s-\omega_{s_0}}{\triangle\omega_R}\right)^2\right)V_R} \tag{1.72}$$

with $\tau_s = \frac{Q_s}{\omega_{s_0}}$ the lifetime of the Stokes photons in the cavity. But this equation only takes into account the stimulated Raman scattering. If we consider the relationship between spontaneous and stimulated Raman scattering described in equation 1.60, then this equation becomes :

$$\frac{dN_s}{dt} = -\frac{N_s}{\tau_s} + \frac{G_r N_p (N_s+1)}{1+4\left(\frac{\omega_s-\omega_{s_0}}{\triangle\omega_R}\right)^2} \tag{1.73}$$

with $G_r = \frac{c^2}{n_0^2}\frac{\hbar\omega_p g_R^B}{V_R}$ the Raman gain of the cavity. The gain of a Stokes photon resulting in the loss of a pump photon, the equation on the electric field amplitude of the pump laser 1.20 then becomes :

$$\frac{dA_p}{dt} = i(\omega_p-\omega_{p_0})A_p - \frac{A_p}{2\tau_p} - \frac{G_r A_p (N_s+1)}{2\left(1+4\left(\frac{\omega_s-\omega_{s_0}}{\triangle\omega_R}\right)^2\right)} + \sqrt{\frac{\sqrt{T_{p_{max}}}P_{p_{in}}}{2\tau_p}} \tag{1.74}$$

with $\tau_p = \frac{Q_p}{\omega_{p_0}}$ the lifetime of the pump photons in the cavity. For these equations to be useful to us, however, we must add to them the other nonlinear optical effects we described in section 1.4.2. These effects will indeed be the main obstacle to the stimulated Raman scattering in our cavity and thus to the obtention of a Raman laser, particularly the free-carrier absorption which is the largest of the various absorptions in our cavities, and must be taken into account if we want to accurately model the behavior of our cavities. The equations of the doubly resonant cavity then quickly become much more complicated :

$$\frac{dA_p}{dt} = -\left(\frac{1}{\tau_p} + \gamma_{p_r}^{FCA}N_e + \gamma_{pp}^{TPA}N_p + (\gamma_{ps}^{TPA}+\gamma_{sp}^{TPA})N_s + \frac{G_r(N_s+1)}{1+4\left(\frac{\triangle\omega_s}{\triangle\omega_R}\right)^2}\right)\frac{A_p}{2} + \tag{1.75}$$

$$+i\triangle\omega_p A_p + \sqrt{\frac{\sqrt{T_{p_{max}}}P_{p_{in}}}{2\tau_p}}$$

$$\frac{dN_s}{dt} = -\left(\frac{1}{\tau_s} + \gamma_{s_r}^{FCA} N_e + \gamma_{ss}^{TPA} N_s + (\gamma_{ps}^{TPA} + \gamma_{sp}^{TPA}) N_p\right) N_s + \frac{G_r N_p (N_s + 1)}{1 + 4\left(\frac{\triangle\omega_s}{\triangle\omega_R}\right)^2} \tag{1.76}$$

$$\frac{dN_e}{dt} = -\frac{N_e}{\tau_{fc}} + \sum_{I,J=p,s}\sum \left(\frac{1}{2}\gamma_{IJ}^{TPA} N_I N_J\right) + \sum_{I=p,s} \gamma_I^l N_I \tag{1.77}$$

$$\rho_{Si} C_p^{Si} V_{eff}^T \frac{d\triangle T}{dt} = -\frac{\triangle T}{R_T} + \sum_{I,J=p,s}\sum \left(\hbar\omega_I \gamma_{IJ}^{TPA} N_I N_J\right) + \sum_{I=p,s} \hbar\omega_I \left(\gamma_{I_r}^{FCA} N_e N_I + \gamma_I^l N_I\right) \tag{1.78}$$

$$\triangle\omega_I = \omega_I - \omega_{I_0} + \gamma_{I_i}^{FCD} N_e + \gamma_I^T \triangle T \tag{1.79}$$

where $\tau_I = \frac{Q_I}{\omega_{I_0}}$ is the lifetime of the photons $N_I = \frac{|A_I|^2}{\hbar\omega_I}$ inside the cavity (where $I = p,s$ represents either the pump or the Stokes mode), $G_r = \frac{c^2}{n_0^2}\frac{\hbar\omega_p g_R^B}{V_R}$ is the Raman gain, $\gamma_{I_r}^{FCA} = \frac{c}{n_0}\frac{\sigma_r}{V_{FCA}^I}$ and $\gamma_{I_i}^{FCD} = \frac{\omega_{I_0}}{n_0}\frac{\sigma_i}{V_{FCA}^I}$ the coefficients of free-carrier absorption and dispersion, $\gamma_I^l = \frac{c}{n_0}\frac{\hbar\omega_{I_0}\alpha_{lin}}{R_{eff}^I}$ those of the linear absorption, and $\gamma_I^T = \frac{\omega_{I_0}}{n_0} n_T$ those of the thermal dispersion. The coefficients $\gamma_{IJ}^{TPA} = \frac{c^2\hbar\omega_I\beta^{TPA}}{n_0^2 V_{TPA}^{IJ}}$ represent the two-photon absorption (where I and J represent either the pump or the Stokes modes) : there are actually four different coefficients here because there are four possible kinds of two-photon absorption in our cavity - two pump photons, a pump photon + a Stokes photon, a Stokes photon + a pump photon, or two Stokes photons. The two pump photons absorption will be of course the most important because there is usually more pump photons than Stokes photons in the cavity, but the other kinds of two-photon absorption will be significant from the moment when stimulated Raman scattering predominates and when many Stokes photons are created. The coefficients associated with the Kerr effect are not shown because they are actually insignificant for the powers that we used compared to the other forms of dispersion (see Chapter 2). R_T et V_{eff}^T represent respectively the thermal resistance and the thermal effective volume of the cavity. The different characteristic volumes V_{TPA}^{IJ}, V_{FCA}^I and the fractions R_{eff}^I are then defined as :

$$V_{TPA}^{IJ} = \frac{\left(\iiint_V n(\overrightarrow{r})^2 \left\|\overrightarrow{E}_I(\overrightarrow{r})\right\|^2 dr^3\right)\left(\iiint_V n(\overrightarrow{r})^2 \left\|\overrightarrow{E}_J(\overrightarrow{r})\right\|^2 dr^3\right)}{\iiint_{Si} n_0^4 \left\|\overrightarrow{E}_I(\overrightarrow{r})\right\|^2 \left\|\overrightarrow{E}_J(\overrightarrow{r})\right\|^2 dr^3} \tag{1.80}$$

$$V_{FCA}^{I} = \frac{\left(\iiint\limits_{V} n(\overrightarrow{r})^2 \left\| \overrightarrow{E}_I(\overrightarrow{r}) \right\|^2 dr^3\right)\left(\iiint\limits_{Si} N_e^d(\overrightarrow{r}) dr^3\right)}{\iiint\limits_{Si} N_e^d(\overrightarrow{r}) n_0^2 \left\| \overrightarrow{E}_I(\overrightarrow{r}) \right\|^2 dr^3} \tag{1.81}$$

$$R_{eff}^{I} = \frac{\iiint\limits_{V} n(\overrightarrow{r})^2 \left\| \overrightarrow{E}_I(\overrightarrow{r}) \right\|^2 dr^3}{\iiint\limits_{Si} n_0^2 \left\| \overrightarrow{E}_I(\overrightarrow{r}) \right\|^2 dr^3} \tag{1.82}$$

These equations will be used in Chapter 3 to describe the behavior of a Raman laser fabricated in a silicon photonic crystal doubly resonant nanocavity.

1.5 Conclusion.

In this chapter, we described photonic crystals, first from a theoretical point of view, defining these structures and the types of photonic crystals. We explained why we chose to use two-dimensional photonic crystals etched in a silicon membrane because of their greater ease of fabrication and their greater compatibility with integrated optics and silicon optoelectronic. We also described the waveguides W1 designed from these photonic crystals and in particular the Kuramochi kind of cavities [26] in which we made in the experimental measurements which are described in Chapter 2 of this thesis. We also briefly described the methods (plane-wave and FDTD) used by the softwares that were used to model these photonic crystals. We then described in detail the different steps of the fabrication of these photonic crystals and of their suspended access waveguides, fabrication which was carried out in the clean room of the IEF. The different machines and methods used in these steps were presented : the two electron-beam lithography machines available in the clean room (Raith 150 and Nanobeam 4) and their differences, as well as the masks designed using the software L-Edit for this lithography, the Inductively Coupled Plasma Reactive Ion Etching used to etch the holes of the photonic crystal in the silicon substrate, the cutting of the substrate with the diamond blade saw, and the wet etching with hydrofluoric acid used to remove the silica under silicon and obtain a membrane silicon photonic crystal.

We concluded this chapter by a study of the different nonlinear optical effects prevailing in our silicon nanocavities, which allowed us to model the behavior of our cavities and obtain a system of nonlinear equations (on the amplitude of the electric field in the cavity, the number of free carriers, and the temperature) describing the behavior of a silicon nanocavity with a single resonance and to calculate the coefficients associated with the different nonlinear effects in the cavity : the nonlinear two-photon and free-carrier absorptions, and the dispersions due to the free carriers, to the Kerr effect, and to the tem-

perature. This is the model that will be used to study the phenomenon of high-frequency self-induced oscillations in silicon nanocavities in the second chapter of this thesis. We then modified this system of equations to take into account the case of a silicon nanocavity with two resonances, so we could include the spontaneous and stimulated Raman scattering, and thus obtain the equations describing the operation of a Raman laser. This new model will be used in Chapter 3 of this thesis to describe the operation of these Raman lasers and study the Raman scattering in the doubly resonant cavities that we fabricated.

Chapter 2

High-frequency self-induced oscillations in a nanocavity.

2.1 Introduction.

We saw in the previous chapter that nonlinear optical effects are very important in photonic crystal nanocavities, since they depend on the ratio Q/V_m between the quality factor of the cavity and its modal volume V_m. Among these effects, the one that interests us the most is stimulated Raman scattering, since it is the only way to obtain a laser fully in silicon that has been found so far [54, 55, 56, 57, 58]. However, this phenomenon is in competition with many other nonlinear phenomena, including the nonlinear two-photon and free-carrier absorptions, which can easily prevent us from obtaining a Raman laser if they are too important. Although the two-photon absorption coefficient of our cavities can be easily calculated from the FDTD simulation of the cavity, that is not the case of the free-carrier dispersion and absorption (which is much larger than the two-photon absorption), which will depend strongly both on the free-carrier lifetime in the cavity and on the effective volume on which they will expand, which cannot be easily calculated by FDTD. To better understand those free-carrier effects, we decided to study the phenomenon of high frequency self-induced oscillations, a nonlinear effect created by the free-carrier dispersion. This phenomenon consists of a modulation of the output power of the cavity, which is itself linked to a modulation of the transmission of the cavity under the influence of free-carrier dispersion, which will detune the cavity resonance with respect to the laser wavelength. The interest for this phenomenon is very recent in microcavities, since the first paper (theoretical) on the subject was published in May 2011 by Malaguti [59], less than seven months before we observed it in our own nanocavities in January 2012, and the first paper on the observation of the high frequency self-induced oscillations in microring resonators was published by Soltani & co [60] a few months later. We were the first peo-

ple to measure experimentally these high frequency self-induced oscillations in a silicon photonic crystal nanocavity, results we presented in an paper published in May 2013 [1].

This self-pulsing phenomenon is also very interesting because of its applications to microwave photonics, a field that seeks to provide functions with integrated optics and optoelectronics that are difficult to obtain in the radio-frequency domain [61]. In particular, the optical generation and distribution of microwave signals in a very compact system are key techniques of microwave photonics. It has been theoretically shown that self-pulsing at high frequency (up to 100 GHz) can be obtained in resonant systems such as photonic crystal cavities in the presence of strong nonlinear effects [59].

Self-pulsing is an intrinsic property of nonlinear systems characterized by delay-differential dynamics [62]. An key feature of optical microcavities is that the photon lifetime can be in the same range as the free-carrier lifetime. In this case, self-pulsing can be triggered by the interaction between free-carrier dispersion and [59, 63]. These oscillations are obtained for frequencies in the gigahertz range and therefore differ significantly from the oscillations created by the competition between free-carrier and thermal dispersions, which are limited to frequencies in the megahertz range [47, 64].

We measured experimentally for the first time non-attenuated high frequency self-induced oscillations in a silicon photonic crystal nanocavity [1], with a frequency close to 3 GHz. Although this kind of self-pulsing has also been measured in silicon microrings by Soltani, who presented his first results in an article published a few months after we made our measurements [60], the self-induced oscillations in our photonic crystals nanocavity have a much higher frequency than those observed in a microring resonator, whose frequency is only 0.5 GHz. Despite the fact that these oscillations are created by nonlinear effects, they are also quasi-sinusoidal, unlike the oscillations in microring resonators. This remarkable property is explained by the model developed in this chapter.

This chapter is divided into five parts. The first part describes the experimental setup used to measure the oscillations and the nanocavity where they were measured, and presents the experimental results. The second part presents the equations used to model the nanocavity and the simplifications we have made of these equations compared to the model presented in section 1.3 of the previous chapter. We solve this system of equations in the third part by linearizing them for small variations around the steady state values, which allows us to calculate the oscillation frequency and predict whether they will be attenuated or not. The fourth part deals with a resolution of the nonlinear equations by harmonic analysis, which allowed us to calculate their amplitude, as well as the amplitude of the second harmonic, and estimate this way the spectral purity of the oscillations, confirming that they are quasi-sinusoidal. The fifth part compares the experimental results with the results predicted by the theoretical model and the numerical simulations, showing that we have an excellent agreement between the two, which allows us to determine among other things the free-

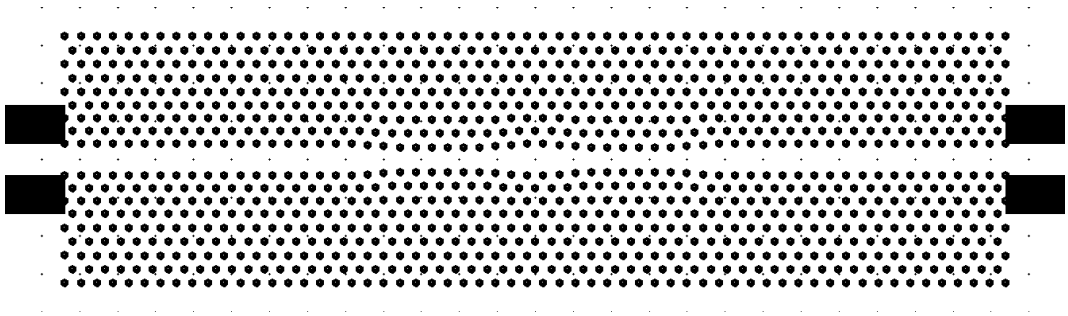

Figure 2.1: A GDS mask of the same type as the one used for the lithography of the cavity with Raith 150. The nanocavity, of the type described previously in figure 1.4, was made by shifting the holes of a waveguide W0.98. This waveguide extends on each side of the cavity over a length of 6 holes, before expanding to become a waveguide W1.05 to allow better coupling with the access ridge waveguides. The total length of the structure is 25 microns. The shifts of the holes were greatly exaggerated on this mask for readability : they are usually too small to be visible to the naked eye.

carrier lifetime for our nanocavities fabricated in a silicon membrane.

2.2 Experimental setup used for the measurements.

The measurements were performed on a Kuramochi-type cavity similar to the one depicted in figure 1.4, which we fabricated using the Raith 150. This cavity, whose period for the photonic crystal is equal to $a = 420$ nm, was designed by shifting the holes of a photonic crystal waveguide W0.98, i.e. a waveguide of width $0.98 \times \sqrt{3}a$ (slightly narrower than the waveguide W1). This waveguide is extended on each side of the cavity to create a barrier of length 6 holes, to ensure the good confinement of the electromagnetic field in the cavity, before being expanded to turn into a waveguide W1.05 (a waveguide of width $1.05 \times \sqrt{3}a$), to ensure a better coupling between the photonic crystal and the input and output [65] access ridge waveguides. The total length of the photonic crystal constituting the nanocavity is about 25 microns (see Fig. 2.1). The structure studied is therefore extremely compact.

To free ourselves from the thermal effects, including the thermal dispersion, and thus consider only the influence of the free-carrier dispersion on the cavity self-pulsing, we decided to modulate the beam of the input laser by using a Mach-Zehnder modulator. This device allows us to generate pulses of length 10 ns, which will be repeated at a frequency of 100 kHz. The peak power of the pulses at the entrance of the photonic crystal is 2 mW. A photodiode with a 6 GHz bandwidth was used to detect the output signal, which we then displayed on an oscilloscope (see Fig. 2.2). A portion of the output signal is redirected to a powermeter in order to measure the average output power.

The measurements were carried out in two stages. Our nanocavity was first measured

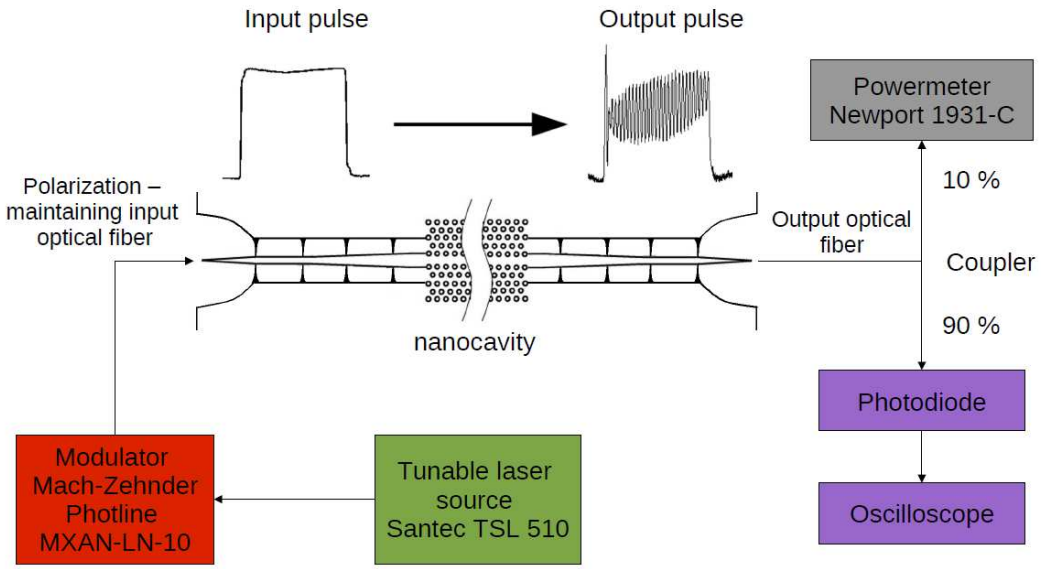

Figure 2.2: Diagram of the experimental setup used to measure the oscillations in the cavity. A continuously tunable laser source was combined with a Mach-Zehnder modulator to send to the entrance of the cavity pulses of length 10 ns, repeated every 100 kHz, with a peak power of 2 mW. The oscillations of the output signal were then visualized using a photodiode connected to an oscilloscope.

immediately after the fabrication in the clean room. It then had a resonance wavelength of $\lambda_0 \simeq 1590$ nm, a quality factor of $Q \simeq 9 \times 10^4$ and a maximum transmission at the resonance of $T_{max} = 47\%$. Oscillations were then observed in the cavity with a period of about 300 ps, for a detuning between the wavelength of the laser and the wavelength of the cavity resonance between -40 pm and -20 pm (the period of the oscillations hardly changed with the detuning). These oscillations were always attenuated and disappeared before the end of the pulse (see Fig. 2.3a), which is hardly useful if you want to design a microwave source. The cavity was then immersed in a mixture of nitric acid HNO_3 - hydrogen peroxide H_2O_2 3:1, a treatment used to reduce the free-carrier lifetime in the cavity and thus the free-carrier absorption [66] by oxidizing the surface of the photonic crystal, which will introduce new surface states which will change the speed of recombination of the free carriers at the silicon surface. After the nitric acid treatment, we repeated the measurements and first found that the wavelength of the cavity resonance had moved of 5 nm to $\lambda_0 \simeq 1585$ nm and that its quality factor had increased to $Q \simeq 1.3 \times 10^5$. This is due to the fact that the silicon was slightly etched by the nitric acid, changing the geometry of the photonic crystal and thus slightly increasing its quality factor. The maximum transmission at the resonance between the entrance and the exit of the photonic crystal had slightly decreased to reach $T_{max} = 41\%$ (see Fig. 2.4). But the main difference compared to before the nitric acid treatment is the presence of non-attenuated oscillations over the whole length of the pulse, for a detuning between the wavelength of the laser and the resonance of the cavity between -30 pm and -10 pm (see Fig. 2.3b). The period of these

oscillations is about 350 ps, which corresponds to a frequency of about 3 GHz. These oscillations are almost sinusoidal.

The origin of this self-pulsing phenomenon is relatively easy to understand : when you turn the laser on, it will create free carriers in the cavity by two-photon absorption, which will detune the frequency of the cavity resonance relative to the laser frequency through the free-carrier dispersion. This detuning will reduce the transmission of the cavity, and thus the energy stored within, which will in turn reduce the number of free carriers. The cavity will then retune itself toward the frequency of the laser, which will again increase the energy in the cavity, and thus the number of free carriers, and so on (see Fig. 2.5). However, obtaining non-attenuated oscillations in a photonic crystal cavity is not so simple. As can be seen, the behavior of the cavity is very dependent on the quality factor and the free-carrier lifetime. Other factors such as the detuning between the wavelength of the pump laser and that of the resonance of the cavity are also important. To predict the conditions under which non-attenuated oscillations are possible, and to calculate the oscillation frequency, we had to accurately model the behavior of the nanocavity.

2.3 The equations of the nanocavity.

We recall here the results of the calculations we did in section 1.4.2. The system of equations describing the temporal behavior of our nanocavity has the following form :

$$\frac{dA}{dt} = -\frac{A}{2\tau} - \frac{\gamma^{TPA}|A|^2 A}{2\hbar\omega} - \frac{\gamma^{FC} N_e A}{V_{eff}^{FC}} + i(\omega - \omega_0 - \frac{\gamma_i^{Kerr}|A|^2}{\hbar\omega} - \gamma_i^T \triangle T)A + \sqrt{\frac{\sqrt{T_{max}}P_{in}}{2\tau}} \tag{2.1}$$

$$\frac{dN_e}{dt} = -\frac{N_e}{\tau_{fc}} + \frac{1}{2}\gamma^{TPA}\frac{|A|^4}{(\hbar\omega)^2} + \gamma^l \frac{|A|^2}{\hbar\omega} \tag{2.2}$$

$$\frac{d\triangle T}{dt} = -\frac{\triangle T}{\tau_T} + \left(\frac{\gamma^{TPA}|A|^2}{\hbar\omega} + \frac{2\gamma_r^{FC} N_e}{V_{eff}^{FC}} + \gamma^l\right)\frac{|A|^2}{\rho_{Si} C_p^{Si} V_{eff}^T} \tag{2.3}$$

with $\tau = \frac{Q}{\omega_0}$ the photon lifetime in the cavity, τ_{fc} the free-carrier lifetime, $\gamma^{TPA} = \frac{c^2}{n_0^2}\frac{\hbar\omega\beta^{TPA}}{V_{TPA}}$ the two-photon absorption coefficient, $\gamma^{FC} = \gamma_r^{FC} + i\gamma_i^{FC} = \frac{c}{2n_0 R_{eff}}(\sigma_r - i\frac{2\omega_0}{c}\sigma_i)$ the free-carrier absorption and dispersion coefficients, $\gamma^l = \frac{c}{n_0}\frac{\alpha_{lin}}{R_{eff}}$ the linear absorption coefficient, $\gamma_i^{Kerr} = -\frac{\omega_0 c}{n_0^2}\frac{\hbar\omega n_2}{V_{TPA}}$ the Kerr effect coefficient, $\gamma_i^T = -\frac{\omega_0}{n_0}n_T$ the thermal dispersion coefficient, $\tau_T = \rho_{Si} C_p^{Si} V_{eff}^T R_T$ the cooling time of the cavity, with R_T the cavity thermal resistance. V_{eff}^{FC} is the effective volume on which the free carriers spread in the silicon,

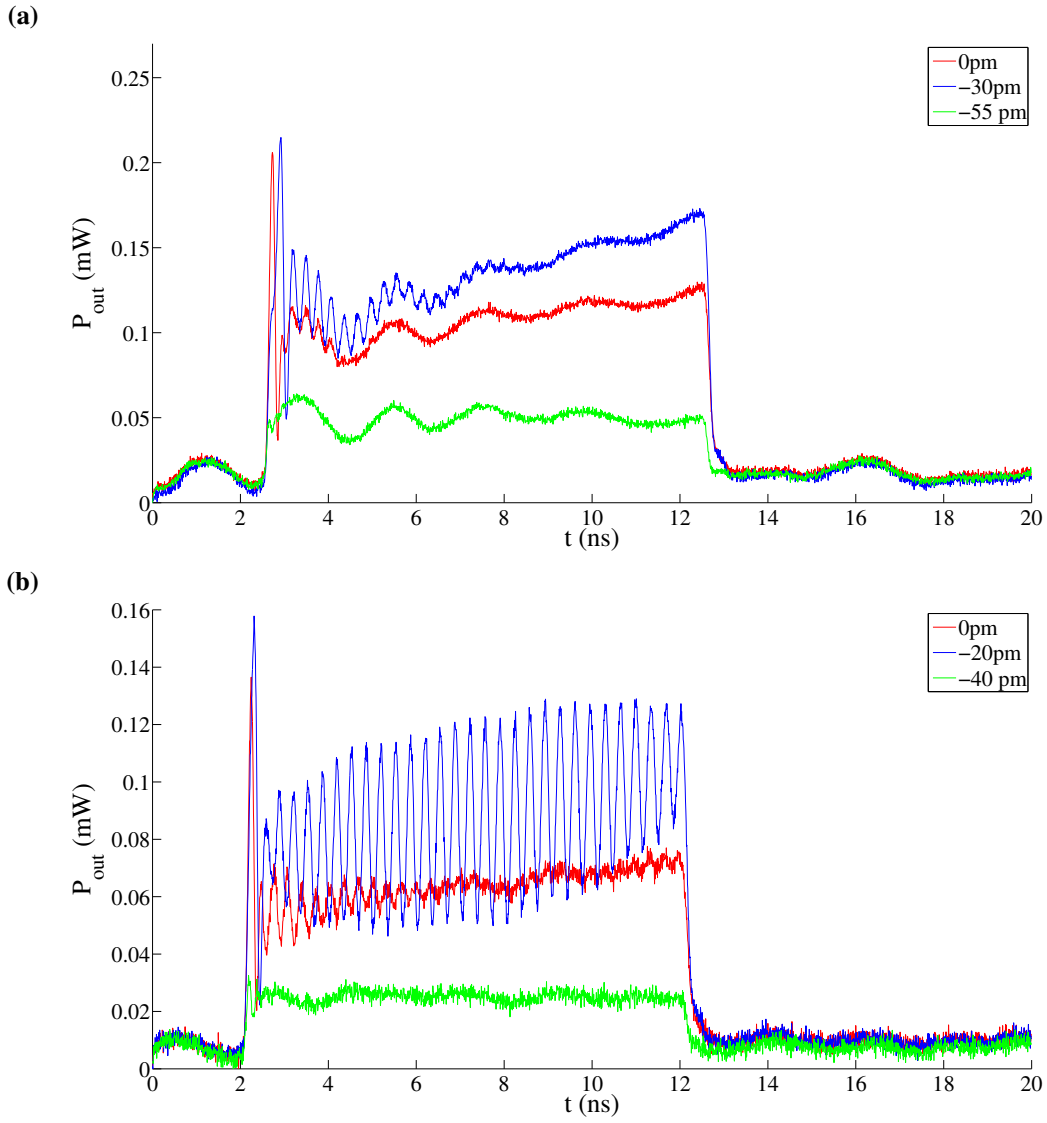

Figure 2.3: The measured output power as a function of time for different detunings between the wavelength of the laser and that of the resonance cavity. The input power is 2 mW and the pulse length is 10 ns. (a) Cavity measured before the chemical treatment with nitric acid. We can see that in this case, oscillations are always attenuated. We can also observe a slow modulation of the output signal (with a period 2 ns), which is actually caused by a parasitic effect due to the measurement equipment. We were able to eliminate this interference effect for the following measurements. (b) Cavity measured after the chemical treatment with nitric acid. We can observe non-attenuated oscillations over the entire length of the pulse for a detuning of -20 pm.

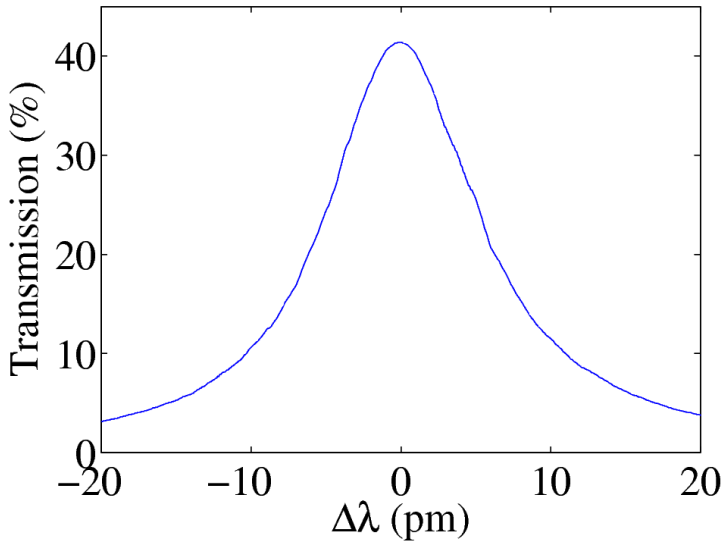

Figure 2.4: The transmission spectrum of the cavity measured at low power after the nitric acid treatment, as a function of the detuning $\triangle\lambda$ between the wavelength of the pump laser and that of the cavity resonance. The resonant wavelength of the cavity is equal to $\lambda_0 \simeq 1585$ nm, the quality factor to $Q \simeq 1.3 \times 10^5$ and the maximum transmission at the resonance between the entrance and the exit of the photonic crystal is $T_{max} = 41\%$.

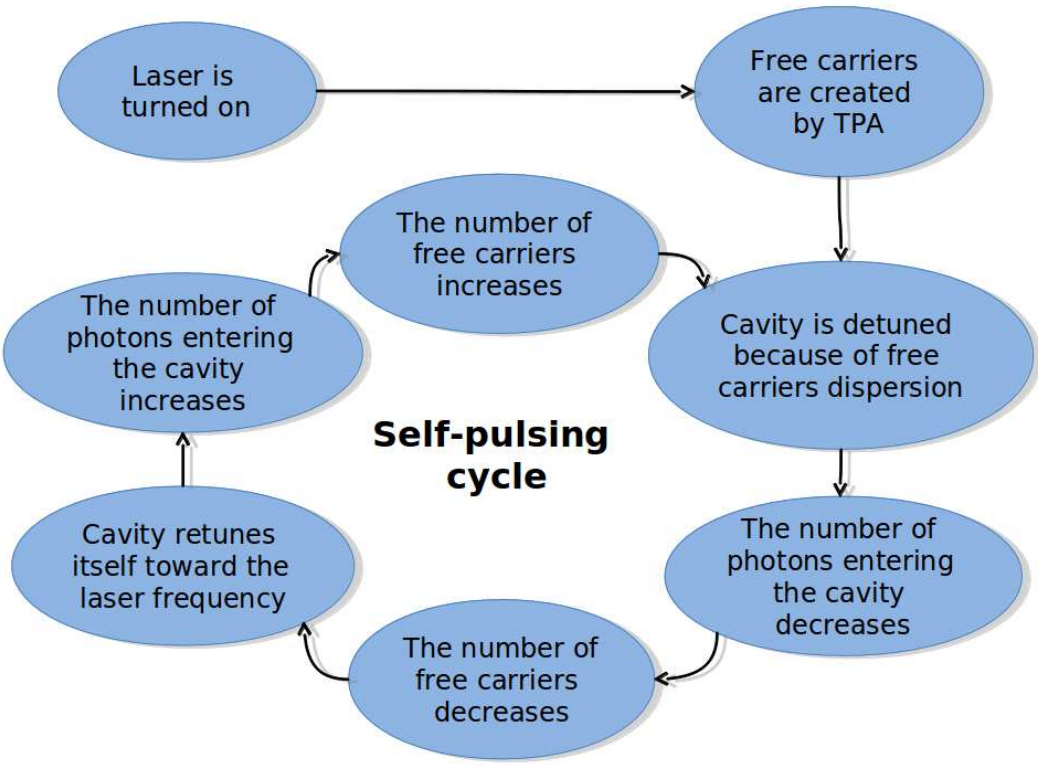

Figure 2.5: The cavity self-pulsing cycle.

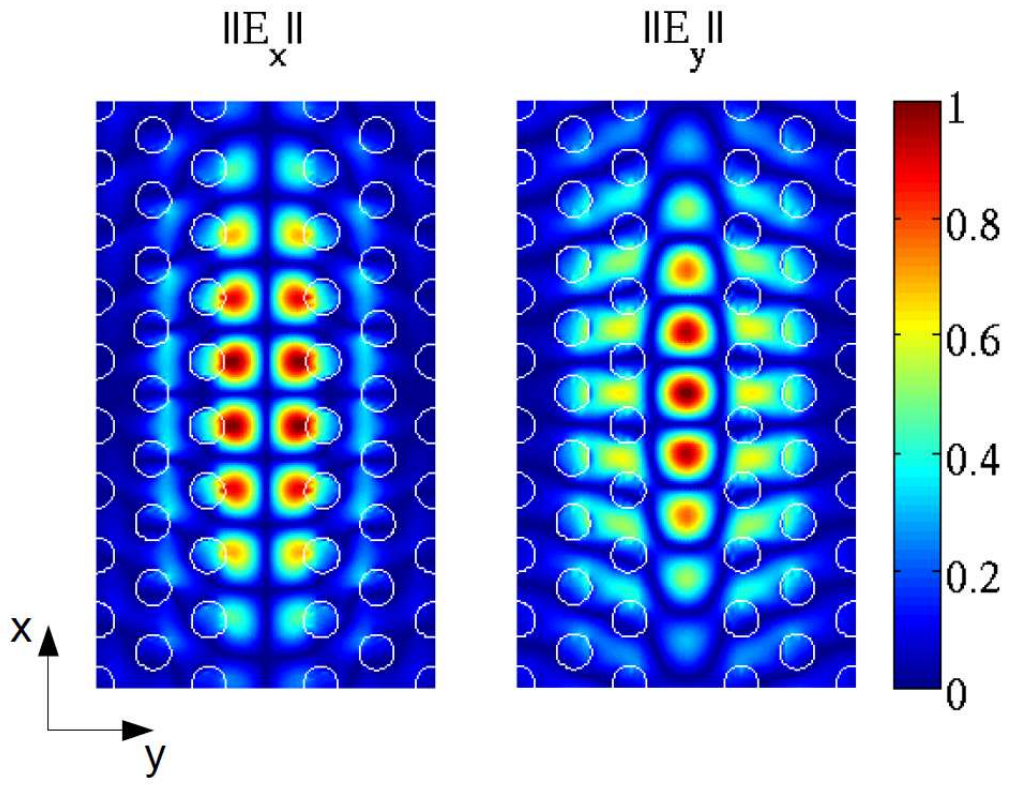

Figure 2.6: The pattern of the electromagnetic field for the resonant mode of the cavity, calculated by FDTD, that we used to determine the characteristic volume of the two-photon absorption in the cavity.

defined as :

$$V_{eff}^{FC} = \frac{\left(\iiint_{Si} n(\overrightarrow{r})^2 \left\|\overrightarrow{E}(\overrightarrow{r})\right\|^2 dr^3\right)\left(\iiint_{Si} N_e^d(\overrightarrow{r}) dr^3\right)}{\iiint_{Si} N_e^d(\overrightarrow{r}) n_0^2 \left\|\overrightarrow{E}(\overrightarrow{r})\right\|^2 dr^3} \tag{2.4}$$

We can see that this effective volume V_{eff}^{FC} differs from the characteristic volume V_{FCA} of the free-carrier absorption, where the integral of the energy was carried out on all of the photonic crystal and not only its silicon part. These two volumes are linked by $V_{eff}^{FC} = V_{FCA}/R_{eff}$. Since these free carriers will be present only in silicon, it makes more sense to use this new volume.

For a cavity of the Kuramochi type, the values of V_{TPA} and R_{eff} calculated by the FDTD simulation are $R_{eff} = 1.1$ and $V_{TPA} = 0.483\ \mu m^3$ (see Fig. 2.6). In fact, the only parameters of the model we used which we can not calculate are the values associated with the behavior of free carriers : the free-carrier lifetime τ_{fc} and their effective volume V_{eff}^{FC} (we would need to make a simulation of the behavior of free carriers in the cavity, which is quite complicated), and those associated with the thermal behavior of the cavity, i.e. the

Parameters of the model	Values for the measured cavity	Origin
τ	0.11 ns	measured
τ_{fc}	$\simeq 0.2$ ns	measured + modeling
τ_T	$\simeq 39$ ns	measured
γ^{TPA}	$1.61 \times 10^4\ s^{-1}$	FDTD
γ^l	$2.88 \times 10^8\ s^{-1}$	FDTD
γ_r^{FC}	$5.98 \times 10^4\ \mu m^3 \cdot s^{-1}$	modeling
γ_i^{FC}	$1.73 \times 10^6\ \mu m^3 \cdot s^{-1}$	modeling
γ_i^{Kerr}	$-3.34 \times 10^4\ s^{-1}$	FDTD
γ_i^T	$-6.33 \times 10^8\ K^{-1} \cdot s^{-1}$	modeling
V_{eff}^{FC}	$\simeq 5.25\ \mu m^3$	measured + modeling
V_{eff}^T	$\simeq 3.0\ \mu m^3$	measured + modeling

Table 2.1: The values of the different parameters used to model the cavity.

cooling time of the cavity τ_T and the effective thermal volume V_{eff}^T. The values of these parameters have been determined from the experimental results. The values of the parameter corresponding to the measured cavity (after the nitric acid treatment) are shown in Table 2.1.

We can still simplify the system of equations above, by noting that for the powers we used to make the measurements ($P_{in} \simeq 2$ mW), we have for steady-state solutions $|A|^2 \simeq 2.84$ fJ and $N_e \simeq 8.35 \times 10^4$. For these two values the number of free carriers generated by the two-photon absorption is an order of magnitude above the number of free carriers generated by the linear absorption. We will neglect in the future in the influence of linear absorption in our model and take $\gamma^l = 0$. Similarly, we can see that the dispersion due to the Kerr effect is an order of magnitude below the free-carrier or thermal dispersions. We will thus also neglect the Kerr effect and take $\gamma_i^{Kerr} = 0$.

The third simplification that we can make is based on the fact that the cooling time of the cavity is a hundred times larger than the photon and free-carrier lifetimes in the cavity, and four times larger than the duration of the pulses we sent into the cavity. Temperature and thermal dispersion will therefore change very slowly compared to the numbers of photons and free carriers. We can therefore assume that the temperature will remain almost constant throughout the duration of the input pulse and neglect at first the influence of temperature and thermal dispersion. The equations of the nanocavity then become :

$$\frac{dA}{dt} = -\frac{A}{2\tau} + i(\omega - \omega_0)A - \frac{\gamma^{TPA}|A|^2 A}{2\hbar\omega} - \frac{\gamma^{FC} N_e A}{V_{eff}^{FC}} + \sqrt{\frac{\sqrt{T_{max}} P_{in}}{2\tau}} \tag{2.5}$$

$$\frac{dN_e}{dt} = -\frac{N_e}{\tau_{fc}} + \frac{1}{2}\gamma^{TPA}\frac{|A|^4}{(\hbar\omega)^2} \tag{2.6}$$

Even taking into account the various simplifications we have made so far, this system

of equations is highly nonlinear and difficult to solve. To predict the behavior of the cavity and calculate the oscillation frequency and their amplitude, we had to use two different methods to simplify this problem : the first method was to linearize this system of equations for small variations around the steady-state values. This method allowed us to calculate the oscillation frequency and predict whether or not they were attenuated, but not to calculate their amplitude. So we then had to solve this system by a harmonic analysis to allow us to determine the amplitudes of the fundamental and second harmonic of the oscillations, and thus show that they are almost sinusoidal.

2.4 Linearization around the steady-state solutions.

To solve this system of equations and calculate the oscillation frequency, we decided first of all to look for the steady-state solutions to these equations and then to linearize them for small variations around these steady-state solutions. We then obtained a real, linearized equation in matrix form, from which we calculated the eigenvalues in order to obtain the oscillation frequency and their gain. We were then able to determine a simplified expression of this system and of the oscillation frequency at high power.

2.4.1 Linearized equation in matrix form.

To obtain a real linearized system in matrix form, we first need to change the first complex equation 2.5 to obtain two real equations. We can do that easily by dividing between real and imaginary parts. However, we found it was easier and more meaningful to decompose the complex amplitude of the signal in the form $A(t) = |A(t)|e^{i\varphi(t)}$. The derivative of the complex amplitude is then equal to:

$$\frac{dA}{dt} = \frac{d(|A|e^{i\varphi})}{dt} = \left(\frac{d|A|}{dt} + i|A|\frac{d\varphi}{dt}\right)e^{i\varphi} \tag{2.7}$$

By injecting this expression in the complex equation 2.5 we then obtain :

$$\frac{d|A|}{dt} + i|A|\frac{d\varphi}{dt} = -\frac{|A|}{2\tau} + i(\omega-\omega_0)|A| - \frac{\gamma^{TPA}|A|^3}{2\hbar\omega} - \frac{\gamma^{FC}N_e|A|}{V_{eff}^{FC}} + e^{-i\varphi}\sqrt{\frac{\sqrt{T_{max}}P_{in}}{2\tau}} \tag{2.8}$$

which gives us two real equations over $|A|$ and φ :

$$\frac{d|A|}{dt} = -\frac{|A|}{2\tau} - \frac{\gamma_r^{FC}|A|N_e}{V_{eff}^{FC}} - \frac{\gamma^{TPA}|A|^3}{2\hbar\omega} + \cos(\varphi)\sqrt{\frac{\sqrt{T_{max}}P_{in}}{2\tau}} \tag{2.9}$$

$$\frac{d\varphi}{dt} = (\omega - \omega_0) - \frac{\gamma_i^{FC} N_e}{V_{eff}^{FC}} - \frac{\sin(\varphi)}{|A|}\sqrt{\frac{\sqrt{T_{max}}P_{in}}{2\tau}} \tag{2.10}$$

With the real equation 2.6 on the number of free carriers N_e, this gives us a system of three real equations.

2.4.1.1 Steady-state solutions.

To linearize the system of real equations around an equilibrium point, we must first determine what are the steady-state solutions $(|A_0|, \varphi_0, N_{e_O})$ of the equations. The easiest equation to solve is that of the free carriers N_e. For $dN_e/dt = 0$, the equation 2.6 gives us :

$$N_{e_0} = \frac{\tau_{fc}\gamma^{TPA}|A_0|^4}{2(\hbar\omega)^2} \tag{2.11}$$

The equations 2.9 and 2.10 give us respectively $\cos(\varphi_0)\sqrt{\frac{\sqrt{T_{max}}P_{in}}{2\tau}} = \frac{|A_0|}{2\tau} + \frac{\gamma_r^{FC}|A_0|N_{e_0}}{V_{eff}^{FC}} + \frac{\gamma^{TPA}|A_0|^3}{2\hbar\omega}$ and $\sin(\varphi_0)\sqrt{\frac{\sqrt{T_{max}}P_{in}}{2\tau}} = (\omega - \omega_0) - \frac{\gamma_i^{FC}N_{e_0}}{V_{eff}^{FC}}$, which allows us to obtain the following relation of for the phase φ_0 :

$$\tan(\varphi_0) = \frac{(\omega - \omega_0) - \frac{\gamma_i^{FC}N_{e_0}}{V_{eff}^{FC}}}{\frac{1}{2\tau} + \frac{\gamma^{TPA}|A_0|^2}{2\hbar\omega} + \frac{\gamma_r^{FC}N_{e_0}}{V_{eff}^{FC}}} = \frac{(\omega - \omega_0) - \frac{\tau_{fc}\gamma^{TPA}\gamma_i^{FC}|A_0|^4}{2(\hbar\omega)^2 V_{eff}^{FC}}}{\frac{1}{2\tau} + \frac{\gamma^{TPA}|A_0|^2}{2\hbar\omega} + \frac{\tau_{fc}\gamma^{TPA}\gamma_r^{FC}|A_0|^4}{2(\hbar\omega)^2 V_{eff}^{FC}}} \tag{2.12}$$

As we can see, it is relatively easy to express these values as a function of the energy $|A_0|^2$ in the cavity. The equations 2.9, 2.10 and 2.12 also give us the relationship $\left((\omega - \omega_0) - \frac{\gamma_i^{FC}N_{e_0}}{V_{eff}^{FC}}\right)^2 \times \left(1 + \coth^2(\varphi_0)\right) \times |A_0|^2 = \frac{\sqrt{T_{max}}P_{in}}{2\tau}$, which we can too express as a five-degree polynomial in $|A_0|^2$, of which the energy $|A_0|^2$ is a root :

$$(\frac{|A_0|}{2\tau} + \frac{\gamma^{TPA}|A_0|^3}{2\hbar\omega} + \frac{\tau_{fc}\gamma^{TPA}\gamma_r^{FC}|A_0|^5}{2(\hbar\omega)^2 V_{eff}^{FC}})^2 + ((\omega - \omega_0)|A_0| - \frac{\tau_{fc}\gamma^{TPA}\gamma_i^{FC}|A_0|^5}{2(\hbar\omega)^2 V_{eff}^{FC}})^2 - \frac{\sqrt{T_{max}}P_{in}}{2\tau} = 0 \tag{2.13}$$

This being a five-degree polynomial, it can have several real roots, leading to a bistability phenomenon in our cavity. If we plot the output power $P_{out} = \frac{\sqrt{T_{max}}|A_0|^2}{2\tau}$ as a function of the input power P_{in}, then we can see that the cavity becomes bistable when the detuning $\triangle\lambda = c\,(1/\omega - 1/\omega_0)$ between the wavelength of the pump laser and the wavelength of the cavity resonance becomes negative. Self-pulsing can only occur when the cavity is on the high-energy branch of the bistability [59]. This bistability does not however influence the oscillations due to the free-carrier dispersion themselves, only the average power output of the cavity.

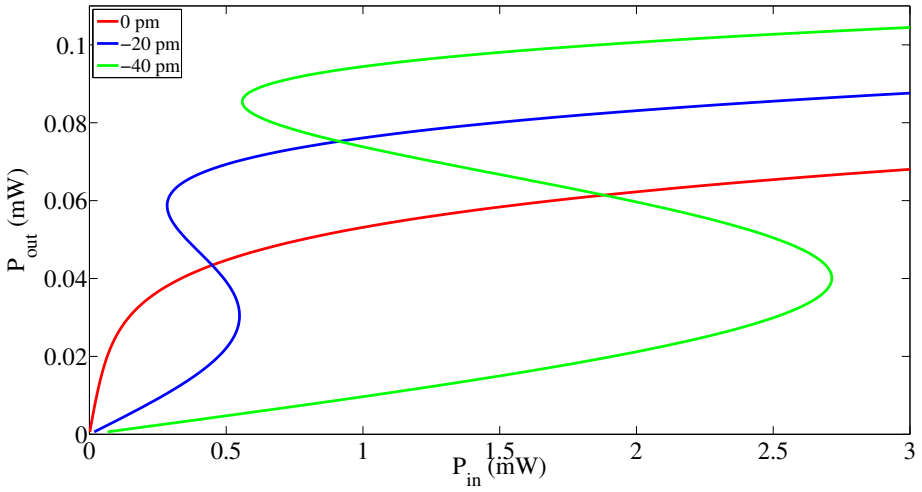

Figure 2.7: The output power of the cavity as a function of the input power in the steady state regime, for different detunings between the wavelength of the pump laser and that of the cavity resonance. Note that when this detuning becomes negative, i.e. when the wavelength of the laser is smaller than that of the resonance, the cavity presents a bistability phenomenon.

2.4.1.2 Small variations around an equilibrium point.

Once the steady-state solutions are known, we can linearize our system of equations for small variations $(\delta A, \delta\varphi, \delta N_e)$ around these solutions. The linearized system of equations can then be expressed as a linear equation in matrix form:

$$\frac{d}{dt}\begin{pmatrix} \delta|A| \\ \delta\varphi \\ \delta N_e \end{pmatrix} = M \begin{pmatrix} \delta|A| \\ \delta\varphi \\ \delta N_e \end{pmatrix} \tag{2.14}$$

where the matrix M is defined as :

$$M = \begin{pmatrix} -\frac{1}{2\tau} - \frac{\gamma_r^{FCA} N_{e_0}}{V_{eff}^{FC}} - \frac{3\gamma^{TPA}|A_0|^2}{2\hbar\omega} & -\sin(\varphi_0)\sqrt{\frac{\sqrt{T_{max}}P_{in}}{2\tau}} & -\frac{\gamma_r^{FC}|A_0|}{V_{eff}^{FC}} \\ \frac{\sin(\varphi_0)}{|A_0|^2}\sqrt{\frac{\sqrt{T_{max}}P_{in}}{2\tau}} & -\frac{\cos(\varphi_0)}{|A_0|}\sqrt{\frac{\sqrt{T_{max}}P_{in}}{2\tau}} & -\frac{\gamma_i^{FC}}{V_{eff}^{FC}} \\ \frac{2\gamma^{TPA}|A_0|^3}{(\hbar\omega)^2} & 0 & -\frac{1}{\tau_{fc}} \end{pmatrix} \tag{2.15}$$

It is then possible to determine the behavior of the linearized system by calculating the eigenvalues of the matrix M. Non-attenuated oscillations are only possible when this matrix has a pair of complex conjugate eigenvalues $\alpha_r \pm i\Omega$ which crosses the imaginary axis into the right half complex plane when we vary the parameters, i.e. such as the real part of the eigenvalues becomes positive : $\alpha_r > 0$. We then say that the matrix is characterized by a Hopf bifurcation, and the period of the oscillations is then equal to

$T = 2\pi/\Omega$.

If we plot the oscillation frequency as a function of input power and detuning $\triangle\lambda$ for the parameters listed in Table 2.1, then we can see that the non-attenuated oscillations are possible only for a detuning inferior to -12 nm and an input power greater than 1.5 mW (see Fig. 2.8a). The minimal frequency of non-attenuated oscillations is 2.5 GHz. It is therefore in the microwave range. This frequency varies very little with the detuning, but gradually increases with the input power. It may be noted that in the case of our nanocavity, the frequency of the non-attenuated oscillations remains below 10 GHz, which is unfortunately a relatively low value for microwaves. Typically, we are limited by the free-carrier lifetime τ_{fc}, which is in the nanosecond range.

2.4.2 Simplified expression of the frequency at high power.

The expression of the system we found in matrix form is very complicated, although it can easily be calculated with MATLAB to plot the different theoretical curves. However, we were able to determine a simplified expression of the oscillation frequency and of the energy in the cavity as a function of the detuning and of the input power at high power (see Fig. 2.8b). To obtain this expression, we first noticed that when $|A_0|^2$ is high enough (typically for $P_{in} \geq 2$ mW)), the equation 2.12 on φ_0 simplifies to:

$$\tan(\varphi_0) = \frac{(\omega-\omega_0) - \frac{\tau_{fc}\gamma^{TPA}\gamma_i^{FC}|A_0|^4}{2(\hbar\omega)^2 V_{eff}^{FC}}}{\frac{1}{2\tau} + \frac{\gamma^{TPA}|A_0|^2}{2\hbar\omega} + \frac{\tau_{fc}\gamma^{TPA}\gamma_r^{FC}|A_0|^4}{2(\hbar\omega)^2 V_{eff}^{FC}}} \sim -\frac{\gamma_i^{FC}}{\gamma_r^{FC}} \tag{2.16}$$

We also know that $\gamma_i^{FC} \gg \gamma_r^{FC}$ (see Table 2.1), which gives us $\tan(\varphi_0) \sim -\infty$ and therefore $\varphi_0 \sim -\frac{\pi}{2}$. The equation 2.13 on $|A_0|^2$ is simplified in the same way and becomes :

$$\frac{\tau_{fc}\gamma^{TPA}\gamma_i^{FC}|A_0|^5}{2(\hbar\omega)^2 V_{eff}^{FC}} - (\omega-\omega_0)|A_0| \sim \sqrt{\frac{\sqrt{T_{max}}P_{in}}{2\tau}} \tag{2.17}$$

If we choose to also neglect the influence of the two-photon and free-carrier absorptions, then the equation 2.15 on the matrix M is equivalent to:

$$M \sim \begin{pmatrix} 0 & \sqrt{\frac{\sqrt{T_{max}}P_{in}}{2\tau}} & 0 \\ \frac{-1}{|A_0|^2}\sqrt{\frac{\sqrt{T_{max}}P_{in}}{2\tau}} & 0 & -\frac{\gamma_i^{FC}}{V_{eff}^{FC}} \\ 0 & 0 & -\frac{1}{\tau_{fc}} \end{pmatrix} \tag{2.18}$$

We know that the eigenvalues of this matrix are the roots of its characteristic polynomial

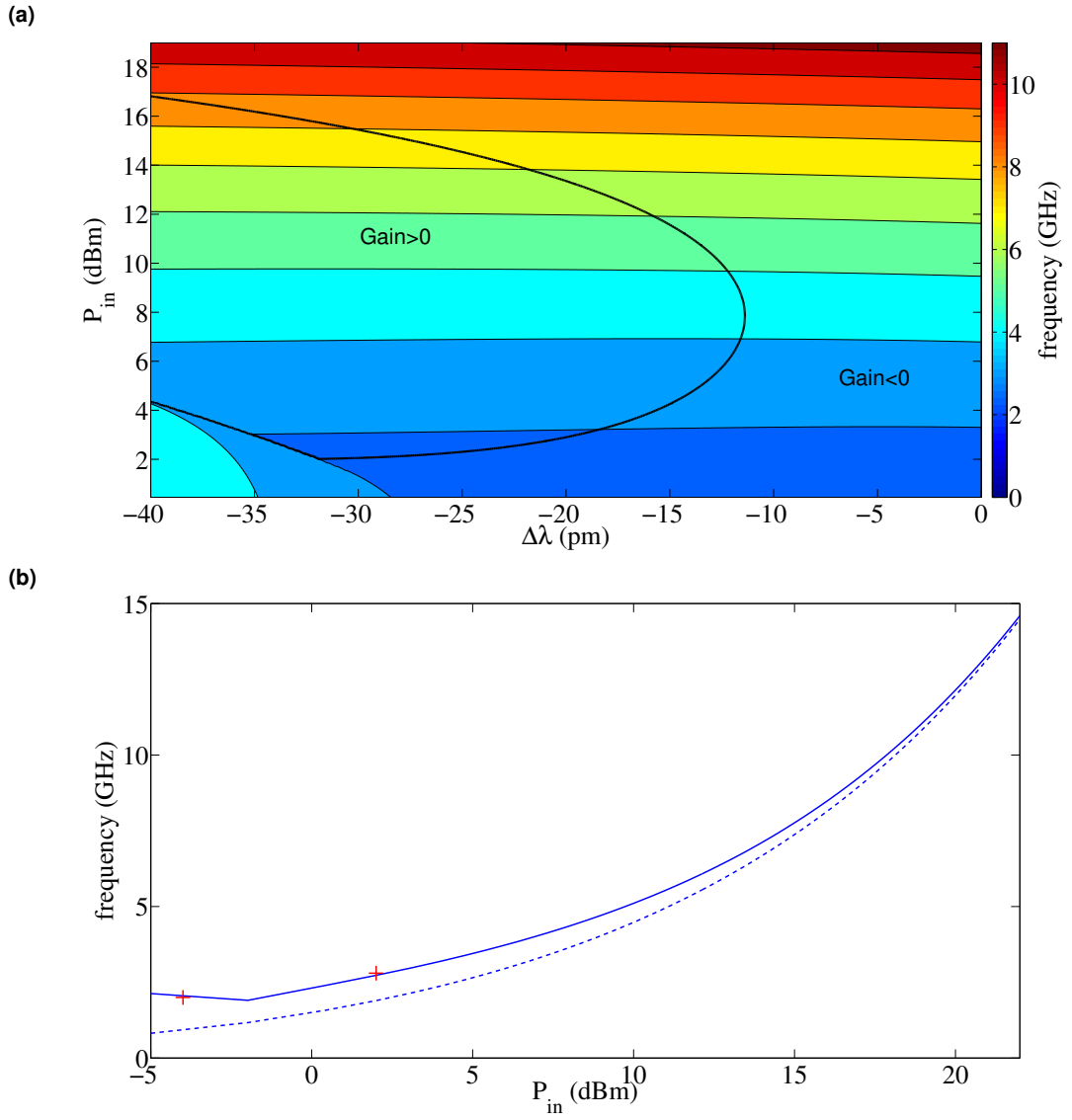

Figure 2.8: (a) The oscillation frequency as a function of the detuning $\triangle\lambda$ and of the input power P_{in}. The oscillations are non-attenuated inside the zone of positive gain, i.e. within the region defined by the black thick line. (b) The oscillation frequency as a function of the input power P_{in} for a detuning $\triangle\lambda = -20$ pm (solid line) and its simplified equivalent expression (doted line) - (see equation 2.23). The two red crosses represent the measured frequencies for $P_{in} = 0.5$ mW (a case where the oscillations are attenuated) and $P_{in} = 2$ mW (the case where we observed the non-attenuated oscillations).

:

$$P(X) = \det(XI - M) = \left(X + \frac{1}{\tau_{fc}}\right)\left(X^2 + \frac{1}{|A_0|^2}\frac{\sqrt{T_{max}}P_{in}}{2\tau}\right) \tag{2.19}$$

from which we can deduce the following equivalence on the oscillation frequency :

$$\Omega \sim \frac{1}{|A_0|}\sqrt{\frac{\sqrt{T_{max}}P_{in}}{2\tau}} \tag{2.20}$$

Numerically, we have $(\omega - \omega_0)|A_0| \ll \sqrt{\frac{\sqrt{T_{max}}P_{in}}{2\tau}}$, which allows us to linearize the equation 2.17 on $|A_0|$:

$$\sqrt[5]{\frac{\tau_{fc}\gamma^{TPA}\gamma_i^{FC}}{2(\hbar\omega)^2 V_{eff}^{FC}}\sqrt{\frac{2\tau}{\sqrt{T_{max}}P_{in}}}}|A_0| \sim \left(1 + \frac{(\omega-\omega_0)|A_0|}{\sqrt{\frac{\sqrt{T_{max}}P_{in}}{2\tau}}}\right)^{\frac{1}{5}} \sim \left(1 + \frac{1}{5}\frac{(\omega-\omega_0)|A_0|}{\sqrt{\frac{\sqrt{T_{max}}P_{in}}{2\tau}}}\right) \tag{2.21}$$

from which we can deduce the following equivalent expression of $|A_0|$ by dividing the equation 2.21 by the term $\sqrt[5]{\frac{\tau_{fc}\gamma^{TPA}\gamma_i^{FC}}{2(\hbar\omega)^2 V_{eff}^{FC}}\sqrt{\frac{2\tau}{\sqrt{T_{max}}P_{in}}}}$:

$$|A_0| \sim \frac{\sqrt[5]{\frac{2(\hbar\omega)^2 V_{eff}^{FC}}{\tau_{fc}\gamma^{TPA}\gamma_i^{FC}}\sqrt{\frac{\sqrt{T_{max}}P_{in}}{2\tau}}}}{1 - \frac{(\omega-\omega_0)}{5}\sqrt[5]{\frac{2(\hbar\omega)^2 V_{eff}^{FC}}{\tau_{fc}\gamma^{TPA}\gamma_i^{FC}}\left(\frac{2\tau}{\sqrt{T_{max}}P_{in}}\right)^2}} \tag{2.22}$$

We can see that the higher the initial detuning $(\omega - \omega_0)$, the higher the average energy in the cavity will be, which is consistent with what the figure 2.7 tells us. This expression allows us to calculate the simplified expression of the oscillation frequency by reinjecting it into equation 2.20. We then obtain the following equivalent expression (see Fig. 2.8b) :

$$\Omega \sim \sqrt[5]{\frac{\tau_{fc}\gamma^{TPA}\gamma_i^{FC}}{2(\hbar\omega)^2 V_{eff}^{FC}} \times T_{max}\left(\frac{P_{in}}{2\tau}\right)^2} - \frac{(\omega-\omega_0)}{5} \tag{2.23}$$

From this expression of the frequency, we can confirm that it is almost independent of the detuning, unlike the energy in the cavity : the term $\frac{(\omega-\omega_0)}{5}$ is indeed almost negligible compared to the first term of expression 2.23, and will therefore not much influence the evolution of the oscillation frequency Ω. It may also be noted that this frequency will increase with the input power, as shown by the results of the figure2.8, but that this increase will only be in $\sqrt[5]{P_{in}^2}$ and very slow, which is why it is very difficult to obtain a frequency of the non-attenuated oscillations above 10 GHz (see Fig. 2.8).

2.5 Amplitude of the oscillations and spectral purity.

Although the method of linearization around the steady-state solutions presented in the section above allowed us to determine the oscillation frequency and to know when they are non-attenuated, it is still relatively limited. Indeed, this method cannot be used to determine the amplitude of the oscillations and it does not give us information on the harmonics of the signal, and so we cannot know whether the oscillations will be sinusoidal or not. So we tried to solve the system of nonlinear equations by another method, i.e. by harmonic analysis.

2.5.1 Numerical simulation of the equations with MATLAB.

It is of course possible to determine the amplitude of the oscillations and their frequency spectrum by numerically solving the system of equations (2.5,2.6) with MATLAB, with the help of the ode15s function (see Fig. 2.9). Then we can see that in the cases where the oscillations are non-attenuated, we will reach very quickly a stable harmonic regime, where the energy in the cavity oscillates in a quasi-sinusoidal manner around an equilibrium point, which is characteristic of non-attenuated, periodic oscillations.

However, solving the equations numerically with MATLAB presents other problems, particularly in terms of computation time, which prevent us from using this method in order to draw the curves representing the evolution of the amplitude of the oscillations as a function of the input power and the detuning. We tried to calculate instead an analytical expression for the energy when the harmonic regime is reached for a constant input power. For this, we used the fact that we knew from our experimental results and our simulations with MATLAB that the evolution of the energy as a function of time is quasi-sinusoidal, and decided to neglect the higher harmonics, and to approximate the energy in the cavity by a sinusoid. By re-injecting this expression of energy in the equation on the free carriers, this also allowed us to approximate N_e as a sinusoid, which allowed us to reduce our nonlinear system of equations to a single linear first order differential equation on the complex amplitude $A(t)$, which is easier to solve. We then solved this equation, first neglecting the nonlinear absorptions, and then in the general case, to find an equation of which the amplitude of the fundamental of the oscillations is a solution, which allowed us to calculate with MATLAB this amplitude and to trace it. We were also able to obtain an equation between the amplitudes of the fundamental and the second harmonic of the oscillations, which allowed us to confirm that the amplitude of the second harmonic was very small compared to the amplitude of the fundamental and that the oscillations were therefore sinusoidal. Finally we plotted the spectrum resulting from these oscillations.

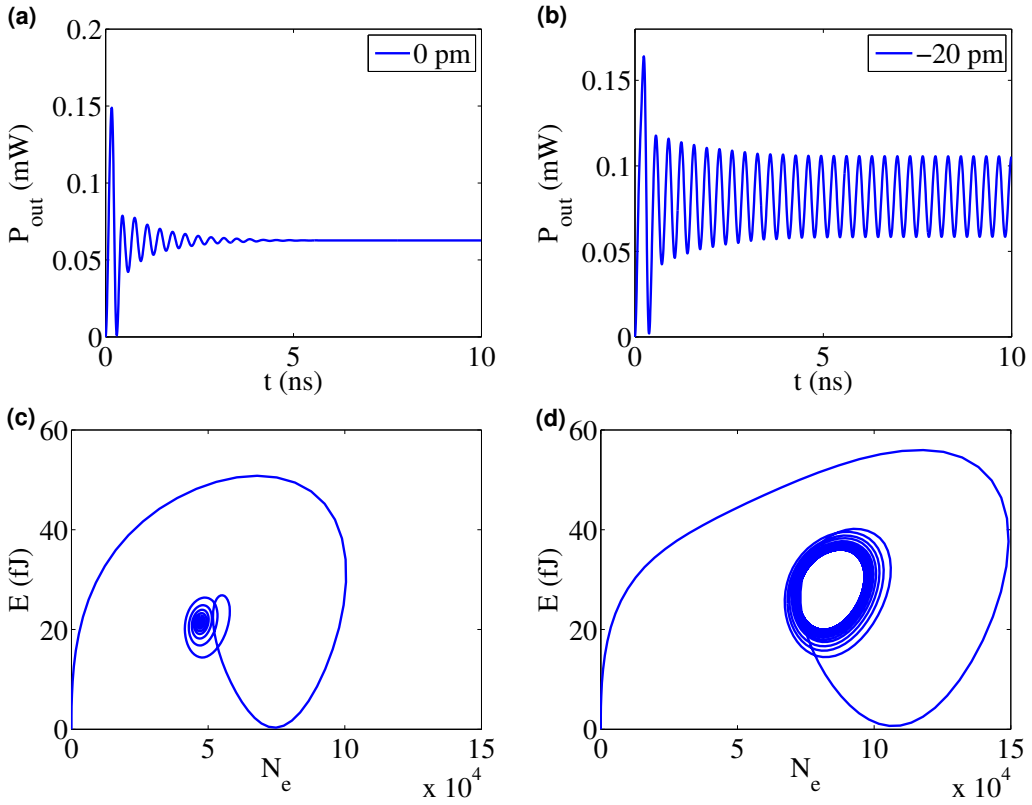

Figure 2.9: Numerical simulation with MATLAB of the oscillations in the cavity for an input power $P_{in} = 2$ mW. (a) and (b) The output power of the cavity as a function of time : (a) for $\triangle\lambda = 0$ pm (when the oscillations are attenuated) and (b) for $\triangle\lambda = -20$ pm (when the oscillations are non-attenuated). (c) and (d) The energy in the cavity $E = |A|^2$ as a function of the number of free carriers (c) for $\triangle\lambda = 0$ pm and (d) for $\triangle\lambda = -20$ pm. We can note that, for $\triangle\lambda = -20$ pm, this energy ends up following a stable path around an equilibrium point, which is characteristic of non-attenuated periodic oscillations.

2.5.2 Solving the equations by an harmonic analysis.

It just remains for us to do these calculations. Since we know that the evolution of the energy over time is quasi-sinusoidal, we can approximate this energy, when the input power is constant and when the harmonic regime is reached (which takes only a few nanoseconds - see Fig. 2.9b), by the following expression :

$$E(t) = |A(t)|^2 \simeq A_0^{(2)} + 2A_1^{(2)} \cos(\Omega t + \varphi_{A_1^{(2)}}) \tag{2.24}$$

where $A_0^{(2)}$ is the average energy in the cavity and $A_1^{(2)}$ the amplitude of the fundamental, with $A_1^{(2)} \ll A_0^{(2)}$. We then have the following approximation for $E^2(t)$:

$$E^2(t) = |A(t)|^4 \simeq (A_0^{(2)})^2 + 4A_0^{(2)}A_1^{(2)} \cos(\Omega t + \varphi_{A_1^{(2)}}) \tag{2.25}$$

By injecting this expression in equation 2.6 on the free carriers N_e, we obtain :

$$\frac{dN_e}{dt} \simeq -\frac{N_e}{\tau_{fc}} + \frac{1}{2}\frac{\gamma^{TPA}}{(\hbar\omega)^2}[(A_0^{(2)})^2 + 4A_0^{(2)}A_1^{(2)} \cos(\Omega t + \varphi_{A_1^{(2)}})] \tag{2.26}$$

which is a first order differential equation whose solution is :

$$N_e(t) = N_0 + 2|N_1| \cos(\Omega t + \varphi_{N1}) \tag{2.27}$$

with φ_{N1} a phase term and where the coefficients N_0 and $N_1 = |N_1|e^{i\varphi_{N1}}$ are worth :

$$N_0 = \frac{\tau_{fc}\gamma^{TPA}(A_0^{(2)})^2}{2(\hbar\omega)^2} \tag{2.28}$$

$$N_1 = \frac{\tau_{fc}\gamma^{TPA}}{2(\hbar\omega)^2}\frac{2A_0^{(2)}A_1^{(2)}e^{i\varphi_{A_1^{(2)}}}}{(1+i\Omega\tau_{fc})} \tag{2.29}$$

By re-injecting this expression of N_e in the equation 2.5 on the complex amplitude $A(t)$, we can then transform this equation into a linear first order differential equation :

$$\frac{dA}{dt} \simeq -(R + F(t))A + \sqrt{\frac{\sqrt{T_{max}}P_{in}}{2\tau}} \tag{2.30}$$

with the following expressions for the coefficients R and $F(t)$:

$$R = \frac{1}{2\tau} - i(\omega - \omega_0) + \frac{\gamma^{FC}N_0}{V_{eff}^{FC}} + \frac{\gamma^{TPA}A_0^{(2)}}{2\hbar\omega} \tag{2.31}$$

$$F(t) = \frac{2\gamma^{FC}|N_1|}{V_{eff}^{FC}}\cos(\Omega t + \varphi_{N1}) + \frac{2\gamma^{TPA}A_1^{(2)}}{2\hbar\omega}\cos(\Omega t + \varphi_{A_1^{(2)}}) \tag{2.32}$$

For times $t \gg \mathrm{Re}\,(1/R)$, the harmonic regime is reached and the solution of the equation 2.30 becomes :

$$A(t) = Ke^{-Rt-\int F(t)}\int_0^t e^{Rt'+\int F(t')}dt' \tag{2.33}$$

with $K = \sqrt{\frac{\sqrt{T_{max}}P_{in}}{2\tau}}$, and where the integral $\int_0^t F(t)$ is equal to :

$$\int_0^t F(t) = \alpha^{FC}\sin(\Omega t + \varphi_{N1}) + \alpha^{TPA}\sin(\Omega t + \varphi_{A_1^{(2)}})) \tag{2.34}$$

where we have $\alpha^{TPA} = \frac{2}{\Omega}\frac{\gamma^{TPA}A_1^{(2)}}{2\hbar\omega}$ and $\alpha^{FC} = \frac{2}{\Omega}\frac{\gamma^{FC}|N_1|}{V_{eff}^{FC}}$.

2.5.2.1 Solving the equations when neglecting the nonlinear absorptions.

In the case of our photonic crystal nanocavity, these coefficients are worth $\alpha^{TPA} = 0.016$ and $\alpha^{FC} = 0.004 + 0.123i$ for an input power $P_{in} = 2$ mW and a detuning $\triangle\lambda = -20$ pm. The imaginary part of α^{FC} then becomes the main contribution to the integral $\int_0^t F(t)$. We can further simplify the calculations by neglecting at first the contributions of other terms in our evaluation of the coefficient R and the integral $\int_0^t F(t)$. The equations 2.31 and 2.34 then become :

$$R \approx \frac{1}{2\tau} + i(\frac{\gamma_i^{FC}N_0}{V_{eff}^{FC}} - (\omega - \omega_0)) \tag{2.35}$$

$$\int F(t) \approx \alpha_i^{FC}\sin(\theta) \tag{2.36}$$

with $\alpha_i^{FC} = \frac{2}{\Omega}\frac{i\gamma_i^{FC}|N_1|}{V_{eff}^{FC}}$ and $\theta = \Omega t + \varphi_{N1}$.

We can develop $e^{\int F(t)}$ by using the Jacobi-Anger expansion :

$$e^{\int F(t)} \approx e^{\alpha_i^{FC}\sin(\theta)} = \sum_n i^{3n}I_n(\alpha_i^{FC})e^{in\theta} \tag{2.37}$$

where the I_n are the modified Bessel functions of the first order. In this expression, only the terms corresponding to n =-1, 0 and 1 have a significant influence on the final values of the amplitudes of the fundamental and the second harmonic. We can therefore neglect

the other terms and we then obtain :

$$e^{\int F(t)} \approx I_0(\alpha_i^{FC}) - iI_1(\alpha_i^{FC})(e^{i\theta} - e^{-i\theta}) \tag{2.38}$$

and

$$\int_0^t e^{Rt' + \int F(t')} dt' = e^{Rt} \left[\frac{I_0(\alpha_i^{FC})}{R} - iI_1(\alpha_i^{FC}) \left(\frac{e^{i\theta}}{R + i\Omega} - \frac{e^{-i\theta}}{R - i\Omega} \right) \right] \tag{2.39}$$

The expression of the amplitude then becomes :

$$A = K \left(\frac{I_0(\alpha_i^{FC})}{R} - iI_1(\alpha_i^{FC}) \left(\frac{e^{i\theta}}{R + i\Omega} - \frac{e^{-i\theta}}{R - i\Omega} \right) \right) e^{-\alpha_i^{FC} \sin(\theta)} \tag{2.40}$$

which gives us for the expression of the energy :

$$E = |A|^2 = K^2 \left| \frac{I_0(\alpha_i^{FC})}{R} - iI_1(\alpha_i^{FC}) \left(\frac{e^{i\theta}}{R + i\Omega} - \frac{e^{-i\theta}}{R - i\Omega} \right) \right|^2 \tag{2.41}$$

By developing the expression 2.41, we obtain :

$$E = E_0 + 2E_1 \cos(\Omega t + \varphi_1) + 2E_2 \cos(2\Omega t + \varphi_2) \tag{2.42}$$

where the coefficients E_0, E_1, E_2 correspond respectively to the average energy in the cavity, to the amplitude of the fundamental and to that of the second harmonic, and are worth :

$$E_0 = K^2 \left(\frac{I_0(\alpha_i^{FC})^2}{|R|^2} + \frac{2|I_1(\alpha_i^{FC})|^2(\Omega^2 + |R|^2)}{(|R|^2 - \Omega^2)^2 + (2\Omega \mathrm{Re}(R))^2} \right. \tag{2.43}$$

$$E_1 = K^2 \frac{2\Omega \mathrm{Im}(R) I_0(\alpha_i^{FC}) |I_1(\alpha_i^{FC})|}{\sqrt{(|R|^2 - \Omega^2)^2 + (2\Omega \mathrm{Re}(R))^2}} \tag{2.44}$$

$$E_2 = K^2 \frac{|I_1(\alpha_i^{FC})|^2}{\sqrt{(|R|^2 - \Omega^2)^2 + (2\Omega \mathrm{Re}(R))^2}} \tag{2.45}$$

For reasons of consistency, this expression of E must be equal to the one originally used equation 2.24, i.e. we must have $E_0 = A_0^{(2)}$, $E_1 = A_1^{(2)}$, which allow us to calculate E_1, and E_2 negligible. We can then assess the importance of the second harmonic E_2 by using the following expression for the ratio E_2/E_1 :

$$\frac{E_2}{E_1} \simeq \frac{|I_1(\alpha_i^{FC})|^2}{2\Omega \mathrm{Im}(R) I_0(\alpha_i^{FC}) |I_1(\alpha_i^{FC})|} \tag{2.46}$$

If we take into account the fact that $|\alpha_i^{FC}| \ll 1$, then we know that the Bessel functions are equivalent to $I_0(\alpha_i^{FC}) \sim 1$ and $I_1(\alpha_i^{FC}) \sim \frac{1}{2}\alpha_i^{FC} = \frac{i\gamma_i^{FC}N_1}{\Omega V_{eff}^{FC}}$, and the expression 2.46 simplifies to :

$$\frac{E_2}{E_1} \sim \frac{i\gamma_i^{FC}}{2\Omega^2 V_{eff}^{FC}} \frac{|N_1|}{\mathrm{Im}(R)} \tag{2.47}$$

We can obtain from the equations 2.28 and 2.29 the following expression for N_1 :

$$N_1 = \frac{\tau_{fc}\gamma^{TPA}}{2(\hbar\omega)^2} \frac{2E_0E_1}{(1+i\Omega\tau_{fc})} \simeq \frac{E_1}{E_0} \frac{2N_0}{(1+i\Omega\tau_{fc})} \tag{2.48}$$

which allows us to express the relation 2.47 as :

$$\frac{E_2}{E_1} \sim C_0 \times \frac{E_1}{E_0} \tag{2.49}$$

where the coefficient C_0 is equal to :

$$C_0 = \frac{\gamma_i^{FC}N_0}{V_{eff}^{FC}} \frac{|R|^2}{\Omega^2 \mathrm{Im}(R)\sqrt{1+\Omega^2\tau_{fc}^2}} \tag{2.50}$$

The coefficient R depends only on the value of N_0, so the coefficient C_0 depends only on the values of N_0 and Ω, which can be easily calculated from the steady-state solutions of the system and the eigenvalues of the linearized system around those steady-state solutions (see the equations 2.11 and 2.23 above).

This expression of the coefficient C_0 is not very telling. However, for input powers $P_{in} \geq$ 2 mW, the equations 2.17 and 2.20 allow us to obtain as equivalent expression for the frequency Ω :

$$\Omega \sim \frac{\gamma_i^{FC}N_0}{V_{eff}^{FC}} - (\omega - \omega_0) \tag{2.51}$$

which gives us as equivalent expression $R \sim i\Omega$, and allows us to finally obtain the following equivalent expression of C_0 :

$$C_0 \sim \frac{\gamma_i^{FC}N_0}{\tau_{fc}\Omega^2 V_{eff}^{FC}} \sim \frac{1}{\Omega\tau_{fc}} \times \left(1 + \frac{(\omega-\omega_0)}{\Omega}\right) \tag{2.52}$$

We can note that C_0 decreases as the frequency increases, i.e. the signal is going to be more and more sinusoidal as the oscillation frequency gets higher, i.e. as the input power gets higher.

The equation $E_1 = A_1^{(2)}$ being transcendental and extremely complicated, we have not developed it here, and we have not been able to find a simple analytical solution to this equation. However, this equation can be easily (and quickly) solved with MATLAB, which allowed us to plot the ratio E_1/E_0 as a function of the input power and detuning (see Fig. 2.10a). The amplitude of the second harmonic can be calculated from E_1 and E_0 with the expression of E_2 presented in equation 2.49 (see Fig. 2.10b).

2.5.2.2 Solving the equations in the general case.

Results in the general case are not very different. If we do not neglect the two-photon and free-carrier absorptions, then the expression 2.40 on the complex amplitude becomes :

$$A = K\left(a_0 + a_1 e^{i\theta} + a_{-1} e^{-i\theta}\right) e^{-\alpha^{FC}\sin(\theta+\varphi)-\alpha^{TPA}\sin(\theta)} \tag{2.53}$$

where the phase terms are equals to $\theta = \Omega t + \varphi_{A_1^{(2)}}$, $\varphi = \varphi_{N1} - \varphi_{A_1^{(2)}} = -\arg(1 + i\Omega\tau_{fc})$ and the coefficients a_0, a_1, a_2 are defined as :

$$a_0 = \frac{I_0(\alpha^{TPA})I_0(\alpha^{FC})}{R} \tag{2.54}$$

$$a_1 = \frac{-i(I_0(\alpha^{TPA})I_1(\alpha^{FC})e^{i\varphi} + I_1(\alpha^{TPA})I_0(\alpha^{FC}))}{R + i\Omega} \tag{2.55}$$

$$a_{-1} = \frac{i(I_0(\alpha^{TPA})I_1(\alpha^{FC})e^{-i\varphi} + I_1(\alpha^{TPA})I_0(\alpha^{FC}))}{R - i\Omega} \tag{2.56}$$

Which gives us as expression for the energy :

$$E = K^2 \left\| a_0 + a_1 e^{i\theta} + a_{-1} e^{-i\theta} \right\|^2 e^{-2\alpha_r^{FC}\sin(\theta+\varphi)-2\alpha^{TPA}\sin(\theta)} \tag{2.57}$$

If we develop $\left\| a_0 + a_1 e^{i\theta} + a_{-1} e^{-i\theta} \right\|^2$ as :

$$\left\| a_0 + a_1 e^{i\theta} + a_{-1} e^{-i\theta} \right\|^2 = b_0 + b_1 e^{i\theta} + b_1^* e^{-i\theta} + b_2 e^{2i\theta} + b_2^* e^{-2i\theta} \tag{2.58}$$

with $b_0 = |a_0|^2 + |a_1|^2 + |a_{-1}|^2$, $b_1 = a_0 a_{-1}^* + a_0^* a_1$ and $b_2 = a_1 a_{-1}^*$, and if we use the Jacobi-Anger expansion to write $e^{-2\alpha_r^{FC}\sin(\theta+\varphi)-2\alpha^{TPA}\sin(\theta)}$ as :

$$e^{-2\alpha_r^{FC}\sin(\theta+\varphi)-2\alpha^{TPA}\sin(\theta)} = d_0 + d_1 e^{i\theta} + d_1^* e^{-i\theta} \tag{2.59}$$

with $d_0 = I_0(2\alpha^{TPA})I_0(2\alpha_r^{FC})$ and $d_1 = i(I_0(2\alpha^{TPA})I_1(2\alpha_r^{FC})e^{i\varphi} + I_1(2\alpha^{TPA})I_0(2\alpha_r^{FC}))$,

then we obtain for E_0, E_1, E_2 the following expressions :

$$E_0 = K^2(b_0 d_0 + b_1 d_1^* + b_1^* d_1) \tag{2.60}$$

$$E_1 = K^2 \left\| b_0 d_1 + b_1 d_0 + d_1^* b_2 \right\| \tag{2.61}$$

$$E_2 = K^2 \left\| b_1 d_1 + b_2 d_0 \right\| \tag{2.62}$$

These expressions of E_0, E_1, E_2 are not very telling, but if we developed them completely, they would be obviously far too complex to be useful to us. However, these expressions are sufficient to allow us to determine the amplitude of the fundamental $A_1^{(2)}$ by solving numerically the equation $A_1^{(2)} = E_1$, and the amplitude of the second harmonic from the expression of E_2 in the general case (see Fig. 2.10). Fortunately, for input powers $P_{in} \geq 2$ mW, we can still find a simpler equivalent expression for E_2/E_1 and for the factor C_0 :

$$\frac{E_2}{E_1} \sim \frac{1}{4}\left(\alpha_i^{FC} - 3\alpha^{TPA}\right) = C_0 \times \frac{E_1}{E_0} \tag{2.63}$$

where the factor C_0 is equivalent to :

$$C_0 \sim \frac{1}{2\Omega} \times \left(\frac{2\gamma_i^{FC} N_0}{\tau_{fc} \Omega V_{eff}^{FC}} - \frac{3\gamma^{TPA} E_0}{2\hbar\omega} \right) \tag{2.64}$$

The main difference between equations 2.52 and 2.64 is the added term $-\frac{1}{2\Omega} \times \frac{3\gamma^{TPA} E_0}{2\hbar\omega}$ to equation 2.64, which results in a lower value of C_0 than in the case where the nonlinear absorptions were ignored. These two equations 2.63 and 2.64 are important because they allow us to easily assess the nonlinearity of the oscillations and to minimize if possible the amplitude of the second harmonic and thus obtain a signal that is as sinusoidal as possible.

We also have a very good agreement between those analytical expressions and our numerical simulations with MATLAB. For example, for a detuning $\triangle\lambda$ = -20 pm, the factor C_0 varies numerically between 0.27 and 0.084 for an input power ranging from 1.5 mW to 20 mW. In particular, for $P_{in} = 2$ mW, we have $C_0 = 0.24$ and $P_1/P_0 = -21.4$ dB, which gives us $P_2/P_1 \simeq -33.6$ dB (P_0,P_1,P_2 correspond respectively to the average power measured at the exit of the cavity, to the amplitude of the fundamental and of the second harmonic). These values are very close to those found by the numerical simulation : $P_1/P_0 = -21.3$ dB, and $P_2/P_1 \simeq -34.7$ dB (see Fig. 2.11). We must note that these values are given in dB for the RF power measured by the photodiode $P^{RF} = R \times I_{diode}^2$. Since the photodiode current is proportional to the optical power and therefore to the energy in the cavity, we have $\left(P_1^{RF}/P_0^{RF}\right)(\text{dB}) = 20 \times \log(E_1/E_0)$, instead of $10 \times \log(E_1/E_0)$ as is usually the case for powers. The amplitude of the second harmonic is very low compared to the fun-

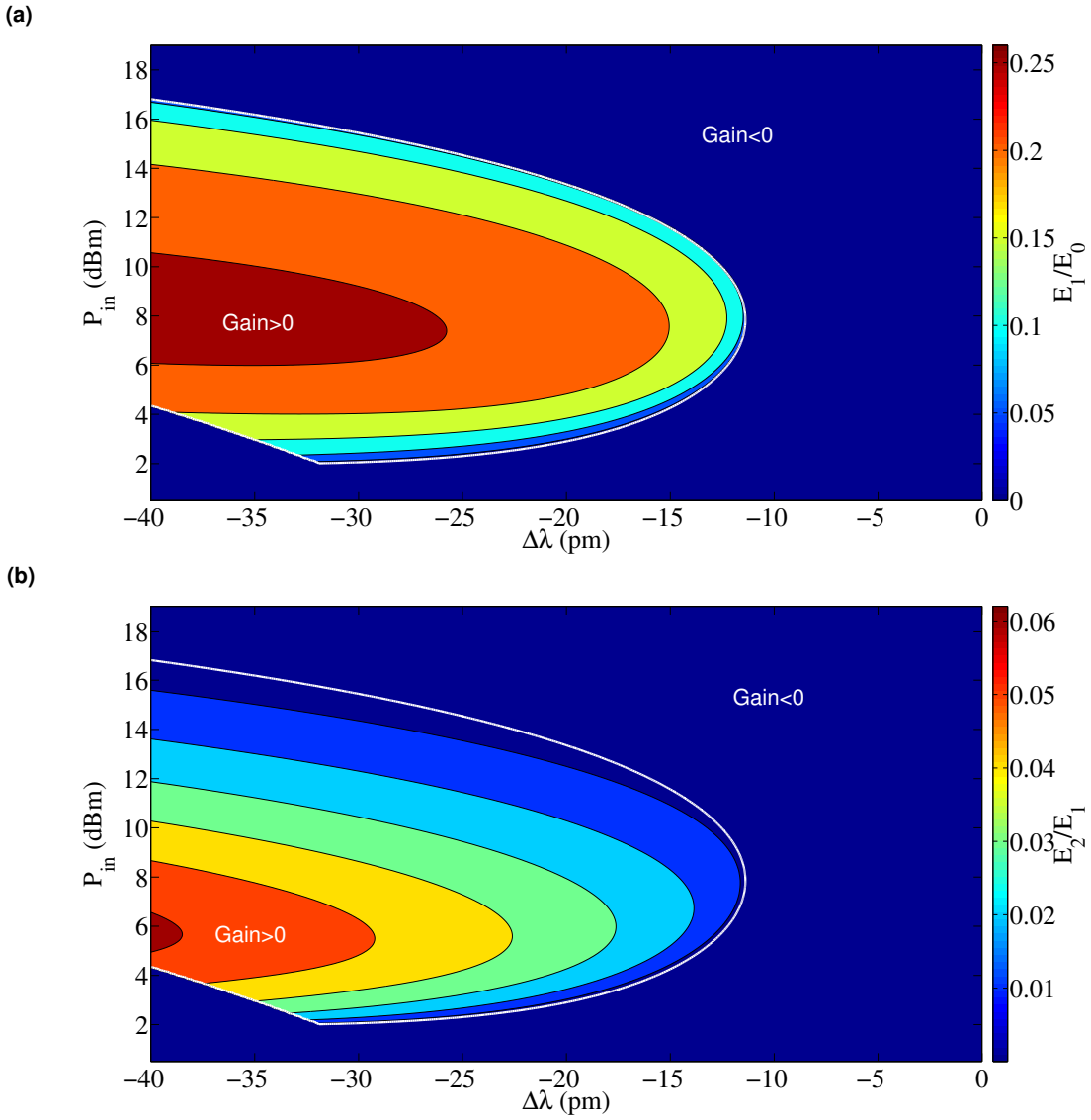

Figure 2.10: (a) The ratio E_1/E_0, calculated from the analytical expression found previously. (b) The ratio E_2/E_1. The higher this ratio is, the more sinusoidal the oscillations are. The zone of positive gain (non-attenuated oscillations) is delineated by the white thick line.

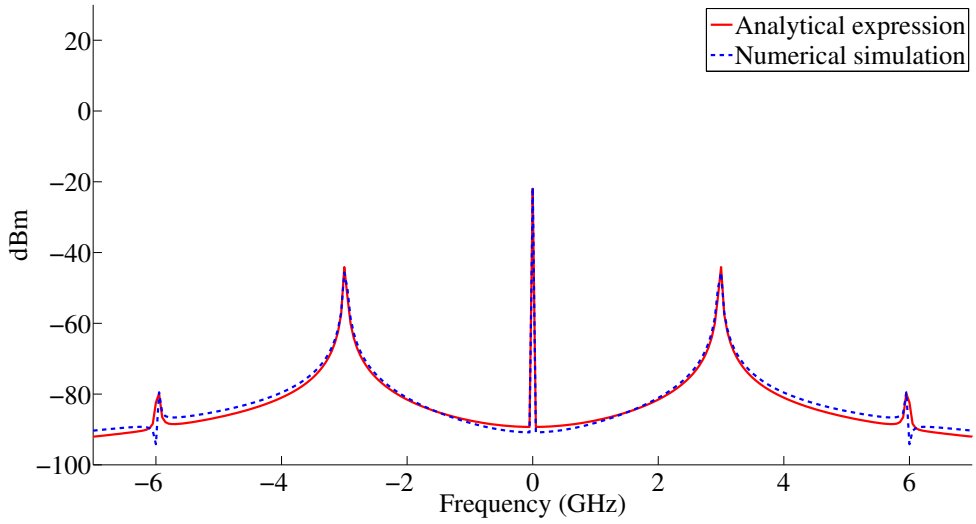

Figure 2.11: The spectrum of the oscillations, calculated both by the analytical expression (see Eq. 2.61 and 2.62) and by a numerical simulation with MATLAB for a detuning $\triangle\lambda = -20$ pm and an input power $P_{in} = 2$ mW. We can note that we have a very good agreement between those two curves. The amplitude of the second harmonic is approximately -34 dB below that of the fundamental.

damental, which justifies the approximation of the energy in the cavity by a sinusoid that we made at the beginning.

2.5.3 Comparison with the case of a microring resonator.

We mentioned before that the oscillations created by free-carrier dispersion were also measured in a silicon microring resonator by Soltani in 2012 [60]. The resonance of the microring had for wavelength $\lambda_0 = 1532$ nm and a quality factor of $Q_0 = 1.5 \times 10^6$, ten times higher than for our cavity. Compared to our nanocavity, the oscillations in the microring had two major drawbacks : first, the oscillation frequency was only 0.5 GHz, compared to 3 GHz for our cavity, which is a consequence of the higher quality factor and the larger modal volume of a microring (see equation 2.23 on the equivalent expression of the oscillation frequency). Second, these oscillations were strongly non-sinusoidal, unlike those in our cavity.

We can easily confirm the results of Soltani by performing a simulation of the microring resonator with MATLAB. Indeed, the equations that we used to describe the behavior of a photonic crystal nanocavity are also valid for other kinds of microcavities such as microrings, provided of course that we replace the different characteristic volumes of the nonlinear effects and the free-carrier lifetime by those of the microring studied by Soltani : $V_{TPA} = 97.1\ \mu m^3$, $V_{FCA} = 89.9 \mu m^3$ and $\tau_{fc} = 0.4$ ns. The only other difference between the equations of the microring and those of the cavity is that the microring has

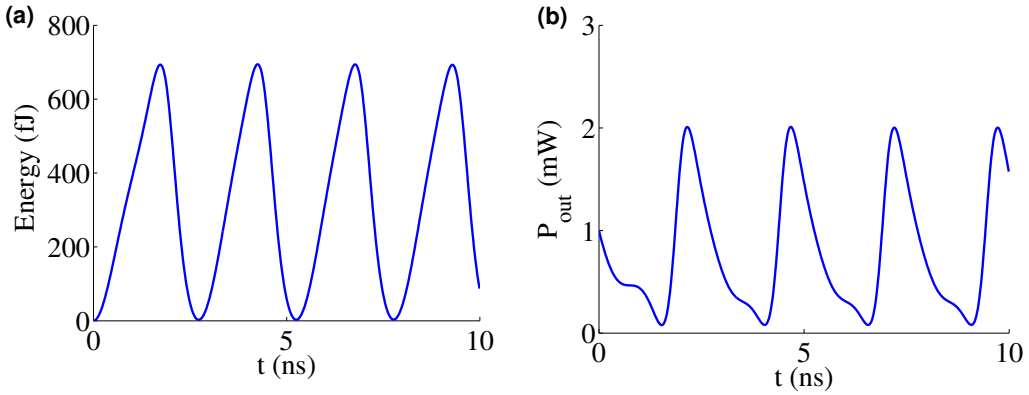

Figure 2.12: Numerical simulation with MATLAB of the oscillations for a microring resonator of the kind described in reference [60], in the case of a detuning of -2.5 pm and an input power of 1 mW : (a) the energy in the microring as a function of time, and (b) the output power of the microring as a function of time. The oscillations are visibly not sinusoidal, unlike those in our cavity.

only one coupling waveguide used both to inject and to collect the energy in the microring. The collected output power of the microring is equal to $P_{out} = \left\| \sqrt{P_{in}} - \sqrt{\frac{\sqrt{T_{max}}}{2\tau}} A \right\|^2$, with $T_{max} = 1$ [60], instead of $P_{out} = \frac{\sqrt{T_{max}}|A|^2}{2\tau}$ as in our nanocavity. With this simulation, it is easy to see that not only the oscillations of the energy in the microring are highly non-sinusoidal, with an almost triangular shape (see Fig. 2.12a), but the different expression of the output power of the microring compared to that of the photonic crystal will further distort the oscillations and amplify their non-sinusoidal appearance (see Fig. 2.12b).

On the other hand, applying the results of the harmonic analysis in section 2.5.2 to the case of a microring is more difficult. Indeed, in the case of microring described by Soltani, the coefficients α^{TPA} and α^{FC} are, according to our simulations, equal to $\alpha^{TPA} = 0.042$ and $\alpha^{FC} = 0.04 + 1.21i$ in the case of a detuning of -2.5 pm and an input power of 1 mW. Since $|\alpha^{FC}| > 1$, we cannot make the approximations $e^{\alpha_i^{FC}\sin(\theta)} \sim I_0(\alpha_i^{FC}) - iI_1(\alpha_i^{FC})(e^{i\theta} - e^{-i\theta})$, $I_0(\alpha_i^{FC}) \sim 1$ and $I_1(\alpha_i^{FC}) \sim \frac{1}{2}\alpha_i^{FC}$ that we did before, and our formulas are no longer totally correct. However, we can still use them to estimate the amplitude of the second harmonic of the oscillations of the energy in the microring. Using the value of the amplitude of the fundamental given by the numerical simulation : $E_1/E_0 = -6$ dB, and taking the value of C_0 given by the formula 2.64 : $C_0 = 0.37$, we then obtain for the ratio between the amplitudes of the second harmonic and the fundamental $E_2/E_1 \simeq -14.6$ dB, which is a value very close to the one given by the numerical simulation $E_2/E_1 = -15$ dB (see Fig. 2.13). We can conclude that the bigger nonlinearity of the oscillations in a microring compared to our photonic crystal cavity has actually two causes : first, the greater value of C_0, which is explained by the lowest value of the oscillation frequency in a microring resonator, and second, the larger amplitude of those oscillations.

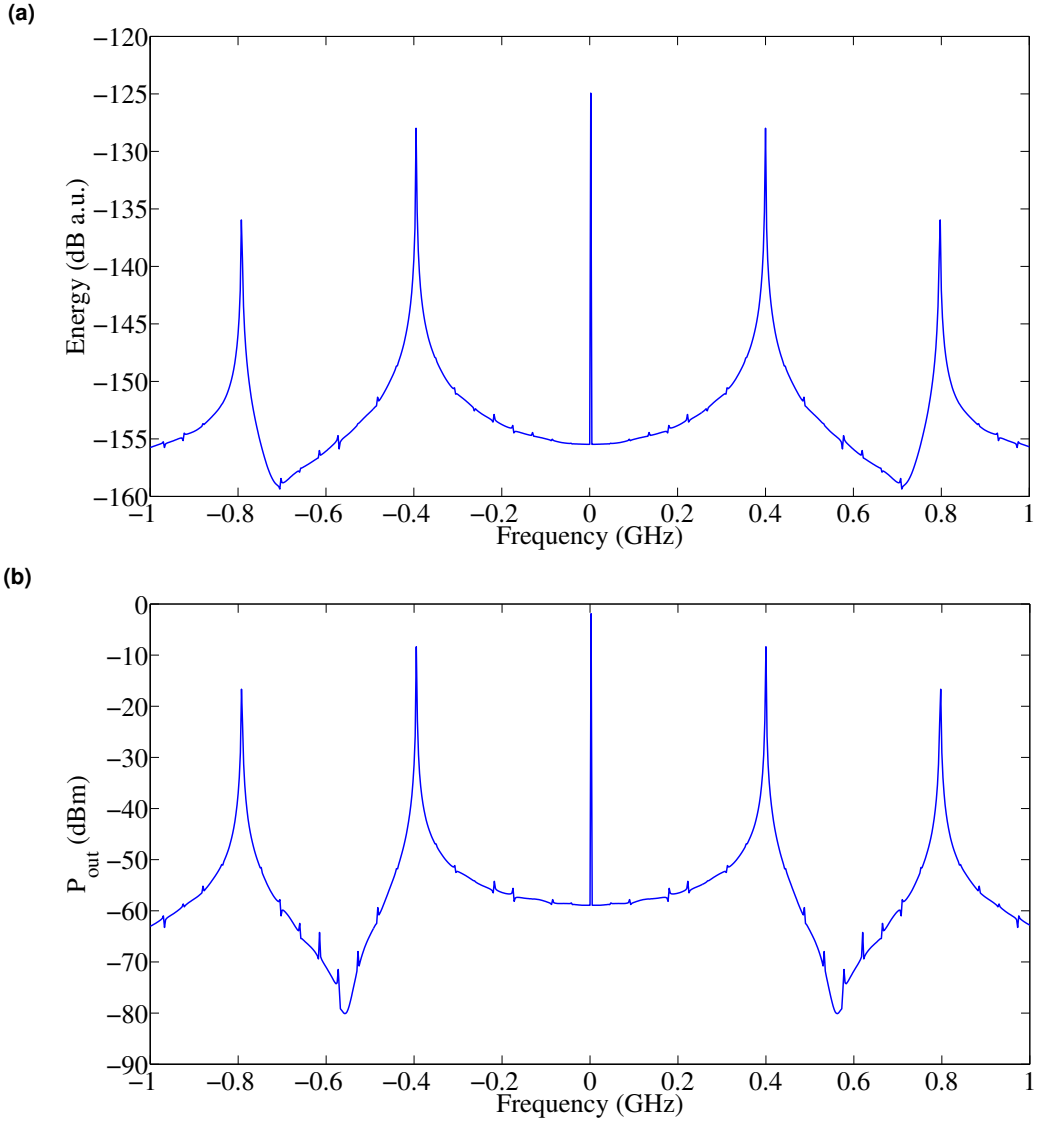

Figure 2.13: The spectrum of oscillations in the microring, calculated using the numerical simulation with MATLAB for a detuning of -2.5 pm and an input power of 1 mW (a) the energy spectrum in the microring and (b) the output power spectrum. The amplitude of the second harmonic is -7.5 dB below that of the fundamental for the energy in the microring and -7.7 dB below the fundamental for the output power.

2.6 Detailled analysis of the experimental results.

We can now use the model of the oscillations in the cavity developed above to explain and analyze our experimental results. We will first begin by recalling these results and by showing that they are consistent with our model's predictions regarding the oscillation frequency and whether these oscillations are attenuated or not. We will then describe how used these results to determine the free-carrier effective volume and free-carrier lifetime of our nanocavity. We will then compare these results with the numerical simulations performed with MATLAB, with and without the thermal effects. Finally, we will study the performances of the microwave source that we could obtain from this nanocavity.

2.6.1 Summary of experimental results.

As we explained previously (in section 2.2), the cavity was actually measured twice, before and after the nitric acid chemical treatment. Before the treatment, we observed in the cavity oscillations with a period of about 300 ps for a detuning on the wavelength of the laser between -40 pm and -20 pm. The period does not (or almost not) changes with the detuning, as required by our model. These oscillations are always attenuated and disappear before the end of the pulse (see Fig. 2.3a). After the treatment, we observed in the cavity non-attenuated oscillations over the entire length of the pulse for a detuning on the laser wavelength between -30 pm and -10 pm (see Fig. 2.3b). The period of these oscillations is included between 330 and 350 ps, which corresponds to a frequency of about 3 GHz.

The simplest explanation for this difference in behavior before and after the nitric acid treatment is that the slight increase of the quality factor of the cavity during the treatment (from 90000 to 130000) has allowed us to make the cavity go from a zone where the gain of the oscillations was negative to a zone where the gain is positive, and where the oscillations are no longer attenuated. If we plot the period of the oscillations as a function of the quality factor of the cavity and of the input power for a detuning of -20 pm, we realize that these oscillations are only possible when the quality factor is greater than 110000 (see Fig. 2.14), which is now the case.

Similarly, it is easy to confirm that the non-attenuated oscillations are only possible for detunings around -20 pm by plotting the period of the oscillations as a function of the input power and the detuning (see Fig. 2.15). If the detuning is too low (for example 0 nm), then we are in the area of negative gain and the oscillations are attenuated. If it is too large (for example -40 pm), we find ourselves in the area of bistability of the cavity and the energy moves to the lower branch of the bistability, where the oscillations are no longer possible. We only find ourselves in the area of positive gain for an input power of

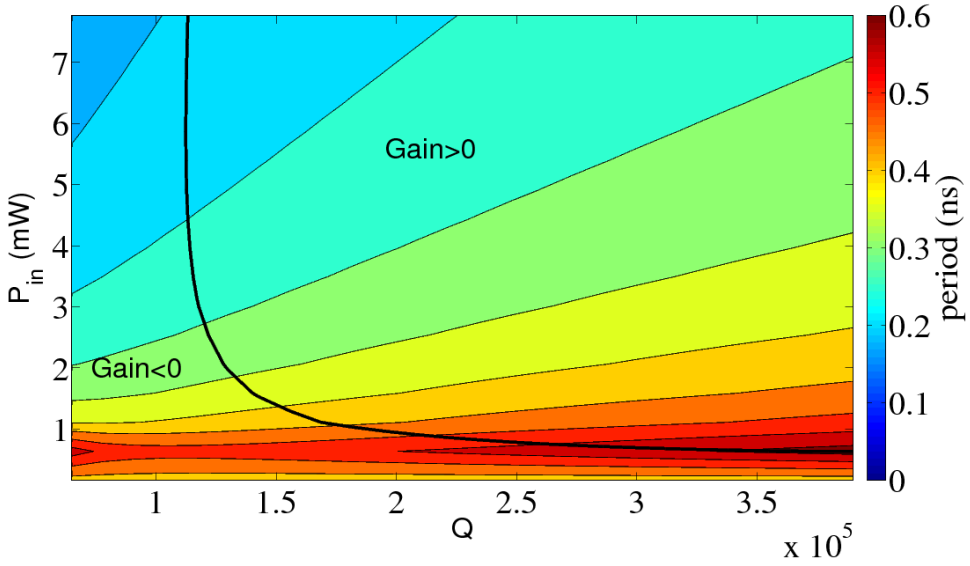

Figure 2.14: Period of the oscillations as a function of the quality factor of the cavity and the input power for a detuning of -20 pm and a free-carrier lifetime of 0.2 ns. The non-attenuated oscillations are only possible within the area of positive gain (delineated by the black line). We can see that a quality factor of at least 110000 is required for these oscillations to happen.

2 mW when the detuning is around -20 pm.

2.6.2 Determining the effective volume and free-carrier lifetime.

It was mentioned earlier that the two parameters of our model whose values we do not know well are the free-carrier lifetime τ_{fc} and the free-carrier effective volume V_{eff}^{FC}, and that we began these measurements in an attempt to determine the free-carrier lifetime in our photonic crystal cavities. We were lucky here. Indeed, if we choose to plot the oscillation frequency as a function of τ_{fc} et V_{eff}^{FC} for a detuning of -20 pm, then we notice that the only way to obtain non-attenuated oscillations with a frequency around 3 GHz is to have V_{eff}^{FC} between 4.62 μm^3 and 5.46 μm^3 and τ_{fc} between 0.256 ns and 0.176 ns (see Fig. 2.16). We therefore chose $V_{eff}^{FC} \simeq 5.25\ \mu m^3$ and $\tau_{fc} \simeq 0.2$ ns for our model because it is for these values that we had the best agreement between the measurements and the simulations with MATLAB. Keeping the same effective volume for the free carriers, we obtain in the same way a free-carrier lifetime of $\tau_{fc} \simeq 0.3$ ns in the cavity before the nitric acid treatment. This value for the free-carrier lifetime is of the same order of magnitude as the lifetime measured in silicon photonic crystal cavities similar to those that we use by Barclay [13], where it is equal to $\tau_{fc} \simeq 0.5$ ns. This lifetime is a little higher than the one we got for the cavity before nitric acid treatment, but this difference could be due to the fact that the cavities measured by Barclay are made of a silicon slab slightly thicker than ours (with a thickness of 340 nm instead of 200 nm), which would less confine the free

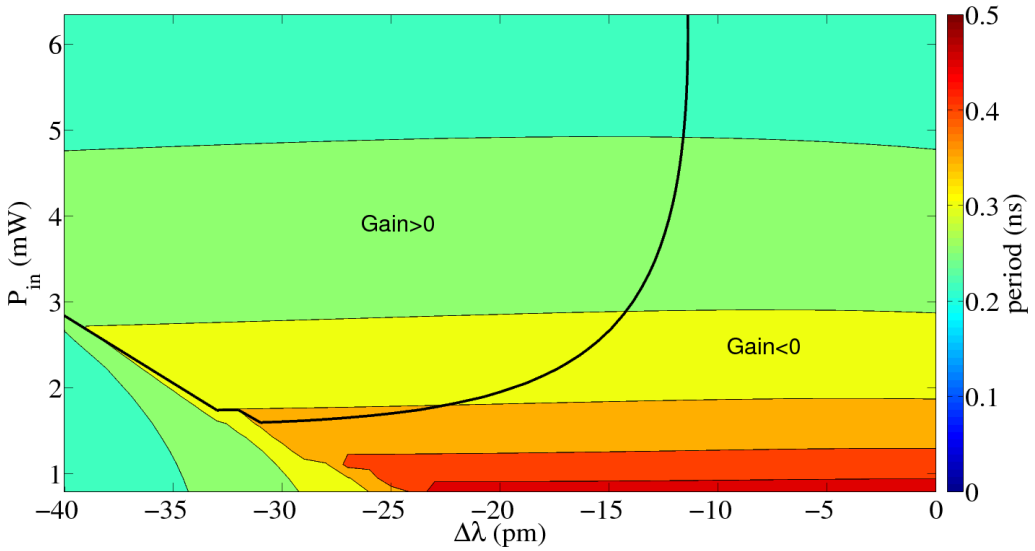

Figure 2.15: The period of the oscillations as a function of the detuning and the input power, for a cavity with a quality factor of 130000 and a free-carrier lifetime of 0.2 ns. Oscillations are non-attenuated within the region of positive gain (within the area defined by the thick black line).

carriers vertically, reducing their probability of recombination and thus slightly increasing their lifetime. We can note that in the microring resonator in silicon measured by Soltani [60], whose thickness is 230 nm, the measured free-carrier lifetime of the free carriers is $\tau_{fc} \simeq 0.4$ ns, which is also very close to the value that we found.

But the effective volume of free carriers found experimentally is ten times greater than the one used in reference [44], where it is calculated using the formula $V_{eff}^{FC} = (2d) \times (\sqrt{3}a) \times h$, where $d \simeq 1.1$ μm is the diffusion length of free carriers, h the slab thickness and $\sqrt{3}a$ is the distance between the air holes nearest to the center of the cavity in the orthogonal direction (a being the photonic crystal period). Using this formula would give us $V_{eff}^{FC} \simeq 0.32$ μm^3. But this model assumes that the diffusion of free carriers stops at the air holes, which is not the case. According to reference [67], the diffusion of free carriers in a photonic crystal is not very different from the diffusion of free carriers in a silicon membrane without holes. In addition, this model assumes that the free-carriers are all created in the cavity center, but the pattern of the electric field of the cavity resonant mode calculated by FDTD is in fact quite large and is included in a volume approximately equal to $(8a) \times (2\sqrt{3}a) \times h$ (see Fig. 2.6). If we assume that the free carriers are uniformly created in this volume and then diffuse into the rest of the cavity, then we can approximate the effective volume of the free carriers by :

$$V_{eff}^{FC} = (8a + 2d) \times (2\sqrt{3}a + 2d) \times h \tag{2.65}$$

This formula gives us $V_{eff}^{FC} = 4.06$ μm^3, which is close to the value of V_{eff}^{FC} that was

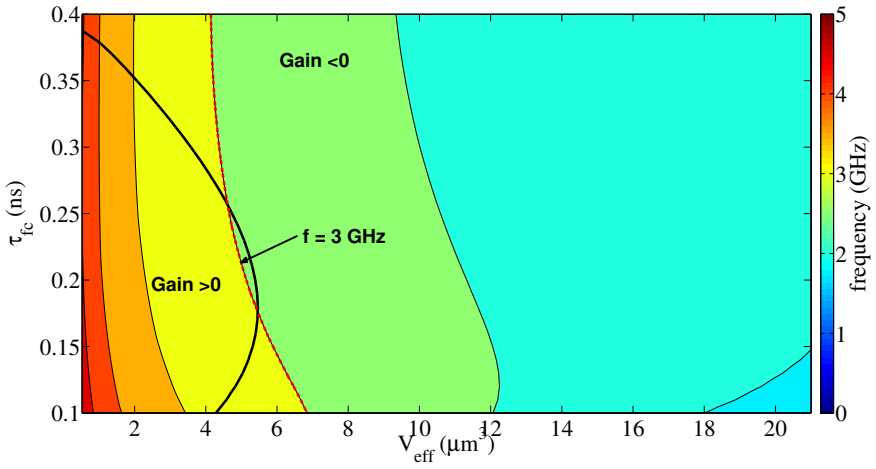

Figure 2.16: The oscillation frequency as a function of the free-carrier lifetime and their effective volume V_{eff}^{FC} for an input power of 2 mW and a detuning of -20 pm. We can note that the only way to obtain non-attenuated oscillations, i.e. within the area of positive gain bounded by the thick black line, with a frequency around 3 GHz (red dashed line), is to have $V_{eff}^{FC} \simeq 5.25\ \mu m^3$and $\tau_{fc} \simeq 0.2$ ns.

deduced from the experimental measurements.

2.6.3 Comparison with the numerical simulations.

If we compare the results of the measurements (see Fig. 2.17a and 2.17b) with the numerical simulations done with MATLAB using the system of equations (2.5,2.6), for pulses of length 10 ns, then we see that the measured average output power slowly increases over time while the simulated average output power remains constant (see Fig. 2.17c and 2.17d). This is due to the fact that we have neglected so far the thermal effects. Indeed, the temperature will rise slowly throughout the duration of the pulse, and the thermal dispersion will therefore slowly increase the negative detuning between the wavelength of the laser and that of the cavity, which will in turn increase the average energy in the cavity and thus the output power (see equation 2.22). A greater negative detuning will also increase the amplitude of the oscillations (see 2.10a), which explains why the measured amplitude of the oscillations is greater than the amplitude of the simulated oscillations. The measured contrast of the oscillations is quite high : $C = (P_{max} - P_{min})/(P_{max} + P_{min}) = 40$ %.

By comparing the measurements with the numerical simulations of the cavity behavior made by taking into account the thermal effects (equation 2.3), then we can determine the values of the cooling time of our cavity and of its effective thermal volume : $\tau_T \simeq 39$ ns and $V_{eff}^T \simeq 3.0\ \mu m^3$. The simulations of our cavity behavior made with these values are shown in the figures 2.17e et 2.17f. We can see that the agreement with our measured

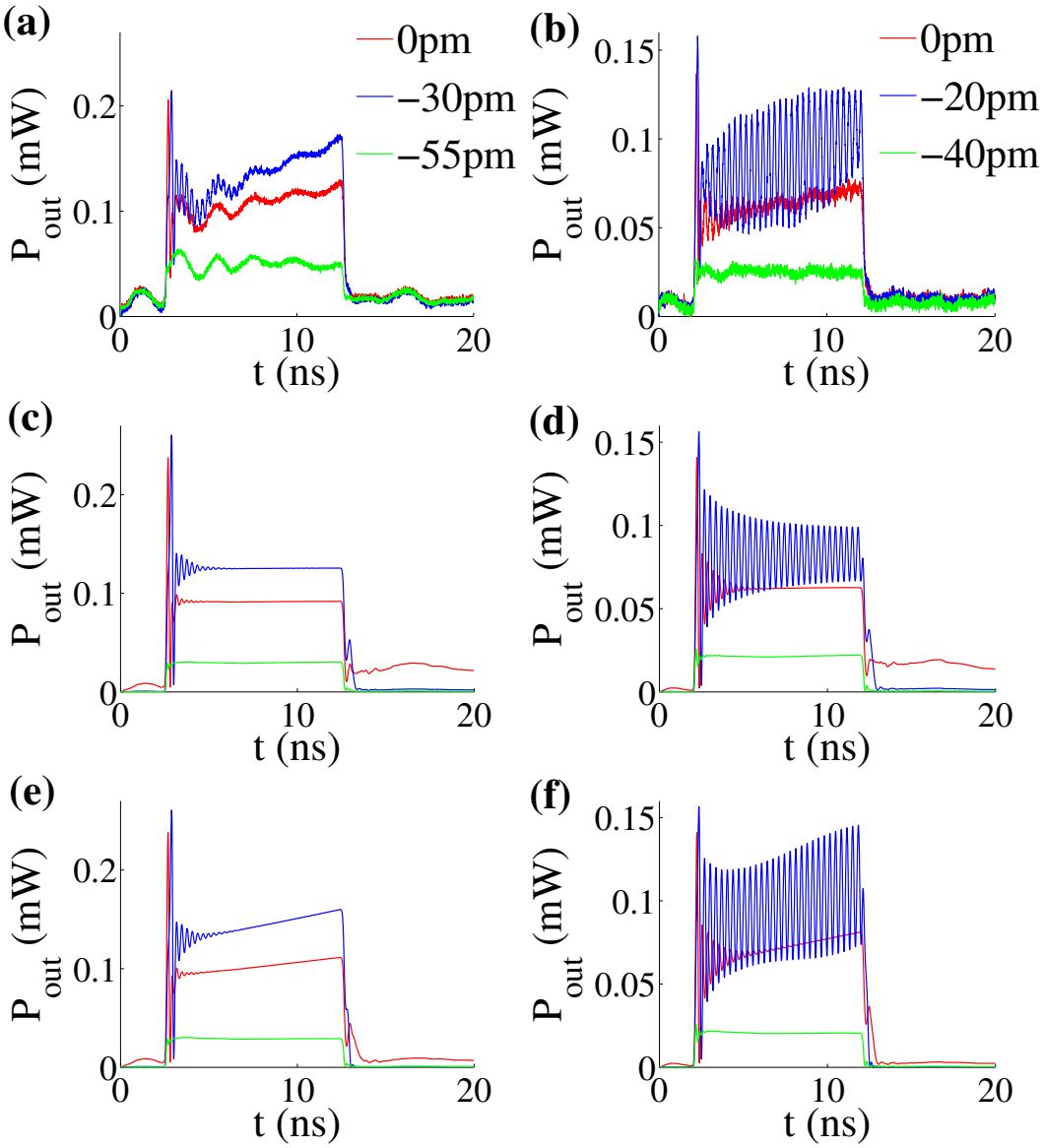

Figure 2.17: (a) and (b) : The measured output power of the cavity as a function of time for different detunings between the wavelength of the laser and that of the cavity : (a) before and (b) after the nitric acid chemical treatment. (c) and (d) : Numerical simulations with MATLAB of the cavity behavior made without taking into account the thermal effects : (c) before and (d) after the the nitric acid chemical treatment. (e) and (f) : Simulations with MATLAB of the cavity behavior, taking into account the thermal effects : (e) before and (f) after the nitric acid chemical treatment.

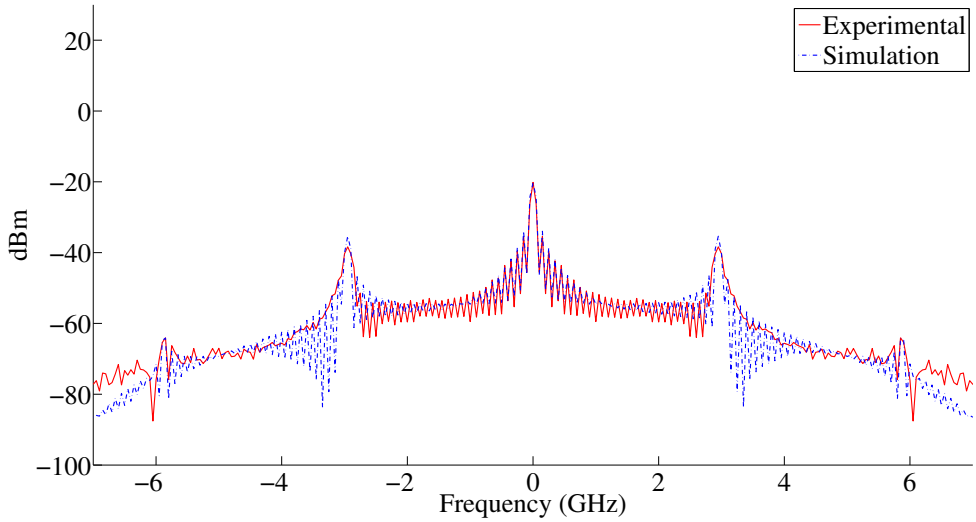

Figure 2.18: The measured and simulated spectra of the oscillations, taking into account the thermal effects, for an initial detuning of $\triangle\lambda = -20$ pm. In both cases, the second harmonic is approximately -26 dB below the fundamental, which means that the oscillations are quasi-sinusoidal.

curves is excellent. If we compare the spectrum (obtained by the Fast Fourier Transform of the signal) of the measured oscillations with that of the oscillations simulated with the thermal effects, we find that we have too a very good agreement between the two spectra (see Fig. 2.18)). In both cases, the amplitude of the second harmonic is -26 dB below that of the fundamental, which is higher than for the oscillations simulated without thermal effects (see Fig. 2.11). This is probably due to the higher amplitude of the oscillations. However, this value is still small enough for the oscillations to be described as quasi-sinusoidal.

2.6.4 Self-pulsing due to the thermal effects.

So far we have pulses used sufficiently short (10 ns) for the influence of thermal effects to be more or less negligible. So we can ask ourselves to what extent it would be possible to use longer pulses, and how the thermal effects will interfere with our oscillations. Unfortunately, when the pulse length is greater than about 20 ns, the thermal dispersion always ends up bringing the cavity in an area where it exhibits bistability, and it then passes abruptly from the higher branch to the lower branch of the bistability, which results in a collapse of the output power and a brutal stop of the oscillations due to free-carrier dispersion. But another type of self-pulsing, this time due to the competition between the thermal dispersion, which will shift the cavity resonance towards the red (i.e. towards greater wavelengths) and the free-carrier dispersion, which will shift the resonance towards the blue (towards shorter wavelengths) can occur, but with much lower frequencies, in the

megahertz range (about 15 MHz for our cavity).

These oscillations due to the thermal effects are not new and have been measured in both microring resonators [47] and photonic crystal cavities [64]. Their lower frequency is due to the fact that the cooling time is usually much larger than the free-carrier lifetime for a nanocavity. The cycle of these oscillations can be described as follows: After the laser is turned on, the cavity will slowly heat and its resonance will slowly shift towards the red, until the cavity becomes bistable and the power collapses. The cavity will then slowly cool and the resonance will shift towards the blue, until there is enough energy in the cavity for the influence of the free-carrier dispersion to become significant, bringing sharply the cavity back to its starting point on the upper branch of the bistability. The very low value of the free-carrier lifetime means that the cavity will pass very quickly from the high branch to the low branch of the bistability (and vice versa), giving an almost rectangular shape to the oscillations (or rather a trapezoidal one), unlike the sinusoidal shape of the oscillations due only to free-carrier dispersion (see Fig. 2.19a).

Although the simulations with MATLAB of the cavity behavior made using our model will correctly predict the presence or absence of thermal oscillations in our cavity (see Fig. 2.19b), there are still some differences between our simulations and our measurements : the period of thermal oscillations seems to increase with time for our measurements, which is not the case for the simulations. In addition, our simulation seems to predict the existence of oscillations due only to free-carrier dispersion whenever the cavity returns to the highest branch of the bistability, which is not the case according to our measurements. We can conclude that our model of the thermal effects in the cavity is probably too simplistic to properly describe the thermal oscillations. Our measurements and our simulations also show that the period of the thermal oscillations and their existence will strongly depend on the initial detuning between the resonance wavelength of the laser and that of the cavity.

2.6.5 Performances of the microwave source and how to improve them.

If we consider that the transmitted signal is detected by a photodetector with a 1 A/W response and a 50 Ohm impedance circuitry, the radio-frequency power delivered by the nanocavity at 2.8 GHz is 20 nW. These performances compare favorably with those achieved with spin-transfer nano-oscillators where a single spin-torque nano-oscillator emits a microwave power up to one nW [68].

The oscillations frequency could be further improved by reducing both the photon lifetime in the cavity (for example by taking a cavity with a quality factor $Q = 10000$, which would give us a photon lifetime equal to $\tau = 8.4$ ps), and the free-carrier lifetime (for both

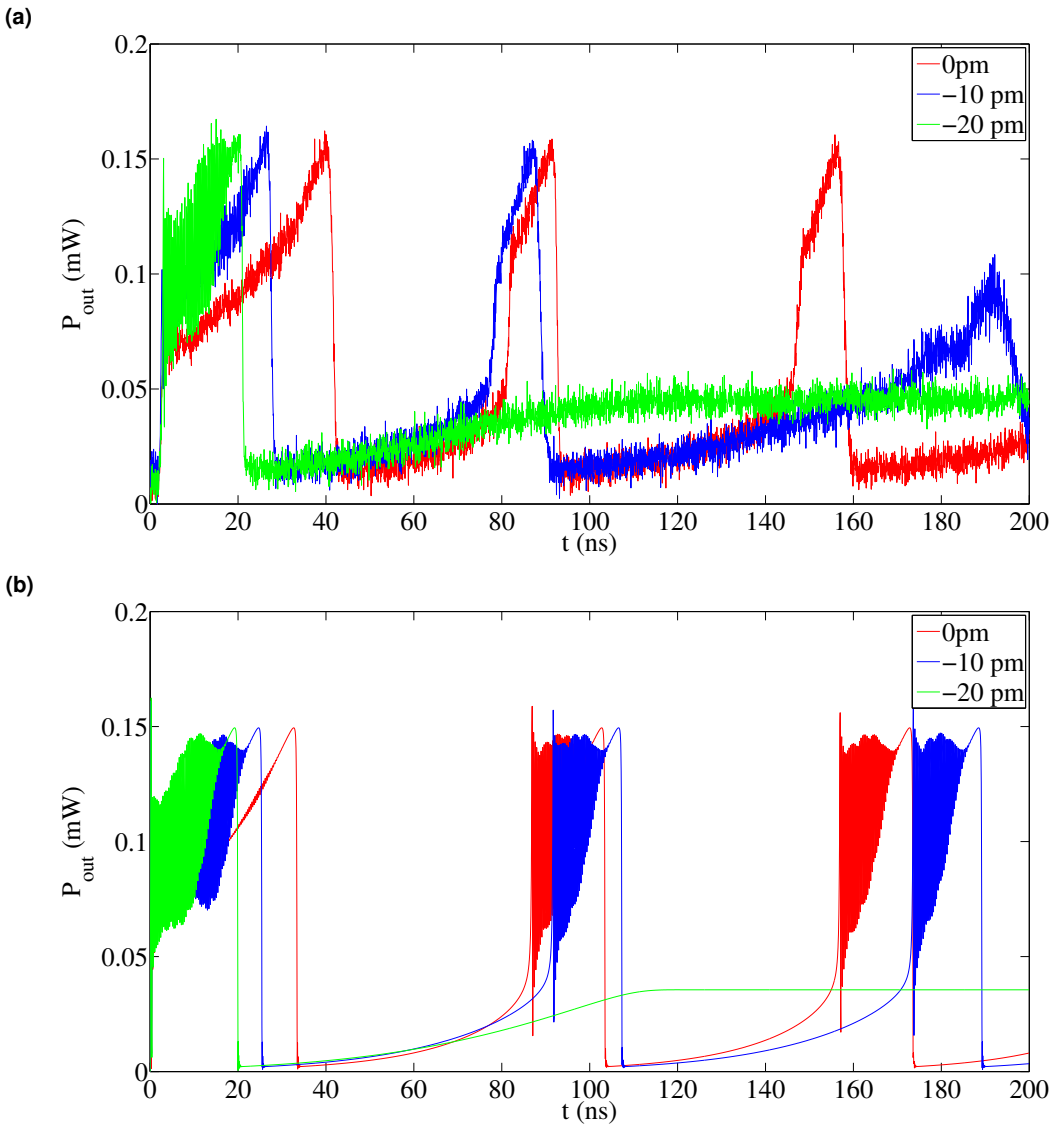

Figure 2.19: The thermal oscillations in our cavity for an input power $P_{in} = 2$ mW and a pulse length of 200 ns for different detunings between the wavelength of the laser and that of the cavity : (a) measured thermal oscillations and (b) simulated thermal oscillations with MATLAB.

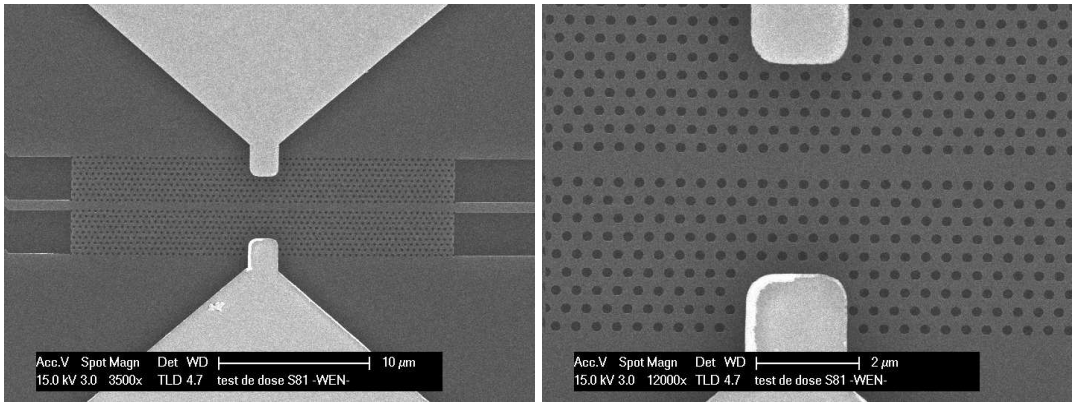

Figure 2.20: A cavity of the type used by L. Haret for his silicon photodetectors, similar to the one in which we measured the oscillations, but on SOI and with a MSM junction with platinum contacts. Left : view from afar of the whole structure with the access waveguides. Right : close up view of the cavity with the metallic contacts.

lifetimes should theoretically be of the same order of magnitude to have non-attenuated oscillations [63]). Free-carrier lifetimes as small as 12 ps have indeed been recently obtained in silicon waveguides using p-i-n junctions with a reverse bias [69].

Another possibility, which we favor because it would require fewer steps of fabrication than a p-i-n junction, would be to use a MSM (Metal-Semiconductor-Metal) junction with metallic contacts in platinum (see Fig. 2.20), similar to those used by my colleague L. Haret in silicon photodetectors [45, 36], to remove the free carriers from the silicon and reduce their lifetime. These photodetectors are based on Kuramochi-type cavities [26] similar to ours, but on SOI (i.e. composed of silicon on a silica substrate rather than of a silicon membrane as in our cavities) and therefore have smaller quality factors, which does not matter here because we want to reduce those quality factors. This type of cavity would also have the advantage of better managing of the thermal effects. The metal contacts would also allow us to recover the RF signal directly, thereby eliminating the need for a fast photodetector to detect the transmitted signal.

If we combine a cavity with a quality factor of 10000 and a transmission coefficient $T_{max} = 75\%$ with a free-carrier lifetime $\tau_{fc} = 10$ ps and an effective volume for the free carriers $V_{eff}^{FC} = 1.05\ \mu m^3$ (the effective volume of free carriers will be smaller for $\tau_{fc} = 10$ ps, since the free-carrier lifetime is now of the same order of magnitude as their diffusion time inside the cavity [67] and they will not have the time to spread out in the cavity), then our model predicted us oscillation frequencies between 30 GHz to 50 GHz for input powers ranging from 50 mW to 150 mW (see Fig. 2.21a), ten times larger than for those we have measured. In a system made of III-V semiconductor such as the one studied in reference [59], these values for the lifetimes lead to an oscillation frequency of 100 GHz, because of the difference between nonlinear coefficients (in particular because of the difference between the two-photon absorption coefficient of silicon and that of the III-

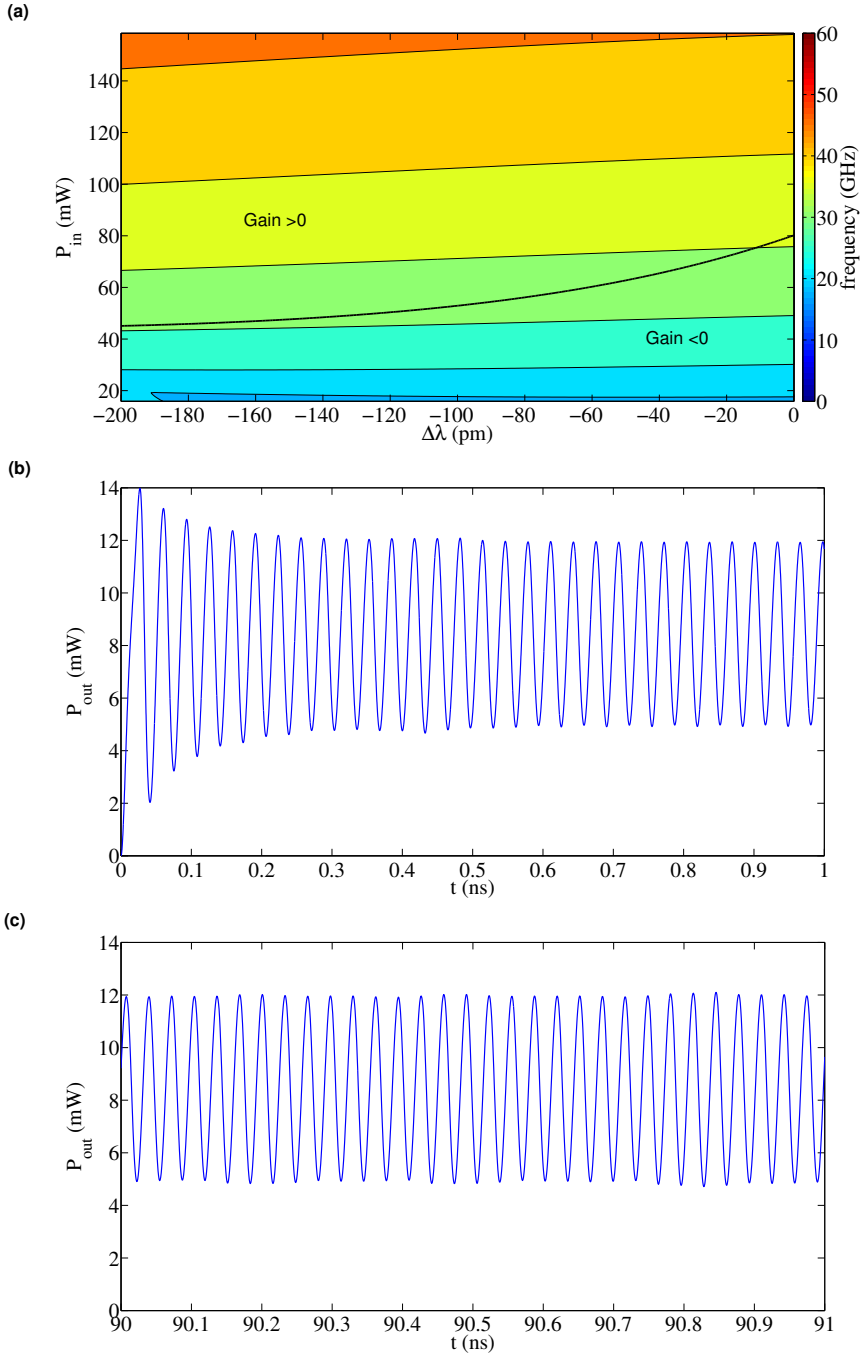

Figure 2.21: (a) The oscillation frequency as a function of the detuning and of the input power for a cavity with a quality factor of 10000, a maximum transmission $T_{max} = 75\%$, a free-carrier lifetime of 10 ps and an effective volume for the free carriers $V_{eff}^{FC} = 1.05$ μm^3. The oscillations are non-attenuated within the region of positive gain (within the area delineated by the thick black line). (b) and (c) Simulations with MATLAB of the output power of the cavity, with the thermal effects, for a detuning $\triangle\lambda = -200$ pm and an input power $P_{in} = 50$ mW. (b) Simulation just after the laser is turned on and (c) after 90 ns. We can see that the average output power remains constant, indicating that the thermal dispersion is negligible.

V materials). For our nanocavity in silicon, we can also note that a free-carrier lifetime of 10 ps would sharply decrease the free-carrier absorption, which the main cause of the rise in temperature of the cavity, and thus make the thermal effects completely negligible, thus eliminating the need to use a pulsed laser with the cavity. This is confirmed by a numerical simulation of the temporal behavior of the cavity for $\triangle\lambda = -200$ pm and $P_{in} = 50$ mW (see Fig. 2.21b and c), which allows us to note that the increase of the output power with time, which is characteristic of the thermal dispersion, is no longer observable on our simulations.

2.7 Conclusion.

To conclude, we experimentally observed for the first time in silicon photonic crystal nanocavities non-attenuated self-induced oscillations with frequencies in the gigahertz range, created by the interaction between two-photon absorption and free-carrier dispersion. We also modeled for the first time the harmonics of these oscillations. The oscillation frequency is here controlled by the photon and free-carrier lifetimes of our cavity. Self-pulsing in photonic crystal cavities presents the advantage of simplicity to realize ultra-compact microwave sources with high spectral purity. The model we have developed for these nanocavities, using the equations of a nanocavity for nonlinear optics exposed in the first chapter of this thesis, is remarkably accurate to describe and explain these oscillations. It shows as well that this high frequency of the oscillations and their high spectral purity are mainly a consequence of the very small modal volume of photonic crystals nanocavities and could not be observed in cavities with larger modal volumes such as microring resonators.

The analysis of the experimental results also allowed us to determine the value of the free-carrier lifetime in our silicon photonic crystal membrane nanocavities, which we did not know precisely before. We will take for subsequent calculations $\tau_{fc} = 0.3$ ns as the value of this lifetime, which is the value we found before the nitric acid treatment of the cavity. The experimental results have also allowed us to estimate the values of the effective volume of the free carriers, the effective thermal volume and the cooling time of the cavity. This will enable us to complete our model of the nanocavities in a nonlinear regime developed in the first chapter of this thesis, and use it to study the phenomenon of Raman scattering in doubly resonant silicon photonic crystal nanocavities in order to obtain silicon Raman nanolasers. This study will cover the whole of the third chapter of this thesis.

Chapter 3

Raman scattering in a nanocavity.

3.1 Introduction.

Raman scattering in silicon has been increasingly studied during the past decade in order to obtain Raman lasers fully in silicon [54, 55, 56, 57, 58]. A conventional laser in silicon is indeed extremely difficult to obtain because silicon has an indirect bandgap, that is to say that the top of the valence band and the bottom of the conduction band are not aligned on the band diagram of silicon : they therefore correspond to different momentums for the free carriers (see Fig. 3.1). In a laser based on a semiconductor with a direct bandgap, such as gallium arsenide or indium phosphide, a photon is emitted each time we have an electron-hole recombination, without change to the momentum (this corresponds to a vertical transition in $\overrightarrow{k}$-space). In the case of a semiconductor with an indirect bandgap, a phonon must be absorbed or emitted in addition to the emission of a photon during a hole-electron recombination, in order to respect the conservation of momentum. For this reason, the emission of photons in these materials is very inefficient, which is why we can not obtain silicon lasers this way [70, 71]. This poses a problem, because silicon is the most widely used semiconductor in microelectronics and the most inexpensive, and to obtain silicon lasers would be very useful in this field.

On the other hand, since stimulated Raman scattering is a phenomenon corresponding to a nonlinear gain, it is possible to use it to obtain silicon lasers. Unfortunately, most of the silicon Raman lasers achieved when this thesis was begun, either in ridge waveguides on SOI [56, 58] or ring cavities [54, 55, 57], were too large, of a size typically in the centimeter range, to be used in microelectronics and integrated optics. But we have seen previously that photonic crystal cavities and waveguides can be used to amplify the strength of nonlinear effects in silicon [9, 12], and therefore the strength of stimulated Raman scattering. For this reason, Raman scattering in photonic crystals waveguides [72, 73, 74, 75] or in nanocavities [76, 77] has been strongly studied in order to obtain

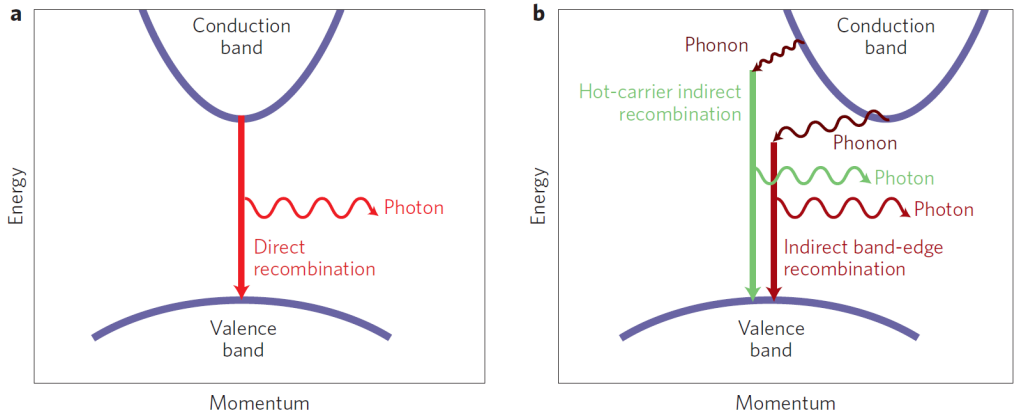

Figure 3.1: Example of electron-hole recombination in a semiconductor: (a) direct bandgap, (b) indirect bandgap (figure reprinted with permission from Macmillan Publisher Ltd : Nature Photonic, Ref. [71], copyright 2013).

more compact Raman lasers. A few months ago, a silicon Raman laser was demonstrated by Takahashi et al. [2] in a photonic crystal nanocavity. The difficulties in obtaining a Raman laser in silicon nanocavity are due primarily to the need for a doubly resonant cavity with a resonance at the frequency of the pump laser and another resonance at the frequency of the Stokes laser in order to enough amplify the Raman scattering, and to the importance of the nonlinear absorptions, which counterbalance the Raman gain in the cavity. Although we were not able to obtain a true Raman laser effect, we will present in this chapter examples of this kind of cavity that we designed and measured.

This chapter is divided into two parts. The first part explains the operation of a Raman laser from a theoretical perspective, using the equations developed in section 1.4.3 of Chapter 1, by finding the steady-state solutions to these equations, and then by calculating from these equations the frequency response of the Raman laser for a small modulation of the input pump power, as well as its noise and linewidth. In the second part, we measure the stimulated Raman scattering in narrow W0.63 waveguides of length 100 microns, and then present an example of a doubly resonant cavity photonic crystals specifically designed from these waveguides to maximize the effect of Raman scattering. We will then measure experimentally the Raman power in this nanocavity in order to determine the value of the Raman gain in silicon and to validate the model that we developed of the Raman laser.

3.2 Raman laser - Theoretical approach.

In this first part, we will model the Raman scattering in a cavity in order to understand what are the important parameters to obtain a laser. Then we will consider the possible applications of this laser to telecommunications, which is one of the classic uses of the

lasers produced in integrated optics. We will seek first the frequency response of the Raman laser to a small modulation of the input pump power, in order to know the modulation properties that such a laser would have. We will then try to determine the noise of the Raman laser, and in particular the relative intensity noise (or RIN), and the frequency noise. An important property of Raman lasers is indeed their very low frequency noise compared to conventional semiconductor lasers, which results in an extremely narrow laser linewidth. This is due to the fact that the Raman gain is perfectly symmetrical, unlike that of a conventional semiconductor laser.

3.2.1 The equations of a Raman laser.

We will first consider the Raman laser from a theoretical point of view, in order to find the important parameters to obtain a laser. For this, we will assume that we have a waveguide or a nanocavity with two resonances ω_{p_0}, ω_{s_0} for the pump and Stokes modes respectively and, to simplify the calculations, we will assume that these resonances are perfectly tuned to the Raman shift, i.e. that we have $\omega_{s_0} = \omega_{p_0} - \omega_R$, where ω_R is the Raman frequency shift, and will ignore all the dispersion effects in our cavity. The equations of this doubly resonant nanocavity then become (see section 1.4.3) :

$$\frac{dA_p}{dt} = -\left(\frac{1}{\tau_p} + \gamma_p^{FCA} N_e + \gamma_{pp}^{TPA} N_p + (\gamma_{ps}^{TPA} + \gamma_{sp}^{TPA}) N_s + G_r(N_s+1)\right)\frac{A_p}{2} + \sqrt{\frac{\sqrt{T_{p_{max}}} P_{p_{in}}}{2\tau_p}} \tag{3.1}$$

$$\frac{dN_s}{dt} = -\left(\frac{1}{\tau_s} + \gamma_s^{FCA} N_e + \gamma_{ss}^{TPA} N_s + (\gamma_{ps}^{TPA} + \gamma_{sp}^{TPA}) N_p\right) N_s + G_r N_p (N_s+1) \tag{3.2}$$

$$\frac{dN_e}{dt} = -\frac{N_e}{\tau_{fc}} + \frac{1}{2}\gamma_{pp}^{TPA} N_p^2 + \frac{1}{2}\gamma_{ss}^{TPA} N_s^2 + \frac{1}{2}(\gamma_{sp}^{TPA} + \gamma_{ps}^{TPA}) N_p N_s + \gamma_p^l N_p + \gamma_s^l N_s \tag{3.3}$$

We can obtain a simplified version of these equations by neglecting at first all the nonlinear effects other than the Raman scattering. We have then the system of equations :

$$\frac{dA_p}{dt} = -\frac{A_p}{2\tau_p} - \frac{G_r}{2} A_p (N_s+1) + \sqrt{\frac{\sqrt{T_{p_{max}}} P_{p_{in}}}{2\tau_p}} \tag{3.4}$$

$$\frac{dN_s}{dt} = -\frac{N_s}{\tau_s} + G_r N_p (N_s+1) \tag{3.5}$$

3.2.2 Steady-state solutions.

To understand the origin of the Raman laser phenomenon, we will first solve these equations for steady-state solutions, which will allow us to plot the output Stokes power as a function of the pump power at the entrance or exit of the cavity and to show that, under favorable circumstances, the cavity behaves in a way similar to that of a conventional laser.

3.2.2.1 Case where we neglect the other nonlinear effects.

If we neglect all the nonlinear optical effects, with the exception of the Raman scattering, then the equation 3.5 gives us in the steady-state regime the following expression for the number of Stokes photons N_s in the cavity :

$$N_s = \frac{\tau_s G_r N_p}{1 - \tau_s G_r N_p} \tag{3.6}$$

This result is easier to interpret if we choose instead to express the number of pump photons N_p in function of the number of Stokes photons Stokes N_s :

$$N_p = \frac{1}{\tau_s G_r} \frac{N_s}{N_s + 1} \tag{3.7}$$

and if we use the equations 3.4 et 3.6 to derive an expression of the input pump power $P_{p_{in}}$ as a function of the number of pump photons N_p :

$$P_{p_{in}} = \frac{\hbar \omega_p N_p}{2\tau_p \sqrt{T_{max_p}}} \left(1 + \frac{\tau_p G_r}{1 - \tau_s G_r N_p}\right)^2 \tag{3.8}$$

When the number of Stokes photons is much below unity : $N_s \ll 1$, i.e. when the spontaneous part of Raman scattering is dominant, then the equation 3.7 takes the form $N_p = N_s/(\tau_s G_r)$. We are in the linear regime. On the other hand, when the number of Stokes photons is much greater than unity: $N_s \gg 1$, i.e. when the stimulated Raman scattering predominates, then the equation 3.7 takes the form $N_p = 1/(\tau_s G_r)$. This means that the number of pump photons N_p remains almost constant, but that the number of Stokes photons N_s can take any value, which is characteristic of the behavior of a laser if we consider that the pump photons play the same role in a Raman laser as free carriers in a conventional semiconductor laser. Indeed, in a conventional laser, once the laser threshold is reached, the free-carrier density is constant irrespective of the electrical current supplied to the laser, while the laser output power increases very rapidly : this phenomenon is called the gain clamping [78]. This similarity between the behavior of a

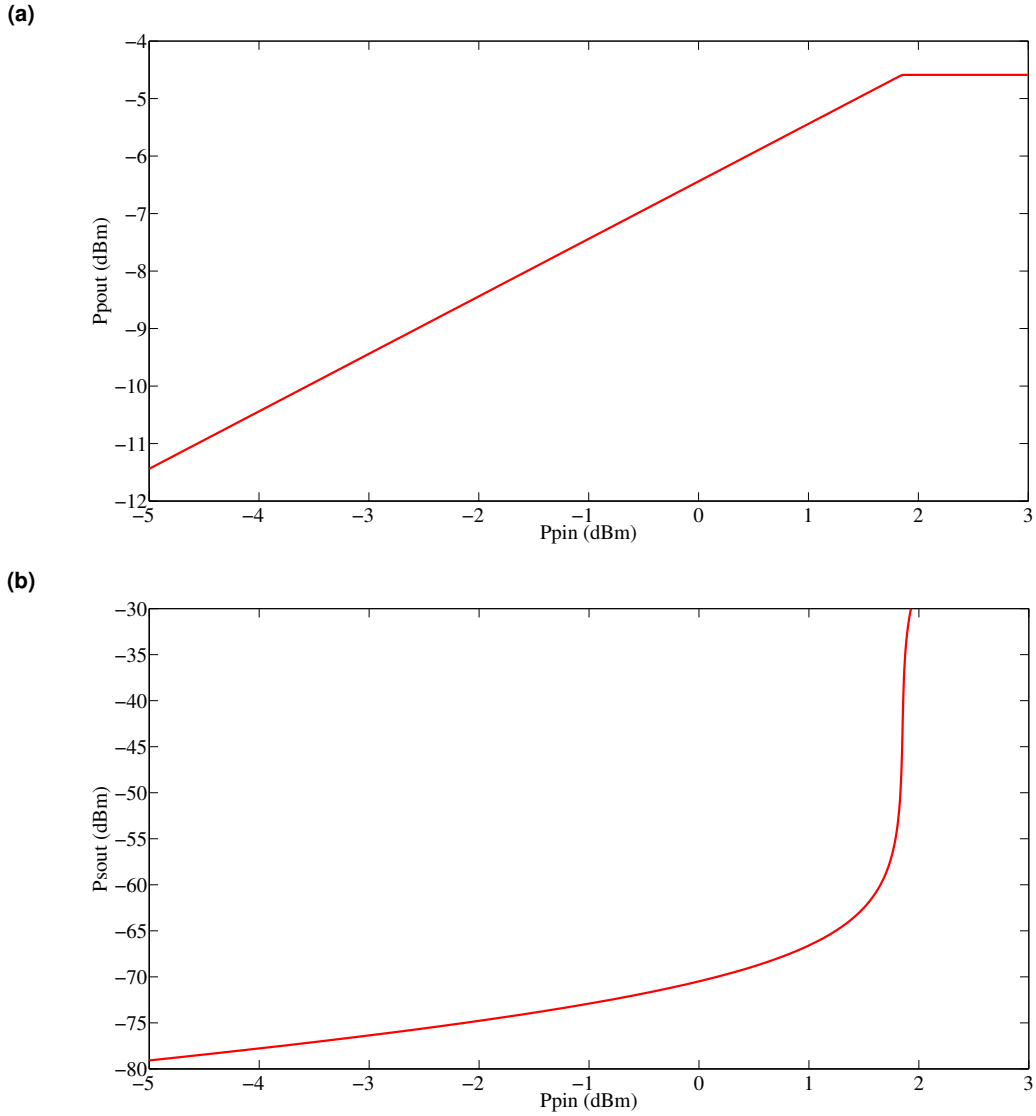

Figure 3.2: (a) The output power of the pump laser plotted as a function of the input power. (b) The output Stokes power plotted as a function of the input pump power. These curves were plotted using the typical parameters of the cavity we studied afterwards (see 3.3), taking $g_R^B = 30$ cm/GW for the Raman gain in bulk silicon. We can see that the pump output power at the cavity exit, which is proportional to the number of pump photons in the cavity, saturates when we are in the lasing mode : All pump photons in "excess", i.e. above the value of the laser threshold, are indeed converted into Stokes photons. This behavior is identical to that of a conventional semiconductor laser, if we consider that the pump photons and the input pump power have the same role in a Raman laser as the free carriers and the input current have in a conventional semiconductor laser.

Raman laser and that of a conventional laser is easy to spot if we plot the output pump power $P_{p_{out}} = \frac{\sqrt{T_{pmax}}\hbar\omega_p N_p}{2\tau_p}$ as a function of the input pump power $P_{p_{in}}$, and if we plot the output Stokes power $P_{s_{out}} = \frac{\sqrt{T_{smax}}\hbar\omega_s N_s}{2\tau_s}$ as a function of the input pump power $P_{p_{in}}$ (see Fig. 3.2).

3.2.2.2 General case.

If we take into account the two-photon and free-carrier absorptions, then the equation 3.7 takes the form of a second-degree polynomial in N_p (obtained from equations 3.2 and 3.3) :

$$a_2 N_p^2 + a_1 N_p + a_0 = 0 \tag{3.9}$$

whose coefficients a_2, a_1, a_0 depend on the number of Stokes photons N_s through the following expressions :

$a_2 = -\frac{1}{2}\gamma_{pp}^{TPA}\gamma_s^{FCA} N_s \tau_{fc}$,

$a_1 = G_r(N_s+1) - (\gamma_{sp}^{TPA} + \gamma_{ps}^{TPA})N_s - \gamma_s^{FCA} N_s \tau_{fc}(\frac{1}{2}(\gamma_{sp}^{TPA} + \gamma_{ps}^{TPA})N_s + \gamma_p^l)$,

$a_0 = -\frac{N_s}{\tau_s} - \gamma_{ss}^{TPA} N_s^2 - \gamma_s^l \gamma_s^{FCA} N_s^2 \tau_{fc}$.

The equation 3.8 on $P_{p_{in}}$ is also modified and become :

$$P_{p_{in}} = \frac{\tau_p \hbar\omega_p N_p}{2\sqrt{T_{max_p}}}\left(\frac{1}{\tau_p} + \gamma_p^{FCA} N_e + \gamma_{pp}^{TPA} N_p + (\gamma_{ps}^{TPA} + \gamma_{sp}^{TPA})N_s + G_r(N_s+1)\right)^2 \tag{3.10}$$

This expression depends on the number of free carriers N_e, which is worth :

$$N_e = \tau_{fc}(\frac{1}{2}\gamma_{pp}^{TPA} N_p^2 + \frac{1}{2}\gamma_{ss}^{TPA} N_s^2 + \frac{1}{2}(\gamma_{sp}^{TPA} + \gamma_{ps}^{TPA})N_p N_s + \gamma_p^l N_p + \gamma_s^l N_s) \tag{3.11}$$

The main difference with the previous expressions is that for each value of the number of photons Stokes N_s, we now have two corresponding values for the number of pump photons $N_p = \frac{-a_1 \pm \sqrt{a_1^2 - 4a_2 a_0}}{2a_2}$ and therefore two corresponding values for the input pump power $P_{p_{in}}$.

Concretely, this means that if we plot the output Stokes power as a function of the input pump power (see Fig. 3.3), we find that the beginning of the curve is similar to the one of the laser in the lossless case (see Fig. 3.2), but when the input power is too high, nonlinear losses become so large that the cavity stop lasing and the output Stokes power collapses. These nonlinear losses are the main obstacle to the obtention of a Raman laser. The fact that the cavity lases or not will depend heavily both on the importance of the Raman

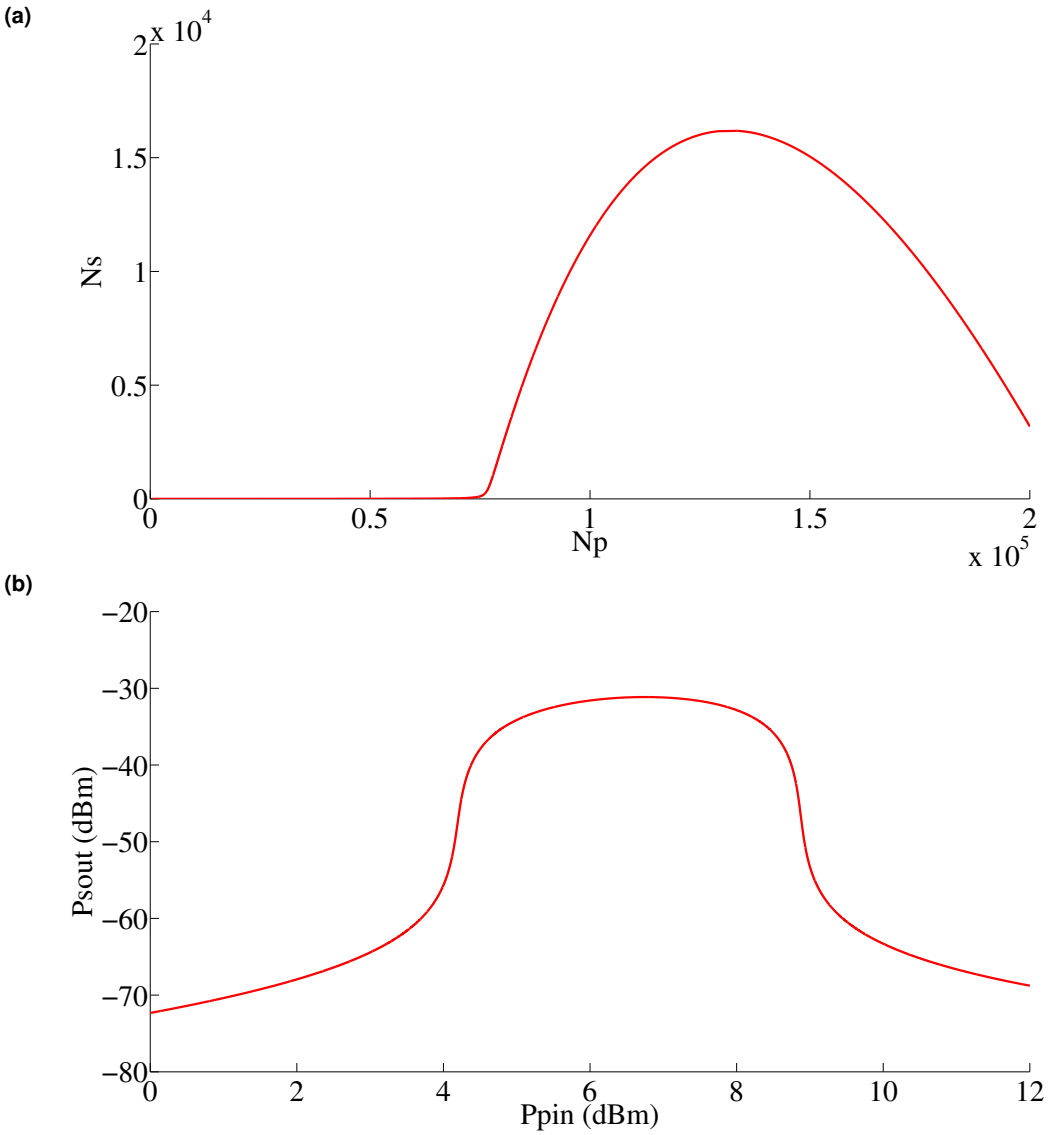

Figure 3.3: (a) The number of Stokes photons as a function of the number of pump photons. (b) The output Stokes power as a function of the input pump power. These curves were plotted using the typical parameters of the doubly resonant cavity we studied afterwards (see 3.3), taking $\tau_{fc} = 0.3$ ns for the free-carrier lifetime, $Q_p = 4900$ and $Q_s = 235000$ for the pump and Stokes quality factors, $g_R^B = 30$ cm/GW for the Raman gain in bulk silicon, and $V_R = 2.78\ \mu m^3$ for the Raman volume.

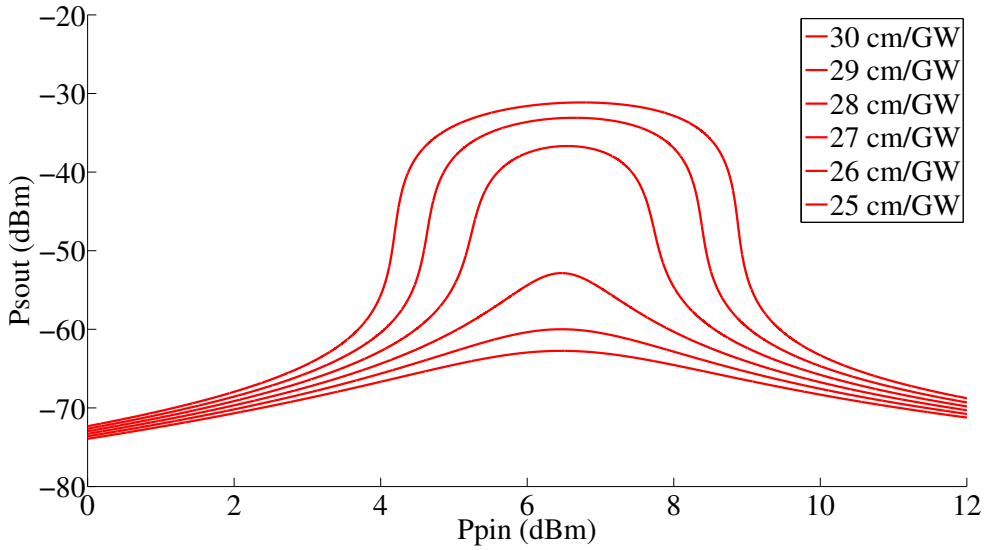

Figure 3.4: The output Raman power plotted as a function of the input pump power to different values of the Raman gain in bulk silicon g_R^B. A difference of a few percents on the value of the Raman gain can make a large difference on whether or not we obtain a Raman laser.

gain in silicon, whose reported value in the literature varies by a factor of 7 between 8.9 cm/GW [52] and 76.5 cm/GW [53], and on the importance of the nonlinear absorptions in the cavity. For example, a variation of a few percent of the value of the Raman gain can make the difference between obtaining a Raman laser or not (see Fig. 3.4).

3.2.3 Frequency response for a small modulation of the Raman laser.

We will now try to determine the frequency response of our Raman laser for a small modulation of the input pump power. We will first simplify the problem by neglecting all nonlinear effects other than the Raman scattering, and linearize the equations of the Raman laser for small variations $(\delta A_p, \delta N_s)$ around the steady-state solutions (A_p, N_s) . We then obtain the following linear differential equation in matrix form [78] :

$$\frac{d}{dt}\begin{pmatrix}\delta A_p\\ \delta N_s\end{pmatrix} = \begin{pmatrix} -\frac{1}{2\tau_p} - \frac{G_r(N_s+1)}{2} & -\frac{G_r A_p}{2} \\ \frac{2G_r A_p(N_s+1)}{\hbar\omega_p} & -\frac{1}{\tau_s} + \frac{G_r A_p^2}{\hbar\omega_p}\end{pmatrix}\begin{pmatrix}\delta A_p\\ \delta N_s\end{pmatrix} + \frac{1}{2}\sqrt{\frac{\sqrt{T_{p_{max}}}}{2\tau_p P_{p_{in}}}}\begin{pmatrix}\delta P_{p_{in}}\\ 0\end{pmatrix} \tag{3.12}$$

If we assume that the modulation of the input pump power is sinusoidal with a pulsation

Ω, then the equation 3.12 becomes :

$$\begin{pmatrix} i\Omega + \frac{1}{2\tau_p} + \frac{G_r(N_s+1)}{2} & \frac{G_r A_p}{2} \\ -\frac{2G_r A_p(N_s+1)}{\hbar\omega_p} & i\Omega + \frac{1}{\tau_s} - \frac{G_r A_p^2}{\hbar\omega_p} \end{pmatrix} \begin{pmatrix} \delta A_p \\ \delta N_s \end{pmatrix} = \frac{1}{2}\sqrt{\frac{\sqrt{T_{p_{max}}}}{2\tau_p P_{p_{in}}}} \begin{pmatrix} \delta P_{p_{in}} \\ 0 \end{pmatrix} \tag{3.13}$$

This equation in matrix form is a Cramer system whose solutions are :

$$\delta A_p = \frac{\frac{1}{2}\sqrt{\frac{\sqrt{T_{p_{max}}}}{2\tau_p P_{p_{in}}}} \left(i\Omega + \frac{1}{\tau_s} - \frac{G_r A_p^2}{\hbar\omega_p}\right) \delta P_{p_{in}}}{\left(i\Omega + \frac{1}{2\tau_p} + \frac{G_r(N_s+1)}{2}\right)\left(i\Omega + \frac{1}{\tau_s} - \frac{G_r A_p^2}{\hbar\omega_p}\right) + \frac{G_r^2 A_p^2 (N_s+1)}{\hbar\omega_p}} \tag{3.14}$$

$$\delta N_s = \frac{\frac{1}{2}\sqrt{\frac{\sqrt{T_{p_{max}}}}{2\tau_p P_{p_{in}}}} \frac{2G_r A_p(N_s+1)}{\hbar\omega_p} \delta P_{p_{in}}}{\left(i\Omega + \frac{1}{2\tau_p} + \frac{G_r(N_s+1)}{2}\right)\left(i\Omega + \frac{1}{\tau_s} - \frac{G_r A_p^2}{\hbar\omega_p}\right) + \frac{G_r^2 A_p^2 (N_s+1)}{\hbar\omega_p}} \tag{3.15}$$

Given that $P_{s_{out}} = \frac{\sqrt{T_{s_{max}}}\hbar\omega_s N_s}{2\tau_s}$, we can deduce from equation 3.15 the modulation transfer function $H(\Omega)$ of the linearized system of equations :

$$H(\Omega) = \frac{\delta P_{s_{out}}}{\delta P_{p_{in}}} = \frac{\frac{\sqrt{T_{s_{max}}}}{2\tau_s}\frac{\hbar\omega_s}{\hbar\omega_p}\sqrt{\frac{\sqrt{T_{p_{max}}}}{2\tau_p P_{p_{in}}}}\left(G_r A_p(N_s+1)\right)}{\left(i\Omega + \frac{1}{2\tau_p} + \frac{G_r(N_s+1)}{2}\right)\left(i\Omega + \frac{1}{\tau_s} - \frac{G_r A_p^2}{\hbar\omega_p}\right) + \frac{G_r^2 A_p^2 (N_s+1)}{\hbar\omega_p}} \tag{3.16}$$

which allows us to calculate the system gain $|H(\Omega)|$ for a modulation of the input pump power of the Raman laser.

In the case of Raman laser that we represented in Fig. 3.2 (where the nonlinear effects other than the Raman scattering are neglected) for the operating point $P_{s_{out}} = -33$ dBm, the cutoff frequency at -3 dB of this transfer function is 6.7 MHz (see Fig. 3.5). Beyond this frequency, the gain of the system for small modulations fall rapidly (-40 dB/decade). Therefore such a laser would let pass only the modulations with frequencies less than 6.7 MHz, which is very low compared to the conventional semiconductor lasers whose cutoff frequencies are of the order of a few GHz. To interpret this result, it suffices to note that we can easily simplify the expression of the modulation transfer function 3.16 if we are very much above the laser threshold, as is the case here. Indeed, we then have $N_s \gg 1$ and $N_p \sim 1/(\tau_s G_r)$, which gives us as equivalent expression for the transfer function :

$$H(\Omega) \sim \frac{\frac{\hbar\omega_s N_s\sqrt{T_{s_{max}}}}{2\tau_s}\sqrt{\frac{G_r\sqrt{T_{p_{max}}}}{2\hbar\omega_p\tau_p\tau_s P_{p_{in}}}}}{(i\Omega)^2 + i\Omega\left(\frac{1}{2\tau_p} + \frac{G_r N_s}{2}\right) + \frac{G_r N_s}{\tau_s}} \tag{3.17}$$

which corresponds to the equation of a second-order low-pass filter with a resonance

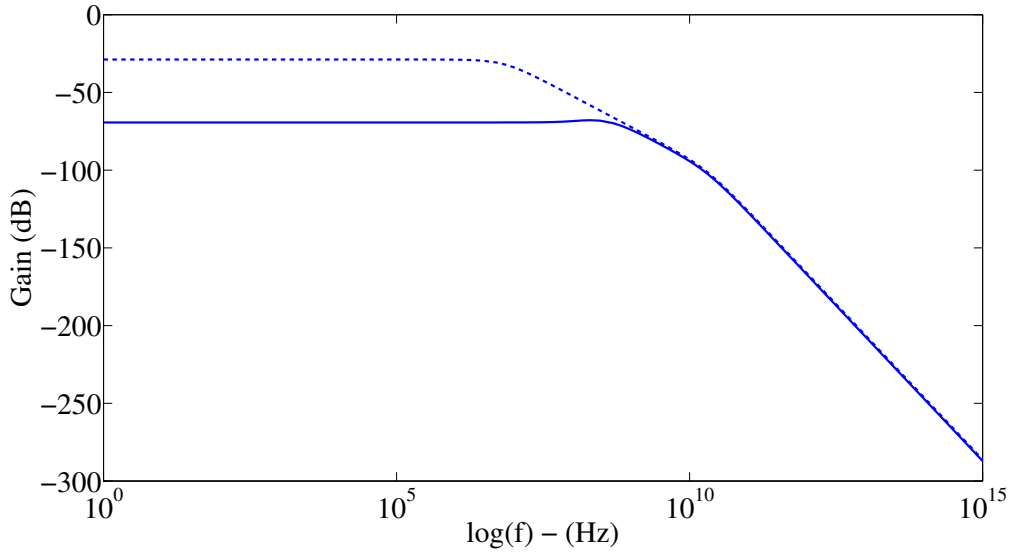

Figure 3.5: The gain of the modulation transfer function $|H(\Omega)|$ for the Raman laser that we represented on Fig. 3.2 and 3.3 for the operating point $P_{s_{out}} = -33$ dBm. The dotted curve represents the gain for the case where the nonlinear effects other than the Raman scattering are neglected and the solid curve the gain if we do not neglect those nonlinear effects. The cutoff frequency at -3 dB of this transfer function is 6.7 MHz in the case where the nonlinear effects other than Raman scattering are neglected, and 630 MHz in the case where we do not neglect those effects.

frequency $f_0 = \frac{\Omega_0}{2\pi} = \frac{1}{2\pi}\sqrt{\frac{G_r N_s}{\tau_s}} = \frac{1}{2\pi}\sqrt{\frac{2G_r P_{s_{out}}}{\hbar\omega_s\sqrt{T_{smax}}}}$ and a damping factor $\gamma_0 = \frac{1}{2\tau_p} + \frac{G_r N_s}{2}$ (which gives us for the quality factor of the second-order transfer function $Q_0 = \frac{2\Omega_0}{\frac{1}{\tau_p}+G_r N_s}$). Numerically, for the case presented above, we have $f_0 = 365$ MHz and $\gamma_0 \simeq \frac{1}{2\tau_p} = 125.6 \times 10^9\ s^{-1}$, which gives us $Q_0 \simeq 2\Omega_0\tau_p = 1.83 \times 10^{-2}$). The combination of the relatively low value of the resonance frequency f_0 and of a relatively high damping factor explains the very low value of the cutoff frequency at -3 dB.

We can compare these values with those of a conventional semiconductor laser. For this type of laser, we have as an approximate expression for the resonance frequency of the modulation transfer function $f_0 = \frac{1}{2\pi}\sqrt{\frac{N_{ph}}{\tau_{ph}}\frac{\partial G_{ls}}{\partial N_e}}$, where N_e is the number of free carriers in the laser cavity, N_{ph} the number of photons, τ_{ph} their lifetime and G_{ls} is the laser gain [78]. This expression is similar to ours if we consider that, in a Raman laser, N_s plays the same role as N_{ph}, N_p the same role as N_e, and the laser gain is $G_{ls} = G_r N_p$ (and therefore that $\frac{\partial G_{ls}}{\partial N_p} = G_r$). For example, for a $In_{0.2}Ga_{0.8}As/GaAs$ quantum-well laser, we typically have $\tau_{ph} = 2.75$ ps, $N_{ph} = 30400$ and $\frac{\partial G_{ls}}{\partial N_e} = 3.23 \times 10^4\ s^{-1}$ (to compare with $\tau_s = 210$ ps, $N_s = 10500$ and $G_r = 1.05 \times 10^5\ s^{-1}$ for the Raman laser discussed above), which gives us a resonant frequency $f_0 = 2.9$ GHz (the damping factor is itself equal to $\gamma_0 = 2.88 \times 10^9\ s^{-1}$, which is much lower than for our Raman laser, because it is proportional to $1/\tau_{fc}$, with $\tau_{fc} = 1.57$ ns, rather than $1/\tau_p$ as in the case of our Raman laser, where $\tau_p = 4.01$

ps and the cutoff frequency at -3 dB of the conventional laser is in the same range as the resonance frequency) [78]. We can infer from this that the lower bandwith of our laser is a consequence of the larger number of (Stokes) photons in the cavity, which is itself due to the very high value of the quality factor of the Stokes resonance of the Raman laser.

Possible solutions to increase this bandwidth would be to either increase the output power of the laser, which is not always possible, since we are actually limited for the value of this output power by the nonlinear absorptions (see Fig. 3.3), or decrease the quality factor of the Stokes resonance, which creates other problems, because this quality factor must be very high to obtain a Raman laser threshold which is low enough and/or to compensate for the losses due to the nonlinear absorptions. A simpler solution would be to decrease the damping factor, which would bring the cutoff frequency at -3 dB nearer the filter resonance frequency and thus increase its bandwidth (the bandwidth of this type of filter is maximum for $Q_0 = 1/\sqrt{2} \approx 0.707$ [78]). For this, we would simply need to increase the value of the pump photons lifetime τ_p in the cavity, which can be done by increasing the value of the quality factor Q_p of the pump resonance.

We can note that, if we add the nonlinear absorptions to our calculation of the transfer function, which gives us a much more complicated expression for the filter (see the appendixes at the end of this thesis), then for the Raman laser that we represented in figure 3.3 (which corresponds to the laser discussed above, but with the nonlinear absorptions coefficients added) and the operating point $P_{s_{out}} = -33$ dBm, the cutoff frequency at -3 dB of this transfer function is 630 MHz (see Fig. 3.5), a much higher value than before. This difference is probably due to a much lower damping factor, because the resonance frequency seems to be in the same range as before. If we were not limited for the output Stokes power by the non-linear absorptions, then we could obtein a cutoff frequency even more important. For example, for a output Stokes power $P_{s_{out}} = -3$ dBm, we would get a cut-off frequency at -3 dB of 1.25 GHz, much better than before, and of the same order of magnitude as for a conventional semiconductor laser.

3.2.4 Relative Intensity Noise of the Raman laser.

We have so far considered only the case of a deliberate modulation of the input pump power of the Raman laser, and have assumed that when we are in the steady-state regime, the numbers of pump and Stokes photons remained constant. However, even in the steady-state regime without modulation of the input pump power, these numbers will fluctuate randomly, which will create a noise floor for the output power of the Raman laser. It is interesting to study the noise in a Raman laser, since they must have linewidth enhancement factors α (or Henry factor) much lower than conventional semiconductor lasers, which would result in a frequency noise and linewidth much smaller for a Raman laser than for

a semiconductor laser. We therefore propose to study these aspects of the noise in Raman microcavity lasers, aspects that have not been studied yet. In addition, the noise in microcavity lasers has been little studied so far. We will first of all consider what are the problems created by the presence of this noise in a laser used for transmitting a signal, and thus define the Relative Intensity Noise (or RIN). We will then calculate the noise spectral density of the pump and Stokes photons in the cavity using the Langevin approach, and deduce from it both the RIN of the Raman laser and the noise on the laser frequency.

3.2.4.1 Definition of the RIN.

We will first consider the problems posed by the presence of noise in a laser used for the transmission of a signal. If the signal transmitted by the laser is analog (with the form $P(t) = P_0 + P_1 \sin(\Omega t) + \delta P(t)$, where $\delta P(t)$ represents the noise, then the signal-to-noise ratio SNR is equal to [78] :

$$SNR = \frac{1}{2}\left(\frac{P_1}{P_0}\right)^2 \frac{P_0^2}{<\delta P^2(t)>} \tag{3.18}$$

where $<>$ is the signal average. If the signal transmitted by the laser is digital, then output power for each bit is either 0 or P_0. We need to have $|\delta P(t)| < \frac{P_0}{2}$ if we do not want to make any mistakes when reading each bit. For example, for a probability of error (bit-error rate) of less than 1 in 10^9 and for a noise having a Gaussian distribution around the average power P_0, we must have $\frac{P_0^2}{<\delta P^2(t)>} > 11.89^2$. For each of these two applications, it is necessary to evaluate the Relative Intensity Noise, or RIN, defined as [78] :

$$RIN = \frac{<\delta P^2(t)>}{P_0^2} \tag{3.19}$$

If we define by $S_{\delta P}(\Omega) = \frac{1}{2\pi}\int <\delta P(\Omega)\delta P^*(\Omega')> d\Omega'$ the spectral density of the noise $\delta P(t)$ then, this noise being completely random, we can write that $<\delta P(\Omega)\delta P^*(\Omega')> = S_{\delta P}(\Omega)\cdot 2\pi\delta(\Omega-\Omega')$, where δ is the Dirac function. If we assume that the noise is measured by a narrow filter centered on the frequency Ω and with a bandwidth $\triangle f$, then we have $<\delta P^2(t)> \approx S_{\delta P}(\Omega)\cdot 2\triangle f$, which allows us to express the RIN in dB/Hz as [78] :

$$\frac{RIN}{\triangle f} = \frac{2S_{\delta P}(\Omega)}{P_0^2} \tag{3.20}$$

To give an example of order of magnitude for the RIN, in the case of a digital signal detected by a filter with a bandwidth 1 GHz and a required probability of error of 1 in 10^9, then we must have a RIN (dB) < -21.5 dB, which requires an average RIN (dB/Hz) of -111.5 dB / Hz.

3.2.4.2 Langevin noise sources.

We will now try to calculate the Relative Intensity Noise (in the case where we neglect the nonlinear absorptions) using the Langevin approach. This approach consists in expressing the laser noise spectral density as a function of the Langevin noise sources $F_p(t)$ and $F_s(t)$, which are considered sources of white noise on the number of pump and Stokes photons respectively in the cavity, and which are assumed to be caused by the shot noise generated by the discontinuous nature of the pump and Stokes photon fluxes entering and exiting of the cavity.

We define now the noise pump and Stokes photons spectral densities as $S_{N_{I=p,s}}(\Omega) = \frac{1}{2\pi}\int < \delta N_I(\Omega)\delta N_I^*(\Omega') > d\Omega'$, and the spectral density of the Langevin noise sources as $< F_I F_J >= \frac{1}{2\pi}\int < F_I(\Omega)F_J^*(\Omega') > d\Omega'$, where I and J designate either the pump or the Stokes. These spectral densities represent the correlations between the different noise sources of the laser. The Langevin noise sources Langevin F_p and F_s being white noise sources, the noise spectral densities $< F_I F_J >$ are uniformly distributed over all frequencies and can be considered constant. We will first calculate the Langevin noise sources spectral densities, before making the connection between these noise sources and the spectral densities of the pump and Stokes photons (we follow here the approach outlined by Coldren & Corzine in Ref. [78]).

The spectral density of the shot noise at the origin of the Langevin noise source is constant and proportional to the corresponding average particle flux. We can thus determine the spectral densities $< F_I F_I >$ simply by summing all the contributions of the shot noise, i.e. by summing of all the the fluxes R_I of the particles N_I coming and going out of the cavity : $< F_I F_I >= \sum|R_I^{in}| + \sum|R_I^{out}|$. This expression can be simplified by using the fact that in the steady state regime, the sum of the outgoing particle fluxes $\sum|R_I^{out}|$ is equal to the sum of the incoming ones $\sum|R_I^{in}|$. We then have $< F_I F_I >= 2\left(\sum|R_I^{in}|\right) = 2\left(\sum|R_I^{out}|\right)$, which gives us the following expressions for $< F_I F_I >$:

$$< F_p F_p >= 2\left(\sum|R_p^{out}|\right) = 2\left(\frac{N_p}{\tau_p} + G_r N_p(N_s+1)\right) \tag{3.21}$$

$$< F_s F_s >= 2\left(G_r N_p(N_s+1)\right) = 2\frac{N_s}{\tau_s} \tag{3.22}$$

On the other hand, to determine the value of the spectral densities $< F_I F_J >$, with $I \neq J$, then we must do only the sum of the fluxes that affect both particles N_I and N_J, i.e. the cases where a particle N_I is converted into particle N_J and vice-versa : $< F_I F_J >= -\left(\sum|R_{I\to J}| + \sum|R_{J\to I}|\right)$. This noise $< F_I F_J >$ is always negative, because when a particle N_I is created ($F_I > 0$), a particle N_J is destroyed ($F_J < 0$), or vice-versa, which means that the noise F_I and F_J are negatively correlated. We can see that this expression is symmetric, and so that we have $< F_I F_J >=< F_J F_I >$. This gives us the following expression for

$< F_I F_J >$:

$$< F_p F_s >=< F_s F_p >= -G_r N_p (N_s + 1) \tag{3.23}$$

It is then relatively easy to make the link between the Langevin noise F on the number of photons N, and the Langevin noise F_A on the amplitude A of the electric field of the corresponding mode. If we denote $A = (A_0 + F_A)\, e^{i\varphi}$, with $A_0 = \sqrt{\hbar\omega N}$ the modulus of the amplitude without the noise and φ its phase, and $F_A = F_r + iF_i$, with F_r and F_{i_i} the parts of the noise F_A in-phase and out-of-phase with A_0 (with $F_r, F_i \ll A_0$), then we have $|A|^2 \simeq A_0^2 + 2A_0 F_r = \hbar\omega\,(N + F)$, which gives us : $F_r = \frac{\sqrt{\hbar\omega}}{2\sqrt{N}} F = \frac{\hbar\omega}{2A_0} F$ and $< F_r F_r >= \frac{\hbar\omega}{4N} < FF >$. Similarly, the Langevin noise on the phase of the amplitude A is equal to $F_\varphi \simeq \frac{F_i}{A_0}$. If we assume that the spectral densities of the real and imaginary parts of the noise are equal, i.e. that $< F_r F_r >=< F_i F_i >$, then we have $< F_\varphi F_\varphi >= \frac{<F_i F_i>}{|A_0|^2} = \frac{<F_r F_r>}{\hbar\omega N} = \frac{<FF>}{4N^2}$. This expression will be used later to calculate the noise on the frequency of the Raman laser.

3.2.4.3 Noise spectral densities of the photons.

There just remains for us to calculate the noise spectral densities of the pump and Stokes photons as a function of the spectral densities of the Langevin noise sources, which is easy to do by adapting the calculations that we did on the frequency response of the Raman laser for small modulations. If we assume here that the input pump power is constant, i.e. that $\delta P_{p_{in}} = 0$, then the equation 3.12 becomes :

$$\frac{d}{dt}\begin{pmatrix} \delta A_p \\ \delta N_s \end{pmatrix} = \begin{pmatrix} -\frac{1}{2\tau_p} - \frac{G_r(N_s+1)}{2} & -\frac{G_r A_p}{2} \\ \frac{2G_r A_p (N_s+1)}{\hbar\omega_p} & -\frac{1}{\tau_s} + G_r N_p \end{pmatrix} \begin{pmatrix} \delta A_p \\ \delta N_s \end{pmatrix} + \begin{pmatrix} \frac{\hbar\omega_p}{2A_p} F_p(t) \\ F_s(t) \end{pmatrix} \tag{3.24}$$

If we transform to the frequency domain, then we obtain a Cramer system, which after resolution gives us the following relationship between (δA_p,δN_s) and (F_p, F_s) :

$$\begin{pmatrix} \delta A_p \\ \delta N_s \end{pmatrix} = \frac{1}{\triangle(\Omega)} \begin{pmatrix} i\Omega + \frac{1}{\tau_s} - G_r N_p & -\frac{G_r A_p}{2} \\ \frac{2G_r A_p (N_s+1)}{\hbar\omega_p} & i\Omega + \frac{1}{2\tau_p} + \frac{G_r(N_s+1)}{2} \end{pmatrix} \begin{pmatrix} \frac{\hbar\omega_p}{2A_p} F_p(\Omega) \\ F_s(\Omega) \end{pmatrix} \tag{3.25}$$

where the determinant $\triangle(\Omega)$ is defined as $\triangle(\Omega) = \left(i\Omega + \frac{1}{2\tau_p} + \frac{G_r(N_s+1)}{2}\right)\left(i\Omega + \frac{1}{\tau_s} - G_r N_p\right) + G_r^2 N_p (N_s + 1)$.

Using these notations, as well as the relation $\delta N_p = \frac{2A_p}{\hbar\omega_p}\delta A_p$, we then obtain from equation 3.25 the following relations between the noise spectral densities of the pump and Stokes photons and the spectral densities of the Langevin noise sources :

$$\begin{pmatrix} S_{N_p}(\Omega) \\ S_{N_s}(\Omega) \end{pmatrix} = \frac{R(\Omega)}{\|\triangle(\Omega)\|^2} \begin{pmatrix} < F_p F_p > \\ < F_s F_s > \\ < F_p F_s > \end{pmatrix} \tag{3.26}$$

where the matrix $R(\Omega)$ is defined as :

$$R = \begin{pmatrix} \Omega^2 + \left(-\frac{1}{\tau_s} + G_r N_p\right)^2 & G_r^2 N_p^2 & 2G_r N_p \left(G_r N_p - \frac{1}{\tau_s}\right) \\ G_r^2 (N_s+1)^2 & \Omega^2 + \left(\frac{1}{\tau_p} + G_r(N_s+1)\right)^2 & G_r(N_s+1)\left(\frac{1}{\tau_p} + G_r(N_s+1)\right) \end{pmatrix} \tag{3.27}$$

We will now use these results to calculate the RIN using the noise spectral density of the Stokes photons, as well as the frequency noise using the noise spectral density of the pump photons.

3.2.4.4 Partition noise and RIN.

We now know the noise spectral density of the Stokes photons in the cavity Stokes S_{N_s}, but to calculate the noise spectral density of the output Stokes power $P_{s_{out}} = \frac{\sqrt{T_{s_{max}}}\hbar\omega_s N_s}{2\tau_s}$ of the Raman laser requires us to add another Langevin noise source F_{out} on this output power. F_{out} is called the partition noise, since it is due to the random division of the Stokes photons at the cavity exit between the photons transmitted out of the cavity and the photons reflected inside the cavity (technically, we should also add a partition noise on the pump power entering the cavity, but the influence of the latter on the total noise is negligible, so we did not take it into account in our equations for simplicity). The noise on the output Stokes power is then equal to :

$$\delta P_{s_{out}}(t) = \frac{\sqrt{T_{s_{max}}}\hbar\omega_s \delta N_s(t)}{2\tau_s} + F_{out}(t) \tag{3.28}$$

which gives us a noise spectral density on the output Stokes power of the Raman laser equal to :

$$S_{\delta P_{s_{out}}}(\Omega) = \left(\frac{\sqrt{T_{s_{max}}}\hbar\omega_s}{2\tau_s}\right)^2 S_{N_s}(\Omega) + Real\left(\frac{\sqrt{T_{s_{max}}}\hbar\omega_s}{\tau_s} < \delta N_s F_{out} >\right) + < F_{out} F_{out} > \tag{3.29}$$

There is no correlation between the partition noise and the pump photons, so we have $< F_p F_{out} >= 0$. If we also consider the fact that $< F_{out} F_{out} >= \hbar\omega_s P_{s_{out}}$ and $< F_s F_{out} >= -P_{s_{out}}$, then we obtain from the equation 3.25 : $< \delta N_s F_{out} >= \left(\frac{i\Omega + \frac{1}{2\tau_p} + \frac{G_r(N_s+1)}{2}}{\triangle(\Omega)}\right) P_{s_{out}}$,

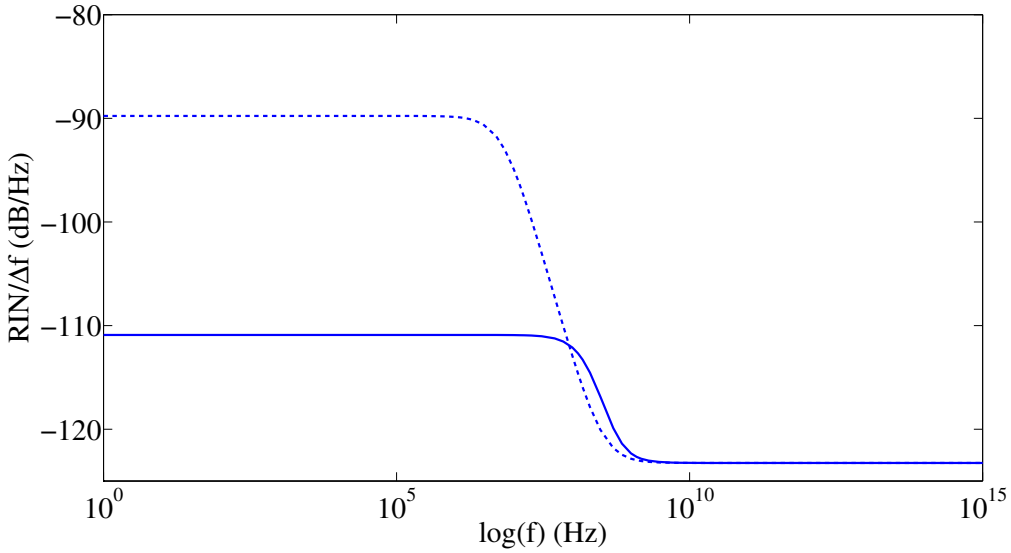

Figure 3.6: The Relative Intensity Noise (RIN) of the Raman laser that we represented in Fig. 3.2 and 3.3, for the operating point $P_{s_{out}} = -33$ dBm. The dotted curve represents the RIN for cases where the nonlinear effects other than the Raman scattering are neglected and the solid curve the case where we do not neglect those nonlinear effects.

and the equation 3.29 then becomes :

$$S_{\delta P_{s_{out}}}(\Omega) = \left(\frac{\sqrt{T_{s_{max}}}\hbar\omega_s}{2\tau_s}\right)^2 S_{N_s}(\Omega) + \hbar\omega_s \left(1 - \frac{\sqrt{T_{s_{max}}}}{\tau_s} Real\left(\frac{i\Omega + \frac{1}{2\tau_p} + \frac{G_r(N_s+1)}{2}}{\triangle(\Omega)}\right)\right) P_{s_{out}} \tag{3.30}$$

In the end, we obtain for the Relative Intensity Noise :

$$\frac{RIN}{\triangle f} = \left(\frac{\sqrt{T_{s_{max}}}\hbar\omega_s}{2\tau_s}\right)^2 \frac{2S_{N_s}(\Omega)}{P_{s_{out}}^2} + \frac{2\hbar\omega_s}{P_{s_{out}}} \left(1 - \frac{\sqrt{T_{s_{max}}}}{\tau_s} Real\left(\frac{i\Omega + \frac{1}{2\tau_p} + \frac{G_r(N_s+1)}{2}}{\triangle(\Omega)}\right)\right) \tag{3.31}$$

The first term of this expression corresponds to the noise generated by the fluctuations of the number of photons in the cavity and the second term to the contribution of the partition noise. For low frequencies, the second term is negligible compared with the first one. However, for high frequencies (i.e. above the cut-off frequency at -3 dB of the modulation transfer function of the laser), the value of the first term drops rapidly and we end up with $\frac{RIN}{\triangle f} = 2\hbar\omega_s / P_{s_{out}}$ dB/Hz, which is the minimum value of the shot noise below which it is impossible to go.

If we plot this Relative Intensity Noise in the case of the Raman laser represented in figure 3.2 (where the nonlinear effects other than the Raman scattering are neglected) for the operating point $P_{s_{out}} = -33$ dBm, then we have $\frac{RIN}{\triangle f} = -89.75$ dB/Hz below the cutoff

frequency at -3 dB of 6.7 MHz of the modulation transfer function of the laser, which is relatively high. Above this cutoff frequency, the RIN fall rapidly to $\frac{RIN}{\triangle f} = -123.26$ dB/Hz, which is in fact the minimal shot noise level $2\hbar\omega_s/P_{s_{out}}$ (see Fig. 3.6). The importance of the RIN is explained by the low value of the output Stokes power $P_{s_{out}}$, which is typical of a nanolaser. Unlike a conventional semiconductor laser, we have no noise peak at the frequency resonance, due to the high damping factor of the modulation transfer function of our Raman laser compared to a conventional semiconductor laser (see section 3.2.3).

We can note that if we do not neglect the nonlinear absorptions (see the appendixes at the end of this thesis), the Relative Intensity Noise is much lower, being equal to $\frac{RIN}{\triangle f} = -111$ dB / Hz below the cutoff frequency at - 3 dB of 6.7 MHz. This lower value is explained by the lower value of the gain of the modulation transfer function in the case where we take into account the nonlinear absorptions (see Fig. 3.5 and 3.6). If we were not limited for the output Stokes power by the non-linear absorptions, then we could obtain a much lower noise. For example, for a output Stokes power of $P_{s_{out}} = -3$ dBm, we would obtain $\frac{RIN}{\triangle f} = -152.38$ dB/Hz below the cutoff frequency at -3 dB (which is in this case of 1.25 GHz), which is almost equal to the shot noise level $\frac{RIN}{\triangle f} = 2\hbar\omega_s/P_{s_{out}} = -153.25$ dB/MHz we have above the cutoff frequency. This is much better than for a conventional semiconductor laser, whose peak noise can reach $\frac{RIN}{\triangle f} = -112$ dB/Hz for an equivalent output power [78].

3.2.4.5 Factor of Henry and frequency noise.

The calculations that we just made can also be used to calculate the frequency noise of the Raman laser from the noise spectral density of the pump photons S_{N_p}. Indeed, the noise on the number of pump photons δN_p creates a noise on the laser frequency δf_s equal to :

$$\delta f_s = \frac{\alpha}{4\pi} G_r \delta N_p \tag{3.32}$$

where α is called the linewidth enhancement factor, or factor of Henry, of the laser. If we know that factor of Henry, then it is easy to estimate the frequency noise of the laser due to the coupling between amplitude and phase, or to calculate the frequency chirping that will be generated by the modulation in amplitude of the laser, using the formula 3.32. If we designate by $n = n_r + in_i$ the complex refractive index of the medium with n_r and n_i real, then the coupling factor is defined by [78] :

$$\alpha = -\frac{dn_r/dN_p}{dn_i/dN_p} \tag{3.33}$$

In the case of a Raman laser, the change of the optical index due to the Raman effect is (see equation 1.64) :

$$n = n_0 - i\frac{c}{2\omega}\frac{g_R^B I_p}{1+2i\left(\frac{\omega_{s_0}-\omega_s}{\triangle\omega_R}\right)} = n_0 - \frac{cg_R^B I_p}{2\omega}\frac{i+2\left(\frac{\omega_{s_0}-\omega_s}{\triangle\omega_R}\right)}{1+4\left(\frac{\omega_{s_0}-\omega_s}{\triangle\omega_R}\right)^2} \tag{3.34}$$

where ω_{s_0} is the resonance frequency used for the Stokes, and $\omega_s = \omega_p - \omega_R$ is the frequency of the theoretical maximum of the Raman gain (with ω_R the Raman frequency shift). By taking into account the fact that the optical intensity of the pump mode I_p is proportional to the number of pump photons N_p, we can calculate the factor of Henry of a Raman laser from equations 3.33 and 3.34 :

$$\alpha = -2\left(\frac{\omega_{s_0}-\omega_s}{\triangle\omega_R}\right) \tag{3.35}$$

We can notice that, in the case where the frequency of the maximum of the Raman gain ω_s is equal to the frequency of the Stokes resonance ω_{s_0}, we have $\alpha = 0$, and the frequency noise generated by the noise on the number of pump photons is then zero. Even in cases where the two frequencies are not exactly equal, the factor of Henry is relatively low : in the case of the doubly resonant cavity studied in section 3.3.2, we have $\alpha = -0.27$, which is much lower than for a conventional semiconductor laser, where we typically have $\alpha = 6$. Raman lasers will therefore have à priori the advantage of having a frequency noise much lower than for conventional semiconductor lasers.

Of course, the noise frequency is never going to be completely inexistent, because we need to take into account the fluctuations of the phase of the amplitude A_s due to the shot noise. If we note F_{φ_s} the Langevin noise source on the phase of the amplitude A_s, then equation 3.32 becomes :

$$\delta f_s = \frac{\alpha}{4\pi}G_r\delta N_p + \frac{1}{2\pi}F_{\varphi_s} \tag{3.36}$$

Taking into account the fact that we have $< F_pF_{\varphi_s} >= 0$, $< F_sF_{\varphi_s} >= 0$ (there is no correlation between the phase noise and the noises of the pump and Stokes photons) and $< F_{\varphi_s}F_{\varphi_s} >= \frac{<F_sF_s>}{4N_s^2} \simeq \frac{G_rN_p}{2N_s}$ (see section 3.2.4.2), this gives us for the frequency noise spectral density :

$$S_{\delta f_s}(\Omega) = \left(\frac{\alpha G_r}{4\pi}\right)^2 S_{N_p}(\Omega) + \left(\frac{1}{2\pi}\right)^2 \frac{G_rN_p}{2N_s} \tag{3.37}$$

The first term of this expression represents the frequency noise due to the noise on the pump photons, and the second term represents the inherent phase noise of the laser created by the photons spontaneously emitted in the Stokes mode. It is then possible to determine the full width at half maximum of the laser linewidth from the spectral density using the formula $(\triangle f_s)_{FW} = 2\pi S_{\delta f_s}(0)$. We can see that the last term is equal to $\frac{1}{2\pi}(\triangle f_s)_{ST}$, where $(\triangle f_s)_{ST} = \frac{G_r N_p}{4\pi N_s}$ is the full width at half maximum of the laser linewidth (above the laser threshold) calculated using the Schawlow-Townes linewidth formula [78]. In the case of the Raman laser that we represented on figure 3.2, for the operating point $P_{s_{out}} = -33$ = -33 dBm, we have$(\triangle f_s)_{ST} = 36.1$ kHz, which gives us, in the case where $\alpha = -0.27$, a full linewidth at half maximum of the laser $(\triangle f_s)_{FW} = 38.8$ kHz. This linewidth is much smaller than for conventional semiconductor lasers. This difference is explained by the greatest gain of the conventional laser, resulting in a greater spontaneous emission coefficient in a semiconductor laser than in a Raman laser. For example, for a quantum-well $In_{0.2}Ga_{0.8}As/GaAs$ laser, we typically have for the spontaneous emission coefficient $R_{sp} = 4.08 \times 10^{11}\ s^{-1}$ and a number of photons $N_{ph} = 30400$, which gives us for the laser linewidth $(\triangle f_s)_{ST} = \frac{R_{sp}}{4\pi N_{ph}} = 1.07$ MHz using the Schawlow-Townes formula, and a full linewidth of $(\triangle f_s)_{FW} = 39.6$ MHz for $\alpha = 6$ [78] (to compare with $R_{sp} = G_r N_p = 4.78 \times 10^9\ s^{-1}$ for the Raman laser with $P_{s_{out}} = -33$ dBm, where $G_r = 1.05 \times 10^5\ s^{-1}$, $N_p = 45500$ and $N_s = 10500$).

We can note that it is very likely that the actual value of α will also be more important than the one we have calculated here. Indeed, the frequency will also vary with the number of pump photons through the free-carrier and thermal dispersions and nonlinear absorptions that we have neglected here, which will modify the equation 3.32 and the factor of Henry :

$$\delta f_s = \delta\omega_s/(2\pi) = \frac{\alpha_R}{4\pi} G_r \delta N_p - \frac{1}{2\pi}\left(\gamma_{s_i}^{FCD}\delta N_e + \gamma_{s_i}^{T}\delta T\right) \tag{3.38}$$

In the case of Raman laser that we have shown in figure 3.3, for the operating point $P_{s_{out}} = -33$ dBm, in the steady-state regime, if we take into account the fact that $N_s \ll N_p$, then we have $N_e \approx \tau_{fc}\frac{1}{2}\gamma_{pp}^{TPA}N_p^2$ and $\triangle T \approx R_T\hbar\omega_p\gamma_{p_r}^{FCA}N_pN_e$, which gives us $\delta N_e \approx \tau_{fc}\gamma_{pp}^{TPA}N_p\delta N_p$ and $\delta T \approx \frac{3}{2}R_T\hbar\omega_p\gamma_{p_r}^{FCA}\tau_{fc}\gamma_{pp}^{TPA}N_p^2\delta N_p$, and for the factor of Henry :

$$\alpha = \alpha_R - \frac{2\tau_{fc}\gamma_{pp}^{TPA}N_p}{G_r}\left(\gamma_{s_i}^{FCD} + \frac{3}{2}\gamma_{s_i}^{T}R_T\hbar\omega_p\gamma_{p_r}^{FCA}N_p\right) \tag{3.39}$$

This gives us, if we take $\alpha_R = -2\left(\frac{\omega_{s_0}-\omega_s}{\triangle\omega_R}\right) = 0$, a factor of Henry equal to $\alpha = 9.7$, or equal to $\alpha = 14.9$ if we only take into account the influence of the free-carrier dispersion

(the thermal dispersion only has influence on the low frequency modulation/noise, since the cooling time of the cavity is much higher than the free-carrier lifetime), which gives us in the case of the Raman laser that we represented on figure 3.3 and the operating point $P_{s_{out}} = -33$ dBm, a total linewidth at half maximum of $(\triangle f_s)_{FW} = 261$ kHz, and suggests that we will still have a fairly low frequency noise. Of course, it is possible to greatly decrease the factor of Henry by decreasing the free-carrier lifetime with a junction MSM, as suggested later in Section 3.3.2. For a free-carrier lifetime of $\tau_{fc} = 10$ ps instead of 0.3 ns, we would have $\alpha = 0.5$ and the full linewidth at half maximum would fall back to $(\triangle f_s)_{FW} = 41.5$ kHz.

We can see that a Raman laser would à priori be more advantageous than a conventional semiconductor laser in terms of noise, both in regard to the RIN, the frequency noise, and the laser linewidth.

3.3 Raman scattering in a doubly resonant cavity.

We will now consider a real example of Raman scattering in a doubly resonant nanocavity. We will first present the waveguides W0.63 (i.e. the waveguides whose width is $0.63\sqrt{3}a$, where a is the period of the photonic crystal), which are waveguides where we could measure stimulated Raman scattering, and on which we based the design of our nanocavity. We will then present the design of our nanocavity and its operation, and we will eventually measure the Raman scattering in this cavity, in order to determine the value of the Raman gain in this nanocavity, as well as the mechanisms that limit the Raman scattering, and consider how we can reduce their influence in order to obtain a Raman laser. We will end this section by comparing our doubly resonant cavity with the Raman nanolaser in silicon that was demonstrated a few months ago by Takahashi [2].

3.3.1 Stimulated Raman scattering in W0.63 waveguides of length of 100 microns.

Most studies on Raman scattering in photonic crystals have been made in W1 waveguides [72, 74, 79, 80]. These waveguides have only one resonance, usually used for the Stokes resonance, which greatly limits the effectiveness of Raman scattering in these waveguides : stimulated Raman scattering has been observed in these waveguides only in the case of a pulsed pump laser [80]. In silicon, stimulated Raman scattering has been observed with a continuous pump laser only in the narrow W0.66 waveguides (i.e. waveguides whose width is equal to $0.66\sqrt{3}a$, where a is the period of the photonic crystal), by my colleague Z. Han [75].

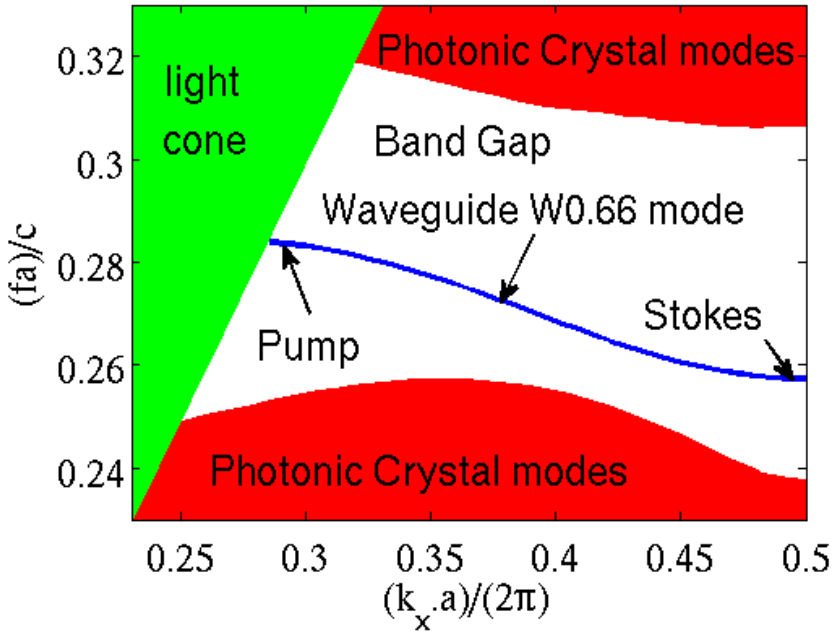

Figure 3.7: The band diagram of a waveguide W0.66 calculated using the software MPB. The locations of the pump and Stokes modes are shown on the band diagram. The difference between these two modes is almost equal to the Raman shift of 15.6 THz for a photonic crystal with a period equal to $a = 438$ nm.

The interest of these W0.66 waveguides compared to the W1 waveguides, in addition to the better containment of electromagnetic field due to the fact that they are narrower, is that their band diagram has two areas where the group velocity is almost zero, unlike W1 waveguides where there is only one of these areas, and where the interactions between light and matter are therefore maximum (and where the Raman scattering is therefore maximum). By selecting well the period of the photonic crystal, we can arrange for the frequency difference between these two areas of low group velocity to be almost equal to the Raman shift in silicon of 15.6 THz [75]. One of these areas can then be used for the pump laser mode, and the other for the Stokes mode (see Fig. 3.7). Due to the mismatch between the modes of the W0.66 waveguide and the ridge access waveguides, the W0.66 waveguide will behave like a Fabry-Perot cavity and will present a large number of resonance peaks on its transmission spectrum, so that it will be relatively easy to find two resonances corresponding to the frequencies selected for the pump and Stokes modes.

As we saw in section 1.4.3 of Chapter 1, the characteristic volume of Raman scattering varies with the direction of propagation (i.e. the direction of the wave vector) of the electromagnetic waves relative to the orientation of the crystal lattice of silicon. If we calculate the Raman volume for one period of the W0.66 waveguide using the formula 1.69 for different directions of the waveguides, then we can see that the size of this volume is minimal when the wave vector of the pump laser is parallel to the crystallographic direc-

tion [100] of silicon, and the Raman gain G_r will then be maximum in this direction. For example, for the direction [100] of silicon, the Raman volume is 0.1 μm^3 over one period of the W0.66 waveguide, compared to 0.16 μm^3 for the direction [110] of silicon, which is the direction normally used to maximize Raman scattering in W1 waveguides [21, 75]. Our structures and cavities based on W0.66 waveguides will therefore be oriented in the direction [100] of silicon in order to maximize the Raman gain.

Stimulated Raman scattering was measured in a W0.66 waveguide at the IEF by my colleague Zheng Han just before the beginning of my thesis [75, 21]. This measurement was performed in a W0.66 waveguide of length 50 microns with a period of 438 nm. The chosen pump and Stokes resonances had for quality factors $Q_p = 2400$ for the pump and $Q_s = 18000$ for the Stokes. However, even if we could observe the beginning of stimulated Raman scattering in this waveguide, it was obviously still well below the threshold required to obtain a Raman laser, which was for this waveguide of 31 mW for the output pump power when one neglects the other nonlinear effects, especially the two-photon and free-carrier absorptions, which gives us an unrealistic input pump power when using a continuous pump laser.

In fact, the pump power that we can send inside the cavity is limited by the poor heat dissipation of the tapers of the access waveguides : if we increase too much the laser input power, the taper may melt, thus destroying the entrance of the access waveguide and making the sample useless. If we want to obtain a Raman laser, we must first try to reduce the threshold of this Raman laser. We have seen that when we neglect other nonlinear effects, we have above the laser threshold $N_p \sim 1/(\tau_s G_r)$, which gives us a threshold value for the pump power at the exit of the photonic crystal of $P_{p_{out}}^{seuil} = \frac{\sqrt{T_{pmax}}}{2\tau_p} \frac{\hbar\omega_p}{\tau_s G_r}$, which gives us, using the formula $G_r = \frac{c^2}{n_0^2} \frac{\hbar\omega_p g_R^B}{V_R}$, a threshold power of $P_{p_{out}}^{seuil} = \frac{n_0^2}{c^2} \frac{\sqrt{T_{pmax}}}{2\tau_p\tau_s} \frac{V_R}{g_R^B}$. There are two ways to reduce the Raman threshold : one is to increase the value of the Raman gain G_r, which we can only do by decreasing the Raman volume V_r, which can be done either by optimizing the overlap between the pump modes and Stokes or by decreasing the length of the waveguide, and the other is to increase the lifetimes $\tau_p = \frac{Q_p}{\omega_{p_0}}$ and $\tau_s = \frac{Q_s}{\omega_{s_0}}$ of the pump and Stokes photons, which can only be done by increasing the values of the quality factors of the pump and Stokes resonances.

We initially tried to increase the quality factors of the pump and Stokes resonances by increasing the length of the waveguides, from a length of 50 microns to a length of 100 microns, although this method has the disadvantage of doubling the size of the Raman volume. Nevertheless, we managed to double the quality factor of the pump and to multiply by ten the quality factor of the Stokes, which allowed us to divide by ten the theoretical threshold value, even if the Raman volume increases. We measured Raman scattering in two waveguides of length 100 microns. These new waveguides were slightly narrower, being W0.63 waveguides, i.e. with a width $0.63\sqrt{3}a$, with a the period of the photonic

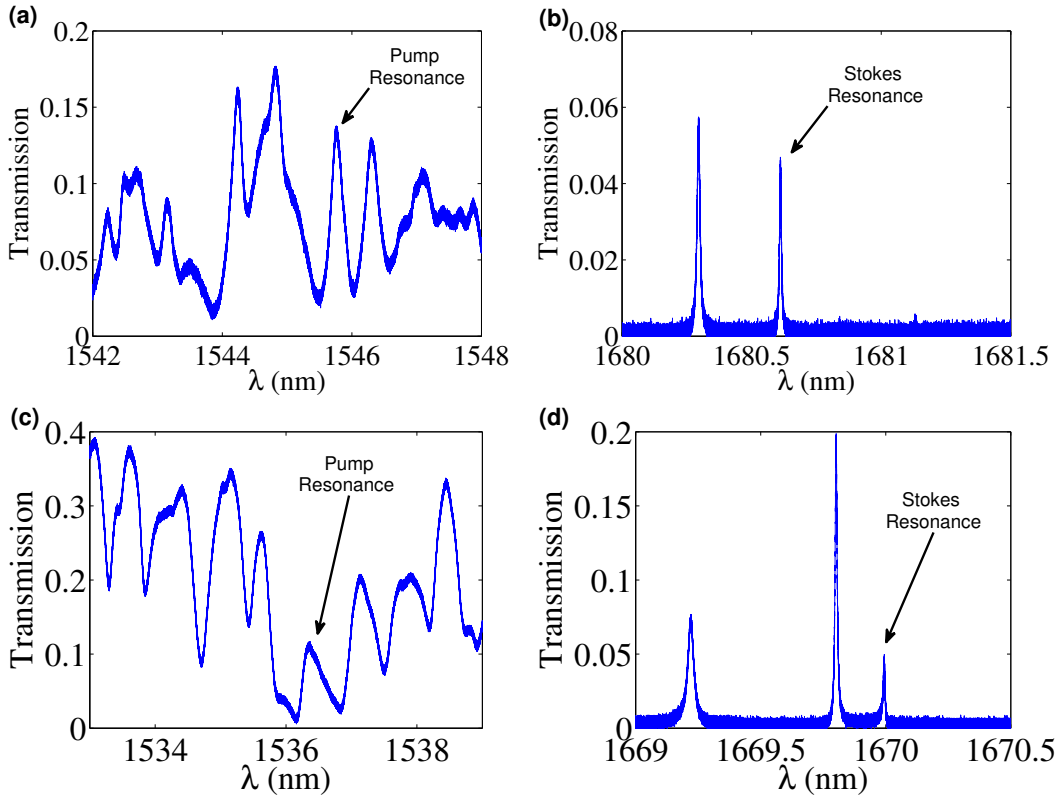

Figure 3.8: Pump and Stokes resonances chosen for the W0.63 waveguides of length 100 microns that we measured. (a) The transmission spectrum of the first waveguide for the pump resonance : its wavelength is $\lambda_{p_0} = 1545.74$ nm, its quality factor $Q_p = 7300$, and its maximum transmission $T_p = 0.135$. (b) The transmission spectrum of the first waveguide for the Stokes resonance : its wavelength is $\lambda_{s_0} = 1680.475$ nm, its quality factor $Q_s = 207000$, and its maximum transmission $T_s = 0.046$. (c) The transmission spectrum of the second waveguide for the pump resonance : its wavelength is $\lambda_{p_0} = 1536.35$ nm, its quality factor $Q_p = 4200$, and its maximum transmission $T_p = 0.1$. (d) The transmission spectrum of the second waveguide for the Stokes resonance : its wavelength is $\lambda_{s_0} = 1669.79$ nm, its quality factor $Q_s = 220000$, and its maximum transmission $T_s = 0.05$.

crystal, rather than W0.66 weveguides. As for the previous waveguide, these two waveguides had many Fabry-Perot resonances, due to the mismatch between the modes of the W0.63 waveguide and those of the ridge access waveguides.

The first waveguide we measured had for period of the photonic crystal 444 nm, and the resonance that we chose for the Stokes had for wavelength $\lambda_{s_0} = 1680.475$ nm, with a quality factor $Q_s = 207000$ (ten times larger than for the waveguide of length 50 microns) and a maximum transmission $T_s = 0.046$ between the entrance and the exit of the photonic crystal (see Fig. 3.8b). The closer resonance to the "ideal" pump frequency " $f_{s_0} + f_R$ (with $f_R = \omega_R/(2\pi) = 15.6$ THz the frequency of the Raman shift) had for wavelength $\lambda_{p_0} = 1545.74$ nm, with a quality factor $Q_p = 7300$ and a maximum transmission $T_p = 0.135$ between the entrance and the exit of the photonic crystal (see Fig. 3.8a). If we choose to pump this resonance, then we will have a detuning between the wavelength of the resonance Stokes λ_{s_0} and the wavelength corresponding to the maximum Raman gain λ_s equal to $\triangle\lambda_s = \lambda_s - \lambda_{s_0} = 0.47$ nm. This detuning is probably the reason why we were only able to observe spontaneous Raman scattering in this waveguide, and no stimulated Raman scattering (see Fig. 3.10), since the full width at half maximum of the Raman gain peak is about 1 nm.

The second waveguide that measured had for period of the photonic crystal 440 nm, and the resonance that we chose for the Stokes had for wavelength $\lambda_{s_0} = 1669.79$ nm, with a quality factor $Q_s = 220000$ and maximum transmission $T_s = 0.05$ between the entrance and the exit of the photonic crystal (see Fig. 3.8d). The closer resonance to the "ideal" pump frequency$f_{s_0} + f_R$ (with $f_R = \omega_R/(2\pi) = 15.6$ THz the frequency of the Raman shift) had for wavelength $\lambda_{p_0} = 1536.35$ nm, with a quality factor $Q_p = 4200$ and maximum transmission$T_p = 0.1$ between the entrance and the exit of the photonic crystal (see Fig. 3.8c). If we choose to pump this resonance, then we will have a detuning between the wavelength of the resonance Stokes λ_{s_0} and the wavelength corresponding to the maximum Raman gain λ_s equal to $\triangle\lambda_s = \lambda_s - \lambda_{s_0} = 0.057$ nm, much better than for the previous waveguide. It is in this waveguide that we observed the stimulated Raman scattering (see Fig. 3.11).

The measurements we did for our waveguides of length W0.63 were performed using a continuous tunable pump laser, which we connected to an erbium-doped fiber amplifier to obtain the input power necessary to do the measurements. A band-pass filter centered on the pump wavelength removes the noise due to the erbium amplifier, before sending it to the W0.63 waveguide. A portion of the collected output signal is redirected using a coupler to a powermeter to measure the output pump power. The rest of the output signal is sent to a band-pass filter centered on the Stokes wavelength, which allows us to remove the output power at the pump frequency and retain only the Raman scattering, before being sent to an optical spectrum analyzer that will allow us to measure the output

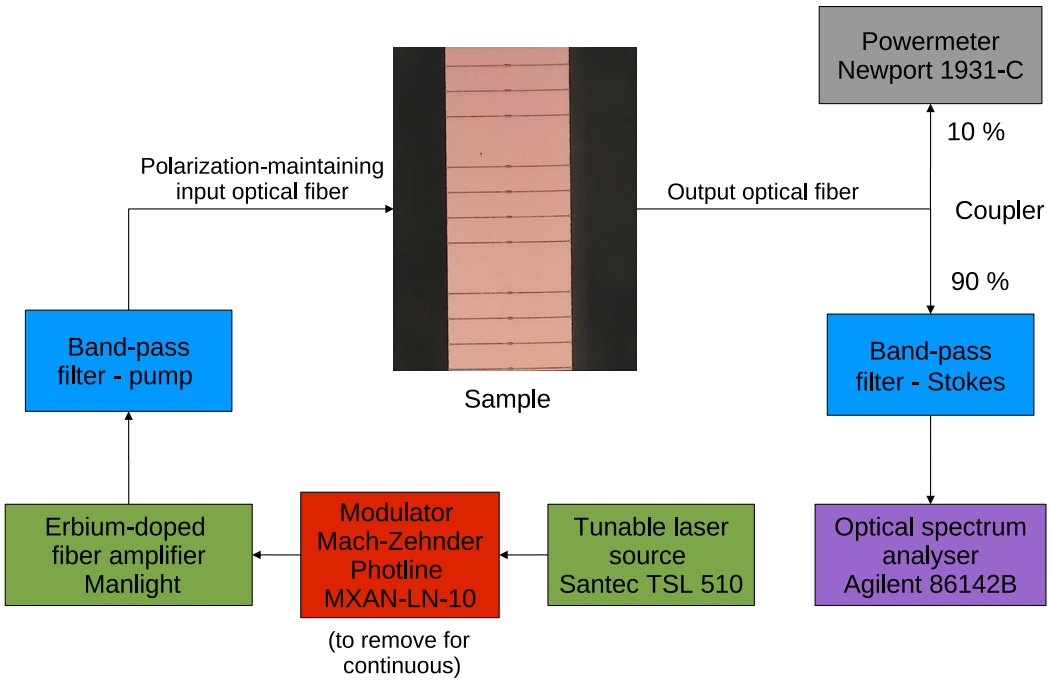

Figure 3.9: Diagram of the setup used to measure the Raman scattering in our photonic crystals W0.63 waveguides.

power collected at the Stokes wavelength (see Fig. 3.9). We then added to this device a Mach-Zehnder modulator in order to perform measurements with a pulsed laser (similar to the method used in Chapter 2 of this thesis for the self-pulsing measurements), which allowed us to raise the power of the pump laser even higher without risking to melt the input taper. We were thus able to make measurements with pulses of length 50 ns, 25 ns and 12.5 ns, repeated every 100 ns.

The measures on the second waveguide where we observed stimulated Raman scattering were first carried out for a pump wavelength of $\lambda_p = 1536.30$ nm, for which we theoretically have $\triangle\lambda_s = \lambda_s - \lambda_{s_0} \simeq 0$ nm. Unfortunately, the results of the measurements made on the waveguide of the length 100 microns are not as good as the ones made on the waveguide of length 50 microns. The plot of the Stokes power at the cavity exit as a function of pump power at the cavity entrance is in conformity with the theoretical model of the Raman laser : The Stokes power increases non-linearly with the input pump power initially, indicating the presence of stimulated Raman scattering, but saturates at high power when the other non-linear effects, and particularly the absorption effects and the thermal dispersion they generate, become larger than the Raman scattering (see Fig. 3.11c). However, when the input pump power is sufficiently high, the pump power at the cavity exit begins to fall (see Fig. 3.11a) as the Stokes output power continues to slowly increase, resulting in a folding of the plot of the output Stokes power as a function of the output pump power (see Fig. 3.11b) : for the same value of $P_{p_{out}}$, we have two values of $P_{s_{out}}$, which is not predicted by the model of the Raman laser (see Fig. 3.3a). This phenomenon can be observed both with the continuous and with the pulsed modes of the pump laser.

There are several possible explanations for this phenomenon. The first is that the model that we have developed being for a nanocavity, i.e. small enough so that the complex amplitude $A(t)$ of the envelope of the electric field can be considered to be the same in the entire cavity. A waveguide of length 100 microns being much larger than a typical nanocavity, it is possible that this assumption is no longer valid, and that our model can therefore not model very well the behavior of a waveguide of length 100 microns. We should probably rather seek a solution for the complex amplitude of the form $A(x,t)$, with an electric field $\overrightarrow{E}(\overrightarrow{r},t) = A(x,t)\overrightarrow{E}_0(x,y,z)e^{-i\omega t}$, where $\overrightarrow{E}_0(x,y,z)$ is periodic in x with a period a and represents the profile of the electric field over one period of the W0.63 waveguide. The second explanation is also linked to the greater length of the waveguide : it is possible that, because of the imperfections of the electron beam lithography, the width of the waveguide, or the diameter of the holes in the photonic crystal, are not homogeneous throughout the waveguide, creating a micro-cavity within this waveguide every time these defects are too large, which would disrupt the overall behavior of the waveguide. The greater length of the waveguide compared to a nanocavity will indeed

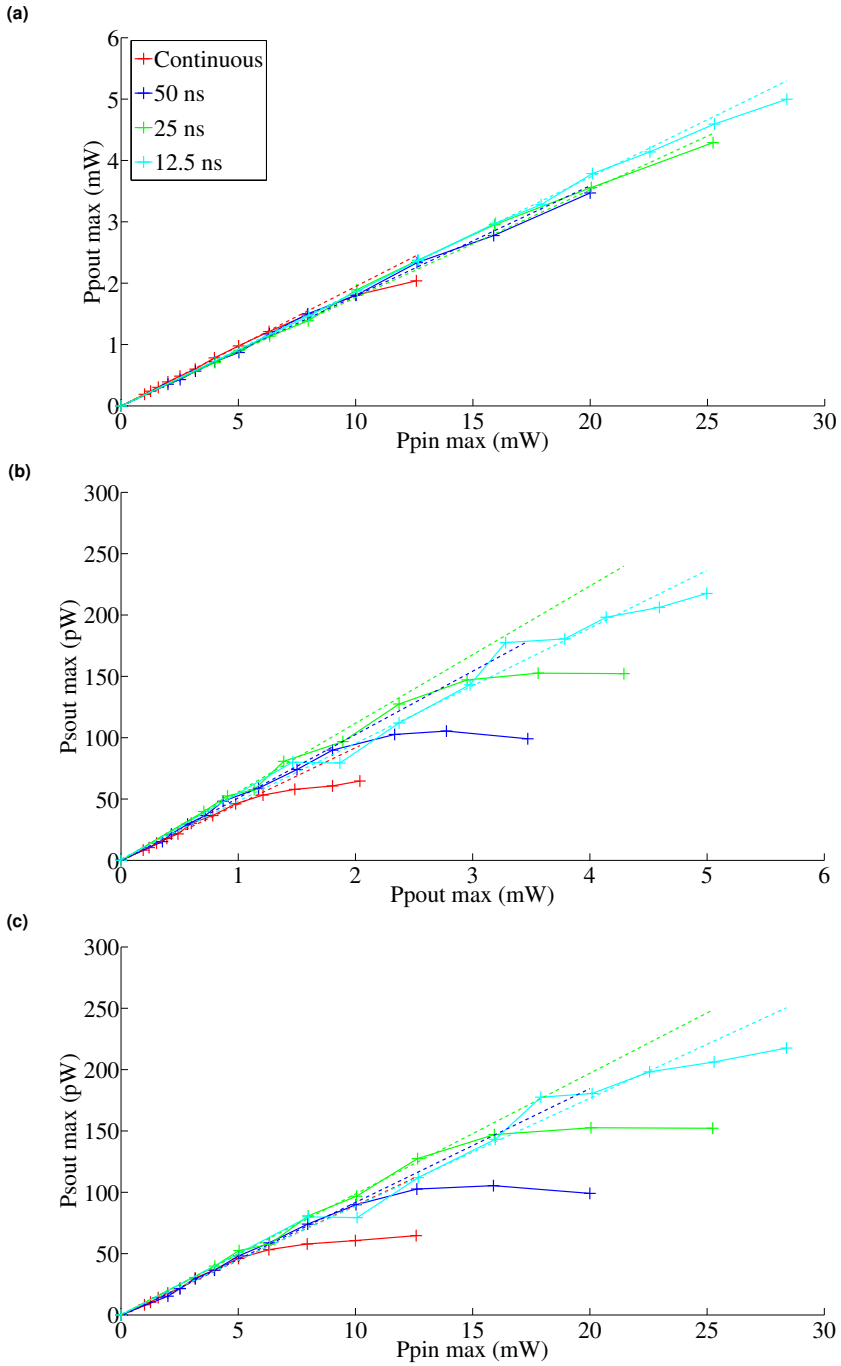

Figure 3.10: Raman scattering measurements in the first W0.63 waveguide of length 100 microns, for a continuous laser and for pulses of lengths of 50 ns, 25 ns and 12.5 ns, repeated every 100 ns. The values shown for the pulsed measurements for the pump power $P_{p_{in}}$ at the entrance of the photonic crystal correspond to the peak powers of these pulses, and the values for the pump and Stokes powers at the exit of the photonic crystal $P_{p_{out}}$ and $P_{s_{out}}$ are the powers averaged on the duration of these pulses. (a) $P_{p_{out}}$ as a function of $P_{p_{in}}$. (b) $P_{s_{out}}$ as a function of $P_{p_{out}}$. (c) $P_{s_{out}}$ as a function of $P_{p_{in}}$. The solid curves represent the measurements made on the waveguide, and the dashed curves are linear adjustments made using the first measured five points (the slight differences between these adjustments for (b) and (c) are due to the important noise on the measures of the output Stokes power, which causes slight uncertainty on the values of this power). Only spontaneous Raman scattering can be observed.

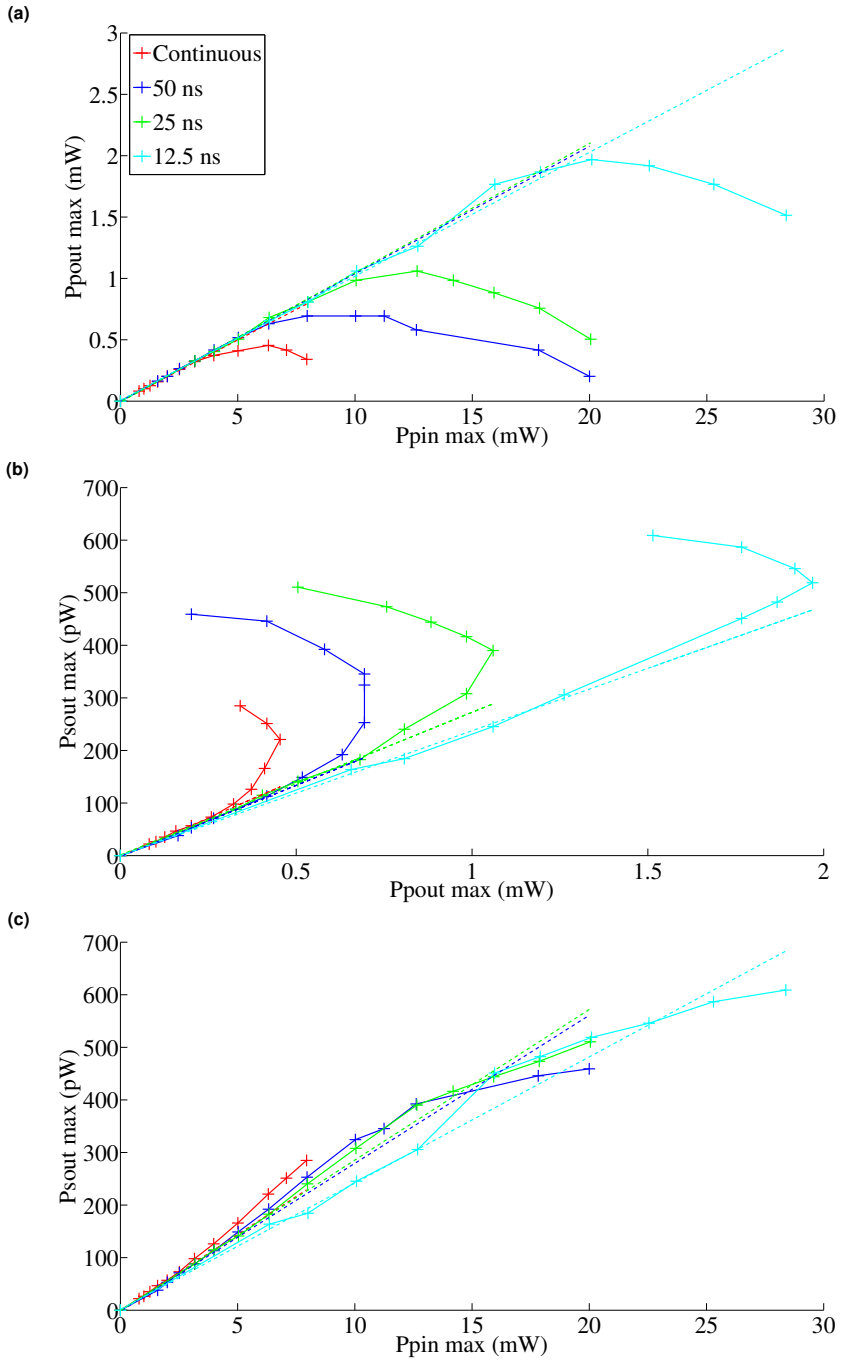

Figure 3.11: Raman scattering measurements in the second W0.63 waveguide of length 100 microns, for a continuous laser and for pulses of lengths of 50 ns, 25 ns and 12.5 ns, repeated every 100 ns, for a pump laser wavelength $\lambda_p = 1536.30$ nm. (a) $P_{p_{out}}$ as a function of $P_{p_{in}}$. (b) $P_{s_{out}}$ as a function of $P_{p_{out}}$. (c) $P_{s_{out}}$ as a function of $P_{p_{in}}$. We can note both the obvious presence of stimulated Raman scattering in figures (b) and (c), but also the behavior which was not predicted by the model of $P_{s_{out}}$ as a function of $P_{p_{out}}$.

increase the likelihood to have one of these defects present within the waveguide. It could mean, for example, that the output pump power is not proportional to the energy in the waveguide, but decreases because of a defect just at the exit of this waveguide. Another observation we can make is that the resonance used to pump the second waveguide seems asymmetrical, and that it is therefore not a Lorentzian peak as we assumed it to be in our modeling, and that we should perhaps also modify our equations to take this into account.

We can notice that, in all cases, we obtain values for the measured output Stokes power $P_{s_{out}} = \frac{\sqrt{T_{s_{max}}}\hbar\omega_s N_s}{2\tau_s}$ corresponding to a number of Stokes photons N_s present within the guide going up to 9 photons, which shows that we are already in a case in which the stimulated Raman scattering coefficient $G_r N_p N_s$ predominates over the spontaneous Raman scattering coefficient $G_r N_p$, i.e. in which we have $N_s > 1$. Could we therefore consider that the second waveguide is a Raman laser, that we are above the threshold when $N_s > 1$, and that only the other nonlinear effects prevent us from obtaining a number of Stokes photons higher than 10 ? It is hard to say. The beginning of the curves looks indeed a little like a laser. But although nanolasers with photon numbers less than 10 have already been demonstrated [81], those had threshold power much lower than ours (in the microwatt range), and worked well above threshold. To be useful, a Raman laser should have a number of Stokes photons well over 10, especially with a threshold power in the milliwatt range. In the Raman nanolaser presented by Takahashi [2] and studied later in section 3.3.3, the number of Stokes photons in the cavity can go up to 8000 photons. It is therefore hard to say that we obtained a real laser effect in our second waveguide, despite the fact that the stimulated Raman scattering predominates. However, this result is very encouraging, showing that we are very close to obtaining a Raman laser.

We also conducted a second series of measurements, for pulses of duration 25 ns repeated every 100 ns, by varying the wavelength of the pump laser, to ensure that we were truly at the maximum of the Raman gain. This was not entirely the case, as we got more Stokes power for a pump wavelength of 1536.25 nm than for the pump wavelength previously used of 1536.30 nm (see Fig. 3.12). It is therefore likely that we actually have $\triangle\lambda_s = \lambda_s - \lambda_{s_0} \simeq 50$ nm when $\lambda_p = 1536.30$ nm instead of $\triangle\lambda_s \approx 0$ nm as we thought previously. This suggests an alternative explanation for the behavior of the waveguide for $\lambda_p = 1536.30$ nm instead of stimulated Raman scattering : When the input pump power is high enough, the pump and Stokes resonances will shift toward the red (toward higher wavelengths) due to the thermal dispersion, increasing the negative detuning $\triangle\lambda_p = \lambda_p - \lambda_{p_0}$ between the wavelengths of the laser and the pump resonance and decreasing the output pump power, but also decreasing the detuning $\triangle\lambda_s$ between the Stokes wavelength and the Stokes resonance, thus allowing for an increase of the Stokes power. But this change of the wavelength is only of 50 pm, which is very small compared to the width of the Raman gain peak, and therefore results in an increase of the Raman gain

fairly small, and it does not explain why the value of $P_{s_{out}}$ as a function of $P_{p_{out}}$ increases so much when the pump wavelength is changed (although this could be an explanation for the slight increase of $P_{s_{out}}$ as a function of $P_{p_{in}}$). We can see that in the case where we get the most Raman power (for a pump wavelength of 1536.25 nm), the plot of $P_{s_{out}}$ as a function of $P_{p_{out}}$ behaves almost like the plot of a Raman laser ($P_{p_{out}}$ remains constant above a certain value of the input power but $P_{s_{out}}$ continues to increase), although this is not the case for $P_{s_{out}}$ as a function of $P_{p_{in}}$, where we hardly see the stimulated Raman scattering on this curve, and although we would expect $P_{s_{out}}$ to increase much faster if it really was a Raman laser.

I then tried to compare the results of the continuous measurements with the curves obtained by performing simulations with MATLAB using the equations of a doubly resonant cavity presented in section 1.4.3. I chose to look at the results for the continuous measurements rather than the pulsed ones as they are easier to simulate and more accurate because they don't take into account the transient response that we will have for a pulsed pump laser, and look only at the steady-state values. These simulations have been performed by changing the equations 3.9, 3.10 and 3.11 on the steady-state values of N_s, N_p, N_e and $P_{p_{in}}$ to include the free-carrier and thermal dispersions. We first performed these simulations by taking the characteristic volumes for the Raman and two-photon absorption calculated with MEEP for one period of a W0.63 waveguide and multiplying them by the number of periods of the waveguide of length 100 microns (another possibility to calculate these characteristics volumes which is theoretically more accurate, would have been to simulate the whole W0.63 waveguide with MEEP, which would take too much time for a waveguide of length 100 microns and has therefore not been done. However, a simulation with MEEP of an entire waveguide W0.63 of length 50 microns, with a period of 444 nm, gave us a Raman volume $V_R^{ens} = 12.9\ \mu m^3$, which is very close to the value given by multiplying the Raman volume of one period by the number of periods of the waveguide : $V_R = 112 \times 0.105 = 11.8\ \mu m^3$, so it is likely that there would have been no big difference in the case of the waveguides of length 100 microns). I took $\tau_{fc} = 0.3$ ns for the free-carrier lifetime and then adjusted the value of the Raman gain $G_r = \frac{c^2}{n_0^2} \frac{\hbar \omega_p g_R^B}{V_R}$ to fit the simulated Stokes power with the Stokes power we measured at low power (which corresponds in theory to the spontaneous Raman scattering, as long as the number of Stokes photons in the waveguide stay below 1). We obtained this way $G_r \simeq 2.4 \times 10^4\ s^{-1}$ for the first waveguide and $G_r \simeq 8.2 \times 10^4\ s^{-1}$ for the second waveguide. Unfortunately, these values are problematic. First, if the Raman gain was really that high, then our two waveguides would be lasing according to our simulations (which is not the case) well before the values of the pump power for which we observed the stimulated Raman scattering in our second waveguide (see Fig. 3.13). In addition, with the Raman volumes we calculated for the waveguides ($V_r = 23.7\ \mu m^3$ for the first waveguide and $V_r = 23.5\ \mu m^3$ for the second waveguide), it would give us a value for the Raman gain in the bulk silicon of $g_R^B = 60$

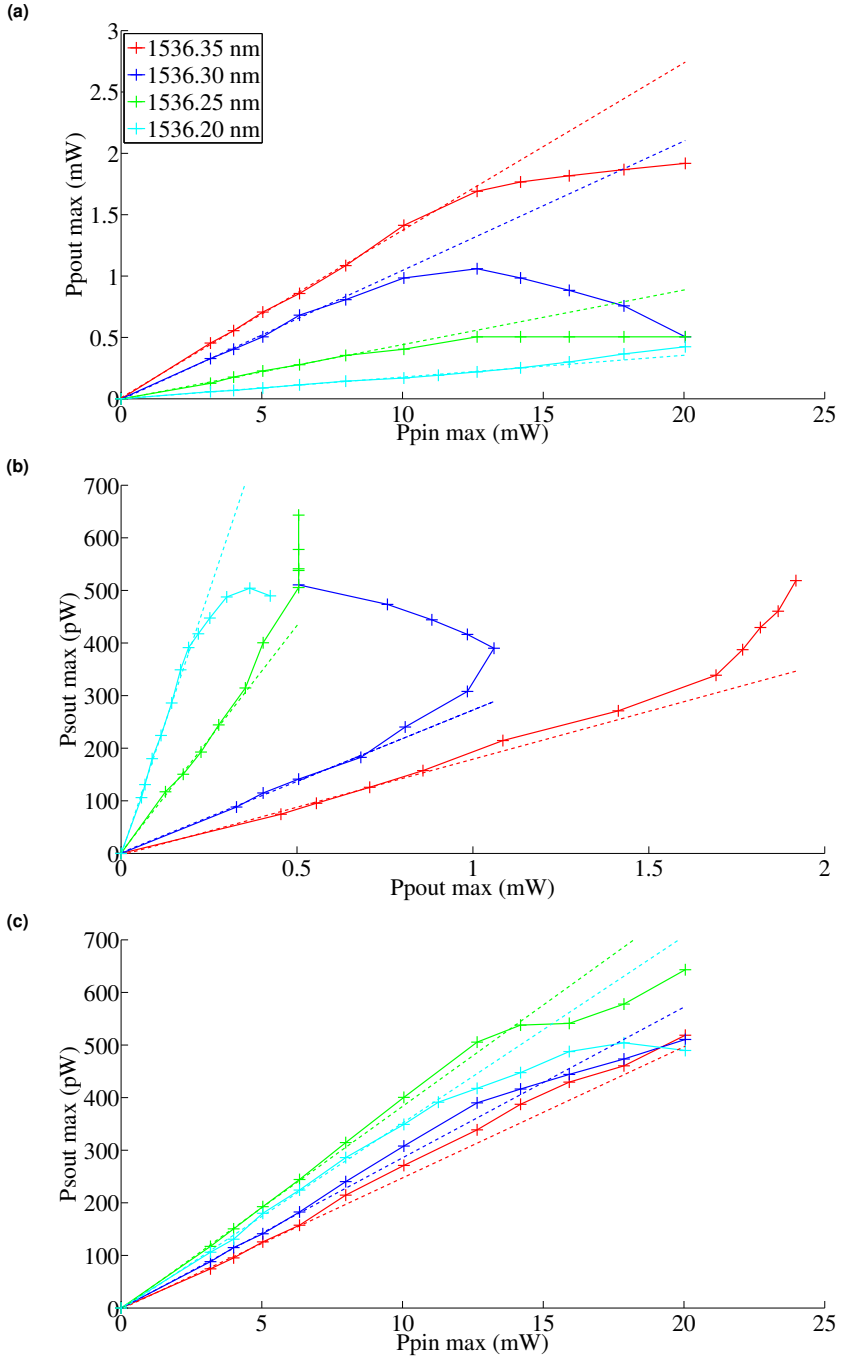

Figure 3.12: Raman scattering measurements in the second W0.63 waveguide of length 100 microns, for pulses of duration 25 ns repeated every 100 ns, for different pump wavelengths. (a) $P_{p_{out}}$ as a function of $P_{p_{in}}$. (b) $P_{s_{out}}$ as a function of $P_{p_{out}}$. (c) $P_{s_{out}}$ as a function of $P_{p_{in}}$. We get more Raman power for a pump wavelength of 1536.25 nm than for the previously used pump wavelength of 1536.30 nm.

Volumes	1er guide (FDTD)	1er guide (simu)	2e guide (FDTD)	2e guide (simu)
V_R	23.7 μm^3	$\simeq$ 10.2 μm^3	23.4 μm^3	$\simeq$ 4.2 μm^3
V_{TPA}^{pp}	13.5 μm^3	$\simeq$ 13.5 μm^3	13.3 μm^3	$\simeq$ 2.4 μm^3
$V_{TPA}^{ps} = V_{TPA}^{sp}$	13.6 μm^3	$\simeq$ 5.8 μm^3	13.5 μm^3	$\simeq$ 2.4 μm^3
V_{TPA}^{ss}	11.1 μm^3	$\simeq$ 4.8 μm^3	11.0 μm^3	$\simeq$ 2.0 μm^3
R_{eff}^{p}	1.22	1.22	1.22	1.22
R_{eff}^{s}	1.31	1.31	1.31	1.31
$V_{p_{eff}}^{FC}$	$\simeq$ 9.3 μm^3	$\simeq$ 3.7 μm^3	$\simeq$ 9.3 μm^3	$\simeq$ 0.56 μm^3
$V_{s_{eff}}^{FC}$	$\simeq$ 10.9 μm^3	$\simeq$ 0.72 μm^3	$\simeq$ 10.8 μm^3	$\simeq$ 0.65 μm^3
V_{eff}^{T}	$\simeq$ 60.0 μm^3	$\simeq$ 60.0 μm^3	$\simeq$ 60.0 μm^3	$\simeq$ 10.8 μm^3
τ_T	$\simeq$ 29.4 ns	$\simeq$ 14.7 ns	$\simeq$ 28.6 ns	$\simeq$ 18.5 ns

TABLE 3.1 – Comparisons between the characteristics volumes of the waveguides given by the FDTD simulations and used for the first series of simulations (are also given the values of the free-carrier and thermal effectives volumes and of the cooling time used for the first series of simulations), and the characteristic volumes obtained by fitting with the measured curves during the second series of simulations, taking $g_R^B = 30$ cm/GW.

cm/GW for the first waveguide and $g_R^B = 200$ cm/GW for the second waveguide. Not only are these values very different, but the second value is much higher than all the measured values of the Raman gain so far, and so is obviously false.

This confirms our hypothesis that our model describing the Raman scattering in doubly resonant cavities is not well suited to the description of this phenomenon in the W0.63 waveguides of length 100 microns. This also suggests that the Raman scattering takes place on much smaller volumes than those that we expected, for example in a micro-cavity created accidentally in the W0.63 waveguide by defects during the electron beam lithography. So we carried out a second series of simulations, setting the value of the Raman gain in silicon at $g_R^B = 30$ cm/GW and trying to adjust this time the Raman volume and the other characteristics volumes of the W0.63 waveguides (and their cooling time) to match as much as possible the simulations with the measurements. This way, we obtain a much better fit with the measurements, except for the last points of the curves (which was expected in the case of our second waveguide, because in this case we have two values of $P_{s_{out}}$ for the same value of $P_{p_{out}}$, which was not predicted by our model). We obtain this way much smaller Raman volumes than those provided by the FDTD : $V_r = 10.2$ μm^3 instead of $V_r = 23.7$ μm^3 for the first waveguide and $V_r = 4.2$ μm^3 instead of $V_r = 23.4$ μm^3 for the second waveguide (see Table 3.1). The values of the other characteristics volumes are much lower than those provided by the FDTD, which would confirm our hypothesis that the Raman scattering is happening in a micro-cavity created accidentally in the W0.63 waveguide by defects of the electron beam lithography rather than in the entire length of the waveguide. We can also note that these new simulations not only confirm the existence of stimulated Raman scattering in the second waveguide, but also

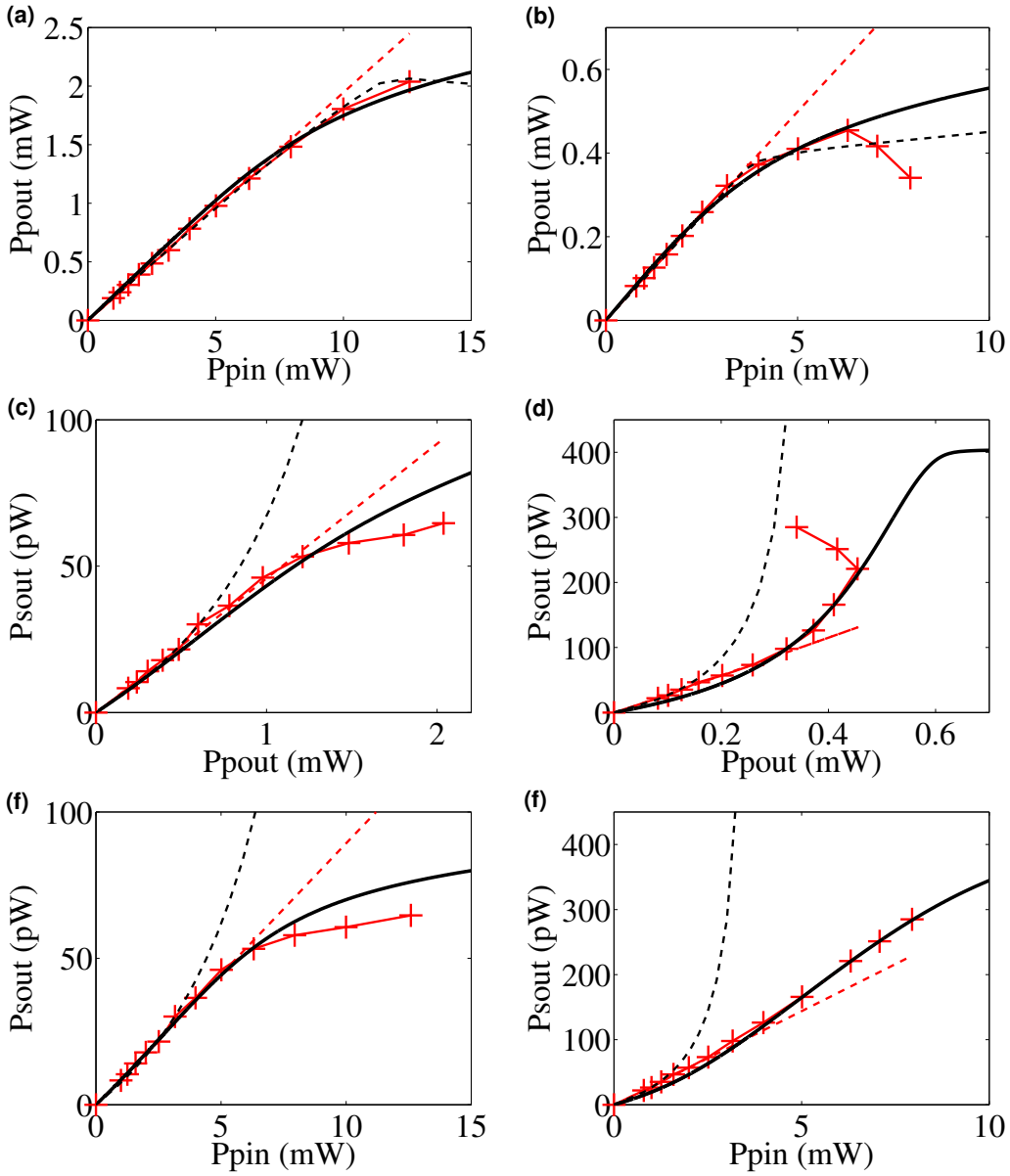

Figure 3.13: Comparison between the results of the measurements made on W0.63 waveguides with a continuous laser (red curves) and the simulations with MATLAB made using the equations of a doubly resonant nanocavity (black curves). The dotted red curves are linear adjustments made from the first five points measured. The black dotted curves correspond to the simulations made using the characteristic volumes calculated by the FDTD, adjusting only the value of the Raman gain. The solid black curves correspond to the simulations made by taking $g_R^B = 30$ cm/GW and then by adjusting the values of the Raman volumes and of the other characteristics volumes. (a) and (b) $P_{p_{out}}$ as a function of $P_{p_{in}}$ (a) for the first waveguide and (b) for the second waveguide. (c) and (d) $P_{s_{out}}$ as a function of $P_{p_{out}}$ (c) for the first waveguide and (d) for the second waveguide. (e) and (f) $P_{s_{out}}$ as a function of $P_{p_{in}}$ (e) for the first waveguide and (f) for the second waveguide.

the fact that we could not obtain a Raman laser in our W0.63 waveguides : the Stokes power will eventually saturate, with a value of N_s remaining below 10, and then will decrease in our simulations, despite the existence of stimulated Raman scattering.

The Raman gains of the waveguides have also slightly changed compared to those used for the first series of simulations : $G_r \simeq 2.8 \times 10^4\ s^{-1}$ instead of $G_r \simeq 2.4 \times 10^4\ s^{-1}$ for the first waveguide and $G_r \simeq 6.8 \times 10^4\ s^{-1}$ instead of $G_r \simeq 8.2 \times 10^4\ s^{-1}$ for the second waveguide, which results in a better agreement between simulations and measurements at high input power than at low input power for the second waveguide : the values given by the simulation are slightly below those given by the measurements (see Fig. 3.13). But it is possible that we overestimated the output Stokes power of the waveguide at low power. Indeed, we can notice in the figure 3.8 that there is another resonance very close in wavelength ($\simeq 0.2$ nm) to the resonance used for the Stokes. Given that the measures of the Stokes power were made with a spectrum analyzer set with a bandwidth of 1 nm, and that the Raman gain also has a width of 1 nm, it is possible that we measured the output Stokes power of this other resonance in addition to the Stokes resonance, artificially inflating the value of the Stokes power. A spectrum performed with the spectrum analyzer using a finer bandwidth, for pulses of duration 25 ns repeated every 100 ns, a pump wavelength of $\lambda_p = 1536.25$ nm and a pump power at the cavity entrance of $P_{p_{in}} = 11$ mW, suggests that this second resonance could contribute up to a third of the total Stokes power we measured (but we can see that even when we remove the Stokes power due to the second resonance, we still have a number of Stokes photons in the cavity going up to 6, so we are still in a regime where the stimulated Raman scattering predominates over the spontaneous Raman scattering).

However, even when the parasite Stokes power generated by the second resonance is removed, it is much more difficult to find a fit between the simulations and the curves measured in the pulsed regime than in the steady-state regime. In particular, we tried to simulate the behavior of the second waveguide for pulses of length 25 ns repeated every 100 ns and a pump wavelength of 1536.25 nm (which is the case where we got the most Raman power and where the curve was the closest to that of a Raman laser), when decreasing by a third the measured Stokes power to remove the parasite Stokes power generated by the second resonance, and taking values for the characteristics volumes similar to those used for the second series of simulations in the steady-state regime. Although these simulations give us output pump and Stokes powers that have the same order of magnitude as those measured, and curves whose behavior is quite close to the measured curves, it is impossible to adjust these values to obtain a fit between the measured and simulated curves that is as good as the one we got for the steady-state regime (see Fig. 3.14).

According to reference [82], the value of the Purcell factor for the Raman scattering in

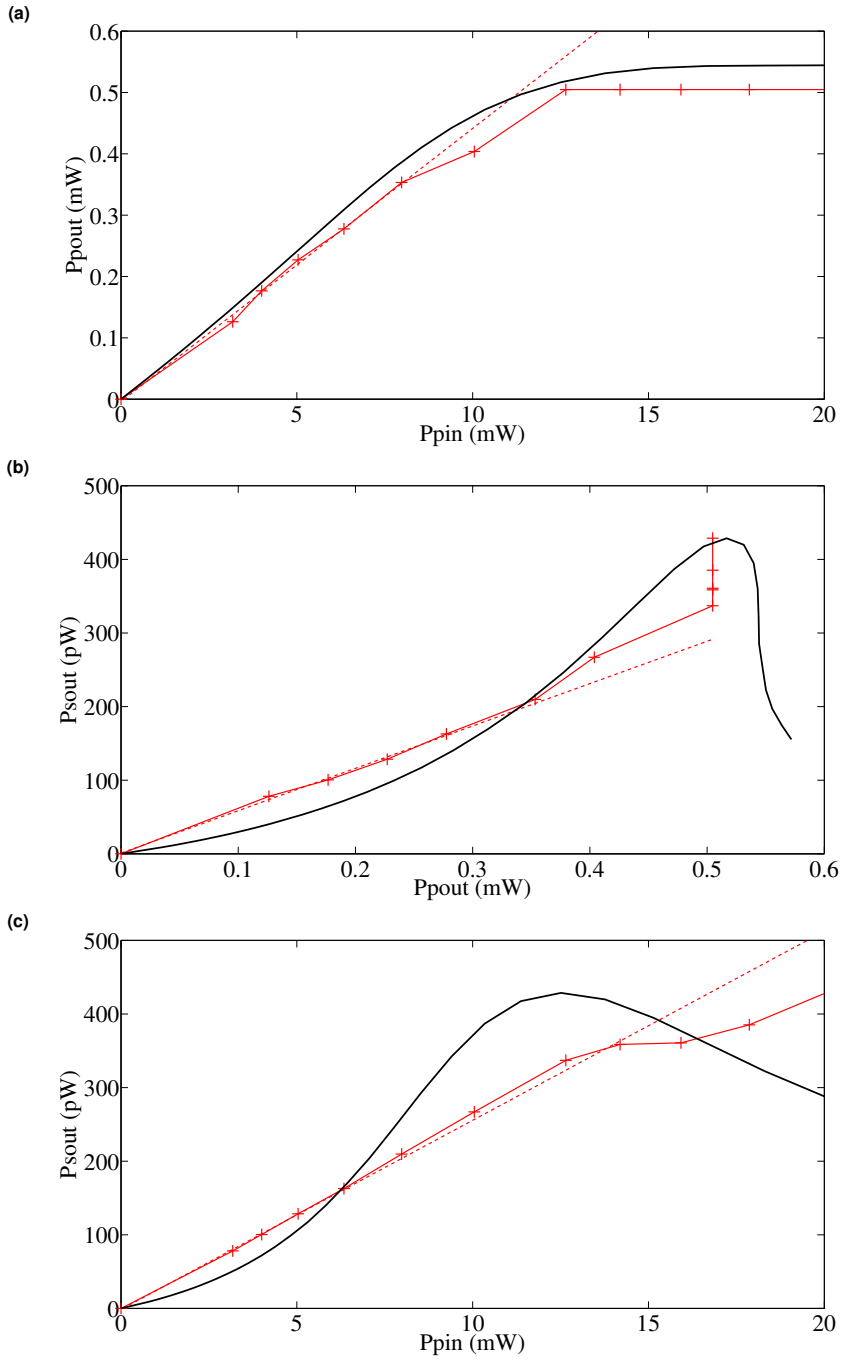

FIGURE 3.14 – Comparison between the results of the measurements made on the second waveguide for pulses of length 25 ns repeated every 100 ns and a pump wavelength of 1536.25 nm (red curves), and the simulations with MATLAB made from the equations of a doubly resonant nanocavity. The red dotted curves are linear adjustments made from the first five points measured. The black curves correspond to a simulation made by taking $g_R^B = 30$ cm/GW and adjusting the values of the Raman volume and of the other characteristics volumes. The measured Stokes power was reduced by a third to remove the parasite Stokes power generated by the second resonance. (a) $P_{p_{out}}$ as a function of $P_{p_{in}}$. (b) $P_{s_{out}}$ as a function of $P_{p_{out}}$. (c) $P_{s_{out}}$ as a function of $P_{p_{in}}$.

our waveguide is equal to $F_R = G_r \cdot \tau_R$, where $\tau_R = 1/\left(4\pi g_R^B hc^2 n_0 \left(2\pi \triangle f_R\right)/\left(3\lambda_p \lambda_s^2\right)\right)$ is the characteristic time of the spontaneous Raman emission in the bulk silicon. At low power, i.e. when $N_s \ll 1$, we have $N_s \approx \tau_s G_r N_p$ and $P_{p_{in}} \approx \frac{\hbar\omega_p N_p}{2\tau_p\sqrt{T_{max_p}}}$, and the Purcell factor can then be calculated from the measured output Stokes power by the formula $F_R = \frac{\tau_R}{\tau_p}\frac{\hbar\omega_p}{\hbar\omega_s}\frac{1}{\sqrt{T_{max_p}T_{max_s}}}\frac{P_{s_{out}}}{P_{p_{in}}}$. This gives us for the second waveguide a Purcell factor of $F_R = 2.5$ for the value of the Raman gain in bulk silicon $g_R^B = 30$ cm/GW we used in the second set of simulations. This measured value is in the same range as the theoretical value of the Purcell factor of the second waveguide $F_R = 1.68$, which we calculated from the formula $F_R = \frac{3}{8\pi^2}\frac{1}{V_R}\frac{Q_R Q_s}{Q_R+Q_s}\left(\frac{\lambda_s}{n_0}\right)^3$, where $Q_R = \left(c/\lambda_s\right)/\triangle f_R$ is the quality factor of the peak of the Raman gain [82], taking the Raman volume value we determined during the second series of simulations : $V_R = 4.2\ \mu m^3$ (of course, with the Raman volume $V_R = 23.4\ \mu m^3$ calculated by the FDTD simulation, we would have got a much smaller Purcell factor). The difference between the measured and theoretical values of the Purcell factor is due to the fact that we got a better agreement between our simulations and measurements at high power than at low power for the second waveguide in the second series of simulations, which is probably related to the fact that we overestimated the output Stokes power at low power by detecting the spontaneous power generated by the nearby second resonance as well. If we decrease by one third the measured Stokes power to remove this parasitic power, then we get for the new value of the Purcell factor $F_R = 1.65$, which is much closer to the theoretical value $F_R = 1.68$. This value is nevertheless higher than the one measured in the W0.66 waveguide of length 50 microns, which had a Purcell factor $F_R = 1.3$ [75]. Assuming that the Raman is emitted only in the Stokes resonance we used for the model, and that the spontaneous emission rate in the modes of the continuum is only slightly modified by the photonic crystal, this Purcell factor of $F_R = 1.65$ gives us for the spontaneous emission factor β_{sp} of the laser we would obtain from this waveguide a value of $\beta_{sp} \approx F_R/(F_R+1) = 0.62$. This value is much higher than for conventional semiconductor lasers (for example, in a quantum-well $In_{0.2}Ga_{0.8}As$/GaAs laser we typically have for the spontaneous emission factor $\beta_{sp} = 0.869 \times 10^{-4}$ [78]), but it is nevertheless of the same order of magnitude as for other semiconductor microlasers with particularly high Q/V_m ratios [81, 83]. Obviously, we should probably also take into account the spontaneous Stokes power generated by the second resonance next to this one to calculate the coefficient β_{sp}, which would decrease its value. If we assume that the Purcell factor of the second resonance F_{R_2} is of the same order of magnitude as the factor of the first resonance F_R, then we would have $\beta_{sp} \approx F_R/(F_R + F_{R_2} + 1) \approx F_R/(2F_R+1) = 0.38$.

Finally, since we have not been able to obtain a true Raman laser effect from the W0.63 waveguides of length 100 microns, we have instead tried to modify these waveguides in order to obtain a doubly resonant nanocavity with a quality factor for the Stokes resonance that would be as important as for the waveguides of length 100 microns, but whose length

(and Raman volume) would be much smaller, so we would not have the problems that have arisen in these waveguides and which were probably caused by their too great length.

3.3.2 Raman scattering in a doubly resonant cavity of length 12 periods.

To design our doubly resonant nanocavity, we started with a W0.63 waveguide with a period $a = 444$ nm for the photonic crystal, of a length corresponding to 12 periods of the photonic crystal. We then tried to turn this waveguide into a Fabry-Perot cavity by slowly narrowing it at each end until it reaches the width of a W0.47 waveguide, in order to to create a barrier and thus to form a cavity. This waveguide was then broaden to form a W0.65 waveguide of length 4 periods to facilitate the coupling between the cavity and the ridge access waveguides (see Fig. 3.15).

If we simulate the structure described above using the MEEP software and plot its transmission spectrum (see Fig. 3.16a), then we obtain for the Stokes resonance a wavelength $\lambda_s = 1674.74$ nm, with a quality factor $Q_s = 677000$ and a maximum transmission $T_s = 0.1$ between the entrance and the exit of the photonic crystal. Of course, this quality factor is for a perfect structure and the inaccuracies of the lithography mean that the real quality factor and the maximum transmission are likely to be lower : in fact, for the cavity in which we made the measurements, this quality factor of the Stokes resonance was only 235000 and its maximum transmission 0.028 (see Fig. 3.16b and Fig. 3.17b). Our nanocavity has some other resonances, although much less than the W0.63 waveguides. One of these resonances has a wavelength $\lambda_p = 1541.06$ nm, with a quality factor $Q_p = 2600$ and a maximum transmission $T_p = 0.19$ between the entrance and the exit of the photonic crystal. We have $f_p - f_s = \frac{c}{\lambda_p} - \frac{c}{\lambda_s} = 15.528$ THz, which is very close to the frequency of the Raman shift $f_R = 15.6$ THz. This resonance can therefore be used for the pump laser. All resonances of the structure do not necessarily correspond to the resonances of the nanocavity : some resonances are from the W0.65 waveguides used for coupling between the cavity and ridge waveguides. These coupling waveguides were indeed designed to be slightly larger than the W0.63 waveguide constituting the cavity, so that their resonances would not be identical to those of the cavity and would not interfere with its operation.

However, obtaining an actual difference between the pump and Stokes resonances precisely equal to the Raman shift is difficult because of the inaccuracy of the electron beam lithography. A small variation of the exposure dose can easily lead to a variation of this difference that is greater than the width of the Raman gain peak. To avoid this problem, we decided to make a series of cavities where we shifted the third row of holes of the photonic crystal on each side of a W0.63 waveguide between -21 nm and 21 nm by step

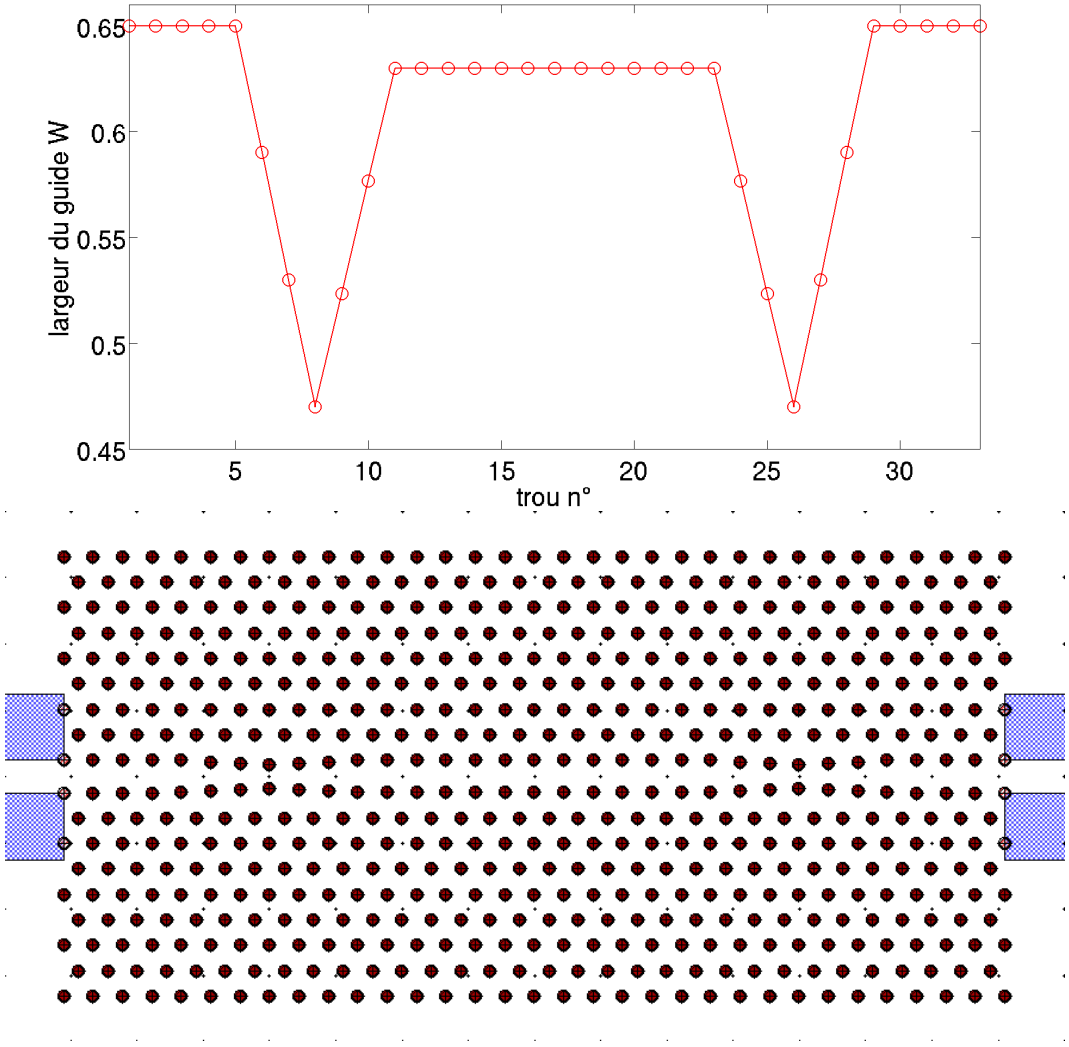

Figure 3.15: Up : The evolution of the width of the waveguide along the first row of holes in the photonic crystal. The cavity consists of 12 periods (or 13 holes) of a W0.63 waveguide of period 444 nm, which is then narrowed (over 3 periods) in order to reach the width of a W0.47 waveguide to confine the electromagnetic field and transform the W0.63 waveguide into a cavity. The guide is then broadened (also over 3 periods) and becomes a W0.65 waveguide with a length of 4 periods in order to obtain a better coupling with the ridge access waveguides. Down : The GDS mask used for the lithography of the cavity with the Nanobeam 4. The total length of the photonic crystal is 15 microns.

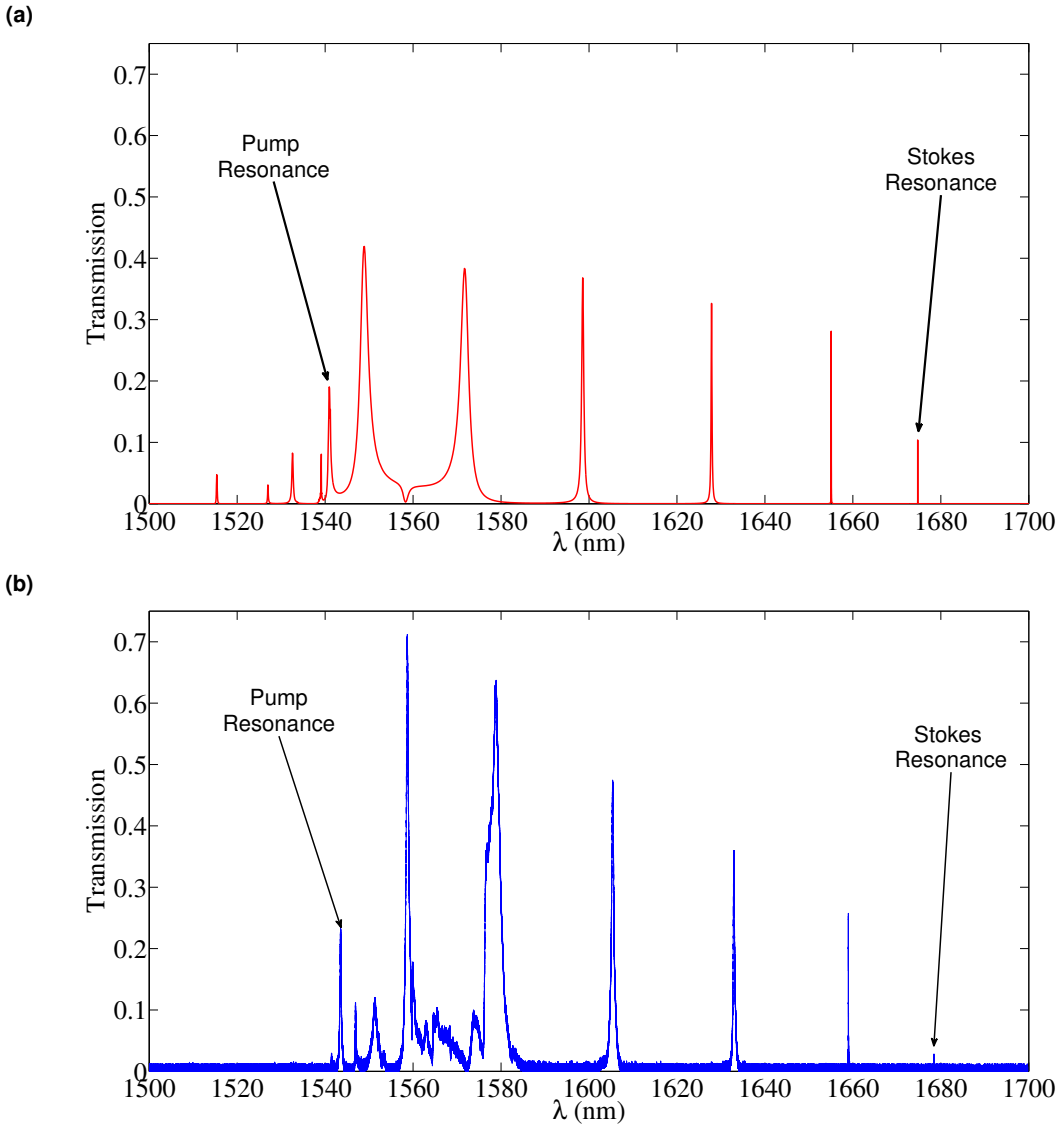

Figure 3.16: (a) The transmission spectrum of the cavity described in figure 3.15, calculated using the software MEEP. (b) The transmission spectrum of the cavity used for our measurements. We have indicated on the figure the resonances that we used for the pump and Stokes modes. We can see that we have quite a good agreement between simulation and measurement for the transmission. There are two main differences between the spectra : the first is that the maximum transmission of the Stokes and its quality factor were divided by three in the measured spectrum with respect to the simulated spectrum. The second is that the pump resonance of the measured spectrum does not match with the pump resonance of the simulated spectrum, but with a resonance located a little to the left on the simulated spectrum. But according to our FDTD simulations, the modes of these two resonances have the same pattern and give us almost identical Raman volumes, so this does not actually matter.

of 3 nm. This allowed us to tune the value of $|(f_p - f_s) - f_R|$ and obtain at least one cavity with $|(f_p - f_s) - f_R| \ll \triangle f_R$, where $\triangle f_R = 105$ GHz is the full width at half maximum of the Raman gain peak in silicon. This is actually the pump resonance frequency f_p which varies : the Stokes resonance frequency f_s is almost not influenced by the shift of the third row of holes. Indeed, the pattern of the Stokes mode is much more confined inside the cavity that the pattern of pump mode (see Fig. 3.18), and is therefore much less affected by this shift. On the other hand, the shift of the third row of holes changes the quality factors of both the pump and Stokes resonances : the quality factor given by our simulations varies between 2100 and 3100 for the pump resonance and between 920000 and 480000 for the Stokes resonance when the shift of the third row of holes varies between -21 and 21 nm. The measured quality factors also vary, between 2300 and 6700 for the pump resonance and between 635000 and 232000 for the Stokes resonance.

We have a fairly good agreement between the simulated transmission spectrum and the measured spectrum for our cavities (see Fig. 3.16). In fact, there are only two main differences between the curves : the first is that the maximum transmission of the Stokes and its quality factor were divided by three in the case of the cavity we measured relative to that of the simulated cavity. The second is that the resonance of the measured spectrum whose wavelength is closest to that of the pump does not match the resonance which was closest to the pump in the simulated spectrum, but corresponds to a resonance located a little to the left on the simulated spectrum. But this does not matter, because according to our FDTD simulations, the patterns of the modes of these two resonances are in fact the same and give us almost identical Raman volumes. These two differences can be explained either by the fact that the cavity we measured had a very slight shift of the third row of holes relative to the simulated cavity, or or by an actual radius of the holes slightly different from the $r = 0.25a$ (where a is the period of the photonic crystal) of the simulated cavity. Indeed, although we adjusted the difference between resonances by shifting the third row of holes, we might as well have adjusted it by varying the radius of the holes, which is the method that was used for the Raman nanolaser presented by Takahashi [2]. We decided not to do so because the quality factors of our cavity predicted by our simulations fell when the radius of the holes became too large or too small. It is also possible that these differences are a consequence of the change of the refractive index of silicon with the wavelength, which we have not taken into account in our equations.

We plotted the evolution of $f_p - f_s$ as a function of the shift of the third row of holes on the figure 3.19 for our simulations of the cavity with MEEP and for the series of cavities that we fabricated, taking for f_p the frequency of the resonance nearest to Raman shift when the shift of the third row of holes is zero (the curve of the simulations is incomplete because we have not been able to identify the pump resonance on the simulated transmission spectra for shifts of the third row of holes greater than 9 nm). We may note that

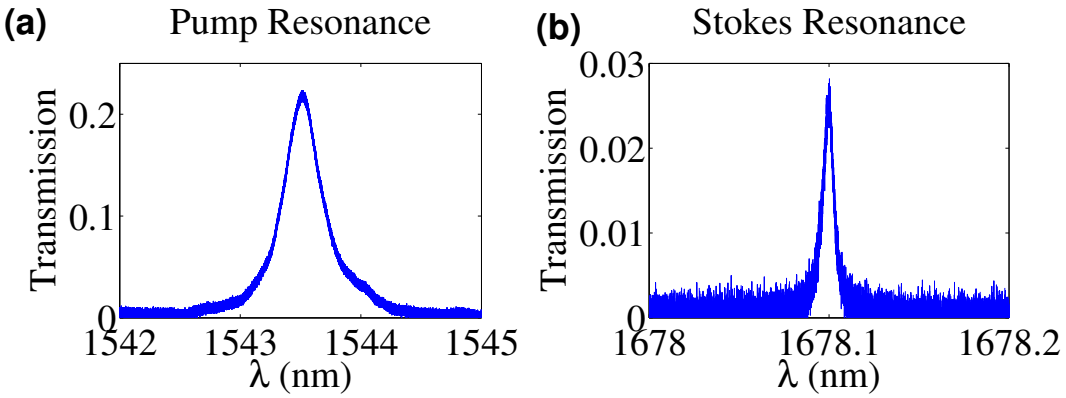

Figure 3.17: The pump and Stokes resonances chosen for our measurements. (a) The resonance used for the pump laser. Its wavelength is $\lambda_p = 1545.45$ nm, and its transmission measured at low power and quality factor are respectively $T_{p_{max}} = 0.218$ and $Q_p = 4900$. (b) The resonance used for the Stokes. Its wavelength is $\lambda_s = 1678.1$ nm, and its transmission measured at low power and quality factor are respectively $T_{s_{max}} = 0.028$ and $Q_s = 235000$.

although the two curves are very similar, the measured curve seems to be shifted compared to the simulated curve, which is probably due to the fact that the resonances we used for the pump were different, as we explained above. We can also see that the evolution of the difference between the resonances is much less regular for the measures than for the simulations, which is probably due to defects of the electron beam lithography.

For the series of cavities we made, the condition $|(f_p - f_s) - f_R| \ll \triangle f_R$ is only fulfilled for a shift of the third row of holes of $d_3 = 12$ nm, for which we have $|(f_p - f_s) - f_R| = 15$ GHz. For this cavity, the resonant wavelength of the pump resonance is $\lambda_p = 1545.45$ nm, with a measured transmission at low power $T_{p_{max}} = 0.218$ between the entrance and the exit of the cavity and a quality factor $Q_p = 4900$ (see Fig. 3.17a), and the resonance wavelength for the Stokes resonance is $\lambda_s = 1678.1$ nm, with a measured transmission at low power $T_{s_{max}} = 0.028$ and a quality factor $Q_s = 235000$ (see Fig. 3.17b), which is much higher than for the W0.66 waveguide of length of 50 microns mentioned in reference [75], but in the same range as for the W0.63 waveguides of length 100 microns that we measured previously. It is in this cavity we made our measurements, and it is the spectrum measured for this cavity that is shown in figure 3.16b.

The doubly resonant cavity described above has two main drawbacks when compared to a W0.63 waveguide. The first is that the transmission at the Stokes resonance is much lower than for a W0.63 waveguide, which is a consequence of the higher quality factor and of the narrowing of the waveguide needed to create the cavity. This makes it more difficult to detect and measure the Raman scattering. The second is the poor overlap between the modes of the pump and Stokes resonances (see Fig. 3.18) : The Stokes mode is indeed in the middle of the cavity, while the pump mode is located at the ends of the cavity, which

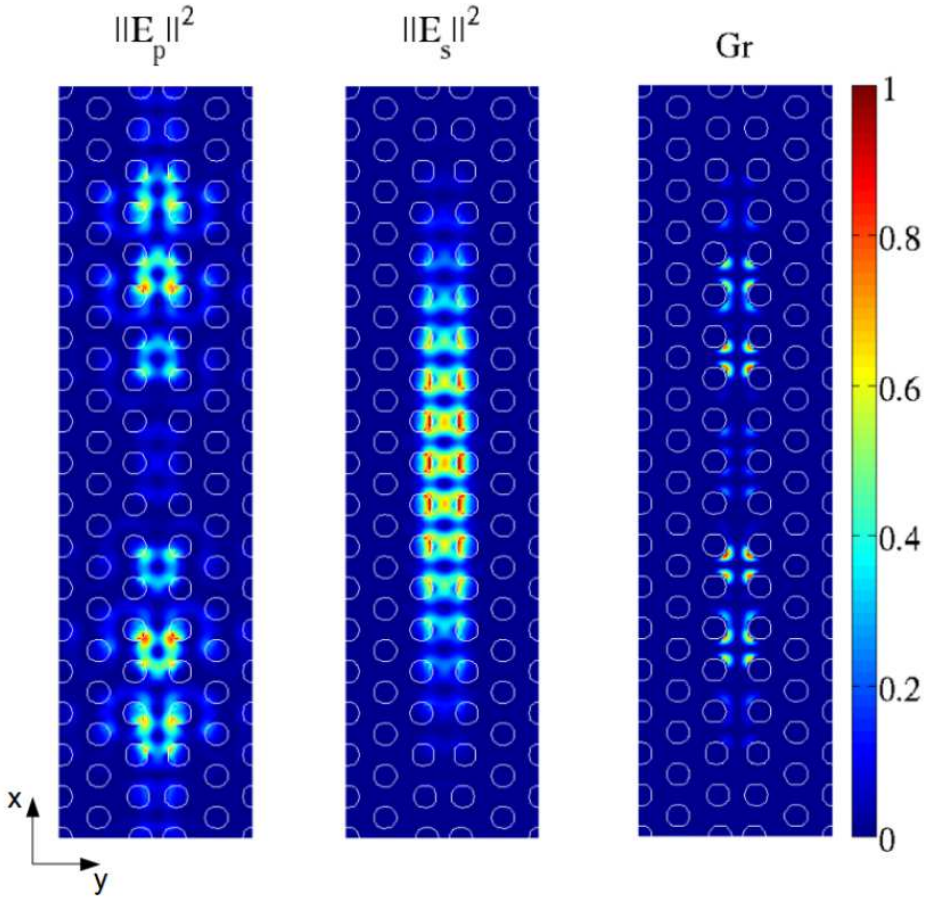

Figure 3.18: The patterns of the energy of the pump (left) and Stokes modes (middle), and of the Raman gain (right) in the doubly resonant cavity, calculated by FDTD using the MEEP software.

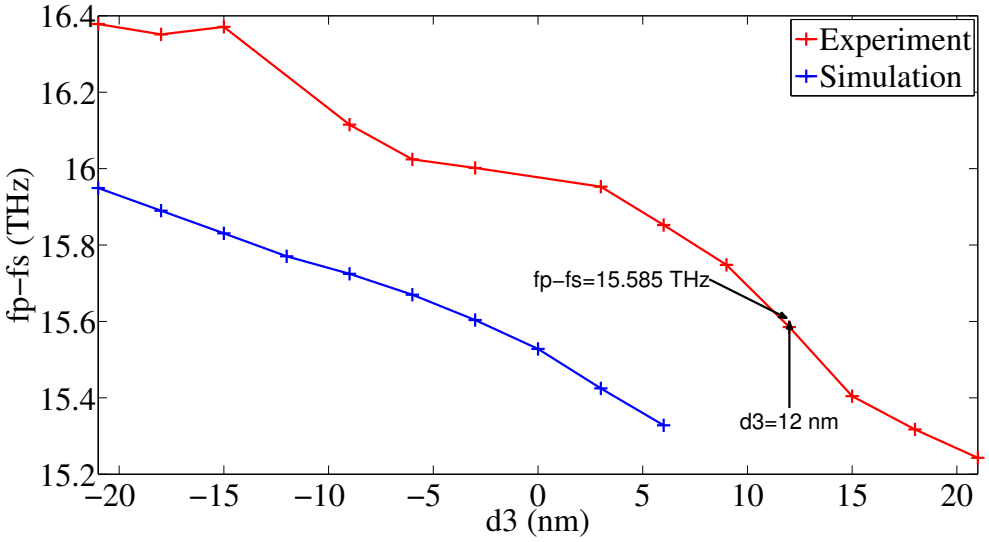

Figure 3.19: The difference between the pump and Stokes resonances as a function of the shift of the third row of holes. In blue : the difference obtained with our simulations using the MEEP software (values for $d_3 \geq 9$ nm are not shown because we have not been able to identify the pump resonance on the transmission spectra simulated with these shifts). In red : The difference measured on the series of cavities that we used to do the experiments. To obtain Raman scattering, we need to have $|(f_p - f_s) - f_R| \ll \triangle f_R$, with $\triangle f_R = 105$ GHz the full width at half maximum of the Raman gain peak. This condition is fulfilled for a shift of the third row of holes equal to $d_3 = 12$ nm, for which we have $|(f_p - f_s) - f_R| = 15$ GHz.

results in a Raman volume of the cavity larger than for a W0.63 waveguide of the same size, and therefore in a lower Raman gain than for this waveguide.

If we compare the characteristics volumes of the various nonlinear effects in the cavity with those of a W0.63 waveguide of length 12 periods (see Table 3.2), we can indeed see that the ratio between the Raman volume $V_R = 2.78\ \mu m^3$, on which will depend the importance of Raman gain, and of the modal volumes V_m^p and V_m^s , on which will depend the importance of the other nonlinear effects, is much more favorable in the case of a W0.63 waveguide in the case of a doubly resonant cavity. However, the Raman volume is smaller than in the case of W0.66 waveguide of length 50 microns, where it was equal to 13 μm^3, so Raman scattering should à priori be more important in our cavity. For comparison, we also calculated the characteristics volumes for a cavity similar to the one used by Takahashi [2] for the Raman nanolaser which he recently demonstrated. For the Takahashi kind of cavity, the Raman volume is worth $V_R = 0.514\ \mu m^3$, i.e. about one fifth of the one in our cavity, which is much more favorable to the obtention of a Raman laser. The relationship between the Raman gain and the modal volumes for this cavity are in the same range as those of the W0.63 waveguide.

Unlike the case of the W0.63 waveguides of length 100 microns presented above, we can not see stimulated Raman scattering in the doubly resonant cavity, only spontaneous

Volumes	Measured cavity	W0.63 waveguide 12 periods	Cavity of Takahashi
V_R	2.78 μm^3	1.26 μm^3	0.514μm^3
V_{TPA}^{pp}	1.19 μm^3	0.718 μm^3	0.419μm^3
$V_{TPA}^{ps} = V_{TPA}^{sp}$	1.69 μm^3	0.728 μm^3	0.492μm^3
V_{TPA}^{ss}	0.498 μm^3	0.595 μm^3	0.394μm^3
V_m^p	0.189 μm^3	0.199 μm^3	0.079μm^3
V_m^s	0.147 μm^3	0.232 μm^3	0.089μm^3
R_{eff}^p	1.33	1.22	1.46
R_{eff}^s	1.38	1.31	1.41
V_R/V_{TPA}^{pp}	2.33	1.76	1.23
V_R/V_m^p	14.7	6.34	6.49
V_R/V_m^s	18.9	5.43	5.79

Table 3.2: The values of the characteristics volumes for the measured cavity, for a W0.63 waveguide of length 12 periods, and for a cavity similar to the one used for the Raman nanolaser of Takahashi [2], calculated using the MEEP software.

Raman scattering (see Fig. 3.20). This is due first to the worst ratio between the Raman volume and the modal volumes in our cavity compared to a W0.63 waveguide, and then to the very high free-carrier absorption in the cavity, which is much higher than what we expected, suggesting that the free-carrier effective volumes for the pump and Stokes modes are much smaller than for the cavity discussed in Chapter 2 of this thesis. This is probably a consequence of the greater confinement of the electromagnetic field in a W0.63 waveguide, which is narrower than the W1 waveguide on which the cavity studied above was based. It is also possible that the higher powers we used resulted in smaller effective volumes for the free carriers. To determine these effectives volumes and the Raman gain of the cavity, we performed a non-linear fit between the measured curves and those simulated from the equations of the doubly resonant cavity. The complete equations describing the behavior of this cavity are (see section 1.4.3):

$$\frac{dA_p}{dt} = -\left(\frac{1}{\tau_p} + \gamma_{p_r}^{FCA} N_e + \gamma_{pp}^{TPA} N_p + (\gamma_{ps}^{TPA} + \gamma_{sp}^{TPA}) N_s + \frac{G_r(N_s+1)}{1+4\left(\frac{\triangle\omega_s}{\triangle\omega_R}\right)^2}\right)\frac{A_p}{2} + \quad (3.40)$$

$$+ i\triangle\omega_p A_p + \sqrt{\frac{\sqrt{T_{pmax}} P_{p_{in}}}{2\tau_p}}$$

$$\frac{dN_s}{dt} = -\left(\frac{1}{\tau_s} + \gamma_{s_r}^{FCA} N_e + \gamma_{ss}^{TPA} N_s + (\gamma_{ps}^{TPA} + \gamma_{sp}^{TPA}) N_p\right) N_s + \frac{G_r N_p (N_s+1)}{1+4\left(\frac{\triangle\omega_s}{\triangle\omega_R}\right)^2} \quad (3.41)$$

$$\frac{dN_e}{dt} = -\frac{N_e}{\tau_{fc}} + \sum_{I,J=p,s}\sum \left(\frac{1}{2}\gamma_{IJ}^{TPA} N_I N_J\right) + \sum_{I=p,s} \gamma_I^l N_I \tag{3.42}$$

$$\rho_{Si} C_p^{Si} V_{eff}^T \frac{d\triangle T}{dt} = -\frac{\triangle T}{R_T} + \sum_{I,J=p,s}\sum \left(\hbar\omega_I \gamma_{IJ}^{TPA} N_I N_J\right) + \sum_{I=p,s} \hbar\omega_I \left(\gamma_{I_r}^{FCA} N_e N_I + \gamma_I^l N_I\right) \tag{3.43}$$

$$\triangle\omega_I = \omega_I - \omega_{I_0} + \gamma_{I_i}^{FCD} N_e + \gamma_I^T \triangle T \tag{3.44}$$

In these equations, the only parameters whose values we do not know well are the Raman gain G_r, the free-carrier absorption and dispersion coefficients $\gamma_{p_r}^{FCA}$, $\gamma_{s_r}^{FCA}$ and $\gamma_{p_i}^{FCD}$, $\gamma_{s_i}^{FCD}$, and the cooling time of the cavity τ_T. The values of the other coefficients were either calculated from the characteristic volumes obtained by the FDTD simulation (see Table3.2), or determined from the measurements made in the second chapter of this thesis. The values of G_r, $\gamma_{p_r}^{FCA}$, $\gamma_{s_r}^{FCA}$ $\gamma_{p_i}^{FCD}$, $\gamma_{s_i}^{FCD}$, τ_T were therefore determined by using the nonlinear fit we made from the measured plots (see Table 3.3 and figure 3.20). This way, we find $G_r \simeq 5.5\times10^4\ s^{-1}$, which gives us for the value of Raman gain in bulk silicon $g_R^B = 16$ cm/GW, and a cooling time of the cavity $\tau_T = 143$ ns, three times higher than for the cavity that we studied in Chapter Two, probably because the total length of the structure is smaller and the heat dissipation poorer. The value of the Raman gain we measured is a little weak, but it is in the range of the values previously reported [84, 53]. Of course, the presence of small defects in the photonic crystal could change the distribution of the modes in the cavity and gives us an actual Raman volume greater than the one calculated by the FDTD and the actual Raman gain would then be greater than the one we measured. The values found for $\gamma_{p_r}^{FCA}$, $\gamma_{s_r}^{FCA}$ $\gamma_{p_i}^{FCD}$, $\gamma_{s_i}^{FCD}$ give us for the free-carrier effective volumes $V_{p_{eff}}^{FC} = 0.473\ \mu m^3$ and $V_{s_{eff}}^{FC} = 0.378\ \mu m^3$. As mentionned before, these volumes are much smaller than for the cavity discussed in Chapter 2. We can note that those volumes have the same factor of proportionality with the modal volumes calculated by the FDTD : $\frac{V_{p_{eff}}^{FC}}{V_m^p} \simeq \frac{V_{s_{eff}}^{FC}}{V_m^s} \simeq 2.5$, which suggest that there is maybe a link between the effective volume of the free carriers and the modal volume of the cavity.

The value of the Purcell factor for the Raman scattering of our nanocavity, which we calculated using the formula $F_R = \frac{\tau_R}{\tau_p}\frac{\hbar\omega_p}{\hbar\omega_s}\frac{1}{\sqrt{T_{max_p}T_{max_s}}}\frac{P_{s_{out}}}{P_{p_{in}}}$ (where $\tau_R = 1/\left(4\pi g_R^B hc^2 n_0 (2\pi\triangle f_R)/\left(3\lambda_p\lambda_s^2\right)\right)$) mentioned previously, is $F_R = 2.9$. This measured value is close to the theoretical value of the Purcell factor for our cavity $F_R = 2.59$ calculated from the formula $F_R = \frac{3}{8\pi^2}\frac{1}{V_R}\frac{Q_R Q_s}{Q_R+Q_s}\left(\frac{\lambda_s}{n_0}\right)^3$. This value is two times higher than the one measured in the W0.66 waveguide of length 50 microns where we had $F_R = 1.3$ [75], and higher than the one of $F_R = 1.65$ we measured in the W0.63 waveguide of length 100 microns in the section 3.3.1. This shows that the spontaneous Raman scattering is much greater in the doubly resonant cavity than in

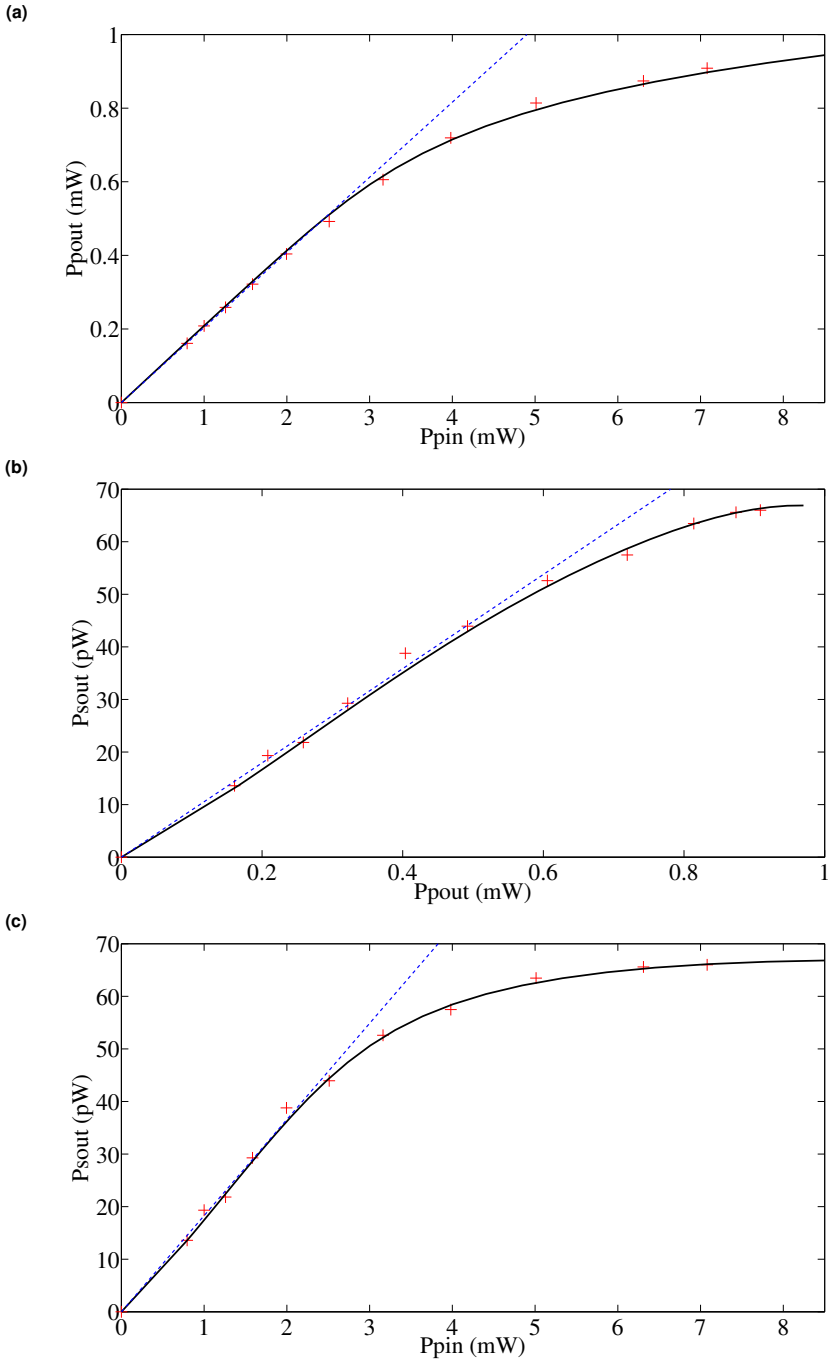

Figure 3.20: The Raman scattering measured in our doubly resonant cavity : (a) The pump power at the exit of the photonic crystal $P_{p_{out}}$ as a function of the pump power at the entrance of the photonic crystal $P_{p_{in}}$, (b) The Stokes power at the exit of the photonic crystal $P_{s_{out}}$ as a function of the pump power at the exit of the photonic crystal $P_{p_{out}}$, (c) The Stokes power at the exit of the photonic crystal $P_{s_{out}}$ as a function of the pump power at the entrance of the photonic crystal $P_{p_{in}}$. The red crosses correspond to the points that we measured, while the black curves are nonlinear adjustments made using the equations described above. The blue dashed curves are linear adjustments made from the first five points measured at low power.

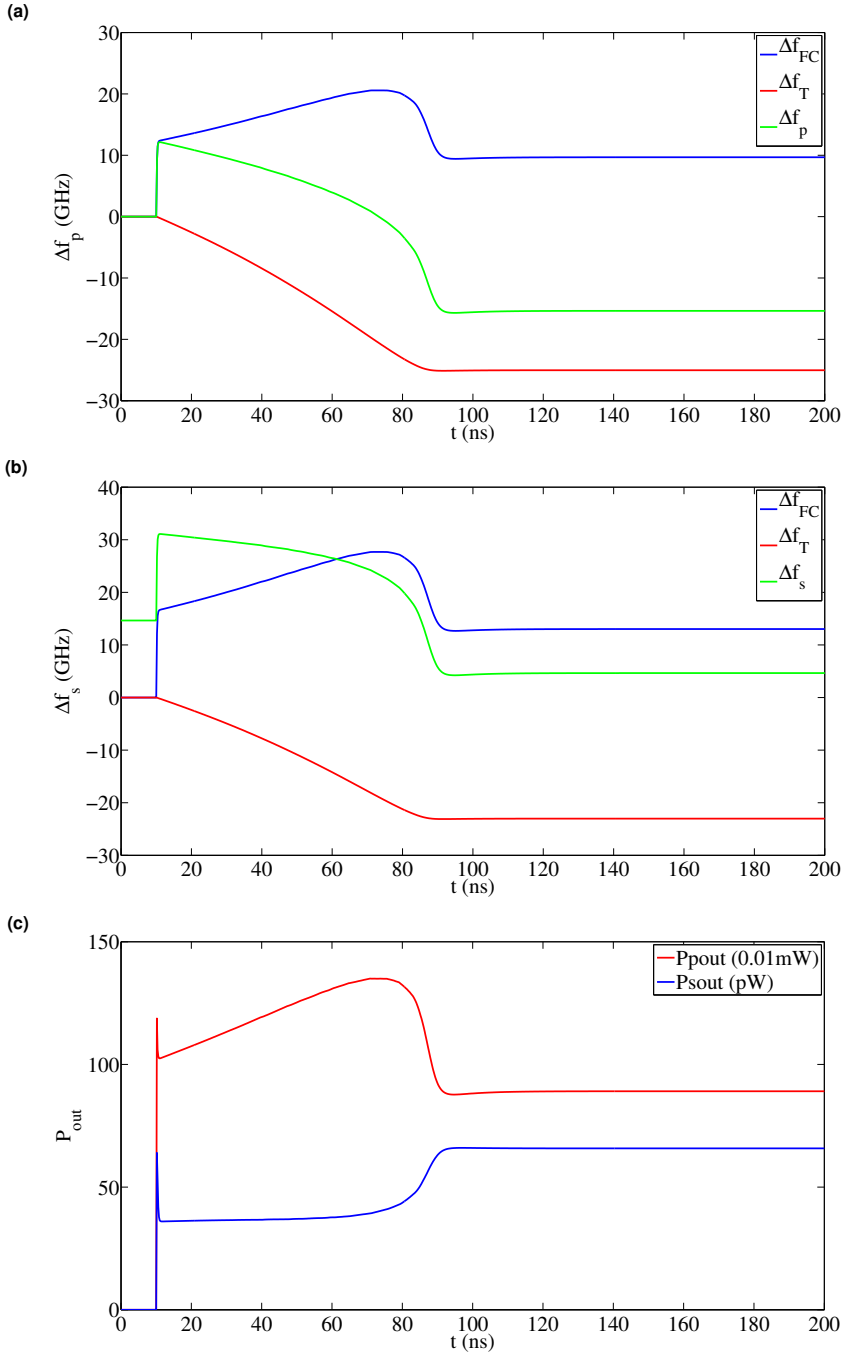

FIGURE 3.21 – MATLAB simulations of the temporal behavior of the cavity and of its transient response, for a pump power at the entrance of the photonic crystal $P_{p_{in}} = 7$ mW. The laser was turned on at $t_0 = 10$ ns. (a) The evolution of the pump detuning $\triangle\omega_p$ (in green), with the contributions from free-carrier (in blue) and thermal dispersions (in red). (b) The evolution of the Stokes detuning $\triangle\omega_s$ (in green), with with the contributions from free-carrier (in blue) and thermal dispersions (in red). (c) The evolution of the output pump power (in red) and of the output Stokes power (in blue). Just after the laser is turned on, the free-carrier dispersion will completely detune the Stokes resonance with respect to the Raman frequency, which will cause a temporary fall of the Raman gain.

Parameters of the model	Values for the measured cavity	Origin
τ_p	4.01 ps	measured
τ_s	0.21 ns	measured
τ_{fc}	0.3 ns	see chapter 2
τ_T	$\simeq$ 143 ns	measured + modeling
G_r	$\simeq 5.5 \times 10^4\ s^{-1}$	measured + modeling
γ_{pp}^{TPA}	$6.73 \times 10^3\ s^{-1}$	FDTD
γ_{ps}^{TPA}	$4.76 \times 10^3\ s^{-1}$	FDTD
γ_{sp}^{TPA}	$4.37 \times 10^3\ s^{-1}$	FDTD
γ_{ss}^{TPA}	$1.48 \times 10^4\ s^{-1}$	FDTD
γ_p^I	$1.19 \times 10^8\ s^{-1}$	FDTD
γ_s^I	$1.15 \times 10^8\ s^{-1}$	FDTD
$\gamma_{p_r}^{FCA}$	$\simeq 1.97 \times 10^5\ s^{-1}$	measured + modeling
$\gamma_{p_i}^{FCD}$	$\simeq 2.93 \times 10^6\ s^{-1}$	measured + modeling
$\gamma_{s_r}^{FCA}$	$\simeq 2.88 \times 10^5\ s^{-1}$	measured + modeling
$\gamma_{s_i}^{FCD}$	$\simeq 3.94 \times 10^6\ s^{-1}$	measured + modeling
γ_p^T	$-6.52 \times 10^8\ K^{-1} \cdot s^{-1}$	FDTD
γ_s^T	$-5.0 \times 10^8\ K^{-1} \cdot s^{-1}$	FDTD
V_{eff}^T	$\simeq 3.0\ \mu m^3$	measured + modeling

Table 3.3: Values of the different parameters used to model the cavity.

the W0.66 waveguide.

Logically, the next step would have been to attempt to measure the Raman scattering in the cavity with a pulsed laser. Unfortunately, our simulations with MATLAB show that at high power, the transient response of the cavity just after the laser is turned on is unfavorable to Raman scattering. Indeed, just after the laser is turned on, the free-carrier dispersion will completely detune the Stokes resonance compared to the Raman frequency, which will cause a temporary fall of the Raman gain $G_r / \left(1 + 4\left(\frac{\triangle\omega_s}{\triangle\omega_R}\right)^2\right)$ (see Fig. 3.21b). The cavity will be partially retuned afterwards, and the gain will increase again, but the consequence is that we would get a much smaller output Stokes power just after the laser is turned on than in the steady-state regime (see Fig. 3.21c), which is hardly favorable to the measurements with a pulsed laser (besides the fact that the output Stokes power is already very low in the steady-state regime, so it would be even more difficult to detect in the pulsed regime). We can also see that the rise time of the Stokes is quite slow, which was expected given the low bandwidth of the Raman laser we would obtain from this cavity (see section 3.2.3). So we did not try to make the measurements with a pulsed laser. We can also note that the pump resonance will be more and more detuned with the pump laser as the input pump power increases (see Fig. 3.21a), which explains in part why the output pump power will saturate at high power, as we can see on the figure 3.20a).

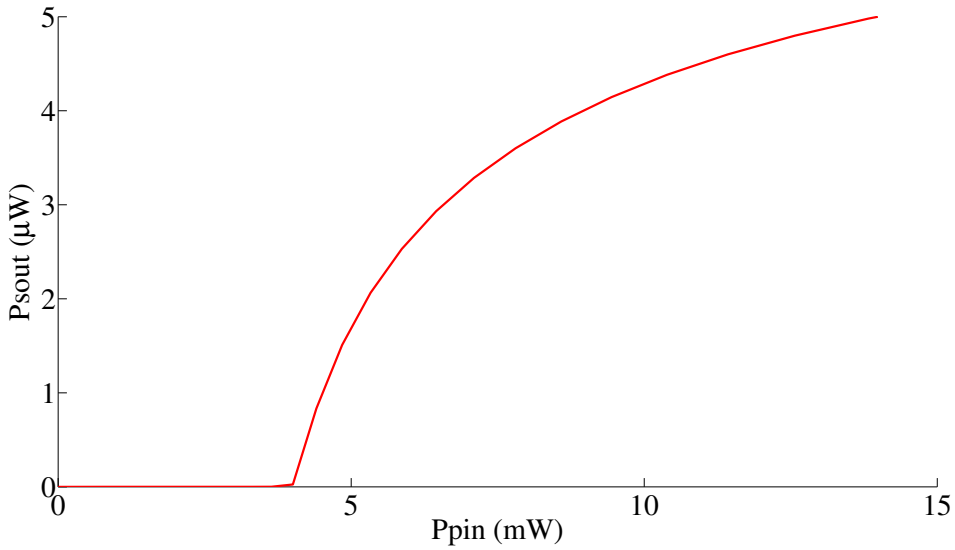

Figure 3.22: Simulation with MATLAB of the behavior of the output Stokes power of a doubly resonant cavity as a function of the input pump power, for a free-carrier lifetime $\tau_{fc} = 10$ ps. We can see that in this case, we would obtain a Raman laser with a threshold of 4 mW on the pump power at the entrance of the photonic crystal, with an output Raman power up to 5 μW.

We still have not obtained a Raman laser from these cavities, because the strength of the nonlinear absorptions in said cavities prevents Raman scattering, in particular the free-carrier absorption. To solve this problem, we plan to remove these free carriers using a MSM (metal-semiconductor-metal) junction with platinum contacts of the kind described in section 2.6.5 of Chapter 2 [45, 36]. But the fabrication of these MSM junctions is a problem because the metal contacts must withstand the hydrofluoric acid during the wet etching step that allows us to obtain a membrane nanocavity (with higher quality factors that a cavity on SOI) by removing the silica underneath the silicon where the photonic crystal is. Although it is easy to find a metal that resists hydrofluoric acid (for example platinum), this acid can still etch slightly the silicon below the metal contacts and make them come off. We are now trying to find an optical resin that would protect the metal contacts during the wet etching step, but our research on this topic was not finished by the time I wrote this thesis.

If we can make these MSM junctions, then it would be relatively easy to reduce the free-carrier lifetime in the cavity and thus solve the problem of free-carrier absorption, which is the main obstacle to the obtention of a Raman laser. According to our simulations, if we could reduce the free-carrier lifetime to $\tau_{fc} = 10$ ps, then we would obtain a Raman laser with a threshold of 0.8 mW for the pump power at the exit of the photonic crystal and of 4 mW for the pump power for the entrance of the photonic crystal (see Fig. 3.22), a value relatively easy to achieve with the material we have. Furthermore, such a low value for the lifetime would not be necessary. A free-carrier lifetime of $\tau_{fc} = 0.1$ ns would indeed be

enough to obtain within our nanocavity a Raman laser with a threshold of approximately 1 mW for the pump power at the exit of the photonic crystal and 5 mW for the pump power at the entrance of the photonic crystal.

3.3.3 Comparison with the Raman laser of Takahashi.

We have already mentioned several times in this thesis that a silicon Raman nanolaser was demonstrated in a doubly resonant cavity a few months ago (in June 2013) by Takahashi [2]. We will now discuss the differences between this cavity and the one we have made which made possible this Raman laser. The cavity used by Takahashi is a double heterostructure cavity consisting of a W1 waveguide parallel to the crystallographic direction [100] of silicon (like our cavity), where the period of the photonic crystal was varied along the waveguide to form a nanocavity (see Fig. 3.23-down). The period of this photonic crystal is 410 nm, the radius of the holes is 130 nm and the height of the silicon slab in which it was etched is 220 nm. The even mode of the W1 waveguide was used for the Stokes and the odd mode for the pump rather than using a mode with the same parity for both resonances as we did for the W0.63 waveguides, which ensures better quality factors for the pump resonance and a better overlap between the pump and Stokes modes, which explains the better Raman volume of this cavity we mentioned before (see Fig. 3.23-up). The frequency difference between these two modes is almost equal to the Raman shift, and this difference was adjusted by varying the size of the holes of the photonic crystal. The pump laser is not injected along this W1 waveguide, but through a coupling waveguide parallel to this waveguide, which allowed them to obtain much better quality factors for the resonances : $Q_p = 140000$ for the pump and $Q_s = 1500000$ for the Stokes, far higher than ours. Although a second extraction waveguide for the Stokes is shown on this schematic, the Stokes power emitted from the cavity was measured by the surface (see Fig. 3.23-down). The measured threshold of the Raman laser is 1 μW for the pump power coupled into the cavity (see Fig. 3.24-up). This pump power coupled into the cavity was estimated from the measured pump power exiting through surface (as for the Stokes power), assuming that the pump power measured through the surface was 20 % of the pump power in the cavity (this estimate assumes that the power leaving the cavity through the extraction waveguides is negligible) [2].

We tried to use our equations of a doubly resonant nanocavity to simulate the behavior of the Raman laser of Takahashi (see Fig. 3.24-down), using the Raman volume of this cavity that we calculated with MEEP (see Table 3.2) and the parameters for the free-carrier lifetime, the effective volume, the cooling time and the effective thermal volume of the cavity we determined for the Kuramochi kind of cavity we studied Chapter 2 (this cavity was also made inside a W1 waveguide and was therefore quite close to the cavity of Takahashi), and adjusting the value of the Raman gain to find the one that best matched

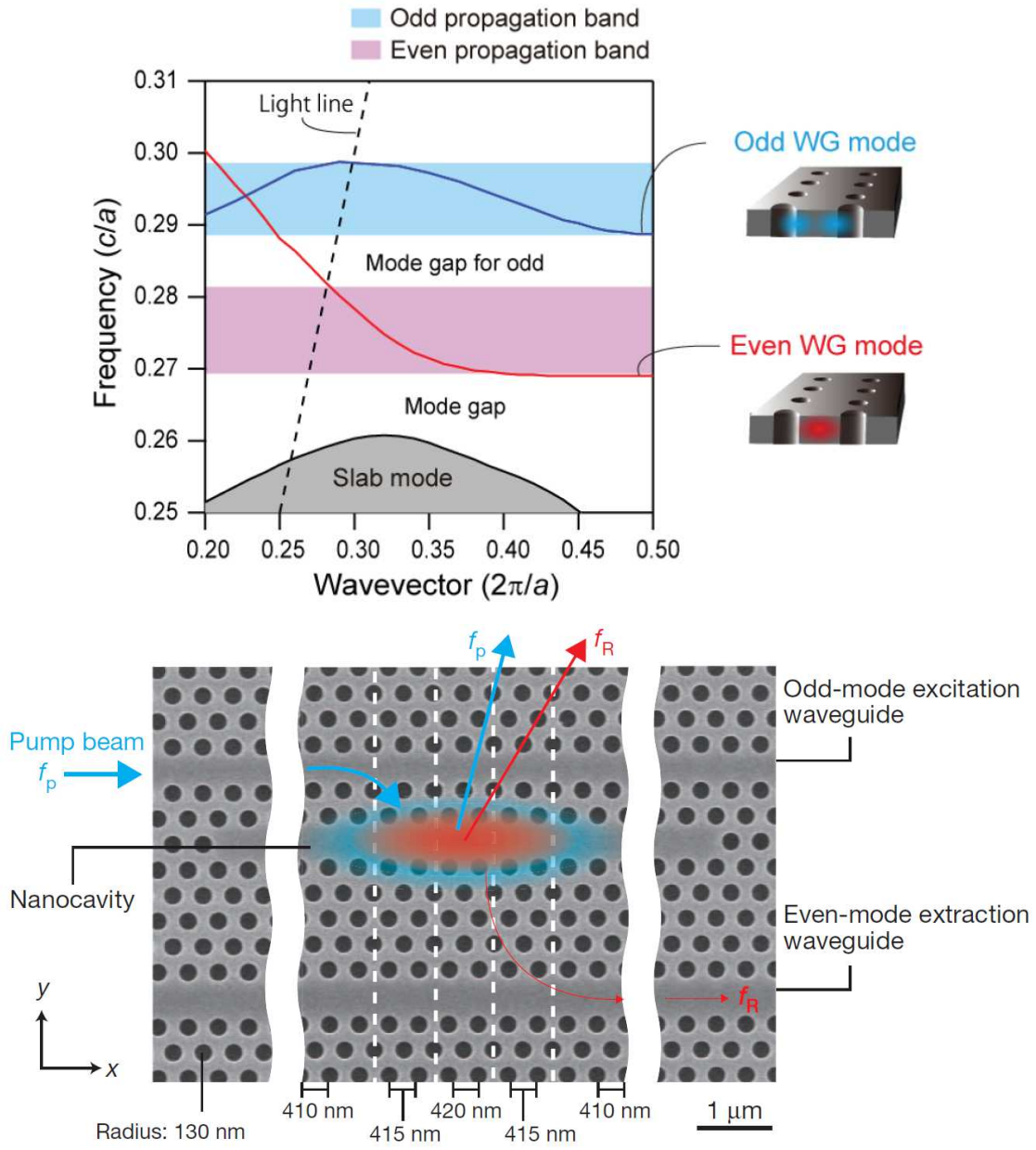

Figure 3.23: Up : the band diagram of a W1 waveguide with the odd and even modes used respectively for the pump and Stokes by Takahashi. Down: Schematic of the double heterostructure cavity used by Takahashi for the Raman nanolaser (figures reprinted with permission from Macmillan Publisher Ltd : Nature, Ref. [2], copyright 2013).

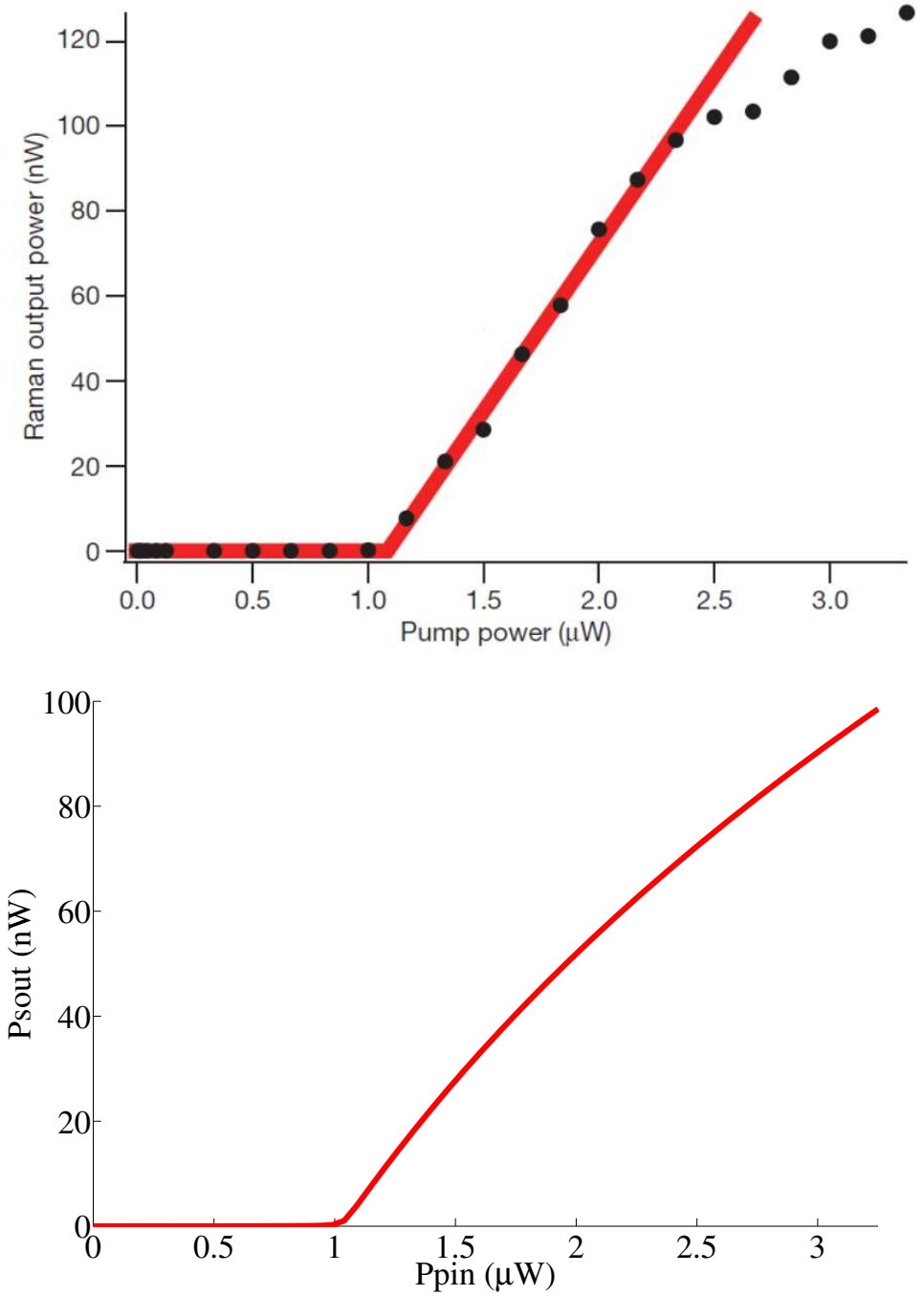

Figure 3.24: Up : The Stokes power measured through the surface of the Raman laser of Takahashi as a function of the pump power coupled into the cavity (figure reprinted with permission from Macmillan Publisher Ltd : Nature, Ref. [2], copyright 2013). Down : A simulation with MATLAB of the Raman laser of Takahashi that we made using our equations for a doubly resonant cavity.

the measurements made by Takahashi. We found this way $G_r \simeq 5.62 \times 10^5\ s^{-1}$ (a value of the Raman gain ten times larger than for our nanocavity), which gives us as value for the Raman gain in the bulk silicon $g_R^B = 28$ cm/GW, using the value of the Raman volume that we calculated, and a theoretical Purcell factor $F_R = 11.9$ (four times higher than for our cavity). This value of the Raman gain seems more reasonable than the one we found for our cavity of 16 cm/GW, because it is closer to the median value of the different Raman gains that have been measured so far, suggesting that the Raman volume given for our cavity by the MEEP simulation was undervalued compared to the actual volume Raman. It should nevertheless be noted that the value given by Takahashi for the laser threshold is based on an estimate of the pump power coupled into the cavity made from the measured pump power coming through the surface, and it is always possible that this estimate is incorrect and that the threshold power is actually higher, which would give us a lower value for the Raman gain. Nevertheless, we have for this value of the gain a very good agreement between our simulations and the curve measured by Takahashi (see Fig. 3.24), both regarding the laser threshold power and the saturation of the output Stokes power under the effect of the free-carrier absorption with increasing pump power, which confirms the validity of the model we have developed to describe the Raman lasers.

Assuming we can obtain a Raman laser from our cavity by using the MSM junction to reduce the free-carrier lifetime, what would be the disadvantages and advantages of this laser compared to the laser of Takahashi ? The main disadvantages would obviously be the higher power threshold, between 4 and 5 mW for the pump power at the entrance of the photonic crystal compared to the threshold of 1 μW for the laser of Takahashi, as well as the more complicated fabrication due to the addition of the platinum contacts. It should be noted that the threshold for the laser of Takahashi is for the pump power coupled into the cavity and that the pump power at the entrance of the photonic crystal is probably higher. In our case, a threshold between 4 and 5 mW for the pump power at the entrance of photonic crystal would correspond to a threshold between 1.8 and 2.3 mW of for the power coupled into the cavity, which is still significantly higher than for Takahashi. This laser would however have the advantage of being easier to modulate in amplitude through the metal contacts, and the output Stokes power would be easier to collect through the output waveguide rather than through the surface. We should also have less free-carrier absorption in our cavity, which would allow us à priori to obtain larger output powers for the Raman laser (up to 5 μW for a free-carrier lifetime of 10 ps (see Fig. 3.22) compared with 125 nW for the Raman laser of Takahashi (see Fig. 3.24).

3.4 Conclusion.

We have studied in this chapter the possibility of obtaining a Raman nanolaser from a silicon photonic crystal cavity from two points of view. First, we studied the Raman laser in a theoretical way, and determined what would be the frequency response of this laser for a small modulation in amplitude, as well as its Relative Intensity Noise and its frequency noise, which would theoretically be lower than for a conventional semiconductor laser. This study has also shown us that obtaining a Raman laser would be highly dependent on the gain of this Raman laser and on the importance of the nonlinear absorptions.

We were then able to measure relatively high stimulated Raman scattering in a narrow W0.63 waveguide of length 100 microns, even if we did not managed to obtain a true laser effect in this waveguide. We then designed and fabricated a doubly resonant nanocavity from one of those W0.63 waveguides. Although we have not been able to obtain a Raman laser from this nanocavity, we still got a very good agreement between the measured spontaneous Raman scattering in the cavity and our numerical simulations, which proves the validity of our model of the Raman laser for the nanocavities. A good agreement was also obtained between the numerical simulations and the Raman laser recently demonstrated by Takahashi. Our theoretical study shows that it would be possible for us to obtain a Raman nanolaser with a threshold below the milliwatt provided we reduce the losses due to the free-carrier absorption in the nanocavity. This could be accomplished by reducing the free-carrier lifetime, for example by removing these free carriers from the silicon with a MSM (metal-semiconductor-metal) junction [45].

General conclusion.

This PhD thesis presents the work I've done on two important nonlinear optical phenomena observed in silicon photonic crystals cavities : the high-frequency self-induced oscillations generated by the free-carrier dispersion and the stimulated Raman scattering which was used to create the Raman lasers.

The study of high-frequency self-induced oscillations allowed us to observe experimentally for the first time non-attenuated oscillations in photonic crystal nanocavities with frequencies in the range of 3 GHz and a high spectral purity. These oscillations would allow us to easily design ultra-compact microwave sources in silicon. The model we have developed for these oscillations shows that the high frequency and high spectral purity of the oscillations are a consequence of the very small modal volume of photonic crystals nanocavities compared to other types of nanocavities such as microring resonators. This model also allowed us to determine the free-carrier lifetime in these cavities and to assess the strength of the free-carrier absorption, the main obstacle to obtaining a Raman laser. It showed us that the oscillation frequency was dependent on the free-carrier and photon lifetimes in the cavity. By sufficiently diminishing both the photon lifetime (using a cavity with shorter barriers) and the free-carrier lifetime (by removing the free carriers from the cavity using p-i-n junctions with a reverse bias or MSM junctions), it is possible to obtain non-attenuated oscillations at much higher frequencies, of the order of 50 GHz.

We then studied the Raman scattering in a nanocavity and modeled the behavior of a Raman laser, and showed by a theoretical study that the frequency noise in Raman lasers is much lower than that of conventional semiconductor lasers. We then measured the Raman scattering in a narrow W0.63 waveguide of length 100 microns, and showed that the stimulated Raman scattering predominated in this waveguide, even though we could not obtain a true laser effect. We then developed a kind of doubly resonant photonic crystal nanocavity to amplify the gain of the Raman scattering and obtain a silicon Raman nanolaser. This nanocavity was designed to be able to "tune" the difference between the two resonances so that it would be equal to the specific frequency shift of Raman scattering in silicon. Although we were able to measure strong Raman scattering in this cavity, we have not been able to obtain a Raman laser, because of the strength of the free-carrier absorption in the nanocavity. However, we got a very good agreement between

our simulations and the measured Raman scattering in this nanocavity, thus validating the model that we developed of the Raman laser in a doubly resonant nanocavity. This model shows us that we could obtain a Raman laser with a threshold in the milliwatt range in our cavity if we could sufficiently reduce the free-carrier lifetime and thus the free-carrier absorption. This could be done by putting on the edges of our cavity metallic contacts (i.e. a MSM junction) to remove the free carriers of the cavity. Researches in this direction are underway.

Appendices.

Frequency response of the Raman laser with the nonlinear absorptions.

If we take into account the nonlinear absorptions to calculate the frequency response of the Raman laser for small variations around the steady-state solutions, then the expression of the transfer function $H(\Omega)$ becomes even more complicated, because we now have a system with three equations, when taking into account the equation on the free carriers. When we linearize the system, we then obtain the following linear matrix differential equation :

$$\frac{d}{dt}\begin{pmatrix}\delta A_p\\ \delta N_s\\ \delta N_e\end{pmatrix} = \begin{pmatrix}m_{11} & m_{12} & m_{13}\\ m_{21} & m_{22} & m_{23}\\ m_{31} & m_{32} & m_{33}\end{pmatrix}\begin{pmatrix}\delta A_p\\ \delta N_s\\ \delta N_e\end{pmatrix} + \frac{1}{2}\sqrt{\frac{\sqrt{T_{p_{max}}}}{2\tau_p P_{p_{in}}}}\begin{pmatrix}\delta P_{p_{in}}\\ 0\\ 0\end{pmatrix} \tag{3.45}$$

where the values of the coefficients of the matrix M are :

$m_{11} = -\frac{1}{2}\left(\frac{1}{\tau_p} + G_r(N_s+1) + \gamma_p^{FCA}N_e + \gamma_{pp}^{TPA}N_p + (\gamma_{ps}^{TPA}+\gamma_{sp}^{TPA})N_s\right)$,

$m_{12} = -\frac{1}{2}A_p\left(G_r + \gamma_{sp}^{TPA} + \gamma_{ps}^{TPA}\right)$, $m_{13} = -\frac{1}{2}\gamma_p^{FCA}A_p$,

$m_{21} = \frac{2A_p}{\hbar\omega_p}\left(G_r(N_s+1) - (\gamma_{sp}^{TPA}+\gamma_{ps}^{TPA})N_s\right)$,

$m_{22} = -\frac{1}{\tau_s} + \frac{G_r A_p^2}{\hbar\omega_p} - 2\gamma_{ss}^{TPA}N_s - \frac{(\gamma_{sp}^{TPA}+\gamma_{ps}^{TPA})A_p^2}{\hbar\omega_p} - \gamma_s^{FCA}N_e$, $m_{23} = -\gamma_s^{FCA}N_s$,

$m_{31} = \frac{2A_p}{\hbar\omega_p}\left(\frac{\gamma_{pp}^{TPA}A_p^2}{\hbar\omega_p} + (\gamma_{sp}^{TPA}+\gamma_{ps}^{TPA})N_s + \gamma_p^{l}\right)$,

$m_{32} = \gamma_{ss}^{TPA}N_s + \frac{(\gamma_{sp}^{TPA}+\gamma_{ps}^{TPA})A_p^2}{2\hbar\omega_p} + \gamma_s^{l}$, $m_{33} = -\frac{1}{\tau_{fc}}$.

We can deduce from equation3.45 the new expression of the modulation transfer function $H(\Omega)$:

$$H(\Omega) = \frac{\delta P_{s_{out}}}{\delta P_{p_{in}}} = \frac{\hbar\omega_s\sqrt{T_{s_{max}}}}{2\tau_s}\sqrt{\frac{\sqrt{T_{p_{max}}}}{2\tau_p P_{p_{in}}}}\frac{m_{21}(i\Omega - m_{33}) + m_{23}m_{31}}{\triangle_m(\Omega)} \tag{3.46}$$

where $\triangle_m(\Omega)$ is defined as :

$$\triangle_m(\Omega) = \det \begin{pmatrix} i\Omega - m_{11} & -m_{12} & -m_{13} \\ -m_{21} & i\Omega - m_{22} & -m_{23} \\ -m_{31} & -m_{32} & i\Omega - m_{33} \end{pmatrix} \tag{3.47}$$

Relative Intensity Noise of the Raman laser with the non-linear absorptions.

With the nonlinear absorptions, we then have for the linear matrix differential equation 3.24 :

$$\frac{d}{dt}\begin{pmatrix} \delta A_p \\ \delta N_s \\ \delta N_e \end{pmatrix} = \begin{pmatrix} m_{11} & m_{12} & m_{13} \\ m_{21} & m_{22} & m_{23} \\ m_{31} & m_{32} & m_{33} \end{pmatrix}\begin{pmatrix} \delta A_p \\ \delta N_s \\ \delta N_e \end{pmatrix} + \begin{pmatrix} \frac{\hbar\omega_p}{2A_p}F_p(t) \\ F_s(t) \\ F_e(t) \end{pmatrix} \tag{3.48}$$

Transforming to the frequency domain, and using the Cramer formulas, we obtain from equation 3.48 the following expression :

$$\begin{pmatrix} \delta A_p \\ \delta N_s \\ \delta N_e \end{pmatrix} = \frac{1}{\triangle_m(\Omega)}\begin{pmatrix} n_{11} & n_{12} & n_{13} \\ n_{21} & n_{22} & n_{23} \\ n_{31} & n_{32} & n_{33} \end{pmatrix}\begin{pmatrix} \frac{\hbar\omega_p}{2A_p}F_p \\ F_s \\ F_e \end{pmatrix} \tag{3.49}$$

where the coefficients of the matrix N and $\triangle_m(\Omega)$ are defined as :

$n_{11} = -\Omega^2 - i\Omega\,(m_{22}+m_{33}) + (m_{22}m_{33} - m_{23}m_{32})$, $n_{12} = i\Omega m_{12} + (m_{13}m_{32} - m_{12}m_{33})$,

$n_{13} = i\Omega m_{13} + (m_{12}m_{23} - m_{13}m_{22})$, $n_{21} = i\Omega m_{21} + (m_{23}m_{31} - m_{21}m_{33})$,

$n_{22} = -\Omega^2 - i\Omega(m_{11}+m_{33}) + (m_{11}m_{33} - m_{13}m_{31})$, $n_{23} = i\Omega m_{23} + (m_{13}m_{21} - m_{23}m_{11})$,

$n_{31} = i\Omega m_{31} + (m_{21}m_{32} - m_{31}m_{22})$, $n_{32} = i\Omega m_{32} + (m_{31}m_{12} - m_{32}m_{11})$,

$n_{33} = -\Omega^2 - i\Omega(m_{11}+m_{22}) + (m_{11}m_{22} - m_{12}m_{21})$.

The equation 3.26 on the noise spectral densities then becomes :

$$\begin{pmatrix} \frac{4N_p}{\hbar\omega_p}S_{N_p} \\ S_{N_s} \\ S_{N_e} \end{pmatrix} = \frac{1}{\|\triangle_m\|^2}\begin{pmatrix} r_{11} & r_{12} & r_{13} & r_{14} & r_{15} & r_{16} \\ r_{21} & r_{22} & r_{23} & r_{24} & r_{25} & r_{26} \\ r_{31} & r_{32} & r_{33} & r_{34} & r_{35} & r_{36} \end{pmatrix}\begin{pmatrix} \frac{\hbar\omega_p}{4N_p} < F_pF_p > \\ < F_sF_s > \\ < F_eF_e > \\ < F_pF_s > \\ < F_pF_e > \\ < F_sF_e > \end{pmatrix} \tag{3.50}$$

where the coefficients of the matrix R are defined as :

$r_{11} = \Omega^4 + ((m_{22}+m_{33})^2 - 2(m_{22}a_{33} - m_{23}a_{32}))\Omega^2 + (m_{22}m_{33} - m_{23}m_{32})^2$,

$r_{12} = m_{12}^2\Omega^2 + (m_{13}m_{32} - m_{12}m_{33})^2$, $r_{13} = m_{13}^2\Omega^2 + (m_{12}m_{23} - m_{13}m_{22})^2$,

$r_{14} = -2\left(((m_{22}m_{33} - m_{23}m_{32}) + m_{12}(m_{22}+m_{33}))\Omega^2 + (m_{22}m_{33} - m_{23}m_{32})(m_{13}m_{32} - m_{12}m_{33})\right)$,

$r_{15} = -2\left(((m_{22}m_{33} - m_{23}m_{32}) + m_{13}(m_{22}+m_{33}))\Omega^2 + (m_{22}m_{33} - m_{23}m_{32})(m_{12}m_{23} - m_{13}m_{22})\right)$,

$r_{16} = 2\left(m_{12}m_{13}\Omega^2 + (m_{13}m_{32} - m_{12}m_{33})(m_{12}m_{23} - m_{13}m_{22})\right)$,

$r_{21} = m_{21}^2\Omega^2 + (m_{23}m_{31} - m_{21}m_{33})^2$, $r_{23} = m_{23}^2\Omega^2 + (m_{13}m_{32} - m_{23}m_{11})^2$,

$r_{22} = \Omega^4 + ((m_{11}+m_{33})^2 - 2(m_{11}m_{33} - m_{13}m_{31}))\Omega^2 + (m_{11}m_{33} - m_{13}m_{31})^2$,

$r_{24} = -2\left(((m_{23}m_{31} - m_{21}m_{33}) + m_{21}(m_{11}+m_{33}))\Omega^2 + (m_{23}m_{31} - m_{21}m_{33})(m_{11}m_{33} - m_{13}m_{31})\right)$,

$r_{25} = 2\left(m_{21}m_{23}\Omega^2 + (m_{23}m_{31} - m_{21}m_{33})(m_{13}m_{21} - m_{23}m_{11})\right)$,

$r_{26} = -2\left(((m_{13}m_{21} - m_{23}m_{11}) + m_{23}(m_{11}+m_{33}))\Omega^2 + (m_{13}m_{21} - m_{23}m_{11})(m_{11}m_{33} - m_{13}m_{31})\right)$,

$r_{31} = m_{31}^2\Omega^2 + (m_{21}m_{32} - m_{31}m_{22})^2$, $r_{32} = m_{32}^2\Omega^2 + (m_{31}m_{12} - m_{32}m_{11})^2$,

$r_{33} = \Omega^4 + ((m_{11}+m_{22})^2 - 2(m_{11}m_{22} - m_{12}m_{21}))\Omega^2 + (m_{11}m_{22} - m_{12}m_{21})^2$,

$r_{34} = 2\left(m_{31}m_{32}\Omega^2 + (m_{21}m_{32} - m_{31}m_{22})(m_{31}m_{12} - m_{32}m_{11})\right)$,

$r_{35} = -2\left(((m_{21}m_{32} - m_{31}m_{22}) + m_{31}(m_{11}+m_{22}))\Omega^2 + (m_{21}m_{32} - m_{31}m_{22})(m_{11}m_{22} - m_{12}m_{21})\right)$,

$r_{36} = -2\left(((m_{31}m_{12} - m_{32}m_{11}) + m_{32}(m_{11}+m_{22}))\Omega^2 + (m_{31}m_{12} - m_{32}m_{11})(m_{11}m_{22} - m_{12}m_{21})\right)$.

and where the values of the Langevin noise sources spectral densities are :

$< F_pF_p >= 2\left(\frac{N_p}{\tau_p} + G_r(N_s+1)N_p + \gamma_{pp}^{TPA}N_p^2 + (\gamma_{sp}^{TPA} + \gamma_{ps}^{TPA})N_pN_s + \gamma_p^{FCA}N_eN_p\right)$,

$< F_sF_s >= 2G_r(N_s+1)N_p$, $< F_eF_e >= \frac{2N_e}{\tau_{fc}}$, $< F_pF_s >= -G_r(N_s+1)N_p$,

$< F_pF_e >= -(\frac{1}{2}\gamma_{pp}^{TPA}N_p^2 + \frac{1}{2}(\gamma_{sp}^{TPA} + \gamma_{ps}^{TPA})N_pN_s + \gamma_p^lN_p)$,

and $< F_sF_e >= -(\frac{1}{2}\gamma_{ss}^{TPA}N_s^2 + \frac{1}{2}(\gamma_{sp}^{TPA} + \gamma_{ps}^{TPA})N_pN_s + \gamma_s^lN_s)$.

The expression of the noise spectral density of the output Stokes power then becomes :

$$S_{\delta P_{s_{out}}}(\Omega) = \left(\frac{\sqrt{T_{s_{max}}}\hbar\omega_s}{2\tau_s}\right)^2 S_{N_s}(\Omega) + \hbar\omega_s\left(1 - \frac{\sqrt{T_{s_{max}}}}{\tau_s}Real\left(\frac{n_{22}}{\triangle_m}\right)\right)P_{s_{out}} \qquad (3.51)$$

which gives us for the Relative Intensity Noise :

$$\frac{RIN}{\triangle f} = \left(\frac{\sqrt{T_{s_{max}}}\hbar\omega_s}{2\tau_s}\right)^2 \frac{2S_{N_s}(\Omega)}{P_{s_{out}}^2} + \frac{2\hbar\omega_s}{P_{s_{out}}}\left(1 - \frac{\sqrt{T_{s_{max}}}}{\tau_s}Real\left(\frac{n_{22}}{\triangle_m}\right)\right) \qquad (3.52)$$

Bibliography

[1] N. Cazier, X. Checoury, L.-D. Haret, and P. Boucaud, "High-frequency self-induced oscillations in a silicon nanocavity," *Optics Express*, vol. 21, pp. 13626–13638, 2013.

[2] Y. Takahashi, Y. Inui, M. Chihara, T. Asano, R. Terawaki, and S. Noda, "A micrometre-scale raman silicon laser with a microwatt threshold.," *Nature*, vol. 498, pp. 470–4, June 2013.

[3] B. S. Song, S. Noda, and T. Asano, "Photonic devices based on in-plane hetero photonic crystals," *Science*, vol. 300, pp. 1537–1537, June 2003.

[4] H. Takano, B. S. Song, T. Asano, and S. Noda, "Highly efficient multi-channel drop filter in a two-dimensional hetero photonic crystal," *Optics Express*, vol. 14, pp. 3491–3496, Apr. 2006.

[5] S. Noda, "Seeking the ultimate nanolaser," *Science*, vol. 314, pp. 260–261, 2006.

[6] M. Nomura, S. Iwamoto, K. Watanabe, N. Kumagai, Y. Nakata, S. Ishida, and Y. Arakawa, "Room temperature continuous-wave lasing in photonic crystal nanocavity," *Optics Express*, vol. 14, pp. 6308–6315, June 2006.

[7] O. Painter, R. Lee, A. Scherer, A. Yariv, J. O'Brien, P. Dapkus, and I. KIm, "Two-dimensional photonic band-gap defect mode laser," *Science*, vol. 284, pp. 1819–1821, 1999.

[8] S. Strauf, K. Hennessy, M. T. Rakher, Y.-S. Choi, A. Badolato, L. C. Andreani, E. L. Hu, P. M. Petroff, , and D. Bouwmeester, "Self-tuned quantum dot gain in photonic crystal lasers," *Physical Review Letter*, vol. 96, 2006.

[9] Y. Akahane, T. Asano, B. S. Song, and S. Noda, "High-Q photonic nanocavity in a two-dimensional photonic crystal," *Nature*, vol. 425, pp. 944–947, Oct. 2003.

[10] B. S. Song, S. Noda, T. Asano, and Y. Akahane, "Ultra-high-Q photonic double-heterostructure nanocavity," *Nature Materials*, vol. 4, no. 3, pp. 207–210, 2005.

[11] Y. Takahashi, Y. Tanaka, H. Hagino, T. Sugiya, Y. Sato, T. Asano, and S. Noda, "Design and demonstration of high-Q photonic heterostructure nanocavities suitable for integration," *Optics Express*, vol. 17, pp. 18093–18102, Sept. 2009.

[12] M. Soljačić and J. D. Joannopoulos, "Enhancement of nonlinear effects using photonic crystals," *Nat. Mater.*, vol. 3, pp. 211–219, Apr. 2004.

[13] P. Barclay, K. Srinivasan, and O. Painter, "Nonlinear response of silicon photonic crystal microresonators excited via an integrated waveguide and fiber taper," *Opt. Express*, vol. 13, no. 3, pp. 801–820, 2005.

[14] C. Monat, B. Corcoran, M. Ebnali-Heidari, C. Grillet, B. J. Eggleton, T. P. White, L. O'Faolain, and T. F. Krauss, "Slow light enhancement of nonlinear effects in silicon engineered photonic crystal waveguides," *Optics Express*, vol. 17, pp. 2944–2953, Feb. 2009.

[15] T. Tanabe, M. Notomi, S. Mitsugi, A. Shinya, and E. Kuramochi, "Fast bistable all-optical switch and memory on a silicon photonic crystal on-chip," *Optics Letters*, vol. 30, pp. 2575–2577, Oct. 2005.

[16] J. F. McMillan, M. B. Yu, D. L. Kwong, and C. W. Wong, "Observation of four-wave mixing in slow-light silicon photonic crystal waveguides," *Optics Express*, vol. 18, pp. 15484–15497, July 2010.

[17] J. Joannopoulos, S. G. Johnson, J. N. Winn, and R. D. Meade, *Photonic Crystals: Molding the Flow of Light (Second Edition)*. 2008.

[18] E. YABLONOVITCH, "Inhibited spontaneous emission in solid-state physics and electronics," *Physical Review Letters*, vol. 58, pp. 2059–2062, May 1987.

[19] S. JOHN, "Strong localization of photons in certain disordered dielectric superlattices," *Physical Review Letters*, vol. 58, pp. 2486–2489, June 1987.

[20] S. Y. Lin, J. G. Fleming, D. L. Hetherington, B. K. Smith, R. Biswas, K. M. Ho, M. M. Sigalas, W. Zubrzycki, S. R. Kurtz, and J. Bur, "A three-dimensional photonic crystal operating at infraredwavelengths," *Nature*, vol. 394, pp. 251–253, 1998.

[21] Z. Han, *Vers le laser Raman à cristal photonique en filière silicium*. PhD thesis, Université Paris Sud XI, 2010.

[22] T. Baba, "Slow light in photonic crystals," *Nature Photonics*, vol. 2, pp. 465–473, Aug. 2008.

[23] H. Benisty, J. M. Lourtioz, A. Chelnokov, S. Combrie, and X. Checoury, "Recent advances toward optical devices in semiconductor-based photonic crystals," *Proceedings Of The Ieee*, vol. 94, pp. 997–1023, 2006.

[24] T. Tanabe, A. Shinya, E. Kuramochi, S. Kondo, H. Taniyama, and M. Notomi, "Single point defect photonic crystal nanocavity with ultrahigh quality factor achieved by using hexapole mode," *Applied Physics Letters*, vol. 91, p. 021110, July 2007.

[25] Y. Taguchi, Y. Takahashi, Y. Sato, T. Asano, and S. Noda, "Statistical studies of photonic heterostructure nanocavities with an average q factor of three million," *Opt. Express*, vol. 19, pp. 11916–11921, Jun 2011.

[26] E. Kuramochi, M. Notomi, S. Mitsugi, A. Shinya, T. Tanabe, and T. Watanabe, "Ultrahigh-Q photonic crystal nanocavities realized by the local width modulation of a line defect," *APPLIED PHYSICS LETTERS*, vol. 88, JAN 23 2006.

[27] Z. Han, X. Checoury, D. Néel, S. David, M. El Kurdi, and P. Boucaud, "Optimized design for 2×10^6 ultra-high Q silicon photonic crystal cavities," *Optics Communications*, vol. 283, no. 21, pp. 4387–4391, 2010.

[28] K. M. LEUNG and Y. F. LIU, "Photon band structures - the plane-wave method," *Physical Review B*, vol. 41, pp. 10188–10190, May 1990.

[29] S. G. Johnson and J. D. Joannopoulos, "Block-iterative frequency-domain methods for maxwell's equations in a planewave basis," *Optics Express*, vol. 8, pp. 173–190, Jan. 2001.

[30] M. Qiu, K. Azizi, A. Karlsson, M. Swillo, and B. Jaskorzynska, "Numerical studies of mode gaps and coupling efficiency for line-defect waveguides in two-dimensional photonic crystals," *Physical Review B*, vol. 64, p. 155113, Oct. 2001.

[31] J. P. BERENGER, "A perfectly matched layer for the absorption of electromagnetic-waves," *Journal of Computational Physics*, vol. 114, pp. 185–200, Oct. 1994.

[32] R. F. W. Pease, "Electron beam lithography," *Contemporary Physics*, vol. 22:3, pp. 265–290, 1981.

[33] J. G. Goodberlet, J. T. Hastings, and H. I. Smith, "Performance of the raith 150 electron-beam lithography system," *Journal of Vacuum Science & Technology B*, vol. 19, pp. 2499–2503, Nov. 2001.

[34] A. M. Hynes, H. Ashraf, J. K. Bhardwaj, J. Hopkins, I. Johnston, and J. N. Shepherd, "Recent advances in silicon etching for mems using the ase (tm) process," *Sensors and Actuators A-physical*, vol. 74, pp. 13–17, Apr. 1999.

[35] G. I. Font, W. L. Morgan, and G. Mennenga, "Cross-section set and chemistry model for the simulation of c-c4f8 plasma discharges," *Journal of Applied Physics*, vol. 91, pp. 3530–3538, Mar. 2002.

[36] L.-D. Haret, *Détecteur en silicium sur cristal photonique par absorption linéaire à deux photons*. PhD thesis, Université paris-Sud, 2012.

[37] X. D. Yang and C. W. Wong, "Coupled-mode theory for stimulated raman scattering in high-q/v-m silicon photonic band gap defect cavity lasers," *Optics Express*, vol. 15, no. 8, pp. 4763–4780, 2007.

[38] A. Yariv, *Optical Electronics in Modern Communications*. Oxford University Press, 1997.

[39] P. J. Petersan and S. M. Anlage, "Measurement of resonant frequency and quality factor of microwave resonators: Comparison of methods," *Journal of Applied Physics*, vol. 84, pp. 3392–3402, Sept. 1998.

[40] R. W. Boyd, *Nonlinear Optics*. Academic Press, 1992.

[41] Q. Lin, O. J. Painter, and G. P. Agrawal, "Nonlinear optical phenomena in silicon waveguides: Modeling and applications," *Optics Express*, vol. 15, pp. 16604–16644, 2007.

[42] H. H. Li, "Refractive index of silicon and germanium and its wavelength and temperature derivatives," *Journal of Physical and Chemical Reference Data*, vol. Volume 9 / Issue 3, p. 98, 1980.

[43] M. Dinu, F. Quochi, and H. Garcia, "Third-order nonlinearities in silicon at telecom wavelengths," *Applied Physics Letters*, vol. 82, pp. 2954–2956, May 2003.

[44] T. Uesugi, B. S. Song, T. Asano, and S. Noda, "Investigation of optical nonlinearities in an ultra-high-Q si nanocavity in a two-dimensional photonic crystal slab," *Optics Express*, vol. 14, pp. 377–386, Jan. 2006.

[45] L.-D. Haret, X. Checoury, Z. Han, P. Boucaud, S. Combrié, and A. D. Rossi, "All-silicon photonic crystal photoconductor on silicon-on-insulator at telecom wavelength," *Opt. Express*, vol. 18, pp. 23965–23972, Nov 2010.

[46] T. Tanabe, H. Sumikura, H. Taniyama, A. Shinya, and M. Notomi, "All-silicon sub-gb/s telecom detector with low dark current and high quantum efficiency on chip," *Applied Physics Letters*, vol. 96, p. 101103, Mar. 2010.

[47] T. J. Johnson, M. Borselli, and O. Painter, "Self-induced optical modulation of the transmission through a high-q silicon microdisk resonator," *Optics Express*, vol. 14, pp. 817–831, Jan. 2006.

[48] T. Johnson, *Silicon Microdisk Resonators for Nonlinear Optics and Dynamics*. PhD thesis, California Institute of Technology, 2009.

[49] B. Jalali, V. Raghunathan, D. Dimitropoulos, and O. Boyraz, "Raman-based silicon photonics," *IEEE Journal of Selected Topics in Quantum Electronics*, vol. 12, pp. 412–421, May-June 2006.

[50] R. W. Hellwarth, "Theory of stimulated raman scattering," *Physical Review*, vol. 130(5), pp. 1850–1852, 1963.

[51] P. A. Temple and C. E. Hathaway, "Multiphonon raman spectrum of silicon," *Physical Review B*, vol. 7(8), p. 3685, 1973.

[52] F. Kroeger, A. Ryasnyanskiy, A. Baron, N. Dubreuil, P. Delaye, R. Frey, G. Roosen, and D. Peyrade, "Saturation of the raman amplification by self-phase modulation in silicon nanowaveguides," *Applied Physics Letters*, vol. 96, p. 241102, June 2010.

[53] R. Claps, D. Dimitropoulos, Y. Han, and B. Jalali, "Observation of raman emission in silicon waveguides at 1.54 um," *Optics Express*, vol. 10, pp. 1305–1313, Nov. 2002.

[54] O. Boyraz and B. Jalali, "Demonstration of a silicon raman laser," *Optics Express*, vol. 12, no. 21, pp. 5269–5273, 2004.

[55] O. Boyraz and B. Jalali, "Demonstration of directly modulated silicon raman laser," *Optics Express*, vol. 13, pp. 796–800, Feb. 2005.

[56] H. S. Rong, R. Jones, A. S. Liu, O. Cohen, D. Hak, A. Fang, and M. Paniccia, "A continuous-wave Raman silicon laser," *Nature*, vol. 433, pp. 725–728, Feb. 2005.

[57] H. S. Rong, S. B. Xu, Y. H. Kuo, V. Sih, O. Cohen, O. Raday, and M. Paniccia, "Low-threshold continuous-wave raman silicon laser," *Nature Photonics*, vol. 1, pp. 232–237, Apr. 2007.

[58] H. S. Rong, S. B. Xu, O. Cohen, O. Raday, M. Lee, V. Sih, and M. Paniccia, "A cascaded silicon Raman laser," *Nature Photonics*, vol. 2, pp. 170–174, Mar. 2008.

[59] S. Malaguti, G. Bellanca, A. de Rossi, S. Combrie, and S. Trillo, "Self-pulsing driven by two-photon absorption in semiconductor nanocavities," *Physical Review A*, vol. 83, p. 051802, May 2011.

[60] M. Soltani, S. Yegnanarayanan, Q. Li, A. A. Eftekhar, and A. Adibi, "Self-sustained gigahertz electronic oscillations in ultrahigh-q photonic microresonators," *Physical Review A*, vol. 85, p. 053819, May 2012.

[61] J. Capmany and D. Novak, "Microwave photonics combines two worlds," *Nature Photonics*, vol. 1, pp. 319–330, June 2007.

[62] K. Ikeda and O. Akimoto, "Instability leading to periodic and chaotic self-pulsations in a bistable optical cavity," *Phys. Rev. Lett.*, vol. 48, pp. 617–620, Mar. 1982.

[63] Y. F. Shaowu Chen, Libin Zhang and T. Cao, "Bistability and self-pulsation phenomena in silicon microring resonators based on nonlinear optical effects," *Optics Express*, vol. 20, no. 7, pp. 7454–7468, 2012.

[64] M. Brunstein, A. M. Yacomotti, I. Sagnes, F. Raineri, L. Bigot, and A. Levenson, "Excitability and self-pulsing in a photonic crystal nanocavity," *Phys. Rev. A*, vol. 85, pp. 031803–, Mar. 2012.

[65] Z. Han, X. Checoury, L.-D. Haret, and P. Boucaud, "High quality factor in a two-dimensional photonic crystal cavity on silicon-on-insulator," *Opt. Lett.*, vol. 36, pp. 1749–1751, May 2011.

[66] T. J. Johnson and O. Painter, "Passive modification of free carrier lifetime in high-q silicon-on-insulator optics," *2009 Conference On Lasers and Electro-optics and Quantum Electronics and Laser Science Conference (cleo/qels 2009), Vols 1-5*, pp. 72–73, 2009.

[67] T. Tanabe, H. Taniyama, and M. Notomi, "Carrier diffusion and recombination in photonic crystal nanocavity optical switches," *Journal Of Lightwave Technology*, vol. 26, pp. 1396–1403, May 2008.

[68] S. Kaka, M. R. Pufall, W. H. Rippard, T. J. Silva, S. E. Russek, and J. A. Katine, "Mutual phase-locking of microwave spin torque nano-oscillators," *Nature*, vol. 437, pp. 389–392, Sept. 2005.

[69] A. C. Turner-Foster, M. A. Foster, J. S. Levy, C. B. Poitras, R. Salem, A. L. Gaeta, and M. Lipson, "Ultrashort free-carrier lifetime in low-loss silicon nanowaveguides," *Optics Express*, vol. 18, pp. 3582–3591, Feb. 2010.

[70] B. Jalali, "Silicon lasers," *APS NEWS*, vol. 15, 2006.

[71] M. Fujita, "Silicon photonics: Nanocavity brightens silicon," *Nat Photon*, vol. 7, pp. 264–265, Apr. 2013.

[72] J. E. McMillan, X. D. Yang, N. C. Panoiu, R. M. Osgood, and C. W. Wong, "Enhanced stimulated raman scattering in slow-light photonic crystal waveguides," *Optics Letters*, vol. 31, no. 9, pp. 1235–1237, 2006.

[73] J. F. McMillan, M. B. Yu, D. L. Kwong, and C. W. Wong, "Observation of spontaneous raman scattering in silicon slow-light photonic crystal waveguides," *Applied Physics Letters*, vol. 93, no. 25, p. 251105, 2008.

[74] X. Checoury, M. El Kurdi, Z. Han, and P. Boucaud, "Enhanced spontaneous raman scattering in silicon photonic crystal waveguides on insulator," *Optics Express*, vol. 17, no. 5, pp. 3500–3507, 2009.

[75] X. Checoury, Z. Han, and P. Boucaud, "Stimulated Raman scattering in silicon photonic crystal waveguides under continuous excitation," *Physical Review B*, vol. 82, JUL 26 2010.

[76] X. D. Yang and C. W. Wong, "Design of photonic band gap nanocavities for stimulated raman amplification and lasing in monolithic silicon," *Optics Express*, vol. 13, pp. 4723–4730, June 2005.

[77] X. D. Yang and C. W. Wong, "Stimulated raman amplification and lasing in silicon photonic band gap nanocavities," *Sensors and Actuators A-physical*, vol. 133, pp. 278–282, Feb. 2007.

[78] L. A. Coldren and S. W. Corzine, *Diode Lasers and Photonic Integrated Circuits*. Wiley, 1995.

[79] K. Inoue, H. Oda, A. Yamanaka, N. Ikeda, H. Kawashima, Y. Sugimoto, and K. Asakawa, "Dramatic density-of-state enhancement of Raman scattering at the band edge in a one-dimensional photonic-crystal waveguide," *Physical Review A*, vol. 78, no. 1, p. 011805, 2008.

[80] H. Oda, K. Inoue, A. Yamanaka, N. Ikeda, Y. Sugimoto, and K. Asakawa, "Light amplification by stimulated Raman scattering in AlGaAs-based photonic-crystal line-defect waveguides," *Applied Physics Letters*, vol. 93, no. 5, 2008.

[81] Y. Ota, K. Watanabe, S. Iwamoto, and Y. Arakawa, "Nanocavity-based self-frequency conversion laser," *Optics Express*, vol. 21, pp. 19778–19789, Aug. 2013.

[82] X. Checoury, Z. Han, M. El Kurdi, and P. Boucaud, "Deterministic measurement of the purcell factor in microcavities through raman emission," *Phys. Rev. A*, vol. 81, p. 033832, Mar 2010.

[83] S. M. Ulrich, C. Gies, S. Ates, J. Wiersig, S. Reitzenstein, C. Hofmann, A. Loffler, A. Forchel, F. Jahnke, and P. Michler, "Photon statistics of semiconductor microcavity lasers," *Physical Review Letter*, vol. 98, p. 043906, 2007.

[84] A. S. Liu, H. S. Rong, and M. Paniccia, "Net optical gain in a low loss silicon-on-insulator waveguide by stimulated raman scattering," *Optics Express*, vol. 12, pp. 4261–4268, Sept. 2004.